REPORT NO. GDC-DCB69-046
CONTRACT NAS 9-9207

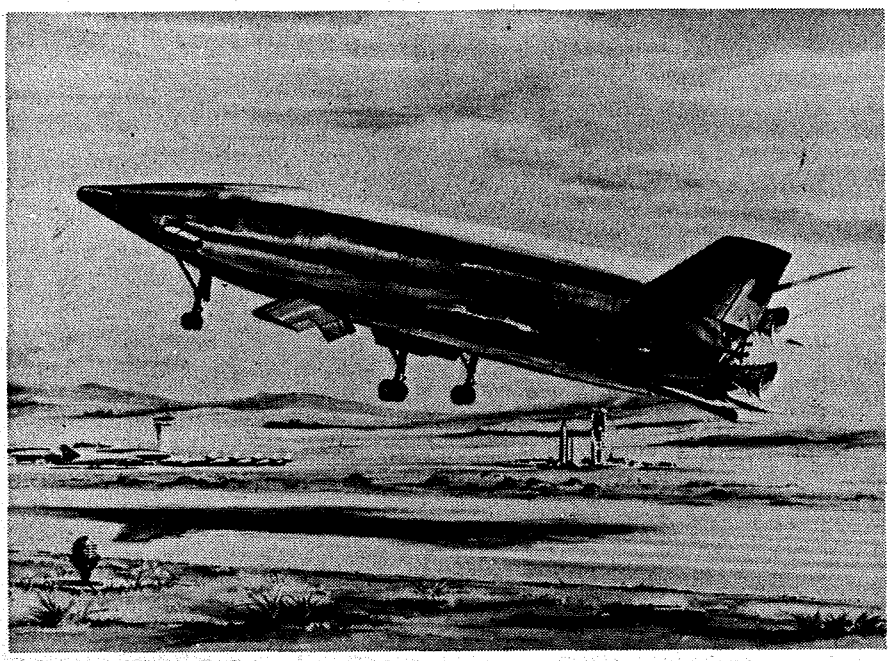

SPACE SHUTTLE
FINAL TECHNICAL REPORT

VOLUME IV ✦ TECHNICAL ANALYSIS AND PERFORMANCE

GENERAL DYNAMICS
Convair Division

REPORT NO. GDC-DCB69-046

SPACE SHUTTLE
FINAL TECHNICAL REPORT

VOLUME IV • TECHNICAL ANALYSIS AND PERFORMANCE

31 October 1969

Prepared by
CONVAIR DIVISION OF GENERAL DYNAMICS
San Diego, California

FOREWORD

This volume of Convair Report No. GDC-DCB 69-046 constitutes a portion of the final report for the "Study of Integral Launch and Reentry Vehicles." The study was conducted by Convair, a division of General Dynamics Corporation, for National Aeronautics and Space Administration George C. Marshall Space Flight Center under Contract NAS 9-9207 Modification 2.

The final report is published in ten volumes:

Volume I	Condensed Summary
Volume II	Final Vehicle Configurations
Volume III	Initial Vehicle Spectrum and Parametric Excursions
Volume IV	Technical Analysis and Performance
Volume V	Subsystems and Weight Analysis
Volume VI	Propulsion Analysis and Tradeoffs
Volume VII	Integrated Electronics
Volume VIII	Mission/Payload and Safety/Abort Analyses
Volume IX	Ground Turnaround Operations and Facility Requirements
Volume X	Program Development, Cost Analysis, and Technology Requirements

Convair gratefully acknowledges the cooperation of the many agencies and companies that provided technical assistance during this study:

NASA-MSFC	Aerojet-General Corporation
NASA-MSC	Rocketdyne
NASA-ERC	Pratt and Whitney
NASA-LaRC	Pan American World Airways

The study was managed and supervised by Glenn Karel, Study Manager, C. P. Plummer, Principal Configuration Designer, and Carl E. Crone, Principal Program Analyst (all of Convair) under the direction of Charles M. Akridge and Alfred J. Finzel, NASA study co-managers.

ABSTRACT

A study was made to obtain a conceptual definition of reusable space shuttle systems having multimission capability. The systems as defined can deliver 50,000-pound payloads having a diameter of 15 feet and a length of 60 feet to a 55-degree inclined orbit at an altitude of 270 n.mi. The following types of missions can be accommodated by the space shuttle system: logistics; propellant delivery; propulsive stage delivery; satellite delivery, retrieval, and maintenance; short-duration missions, and rescue missions.

Two types of reusable space shuttle systems were defined: a two-element system consisting of a boost and an orbital element and a three-element system consisting of two boost elements and an orbital element. The vehicles lift off vertically using high pressure oxygen/hydrogen rocket engines, land horizontally on conventional runways, and are fully reusable. The boost elements, after staging, perform an aerodynamic entry and fly back to the launch site using conventional airbreathing engines. Radiative thermal protection systems were defined to provide for reusability. Development programs, technology programs, schedules, and costs have been defined for planning purposes.

During the study, special emphasis was given to the following areas: System Development Approaches, Ground Turnaround Operations, Mission Interfaces and Cargo Accommodations/Handling, Propulsion System Parameters, and Integrated Electronics Systems.

TABLE OF CONTENTS

TABLE OF CONTENTS, Contd

TABLE OF CONTENTS, Contd

LIST OF FIGURES

LIST OF FIGURES, Contd

LIST OF FIGURES, Contd

LIST OF FIGURES, Contd

LIST OF FIGURES, Contd

LIST OF FIGURES, Contd

LIST OF FIGURES, Contd

LIST OF FIGURES, Contd

LIST OF FIGURES, Contd

LIST OF TABLES

LIST OF TABLES, Contd

SECTION 1

INTRODUCTION

This volume documents the technical analyses used to define the conceptual reusable space shuttle systems with multimission capability studied under NASA Contract NAS 99207. Two types of systems were defined: a two-element system consisting of a boost and an orbital element and a three-element system consisting of two boost elements and an orbital element. The vehicles lift off vertically using high pressure oxygen/hydrogen rocket engines, land horizontally on conventional runways, and are fully reusable. The boost elements, after staging, perform an aerodynamic entry and fly back to the launch site using conventional airbreathing engines. Radiative thermal protection subsystems were defined to provide for reusability.

The configurations presented are conceptual designs, and all the problems have not been resolved. The purpose of the analysis was to explore various configurational concepts and operational approaches to a reusable space shuttle system in order to:

a. Establish technological feasibility of the concepts.

b. Define potential problem areas.

c. Establish requirements for research and technology development.

The technical analyses in this volume include:

Section 2	Aerodynamics
Section 3	Performance
Section 4	Aerothermodynamics
Section 5	Loads
Section 6	Stress
Section 7	Aeroelastic

These analyses showed that the reuseable space shuttle system is a feasible system and established the technology requirements described in Volume X. The technology needs with the most significant influence on vehicle configuration are:

a. Refinement of the aerothermodynamic heating rate predictions and definition of a thermal protection system.

b. Development of the aerodynamic configuration.

c. Further development and tradeoffs between aerodynamic and reaction controls, especially for the booster.

SECTION 2

AERODYNAMICS

The aerodynamic data presented in this section was developed as much as possible from the wind tunnel data obtained from Convair and Convair/NASA joint test programs. This data is presented in part in References 2-1 and 2-2, which present data from the earlier tests. Data from the later tests is being reduced and was partly incorporated in this analysis (as much as time permitted). Where test data was not available on the specific configuration, the approach to analysis was to obtain data from tests of similar configurations and to scale the data by suitable similarity laws or by using existing prediction methods that have proven useful on similar configurations. The data will be presented in two major sections: 2.1 FR-4 three-element configuration and 2.2 FR-3 two-element configuration.

2.1 FR-4 AERODYNAMIC DATA

The lifting body shape of the three-element configuration was based on Convair's experience with hypersonic entry vehicles. A test was performed at Princeton University (Reference 2-3) to evaluate the subsonic aerodynamics of this configuration. The results of these tests were used to generate a vehicle referred to as the inital point design (IPD), in which the basic lines of the hypersonic lifting body shape and the subsonic wing shape were defined. An extensive test program was then undertaken to examine the aerodynamic characteristics of this configuration across the Mach range from hypersonic through subsonic (Table 2-1). This test program was performed separately from the NASA contract to explore the technology of this class of vehicle.

The configuration evolved from this IPD design (called the T-18) is the final FR-1 vehicle and is the basis of the FR-4 vehicles. Since it contains the same body lines as the IPD configuration without the boattail, the basic IPD data has been corrected with test data on boattail effects and has been scaled to the latest vehicles. The effect of removing the boattail has been tested at speeds up to Mach 5, and the T-18 shape has been used in the later test series. Data from the later tests has not been fully incorporated into the vehicle design due to incompatible test and study schedules. Some configuration modification is indicated from the latest tests, principally in reducing body nose-up pitching moment at zero lift and increasing longitudinal control effectiveness. The aerodynamic data will be discussed in the following sequence.

a. Reference area and lengths

b. Launch configuration aerodynamics

c. Hypersonic aerodynamics

d. Viscous interaction effects

Table 2-1. Aerodynamic Test Program Summary

Category	Single Element							Launch Configuration		Staging	Powered Model
Test	Subsonic Force	Subsonic Force	High Reynolds No. Force	Transonic/ Supersonic Force	Hypersonic Force	Hypersonic Pressure	Transonic/ Supersonic Force	Transonic Force and Pressure	Transonic Force	Supersonic Captive Trajectory	Transonic Force Test Powered
Facility	Princeton LSWT	Convair LSWT	NASA/LRC 21-in. Pressure	NASA/MSFC 14-in. Supersonic	AEDC Tunnel C	NASA/LRC	NASA/MSFC 14-in. Supersonic	Cornell Transonic	NASA/MSFC 14-in. Supersonic	Convair HSWT	NSRDC Transonic
Test Conditions	M = 0.1	M = 0.3	M = 0.03	M = 0.8 to 5.0	M = 10	M = 7.8	M = 0.7 to 5.0	M = 0.6 to 1.3	M = 0.8 to 5.0	M = 1.6 and 4.0	M = 0.3 to 0.7
Configuration	General Body	IPD Cruise and T-18	IPD Cruise and T-18	IPD Entry	IPD Entry	IPD Entry	T-18	Three-Body and Two-Stage	Two-Stage	Two-Stage	
Scale	1/60	1/32	1/68	1/194	1/55	1/160	1/150	1/43	1/287	1/194	1/32
Purpose	Exploratory Subsonic Test of Body/Tail Configurations	Buildup Data, Geometry Effects	Reynolds No. Effects on Deployable Wing	Stability and Control	Stability and Control	Limited Pressure Test	Stability and Control with Wing Extension	Longitudinal and Lateral Data, Pressure Distribution	Longitudinal and Lateral Data	Initial Staging Conditions	Power Effects on Aero Characteristics
Test Dates (All 1969) 4 Hours	48 hr Completed 25 Feb	77 hr Completed 3 Jul	40 hr Completed 29 Aug	80 hr Completed 4 Sep	16 hr Completed 24 Sep	16 hr Completed 13 Oct	80 hr Completed 16 Oct	50 hr Completed 21 Jul	40 hr Completed 23 Oct	50 hr Completed 18 Jul	80 hr Scheduled Jan 70
Status	Data Input to T-18 Test and Data Analysis Complete	Low Speed Test Data Input to T-18; Analysis Essentially Complete	Re No. Effects Input to T-18; Analysis Partially Complete	Base for Mach Number Effects (T-18); Analysis Initiated	Data Base for Control Effectiveness at Mach 10 (T-18); Analysis Initiated		Analysis Initiated	Analysis Essentially Complete	Analysis Initiated	Analysis Essentially Complete	Model Design Delivery to NASA MSFC by 24 Nov 69

FOLDOUT FRAME

FOLDOUT FRAME

e. Effect of Mach number

f. Subsonic characteristics

g. Cruise engine effects

h. Tail sizing

2.1.1 REFERENCE AREA AND LENGTHS. Figure 2-1 is a three-view drawing of the FR-4 configuration. Reference parameters for the aerodynamic data are:

	Orbiter	Booster
Reference Area (ft^2)	5565	6072
Reference Length (ft)	191	200
Reference Span (ft)	35.1	35.1
Center of Gravity Location	$0.55\ell_{ref}$	$55\%\ell_{ref}$
Exposed Wing Area Swing/S_{ref}	0.273	0.273
Exposed V-tail Area S_{tail}/S_{ref}	0.281	0.281
Ruddervator Area S_{rud}/S_{ref}	0.0985	0.0985

The small difference between booster and orbiter does not change the aerodynamic characteristics, since they are based on a planform area and length.

2.1.2 LAUNCH CONFIGURATION AERODYNAMICS. Figures 2-2 through 2-7 present the aerodynamic characteristics of the three-body configuration, with all data referenced to the planform area of one body. Figure 2-2 presents the axial force at zero angle of attack as a function of Mach number. The test data were obtained from IPD launch configuration data generated at Cornell Aeronautical Laboratory corrected using Atlas base pressure drag (which shows base thrust above Mach 3). The vehicle synthesis model shown used a Saturn base pressure model, which accounts for the principal difference in the subsonic region. Considering the typical variation of dynamic pressure with Mach number, the difference in ascent drag losses between these two curves is probably small. The synthesis run shows that 370 fps of a 570-fps drag loss occurs below Mach 1.1 (where the estimate is high) and 200 fps above Mach 1.1 (where the estimate is low).

Figures 2-3 and 2-4 present the normal force and side force gradients as functions of Mach number at zero angles of attack and yaw. The loss of V-tail effectiveness with increasing Mach number is the primary reason for the decline in force gradients.

The launch configuration is not symmetric in pitch, so a zero-lift pitching moment must be accounted for during launch. Figure 2-5 presents this moment as a function of Mach number. The V-tail accounts for the nose-down moment at subsonic and

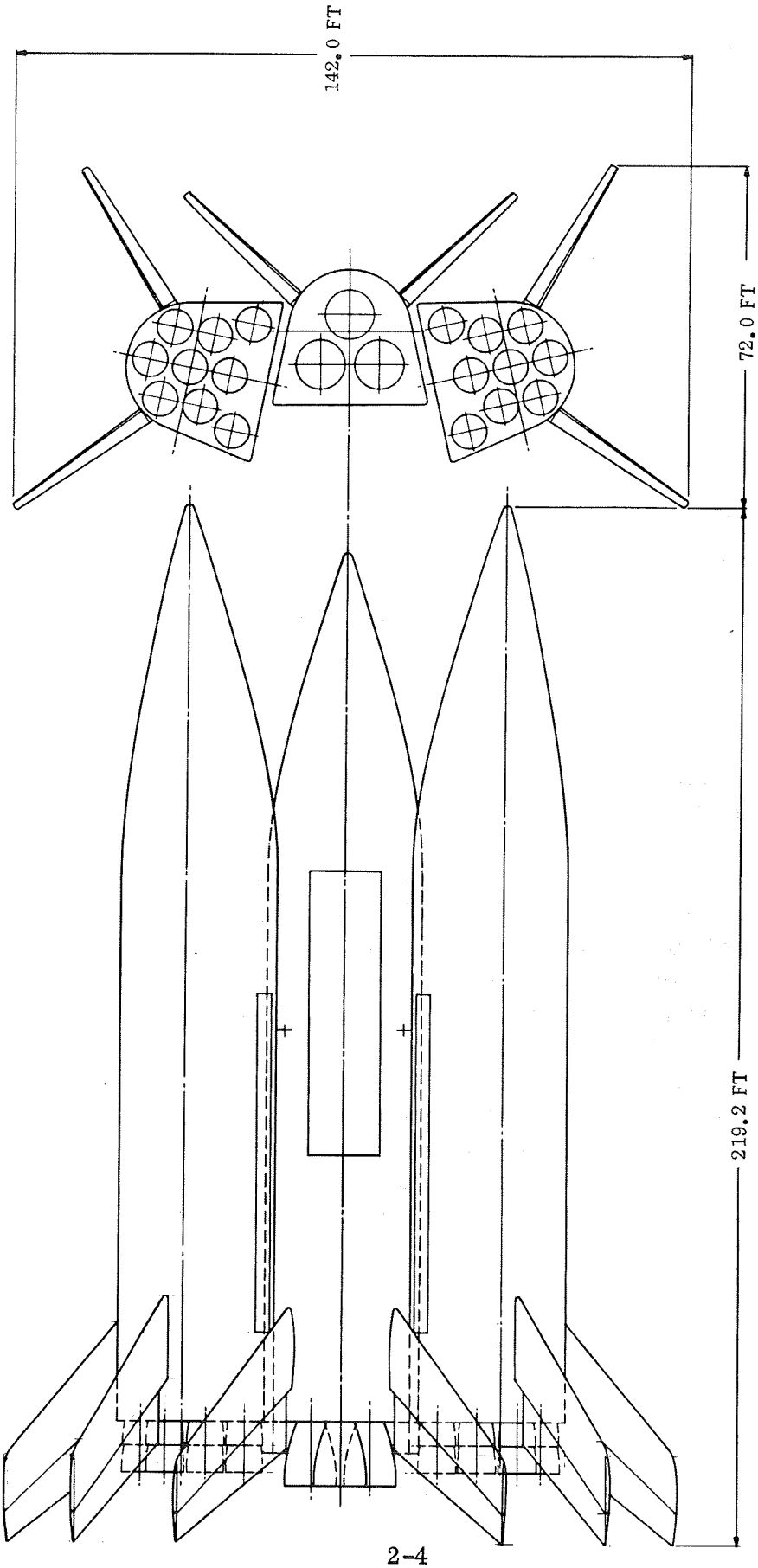

Figure 2-1. FR-4 Launch Configuration

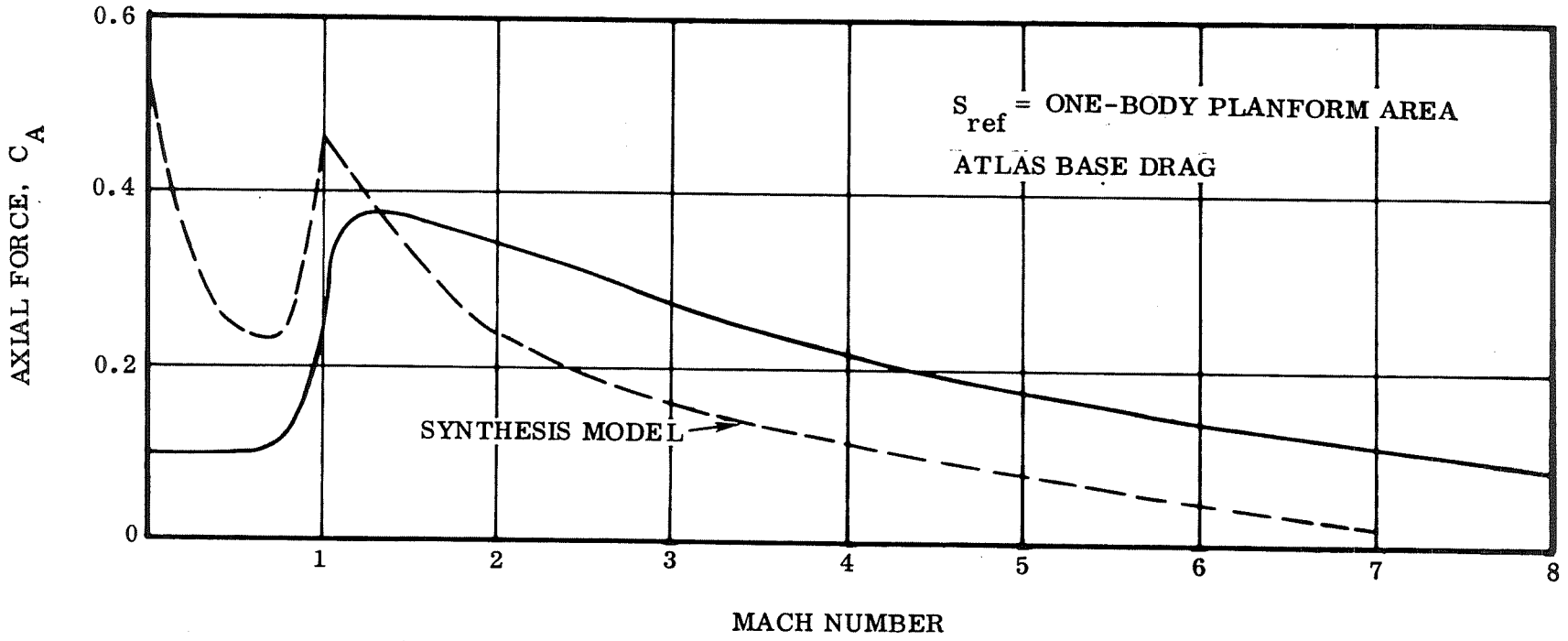

Figure 2-2. FR-4 Launch Configuration Drag (α = 0 degree)

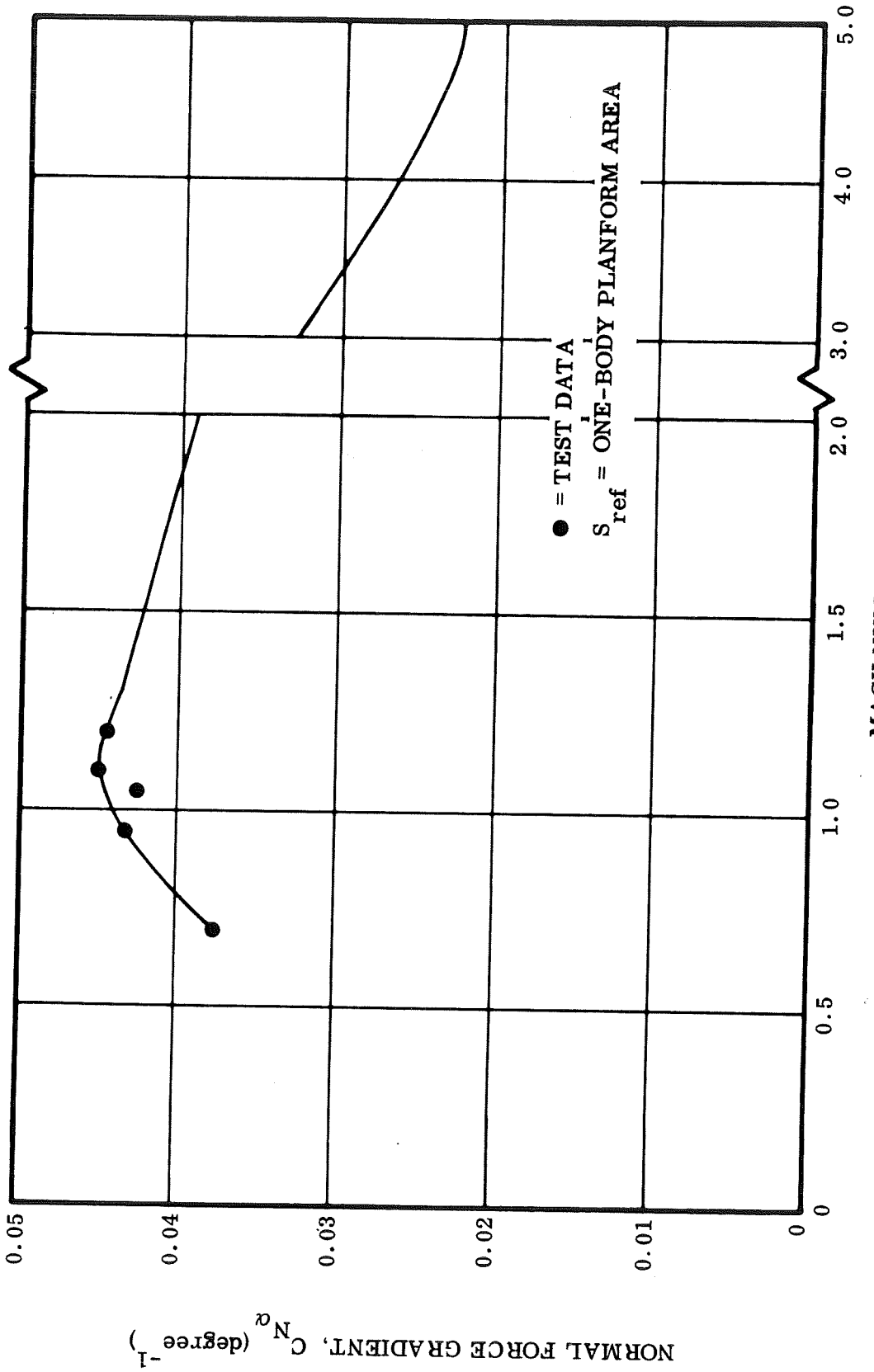

Figure 2-3. FR-4 Launch Configuration Normal Force Gradient (α = 0 degrees)

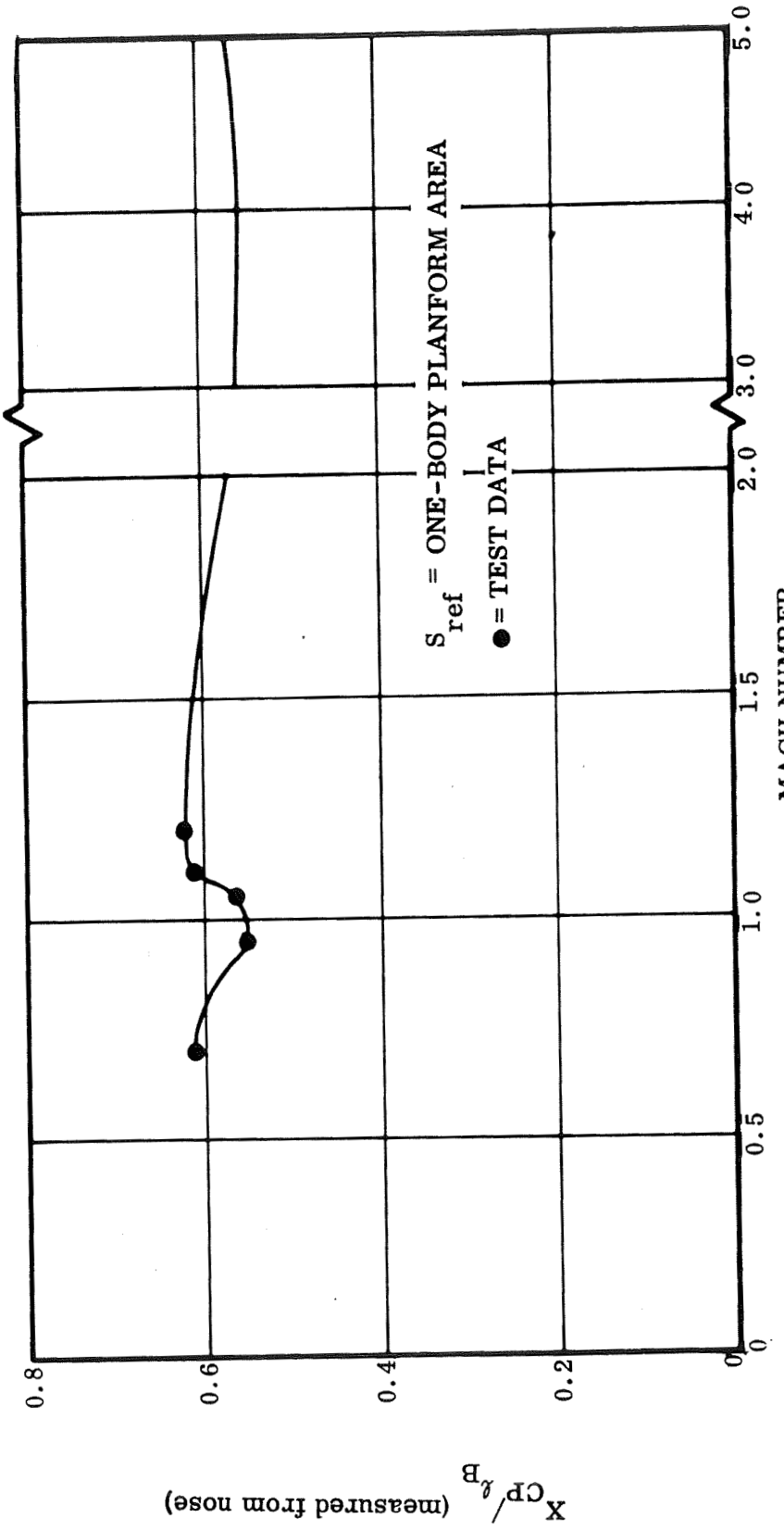

Figure 2-4. FR-4 Launch Configuration Lateral Center of Pressure (α = Degrees, β = 0)

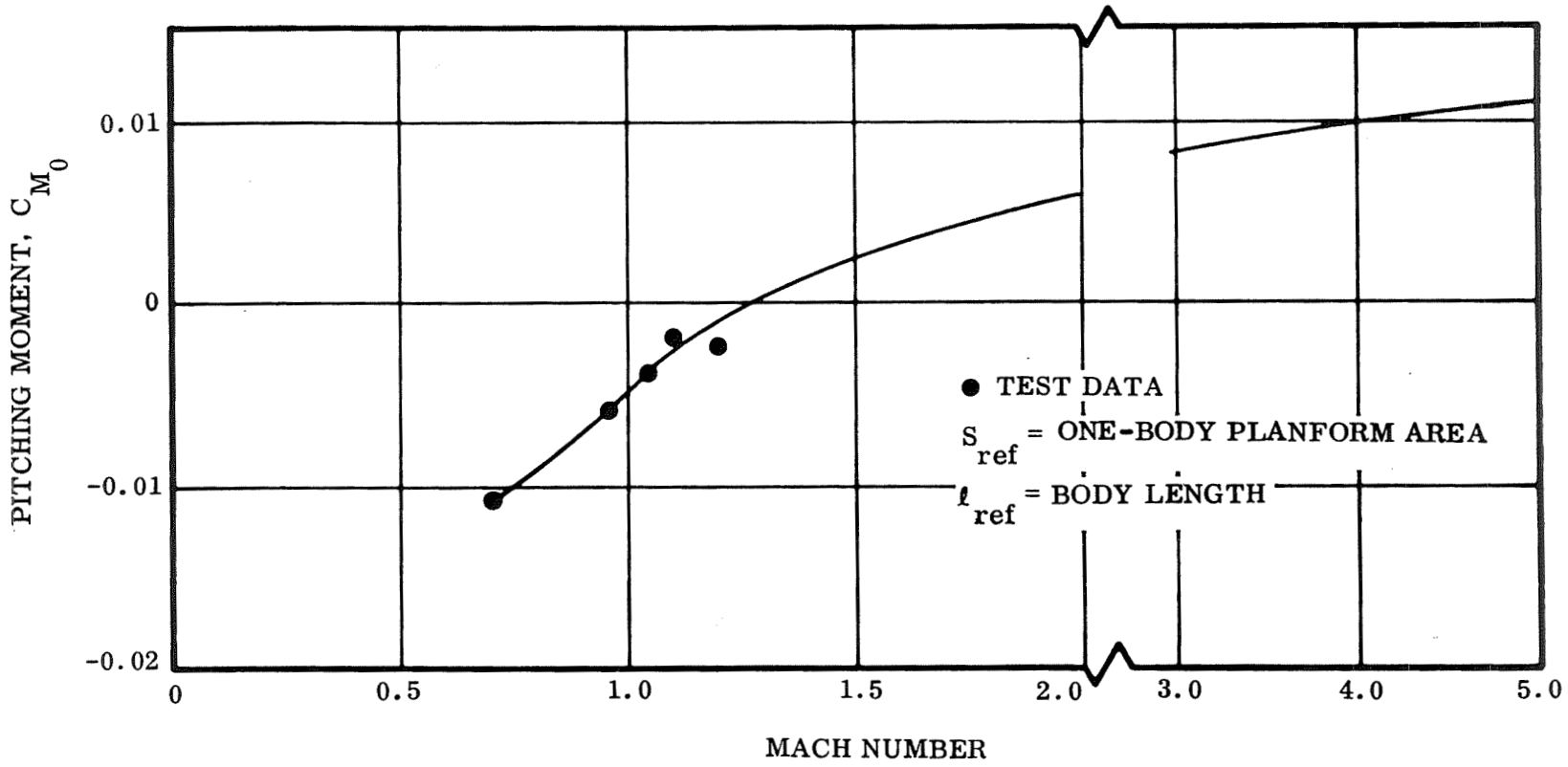

Figure 2-5. FR-4 Launch Configuration Zero-Lift Pitching Moment

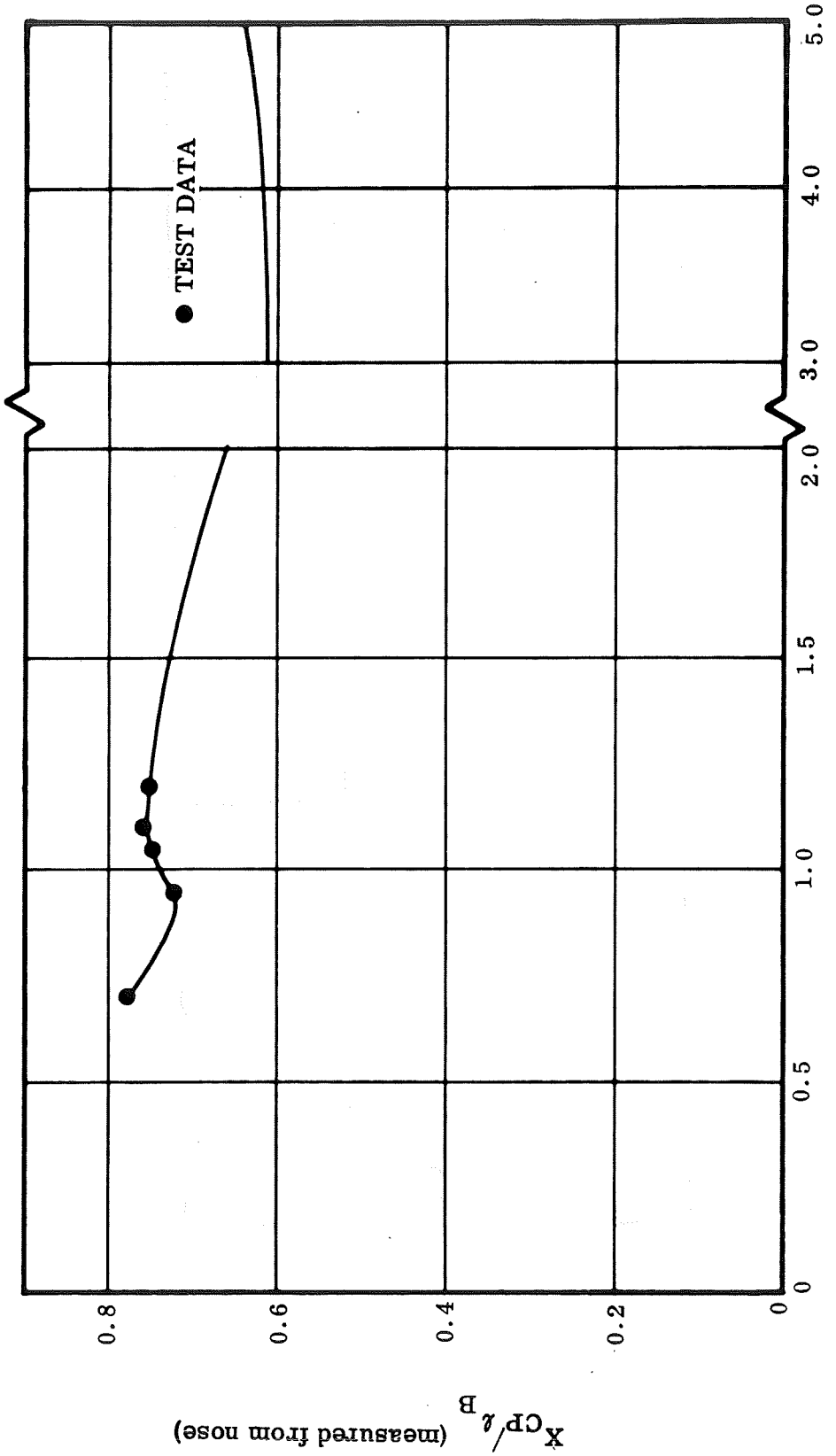

Figure 2-6. FR-4 Launch Configuration Center of Pressure in Pitch (α = 0 Degrees)

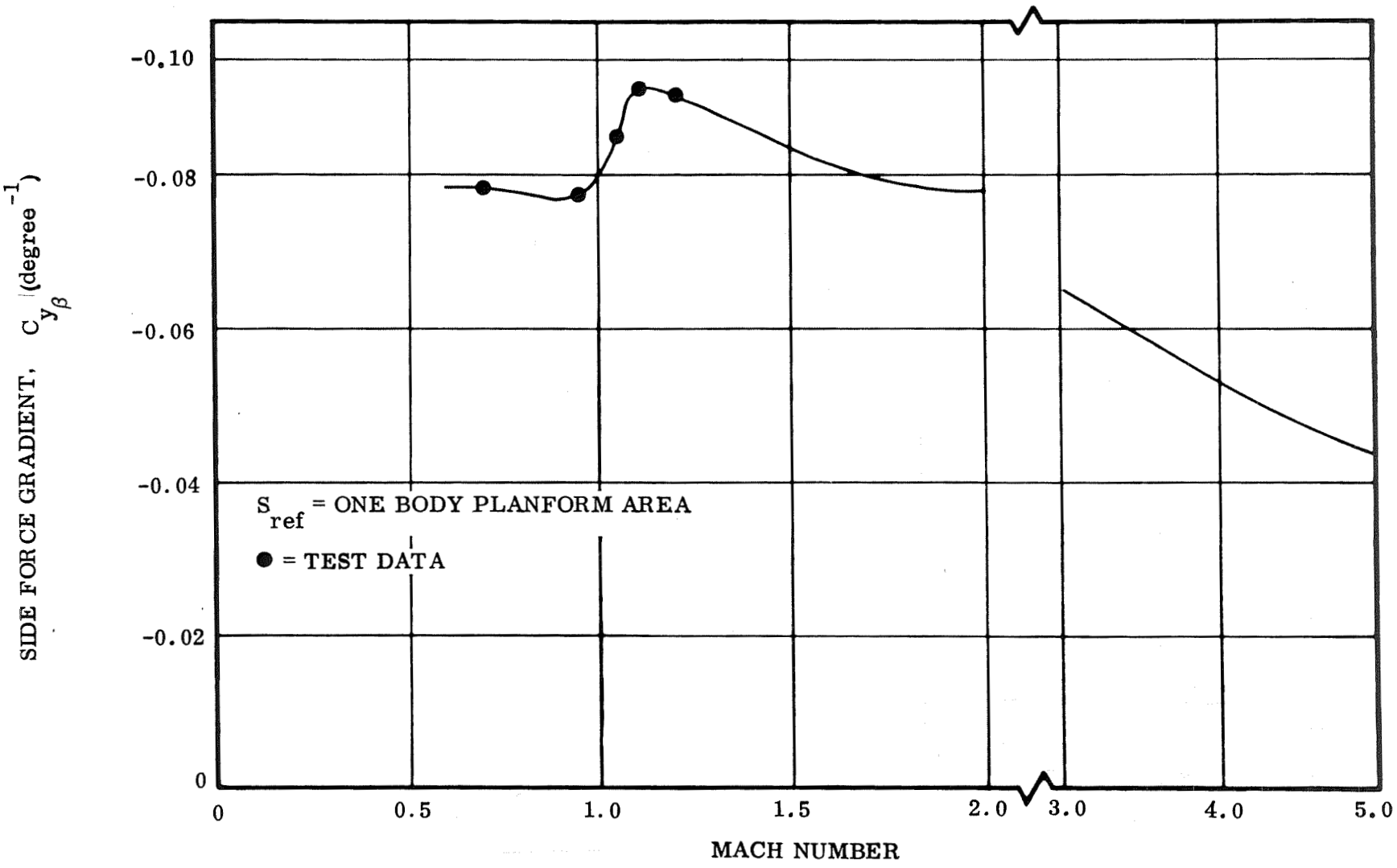

Figure 2-7. FR-4 Launch Configuration Side-Force Gradient (α = 0 Degrees, β = 0)

transonic speeds. The tail loses its effectiveness with increasing Mach number while the body front surface ramp becomes increasingly effective, with the net result of an increasing nose-up moment. Figures 2-6 and 2-7 present the three-element center of pressure for the pitch and yaw planes, which shows the same trends as the other data.

2.1.3 HYPERSONIC AERODYNAMICS. The aerodynamic control surfaces used in the hypersonic speed regime are ruddervators on the V-shaped tail for pitch and roll control. The adverse yaw due to roll is taken out with reaction controls. The orbiter has a complete reaction control subsystem and the booster has two lateral thrusters located in the nose for this purpose. The orbiter element is different from the booster elements in that it has a 10-degree-deflection fixed surface so it will trim at the angle of attack for maximum crossrange. The hypersonic characteristics of both booster and orbiter are based on Mach 10 data obtained in Tunnel C at AEDC on the IPD configuration combined with data generated using the Convair hypersonic aerodynamic program (HAP). This computer program uses empirically modified Newtonian theory for pressures in conjunction with the reference enthalpy method for friction to compute the hypersonic aerodynamic characteristics of an arbitrary body. The characteristics were evaluated at a reference condition of 20,000 ft/sec at a 200,000-foot altitude. Basic characteristics are presented in Figure 2-8, which shows the variation of lift coefficient (C_L), and lift to drag (L/D). It also presents the longitudinal stability in a C_M-C_N plot.

The difference between booster and orbiter trim is caused by the fixed trimming surface on the orbiter. The maximum L/D occurs near an angle of attack of 15 degrees, which is outside the trim range of the orbiter. This represents a potential crossrange capability of over 1500 n.mi., which could be attained by modification of the vehicle. The present crossrange capability of the orbiter is 800 nautical miles, which was a design requirement for the once-around abort case.

The lateral directional characteristics of the FR-4 configuration are presented in Figure 2-9. Untrimmed curves of $C_{n\beta}$, $C_{y\beta}$, and $C_{\ell\beta}$ are presented as functions of angle of attack. The vehicle is directionally stable above an angle of attack of 10 degrees. Trailing-edge down deflections of the ruddervators required to trim to lower angles of attack increase directional stability considerably, as shown by the curve for $\delta_{er} = 20$ degrees.

The roll-control effectiveness of the ruddervators is presented in Figure 2-10 as a function of angle of attack. The figure also shows the yaw induced by asymmetric rudder deflections. This is an adverse yaw due to roll, and is the reason reaction controls would be necessary when employing the ruddervators for roll control.

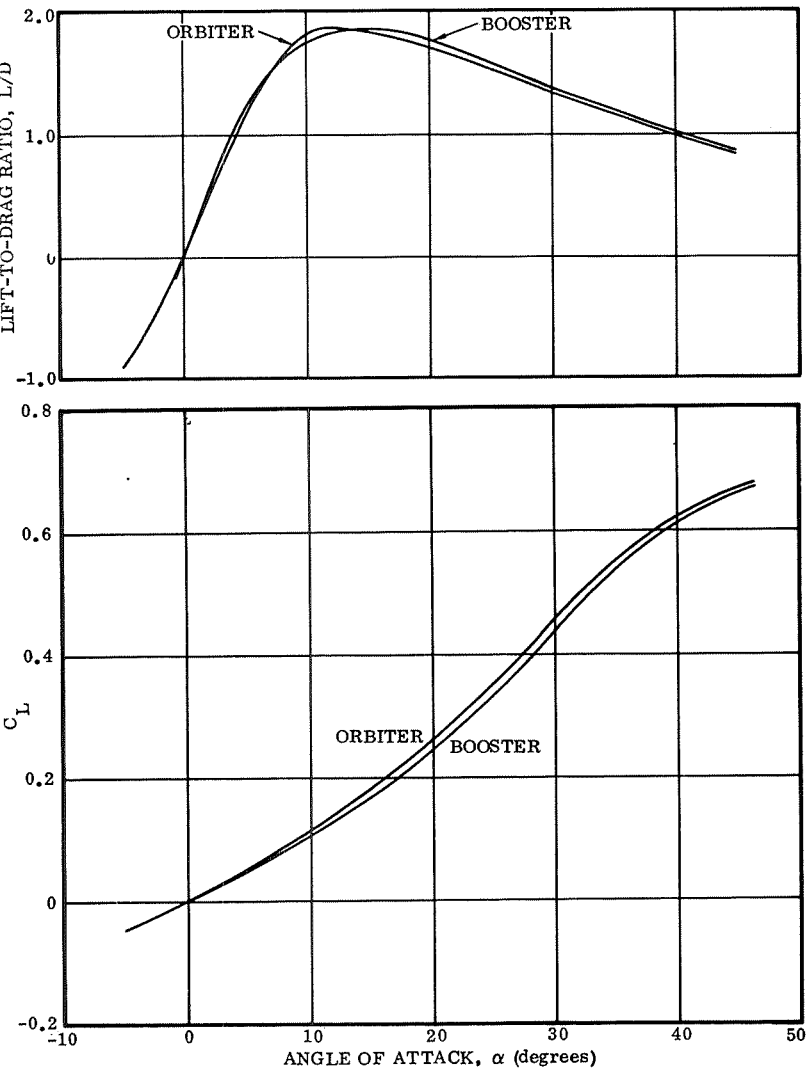

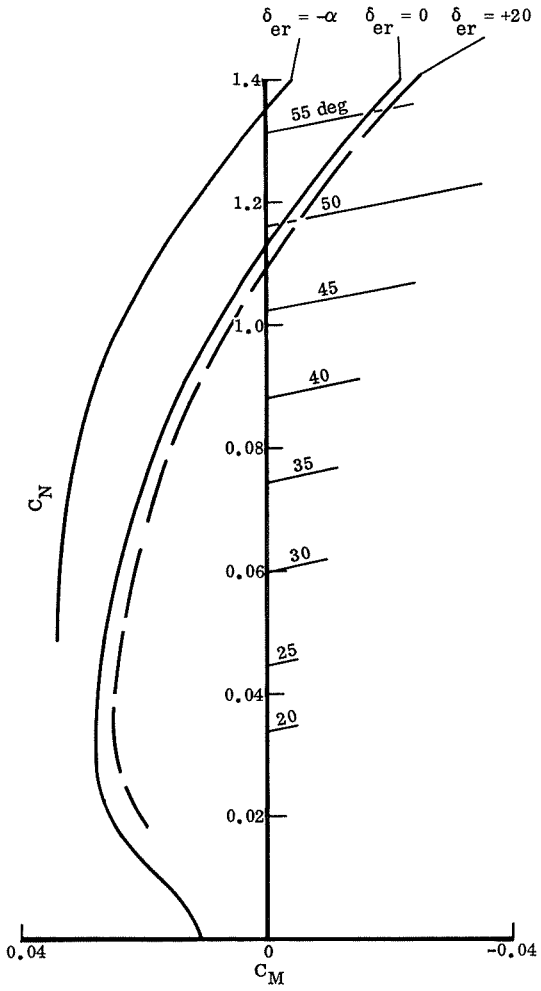

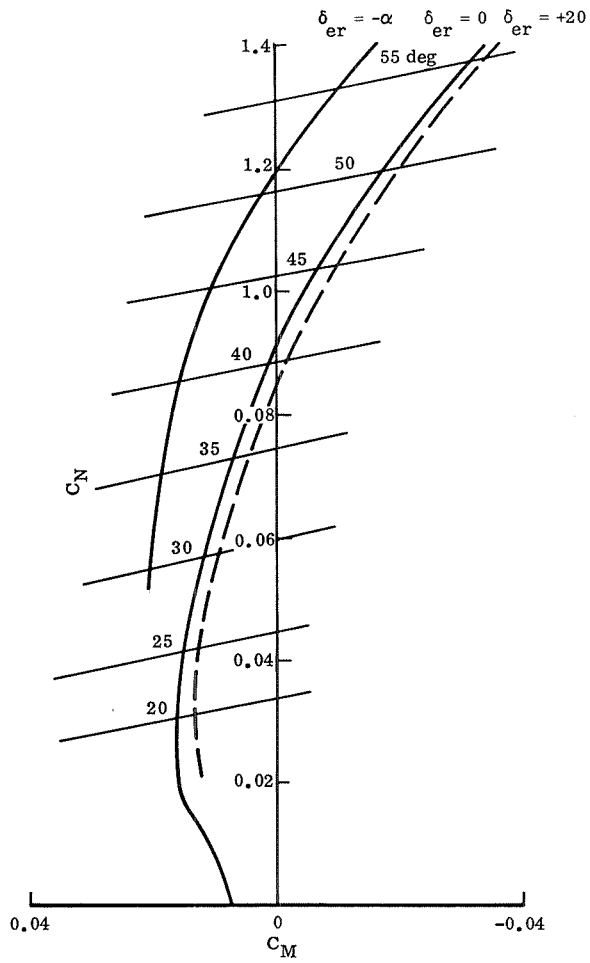

Figure 2-8. FR-4 Hypersonic Characteristics

FOLDOUT FRAME

FOLDOUT FRAME 2

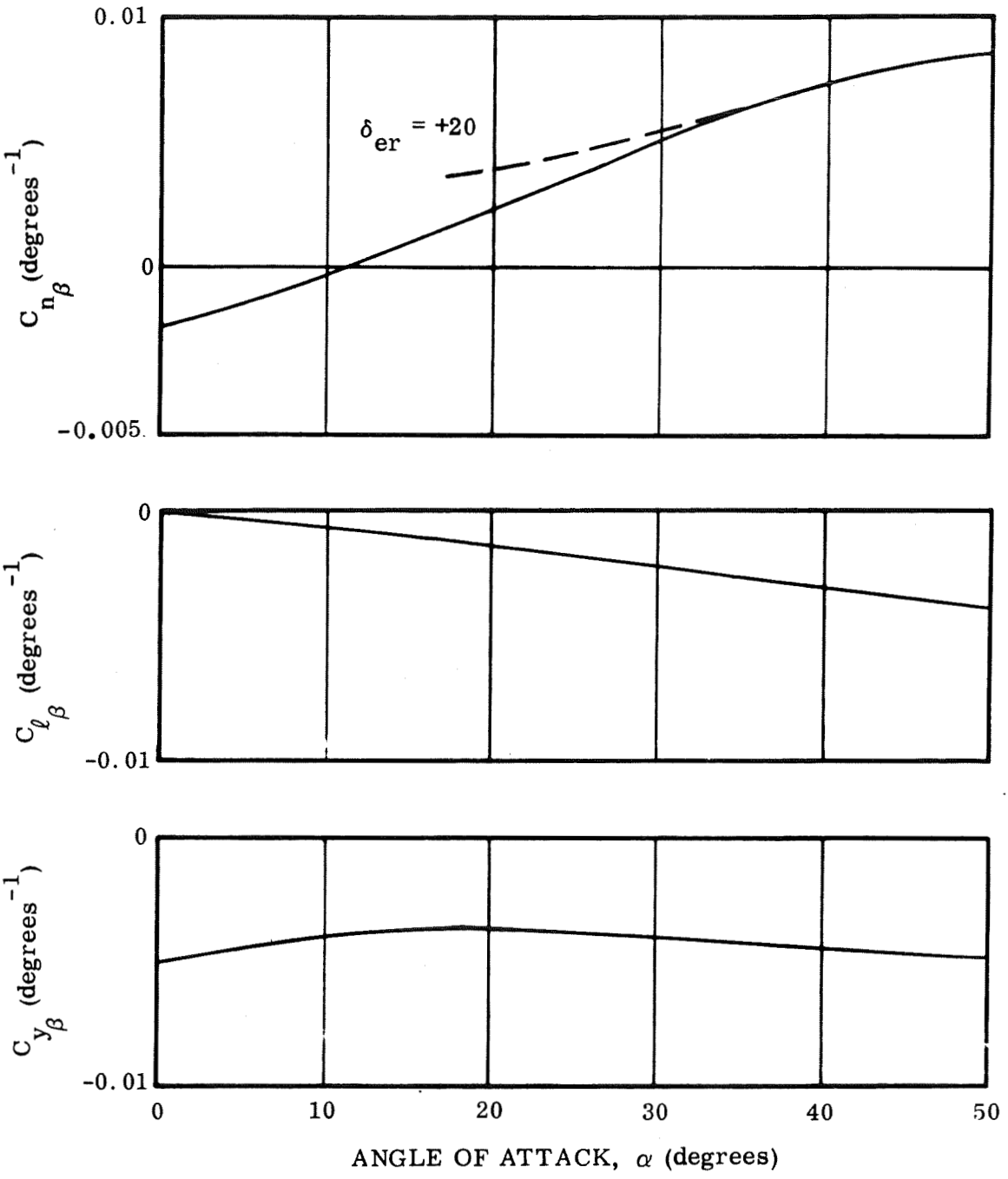

Figure 2-9. FR-4 Hypersonic Lateral Directional Characteristics

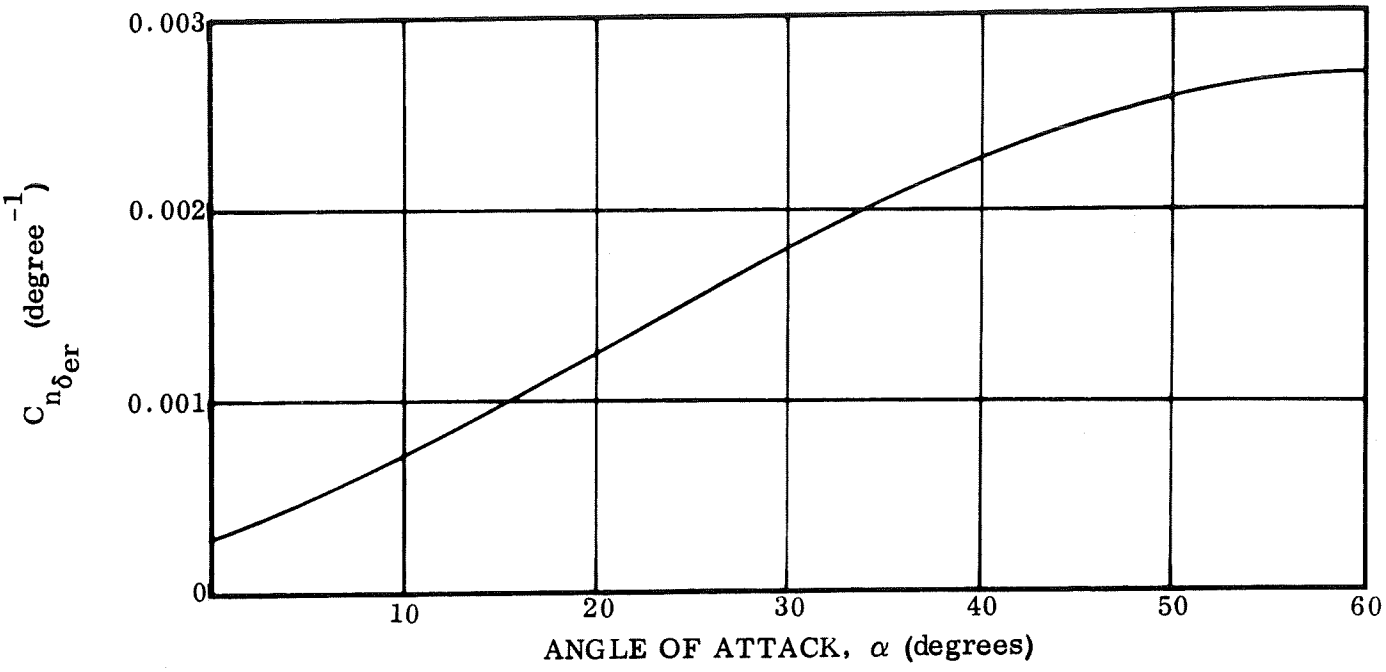

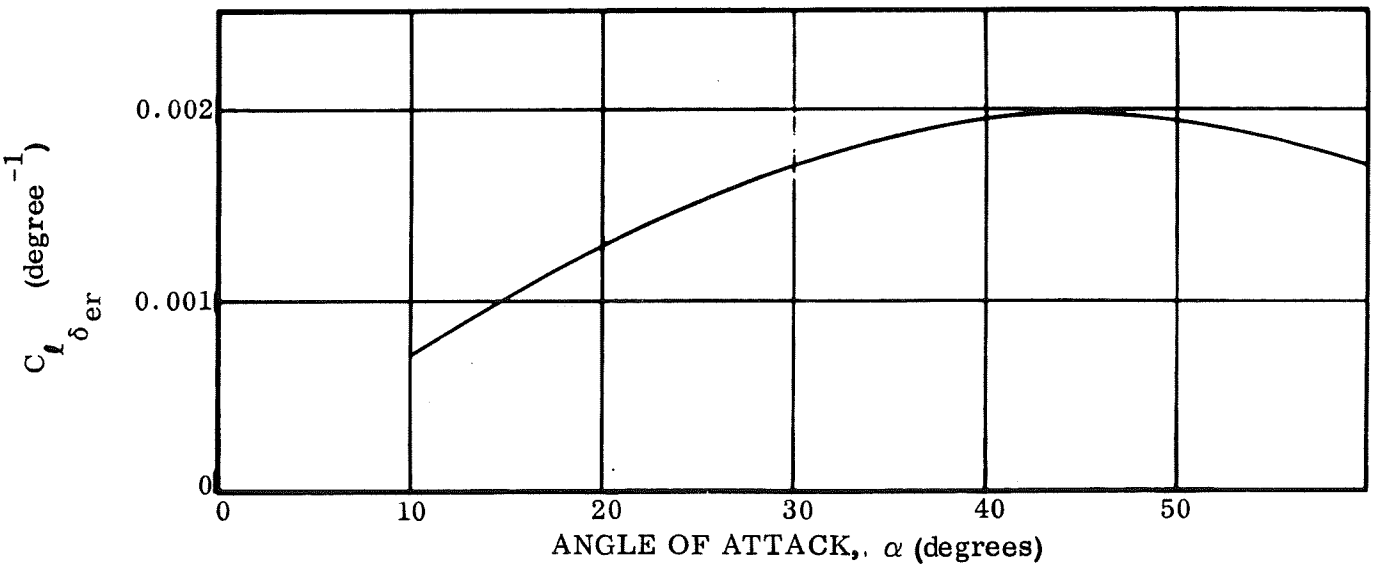

Figure 2-10. FR-4 Hypersonic Ruddervator Effectiveness in Roll and Yaw

2.1.4 VISCOUS INTERACTION EFFECTS. The hypersonic aerodynamic characteristics are known to vary significantly with the hypersonic viscous parameter $M_\infty/\sqrt{R_\infty}$ due to viscous interaction. For entry performance calculations, empirical variations of the trimmed lift-drag ratio, trim angle of attack, and trimmed lift coefficient were used. These variations are based on the methods of Reference 2-4 and other available experimental data. Figure 2-11 shows the variation of the ratio $L/D_{max}/L/D_{max-HAP}$ as a function of the hypersonic viscous parameters. $L/D_{max-HAP}$ refers to the value of L/D_{max} predicted by the HAP program at the nominal hypersonic design point of 20,000 ft/sec at 200,000 feet. These curves are normalized so that the ratio is 1.0 at the nominal hypersonic design point. The medium L/D line was used for FR-4 L/D_{max} entry performance calculations. Figure 2-11 also presents normalized variation of trim angle of attack and lift coefficient at trim as a function of the hypersonic viscous parameter.

2.1.5 EFFECT OF MACH NUMBER. The effect of Mach number on basic body stability and trim was tested on an IPD configuration at AEDC at Mach 10 and at MSFC at Mach numbers up to 5. This data indicates that the hypersonic characteristics appear to be valid down to approximately Mach 3, where the increasing V-tail effectiveness causes the trim angle of attack to decrease to a low angle as shown in Figure 2-12. The test at MSFC, run during October 1969, has verified this trend.

Certain stability and control parameters were generated over the Mach number range for the IPD configuration and are presented in this section. Their aerodynamic parameters were obtained from wind tunnel test data and from analytical estimates at hypersonic speeds. The wind tunnel data includes a recent MSFC test to Mach 5.

Figure 2-13 presents longitudinal stability characteristics across the Mach number range. The slope of the normal force curve and the center of pressure location are presented for several angles of attack. The solid lines represent predicted values, and the dashed line represents test data for the entry configuration at an angle of attack of 15 degrees. The isolated data point represents the cruise and landing configuration (wings deployed). Test data indicates a more forward center of pressure than predicted.

Figure 2-14 presents the lateral directional stability characteristics as derived from test data and from analytical estimates of hypersonic speeds. Curves of $C_{n\beta}$, $C_{y\beta}$, and $C_{l\beta}$ are presented as functions of Mach number for various angles of attack.

It may be generally concluded from these curves that basic static stability increases with angle of attack and decrases with Mach number. These parameters become independent of Mach above Mach 3.

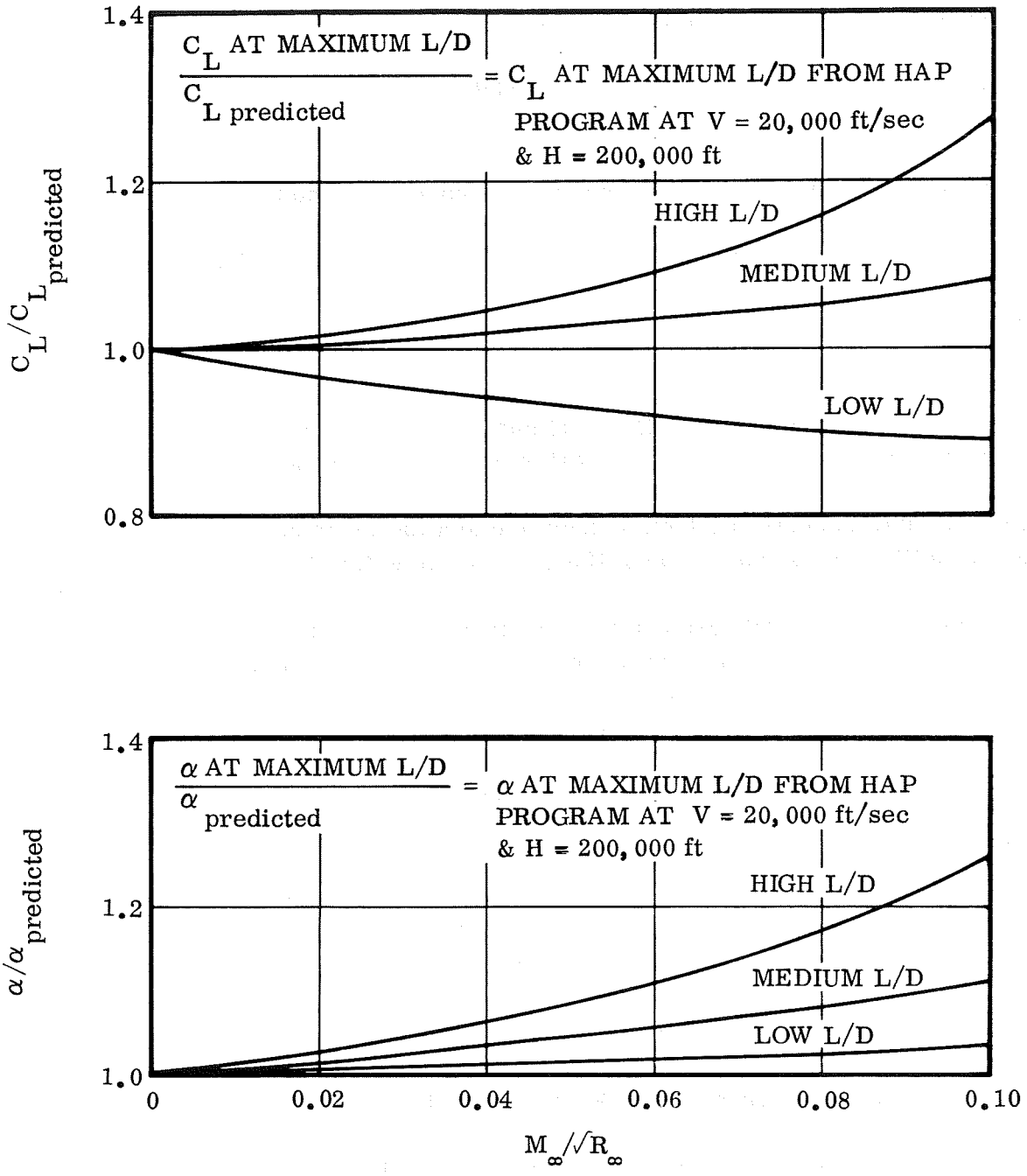

Figure 2-11. FR-4 Hypersonic Viscous Effects in C_L and Angle of Attack at Maximum L/D

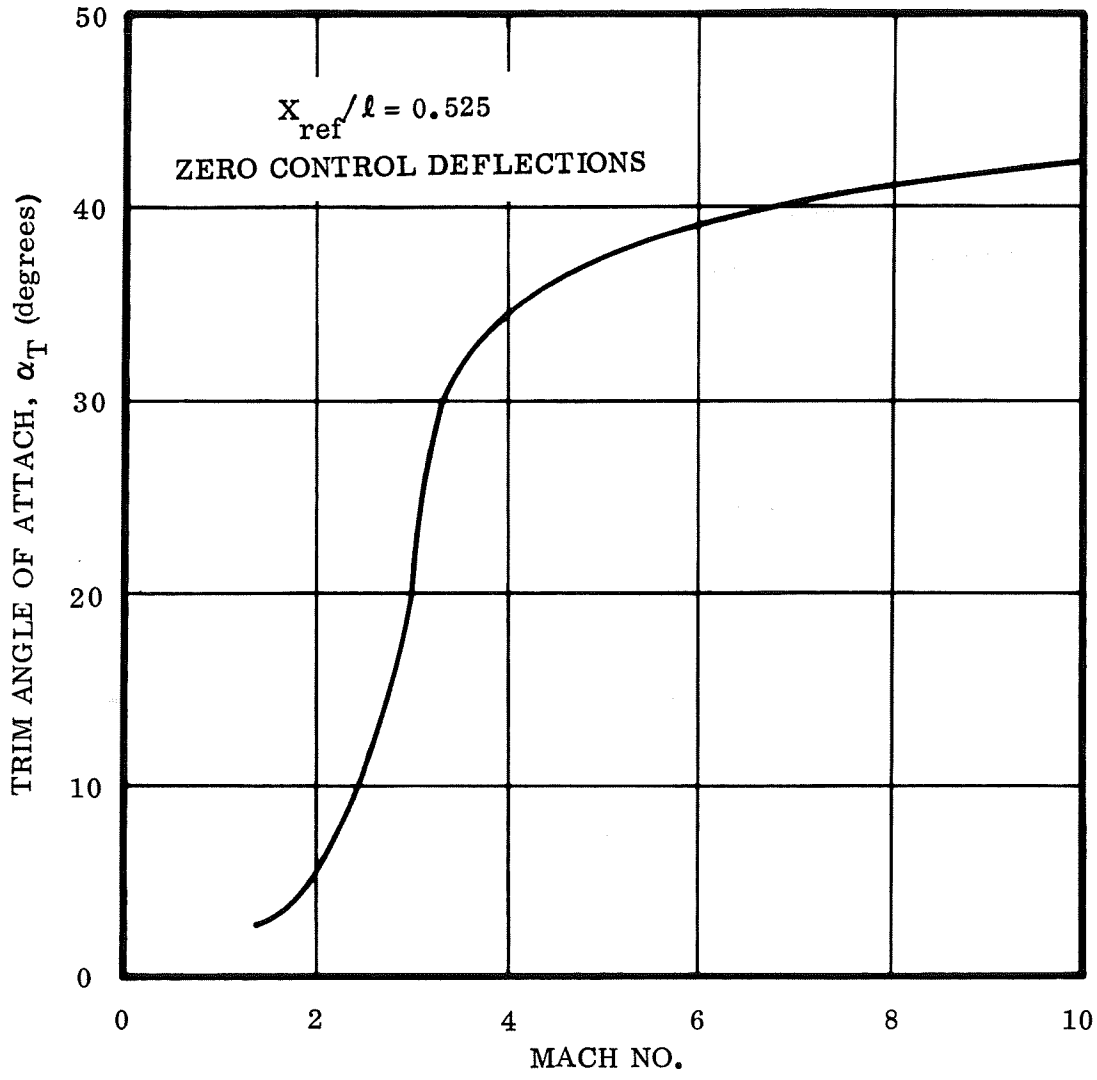

Figure 2-12. IPD Trim Angle of Attack

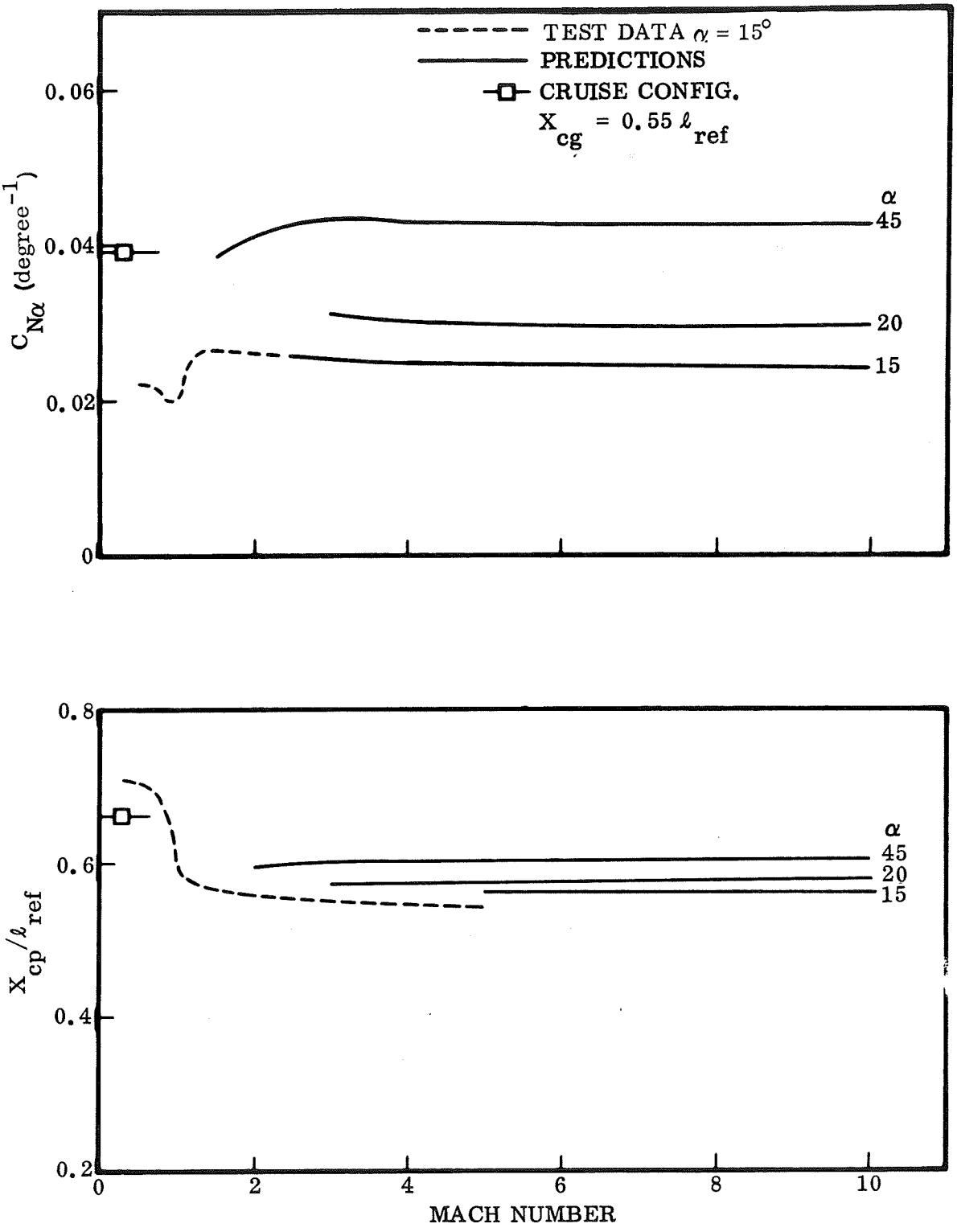

Figure 2-13. FR-4 Longitudinal Stability Characteristics

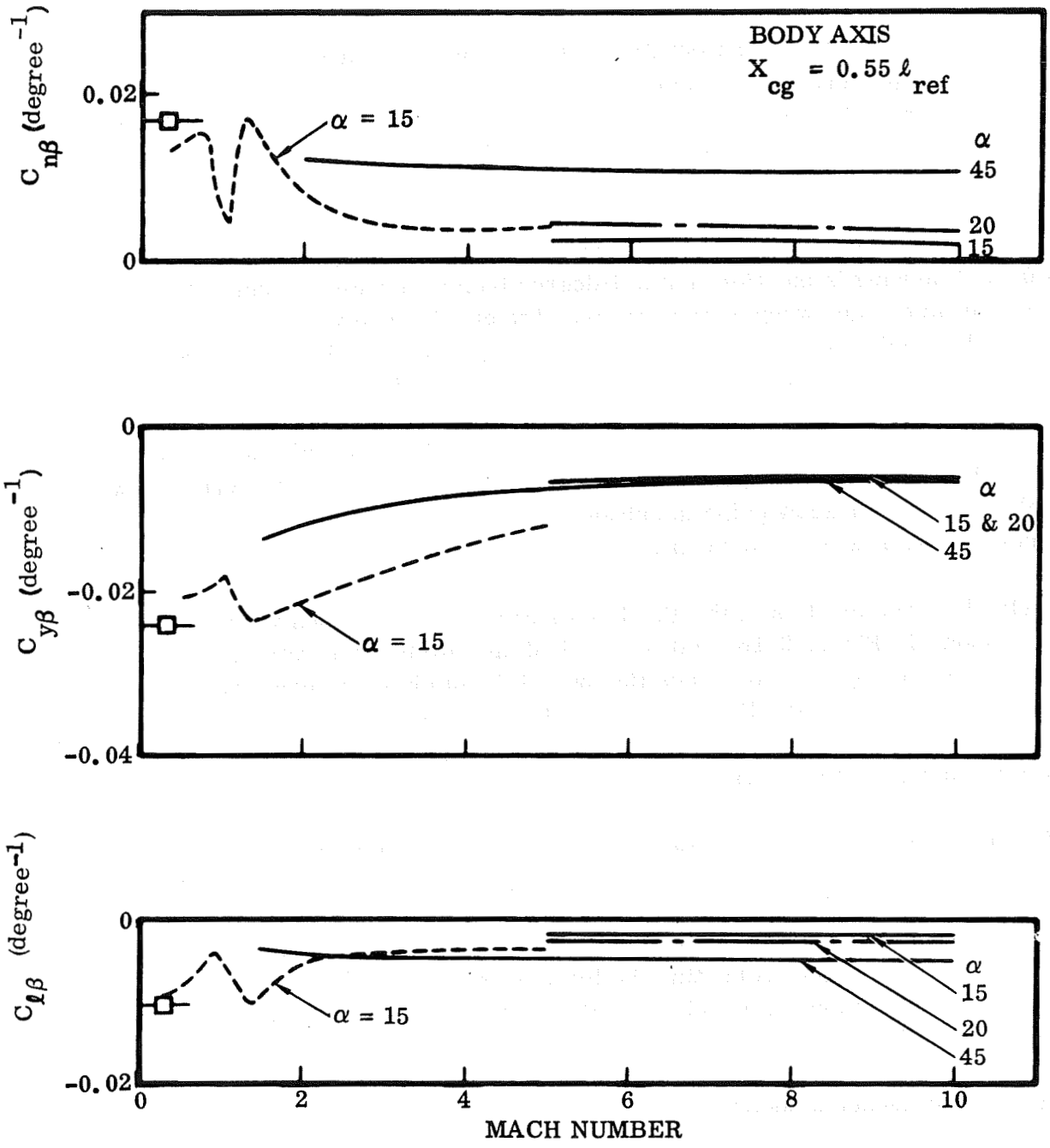

Figure 2-14. FR-4 Lateral-Directional Stability Characteristics

The effectiveness in pitch of the ruddervators over the Mach number range is shown in Figure 2-15. The solid lines represent predictions and the dashed curves are from test data; the ruddervator effectiveness is very high at subsonic Mach numbers and decays to a low constant value above Mach 4.

2.1.6 SUBSONIC CHARACTERISTICS. The subsonic aerodynamic characteristics of the FR-4 booster and orbiter elements vehicle were derived directly from wing tunnel tests of the IPD configuration. The most significant difference is that the wing was moved aft by 2.5 percent of the body length. The IPD data was adjusted to account for these differences. The results of this test are available in Reference 2-1.

The booster and orbiter elements both complete the wing deployment maneuver at Mach 0.6. The wing is positioned at a 6-degree incidence with respect to the body and has a leading edge sweep of 10 degrees. The quarter chord of the wing MAC is located at the nominal center of gravity (55 percent of ℓ_{ref}). The control system in the subsonic regime uses symmetrical ruddervator deflections for pitch control, asymmetric ruddervator deflections for yaw control, and spoilers on the wings for roll control. Use of a Alvarez-Calderon flap (Reference 2-5) to aid the subsonic characteristics was investigated, since previous Convair studies have shown that vehicles with large blunt bodies can show gains in subsonic L/D with flaps. These flaps are deployed at the completion of wing deployment.

Longitudinal characteristics of the FR-4 configuration with various wing flap deflections are shown in Figure 2-16. Lift coefficient and lift-to-drag ratio are presented versus angle of attack. The drag coefficient and the pitching moment coefficient are presented as functions of the lift coefficient. Data for 0-, 25-, and 45-degree flap deflections are presented. The 0-degree deflection represents a fully retracted flap (no increase in wing total area).

The pitching moment curves show that the flaps are self-trimming devices providing trimmed lift coefficient from 0.25 up to 0.69 at a 45-degree flap setting. These trim points are indicated on the L/D curves in Figure 2-17. An uncorrected, trimmed lift-to-drag ratio of 7.1 is attainable with 25 degrees of flaps at an angle of attack of 1 degree and a $C_L = 0.55$. Adjusting the lift-to-drag ratio to full-scale flight conditions results in a maximum ratio of 7.8. Maximum L/D with flaps retracted is 6.8, showing the gain resulting from the use of this simple flap. Figure 2-18 presents the pitch control effectiveness of the ruddervators, which indicates that this control is very effective at subsonic speeds.

The lateral directional characteristics of FR-4 at subsonic speeds are shown in Figure 2-19 as functions of angle of attack. These characteristics are for the basic T-18 configuration with all control surfaces neutralized, and were derived directly from low-speed wind tunnel test data. The T-18 configuration is directionally stable at angles of attack of interest, with a minimum static margin of 35 percent of the reference span.

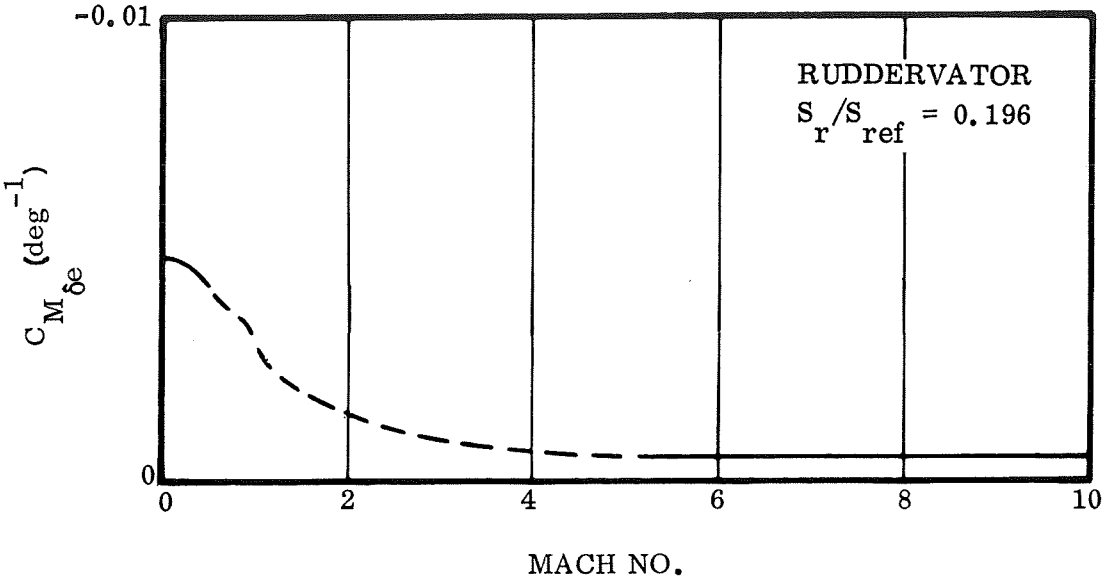

Figure 2-15. FR-4 Pitch Control Effectiveness

The control effectiveness of differential ruddervator deflections is shown in Figure 2-18. Differential rudder deflections are used in the subsonic regime for yaw control. These deflections, however, also produce adverse roll. The yaw control effectiveness and adverse roll effectiveness produced are shown in the figure as functions of angle of attack. Because of this adverse yaw due to roll, spoilers on the wing are employed as the roll-control device in the subsonic regime.

2.1.7 CRUISE ENGINE EFFECTS

2.1.7.1 Thrust Effects. The thrust effects on the lift of the space shuttle subsonic cruise configuration were accounted for by considering:

a. Contribution to lift due to inclination of the thrust vector.

b. Contribution to lift from the force acting on the engine inlet normal to the thrust axis. This force results from a momentum change in the free stream direction when the flow is turned around and through the engine inlet.

c. Contribution to lift from induced effects of the jet exhaust on the wing and tail surfaces. Cruise engine placement on the space shuttle entry configuration requires the consideration of jet exhaust effects on the inboard wing sections. In general, mixing of the jet exhaust with the free stream occurs over a distance of approximately eight exit diameters downstream. For this study, it was assumed that the flow from the engine exhausts is fully developed (mixed) as it passes over the wings and around the tails, thus serving to alter the effective angle of attack of these components.

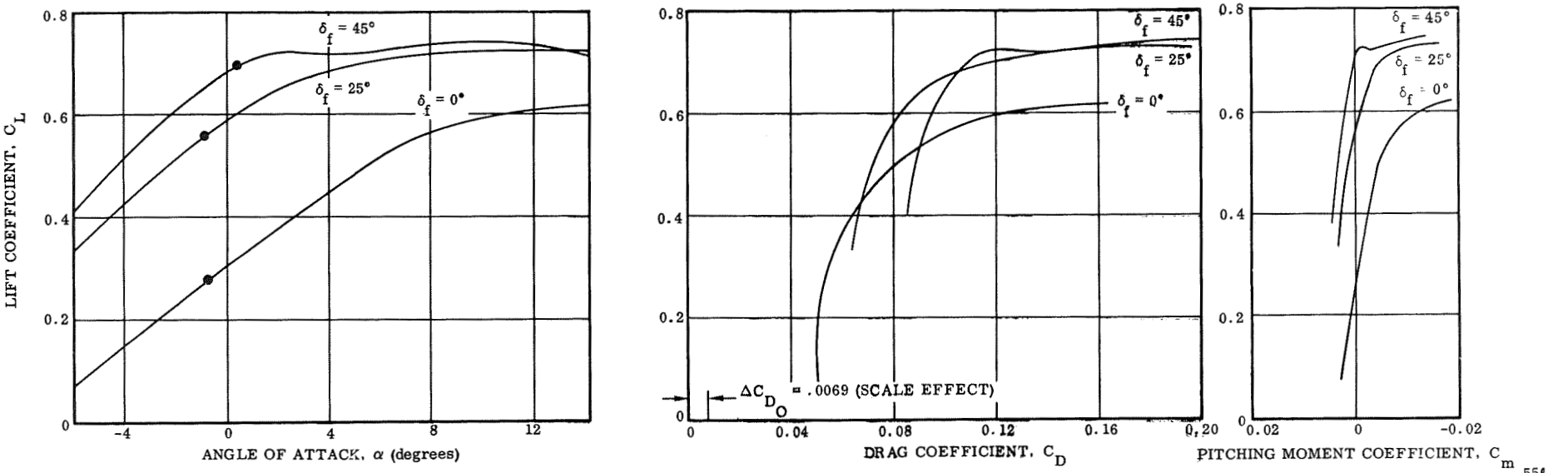

Figure 2-16. FR-4 Subsonic Longitudinal Aerodynamic Characteristics (With Flaps)

FOLDOUT FRAME 1

FOLDOUT FRAME 2

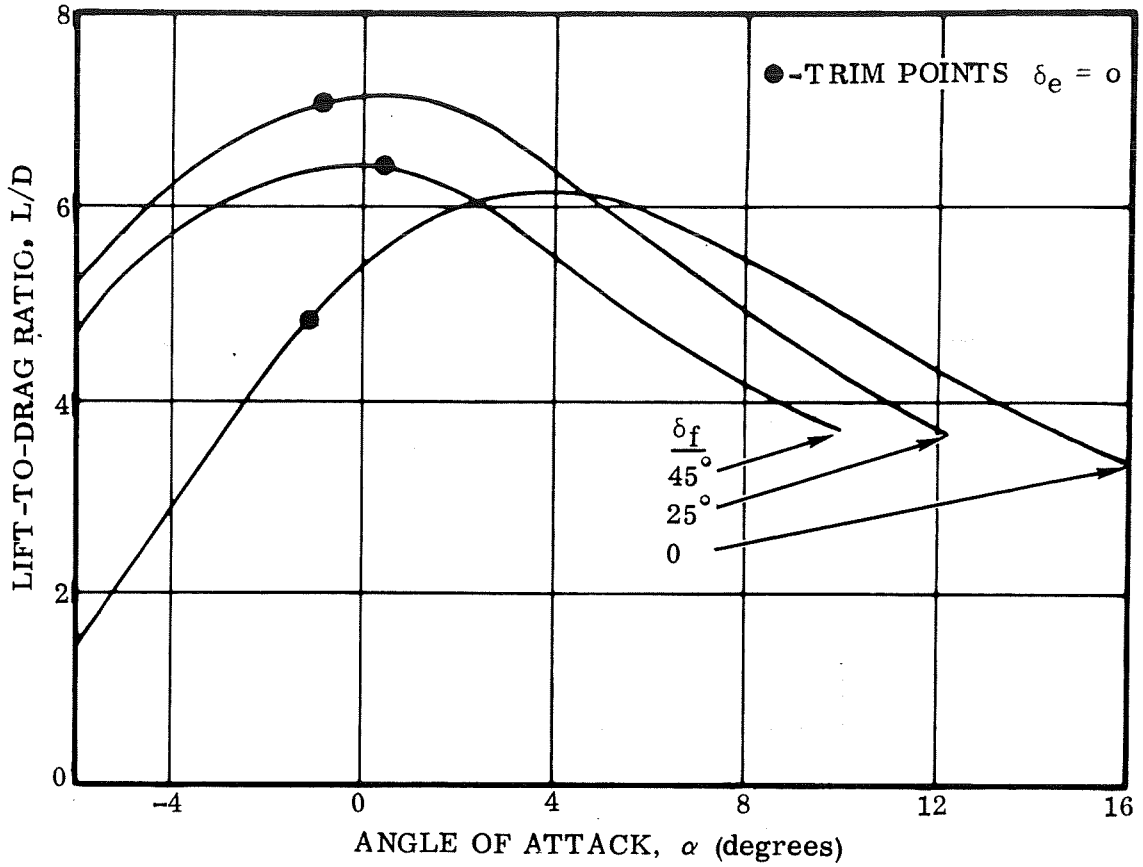

Figure 2-17. FR-4 Trim Points

Jet power effects on the stability and control characteristics of a vehicle are usually relatively minor. For this particular vehicle, however, the length of the respective moment arms associated with engine locations will result in significant contributions to the overall configuration stability characteristics. Effects considered in determining the incremental pitching moments due to power effects are:

a. Pitching moment due to offset of the thrust axis from the body axis.

b. Pitching moment due to normal force at the engine inlet.

c. Pitching moment due to jet interference effects at the vehicle tails.

The most pronounced power effects on subsonic cruise performance are evidenced in the increments applied to the vehicle drag. The location of engines on the forward portion of the fuselage will result particularly in additional skin friction drag due to the large amounts of vehicle wetted area immersed in the engine exhausts. The various increments considered as power effects on vehicle drag are:

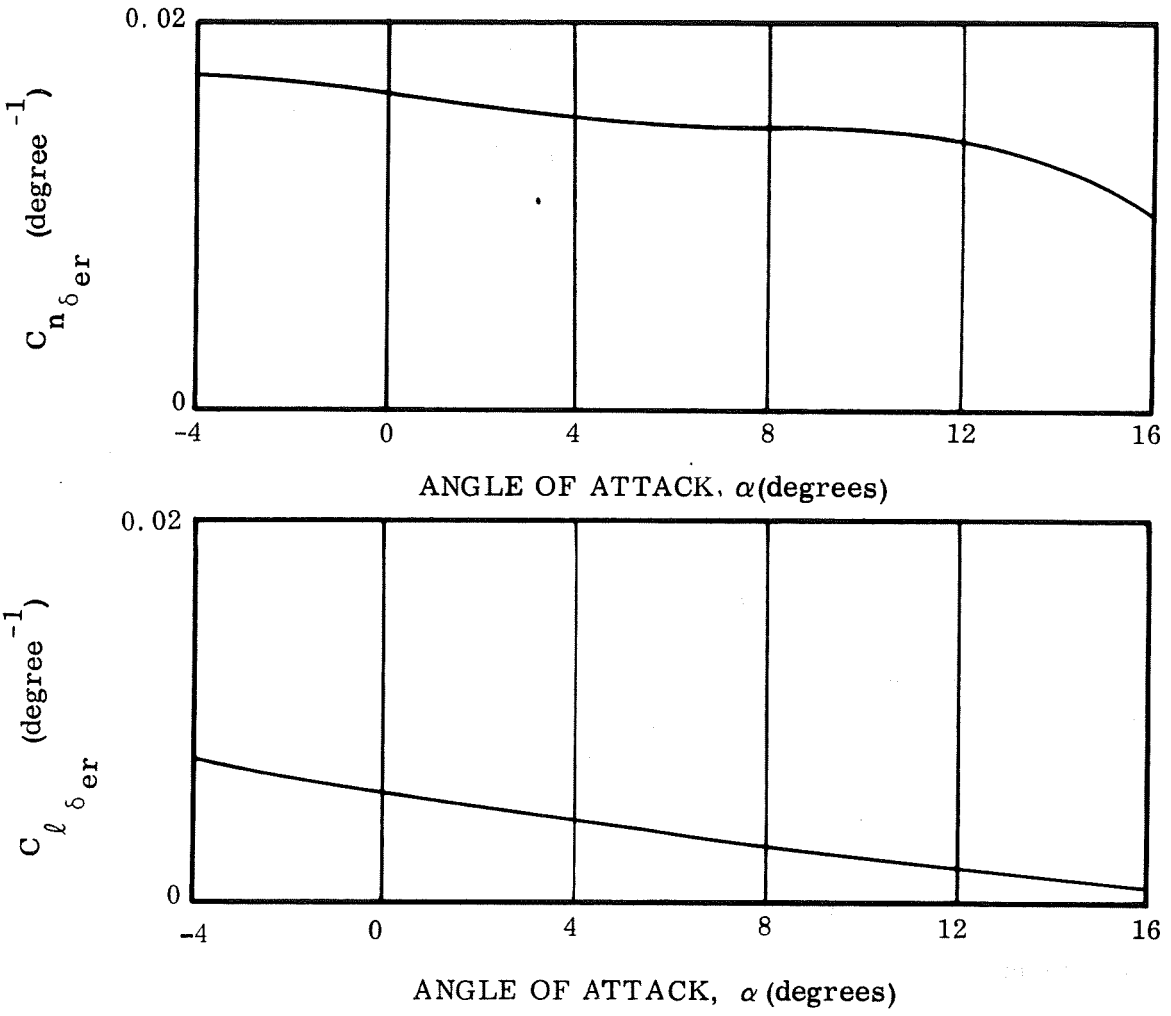

Figure 2-18. FR-4 Control Effectiveness

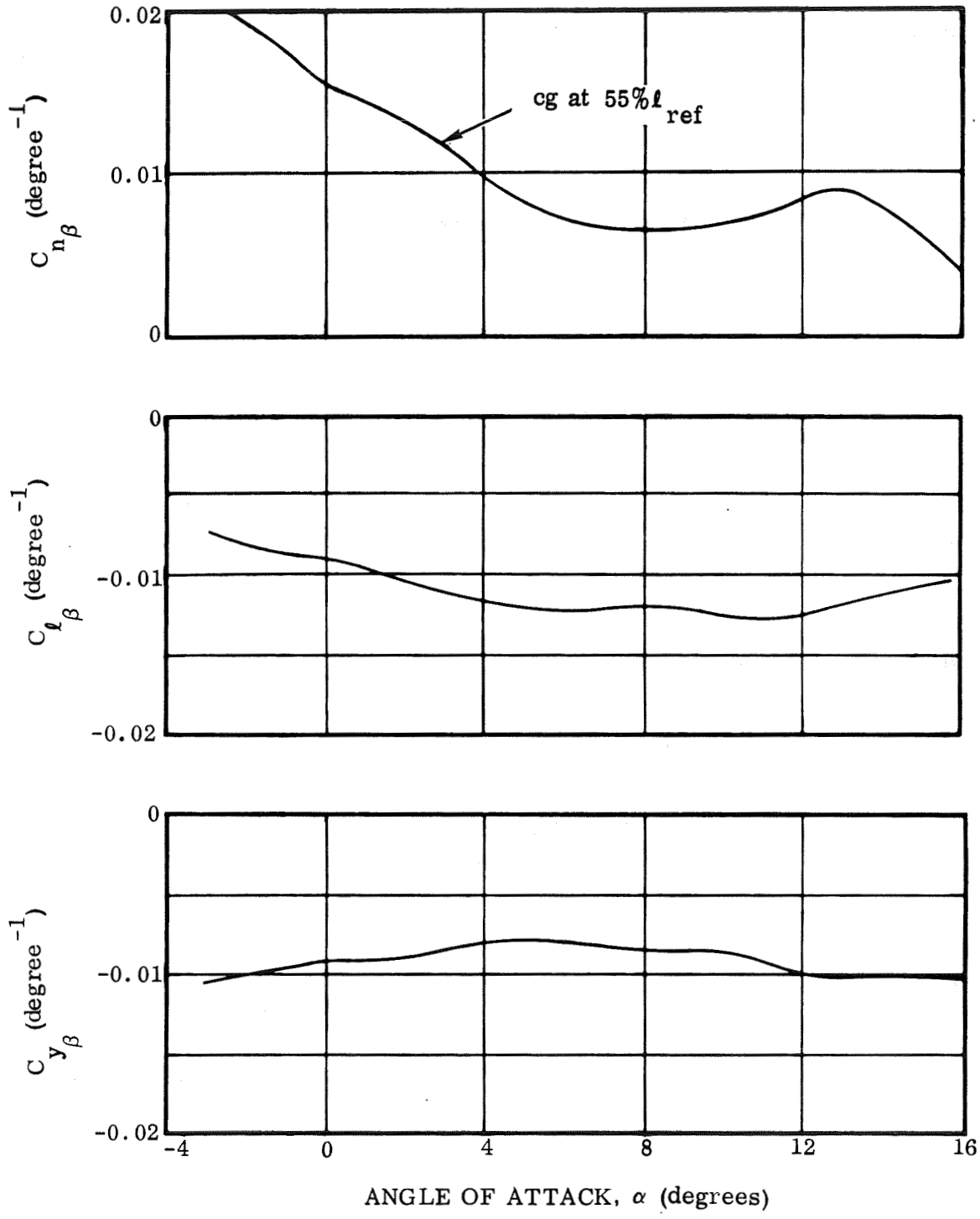

Figure 2-19. FR-4 Subsonic Lateral Directional Aerodynamic Characteristics

a. Skin Friction. Increased skin friction drag caused by the higher local dynamic pressure over all areas immersed in the jet slipstream.

b. Engine Nacelle and Interference Drag. The local skin friction on the engine nacelles is influenced by the presence of the fuselage and is determined as a function of the nacelle wetted area and interference.

c. Base and Afterbody Drag Corrections. Again due to the increased local dynamic pressure from the engine exhausts, these will be significant because of the large base area present.

The effect of thrust on the aerodynamic characteristics of T-18 was calculated for:

Velocity	= 390 ft/sec
Altitude	= 15,000 ft
Thrust/engine	= 14,000 lb

Figure 2-20 presents the assumed dynamic pressure at the centerline of the jet exhaust as a function of distance from the jet exit. The approximate jet exhaust boundary is presented in Figure 2-21.

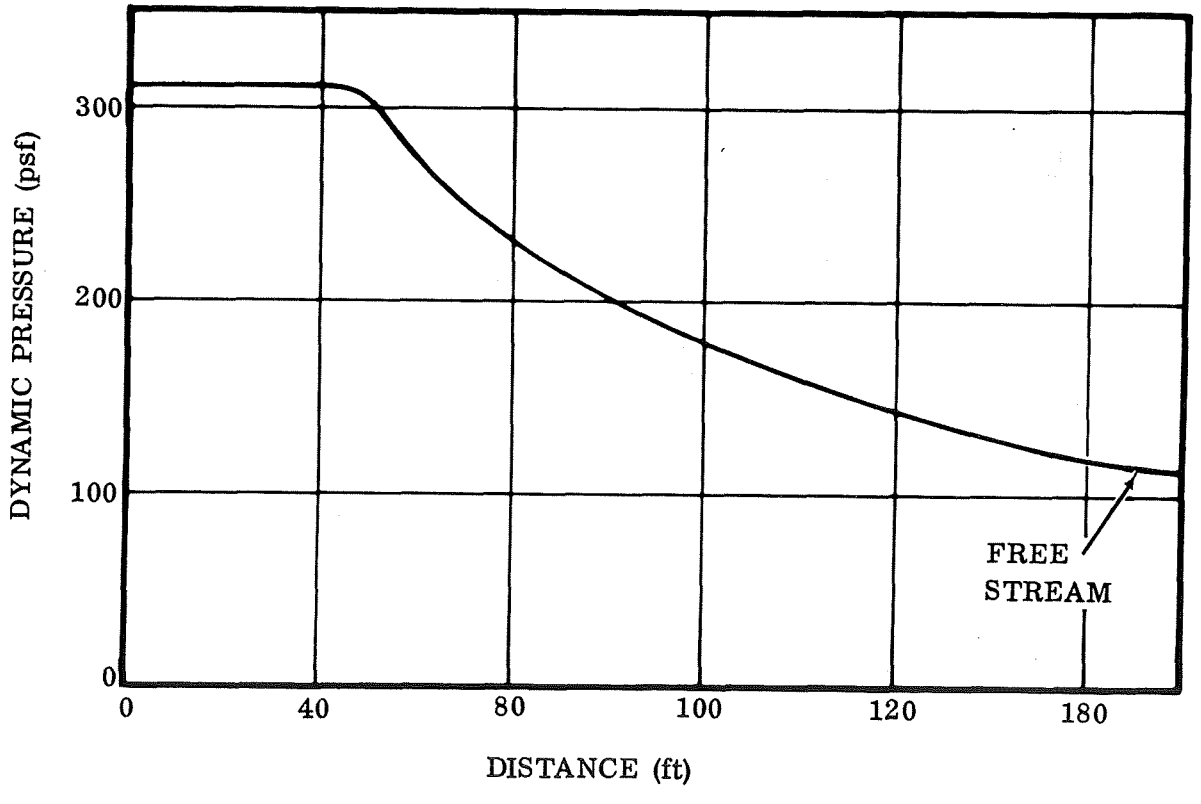

Figure 2-20. FR-4 Centerline Dynamic Pressure in Jet Wake

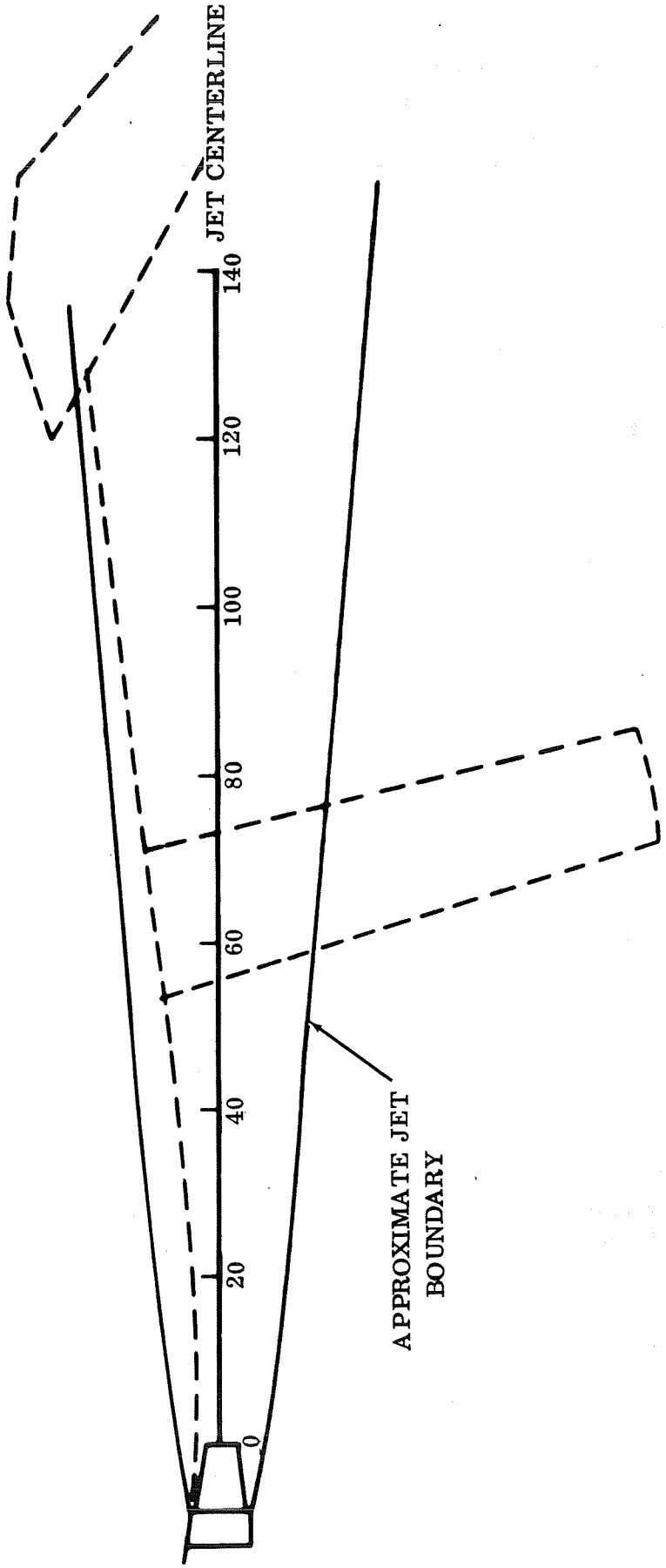

Figure 2-21. FR-4 Approximate Jet Boundary

The total lift increment due to thrust effects is presented in Figure 2-22 as a function of angle of attack. Wind tunnel data (Reference 2-1) was used to determine the lift curve of the wing and tail, and methods presented in Datcom were used to calculate this increment. A favorable lift increment due to thrust is produced.

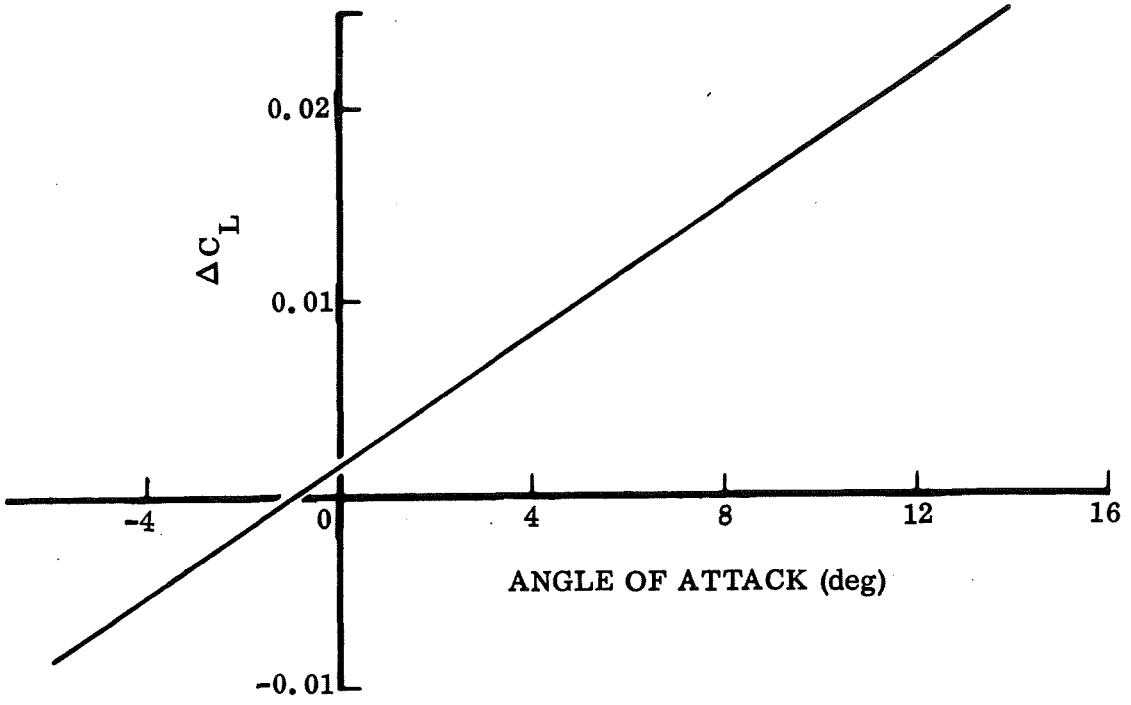

Figure 2-22. FR-4 Lift Increment Due to Thrust Effects

Pitching moment increment is presented in Figure 2-23. This is a destablizing moment increment. The upper engine and the tail produce a nose-down moment shift and the lift increment due to the engine inlet produces the destablizing moment.

The effects of adding engines and jet exhaust to the cruise configuration produce a drag increment of 0.0049. Adding the engines produces the major portion of this drag increment. Engine drag was determined from test data and corrected for configuration and Reynolds number. The additional drag due to increased dynamic pressure from the jet exhaust is relatively small.

2.1.7.2 Engine-Out Cruise. The booster is required to cruise approximately 190 n.mi. back to the launch site after performing the boost mission (Section 3.2.3). The cruise engines are extended at 25,000 feet, and an engine-start trajectory is flown until the engines are started and a 15,000-foot cruise altitude is reached. If one engine cannot be started, the engine-start glide will be continued until the engine-out cruise altitude is reached (approximately 5,000 feet). If the engine has not been started by this time, it is assumed that it can be retracted so that it contributes no drag.

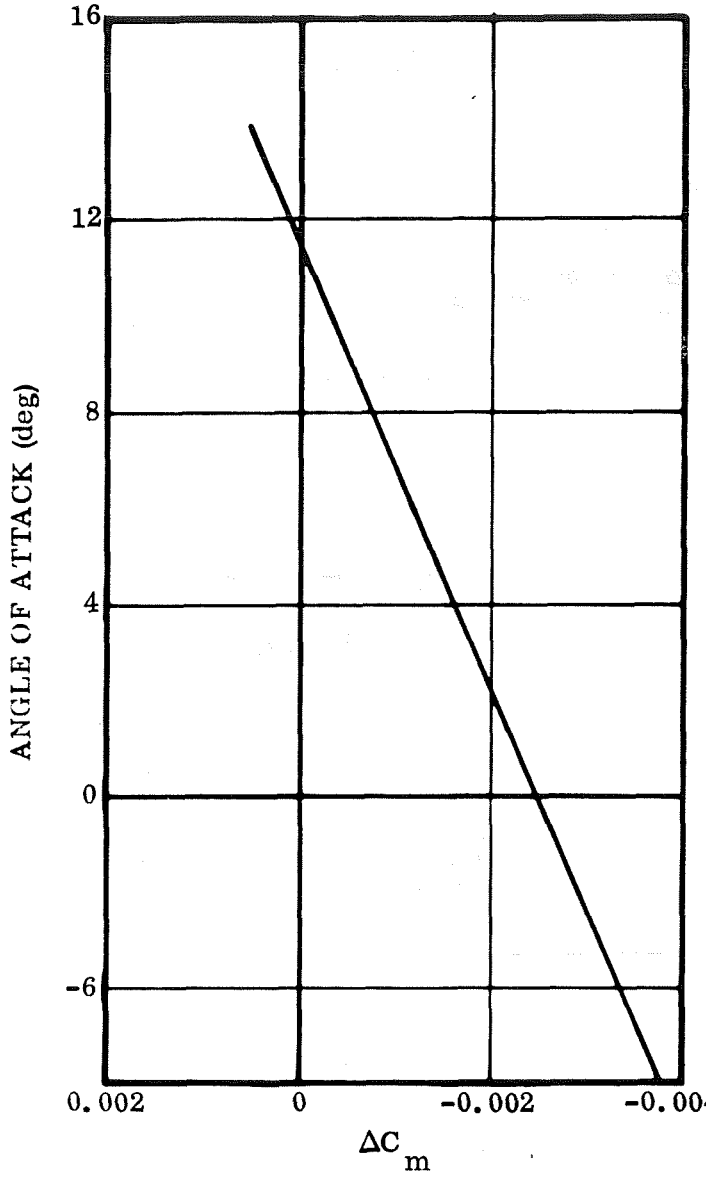

Figure 2-23. FR-4 Pitching Moment Increment due to Thrust Effects.

A sample case was considered in which one of the side engines would not start and the remaining two engines generated 21,900 pounds of thrust each. This results in a nose-down pitching moment coefficient of 0.0012 from the top engine and a yawing moment of 0.0242 from the side engine. The elevator required to trim the nose-down moment is 0.3 degree; the rudder required to trim the yawing moment is 2 degrees. The subsonic wind tunnel data shows a very small drag increment for control deflection and the increase in drag is estimated at 0.0004, reducing the L/D to 7.76 from 7.8.

About 120 pounds of fuel are required to compensate for the reduction in L/D, over and above the engine-out fuel increase due to reduced altitude cruise.

2.1.8 TAIL-SIZE TRADEOFF. A study was performed to determine minimum V-tail size based on three criteria:

a. Base airframe subsonic dutch roll frequency (ω_n).

b. Hypersonic neutral directional stability.

c. Longitudinal requirements.

The results are presented in Figure 2-24, which shows dutch roll frequency (ω_n) as a function of tail size and hypersonic directional stability. The subsonic data is shown as a function of tail size at L/D_{max} with 25 degrees of flap extension on the orbiter. The criteria selected as the minimum acceptable dutch roll frequency are that of the military handling qualities specification for heavy transports, MIL Spec 8785A, Class III. The data shows that the design far exceeds this requirement and as a point of comparison exceeds the C5A value also. Based on this requirement, the tail size could be reduced.

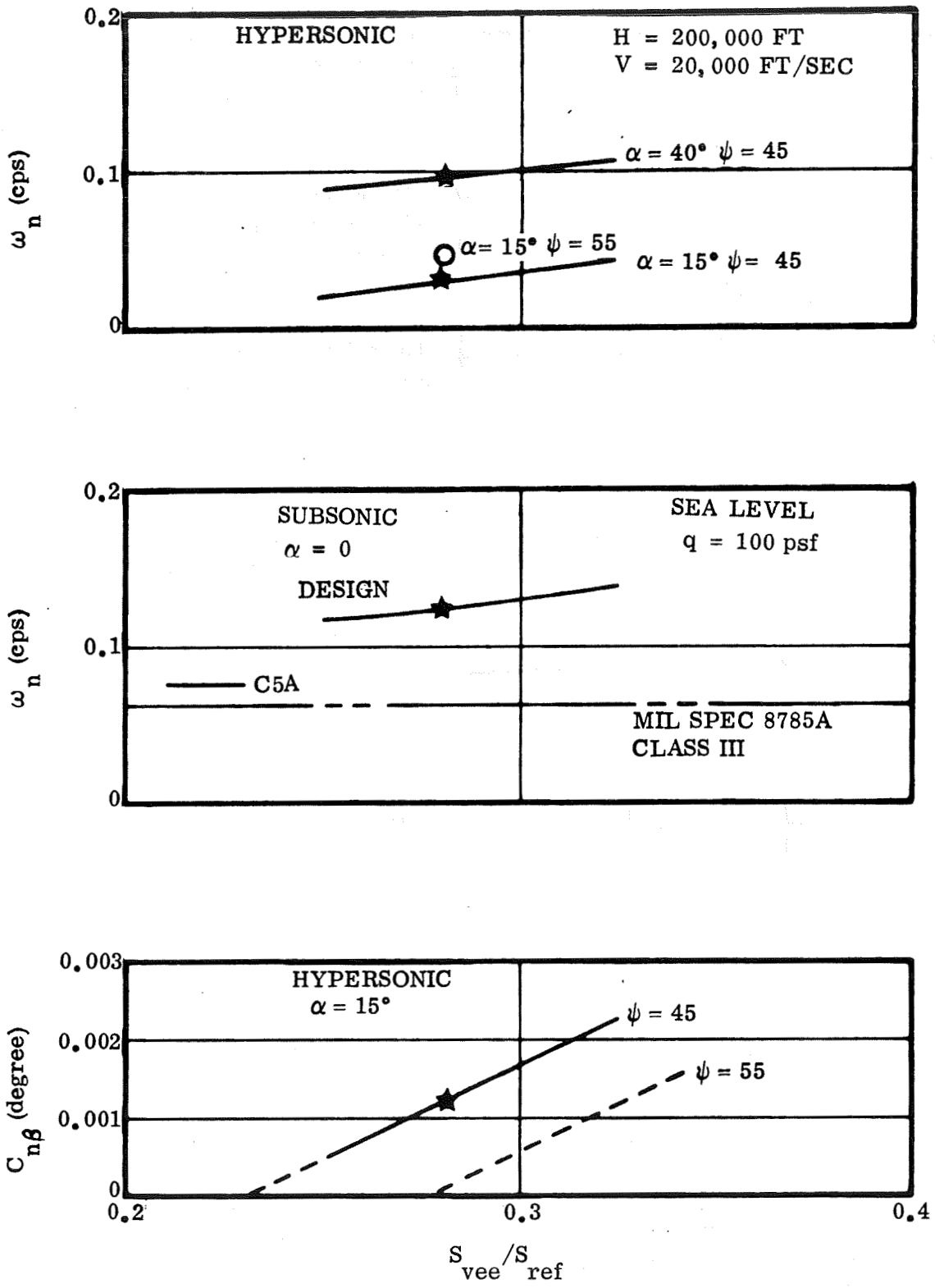

Figure 2-24. FR-4 Tail Size Tradeoff

The vehicle hypersonic directional stability increases with angle of attack; thus the minimum stability will occur at the lowest trim angle of attack. Figure 2-24 presents the data for an angle of attack of 15 degrees, which shows that the tail could be reduced in size or rolled out to 55 degrees from the veritical to provide more area for longitudinal stability. The hypersonic longitudinal control requirements of the vehicle indicate that it would be better to roll the tail out than to reduce tail size.

2.2 FR-3 AERODYNAMICS

The two-element configuration consists of a large booster and a smaller orbiter vehicle, as shown in Figure 2-25. When originally sized, the booster and orbiter vehicles were both scaled from the T-18 vehicle lines discussed in Section 2.1 to make best use of the available aerodynamic test data and vehicle analyses. A test of the original two-stage vehicle was performed on 19-21 October 1969 at MSFC, but the data is not available for this analysis. Figure 2-26 presents the latest FR-3 configuration, which differs from the original two-stage in that the booster was made more blunt to obtain better volume utilization while the orbiter retains the T-18 shape. The FR-3 orbiter is a scaled version of the FR-4 vehicle discussed in the previous section, so the aerodynamic characteristics are the same as those of the FR-4 orbiter.

This section will concentrate on the aerodynamics of the booster, which were generated using the IPD test data to derive incremental wing and tail data coupled with analytic estimates of body data. The data will be presented in the following order:

a. Reference Dimensions.

b. Launch configuration.

c. Hypersonic characteristics.

d. Subsonic characteristics.

2.2.1 REFERENCE DIMENSIONS

	Booster	Orbiter
Reference Area (ft^2)	8166	4905
Reference Length (ft)	210	179.1
Reference Span (ft)	41.1	30.9
Center of Gravity Location		
Entry	0.508 (percent of ℓ_{ref})	
Landing	0.558 (percent of ℓ_{ref})	

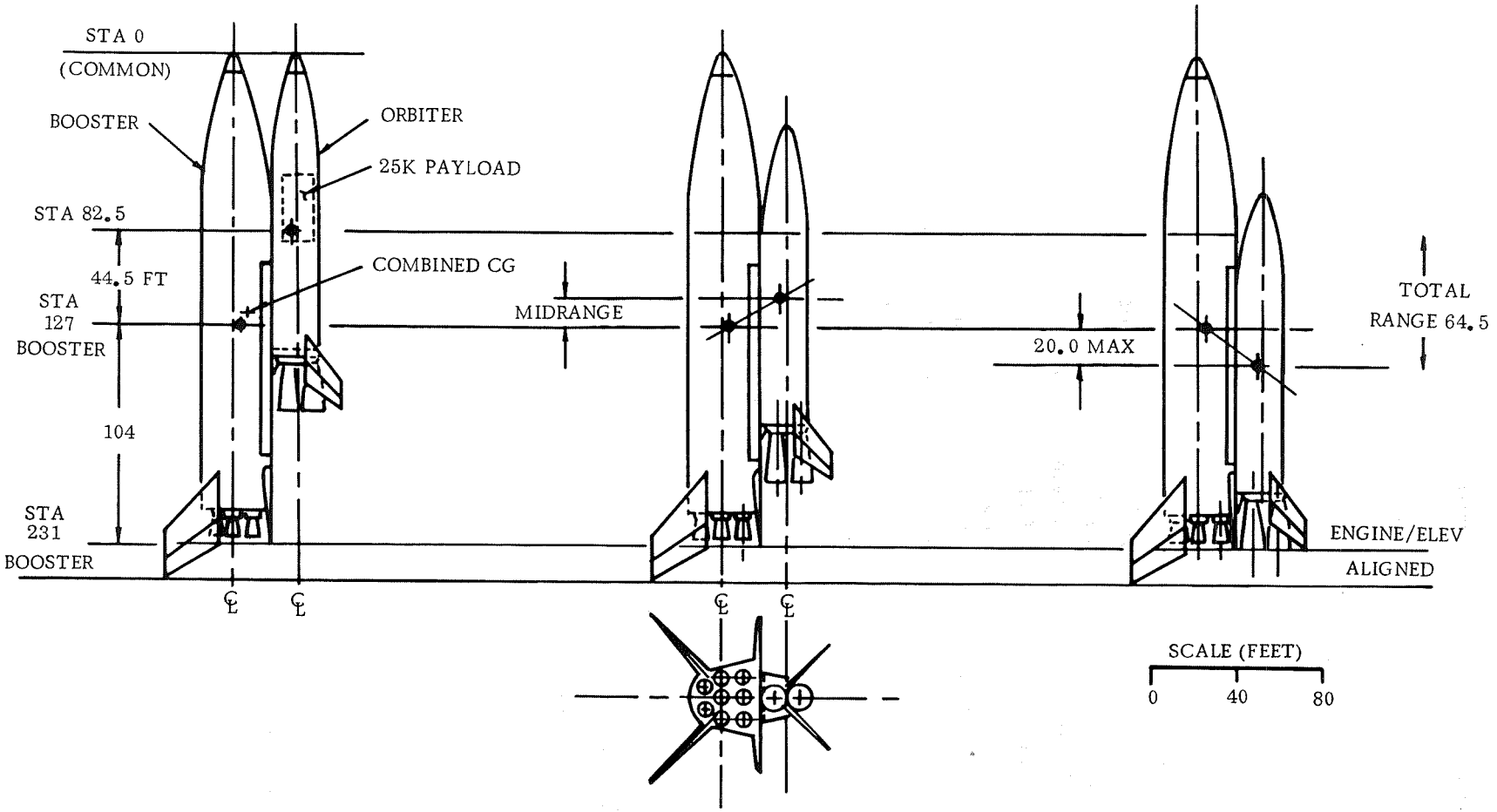

Figure 2-25. Conceptual Two-Stage Configurations

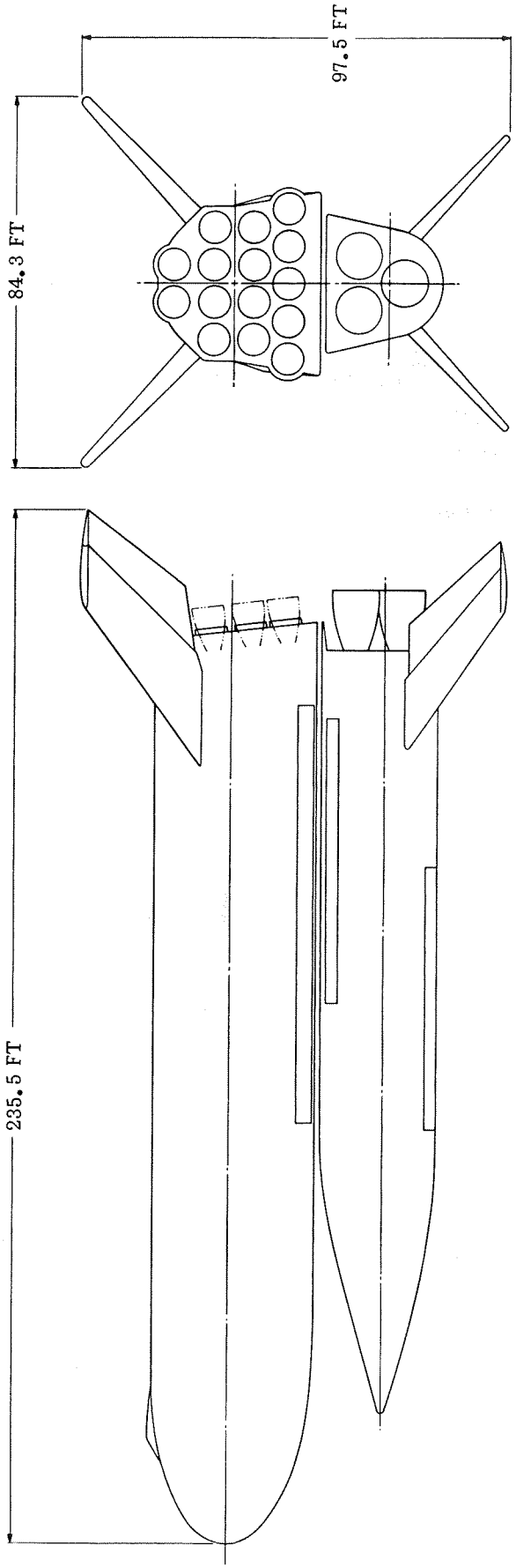

Figure 2-26. FR-3 Launch Configuration

	Booster	Orbiter
Exposed Wing Area S_{wing}/S_{ref}	0.329	0.273
Exposed V-Tail Area S_{tail}/S_{ref}	0.281	0.281
Ruddervator Area S_{rud}/S_{ref}	0.098	0.098

2.2.2 LAUNCH CONFIGURATION. The launch configuration shown in Figure 2-25 was tested at MSFC on 19-22 October 1969. The data from that test is not available for this report and the data presented here was estimated from the single-element and three-element data of Section 2.1.

Figure 2-25 shows that three locations of the orbiter mounted on the booster are under consideration. Figure 2-27 presents the launch drag for the two extreme mounting locations of the orbiter on the booster. Figures 2-28 and 2-29 present the normal and side force gradients and centers of pressure for the configuration with the orbiter at its most forward position on the booster, which should be the most unstable case.

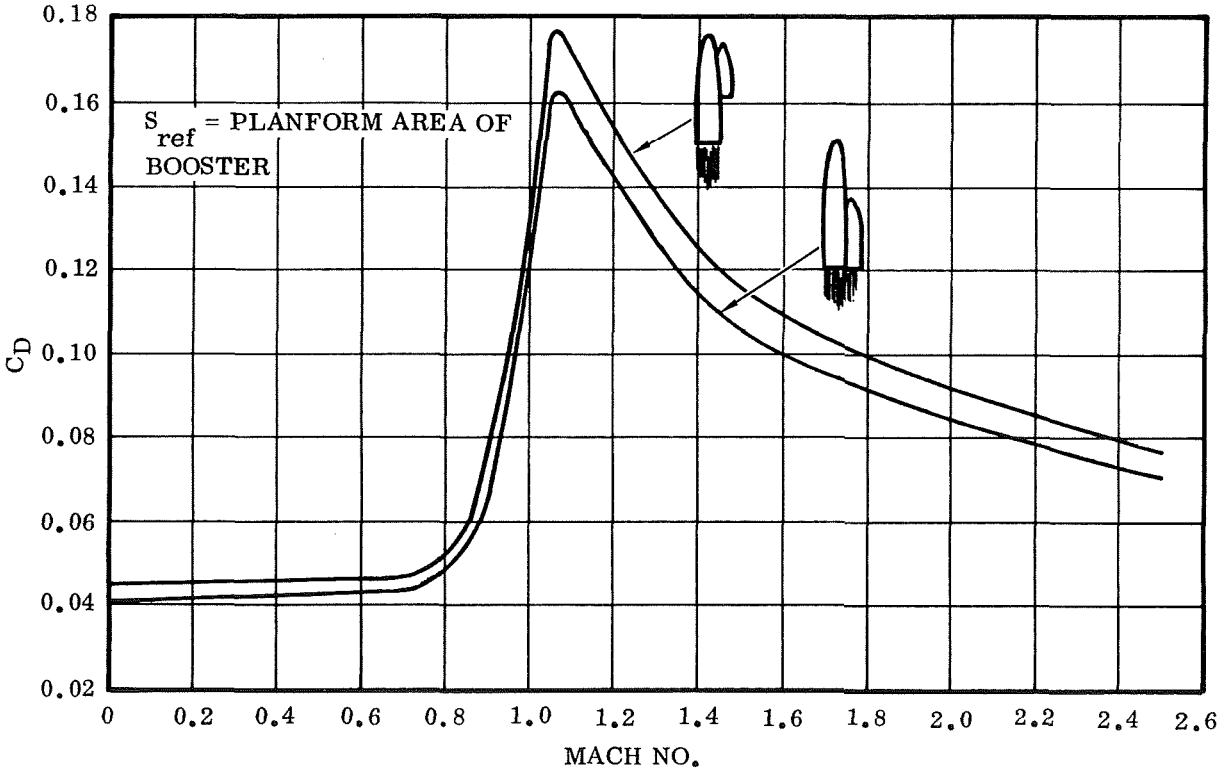

Figure 2-27. Launch Drag

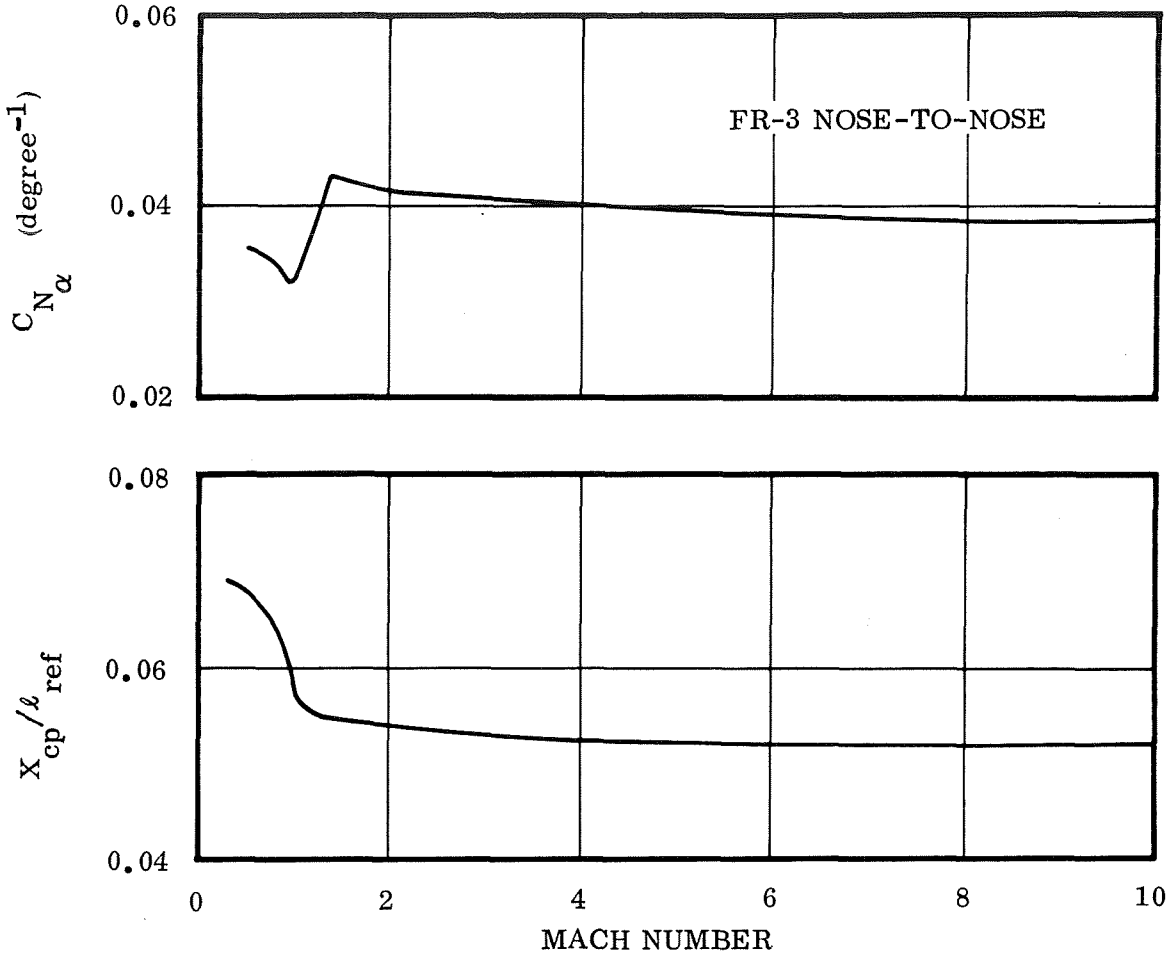

Figure 2-28. FR-3 Normal Force Gradients and Centers of Pressure

2.2.3 HYPERSONIC CHARACTERISTICS. The hypersonic computer program described in Section 2.1 was used to obtain the hypersonic aerodynamic characteristics of the FR-3 booster. As shown in Figure 3-30, the $(L/D)_{max}$ (untrimmed) is 1.25 and occurs at an angle of attack of 22 degrees. The lift ocefficient variation with angle of attack is shown in the curve below the L/D plot. Pitching moment about the entry center of gravity position versus the normal force coefficient is shown. Ruddervator effectiveness around the trim point is shown.

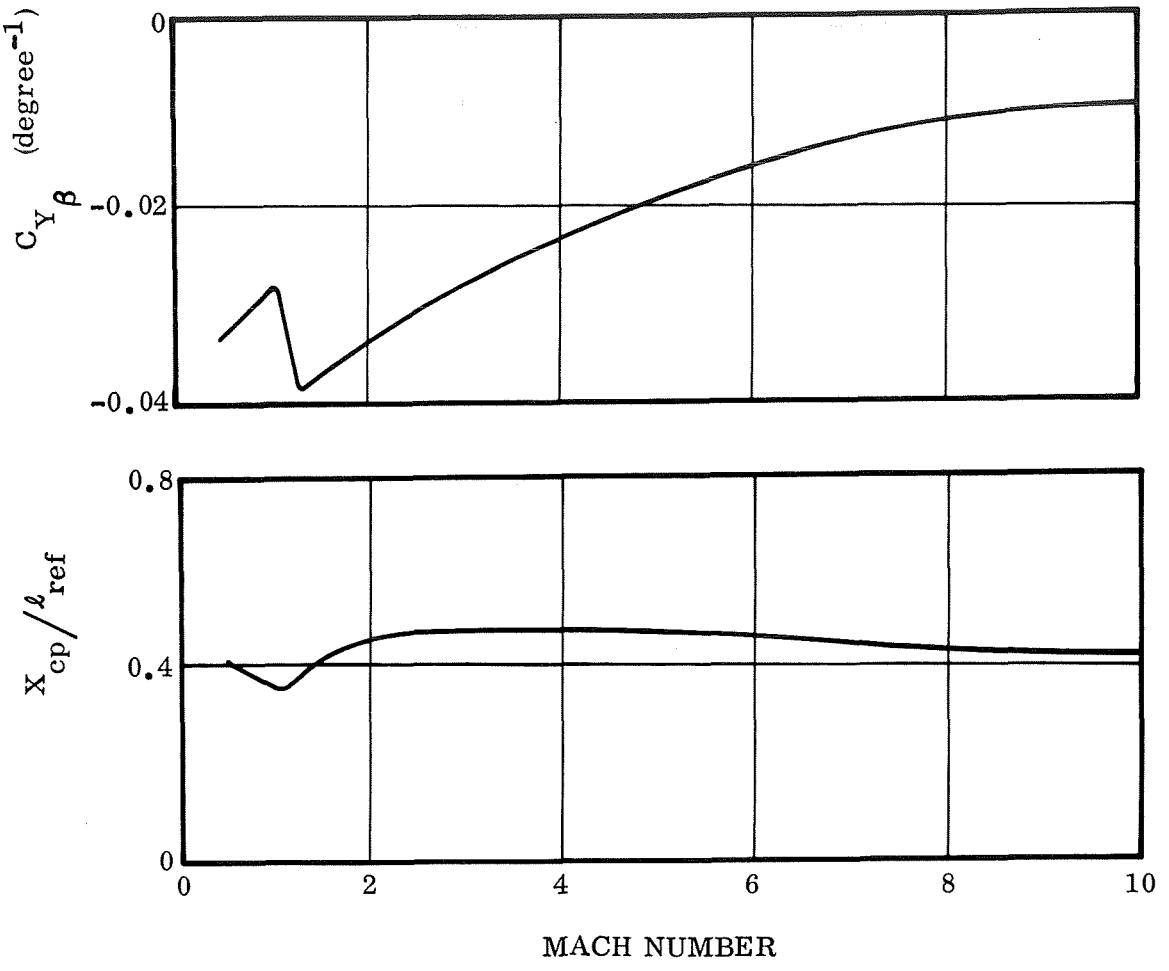

Figure 2-29. FR-3 Side Force Gradients and Centers of Pressure

The directional stability of the FR-3 configuration is shown in the C_{n_β} versus angle of attack plot in Figure 2-30. Again, two additional plots are shown: one for the results of wind tunnel testing of the IPD configuration and one for the HAP data. The HAP data is shown to be conservative. Considering the increase in effectiveness experimentally and the high angle of attack flight conditions the directional characteristics in the hypersonic regime for the FR-3 vehicle are satisfactory.

2.2.4 SUBSONIC CHARACTERISTICS. The subsonic aerodynamic characteristics were generated using incremental wing and tail contributions from the subsonic IPD tests. The body test data was corrected to the new nose shape using empirical methods similar to those of the USAF Stability and Control Datcom.

The FR-3 booster, with its blunt nose is less stable than the FR-3 and FR-4 orbiters or the FR-4 booster for two reasons:

a. Shorter tail moment arm.

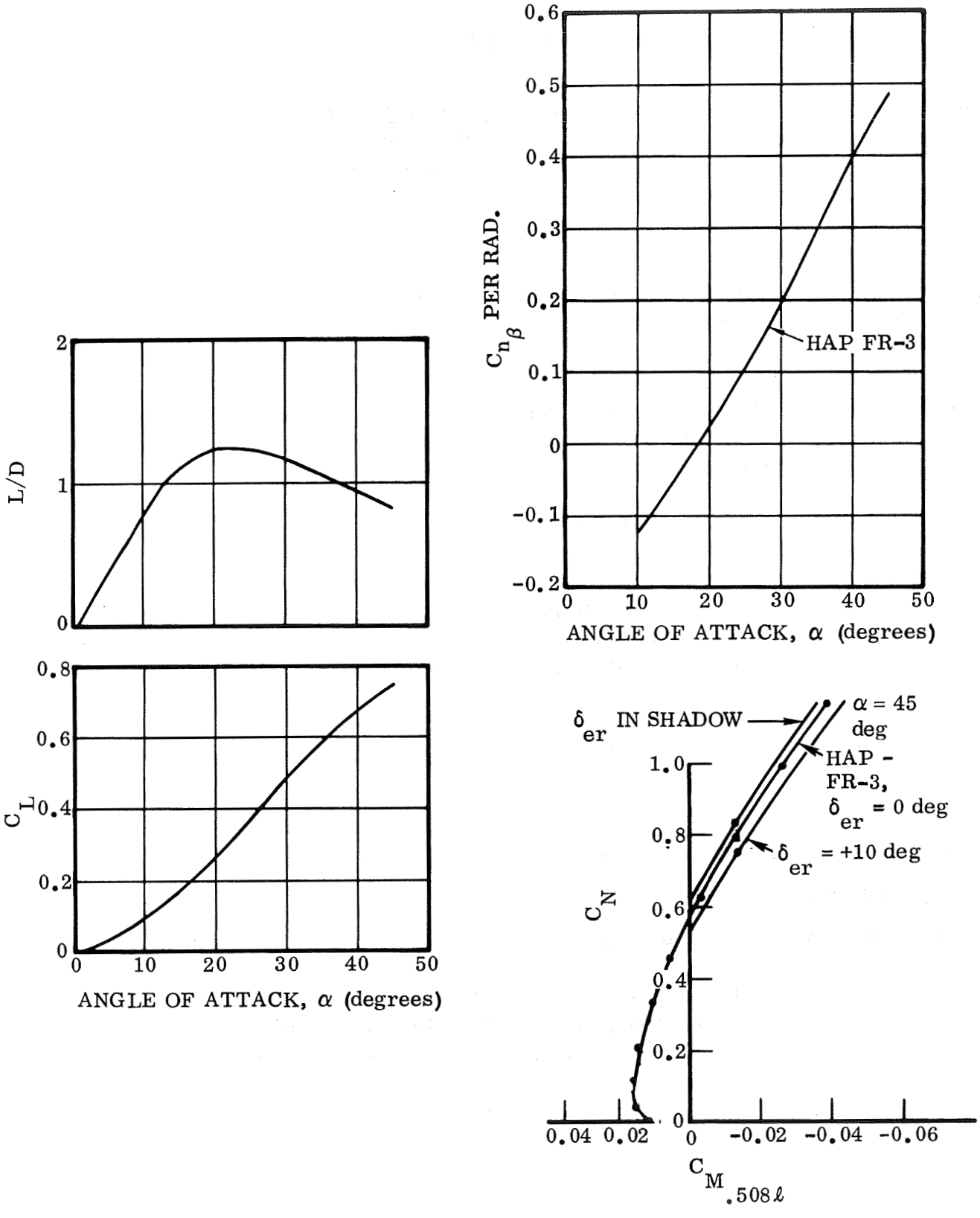

Figure 2-30. FR-3 Hypersonic Characteristics

b. Larger nose-up pitching moment resulting from the blunter nose shape.

Since the vehicle with the 10-degree swept wing was slightly unstable, the wing sweep was changed to 16 degrees. The subsonic test data shown in Reference 2-1 and the Langley test data indicate that changing wing sweep from 10 to 25 degrees caused no appreciable change in wing characteristics, so the 16-degree wing sweep should be acceptable over this range.

A marginally unstable vehicle in pitch is acceptable from a dynamic control standpoint because the large pitch inertia results in relatively low frequency, which is not difficult to control.

Figure 2-31 presents the subsonic longitudinal data for the FR-3 with a 16-degree swept wing with flaps extended 25 degrees; Figure 2-32 presents the lateral-directional data, and Figure 2-33 presents ruddervator control effectiveness.

2.3 CENTER OF GRAVITY PROBLEMS

The aerodynamic data presented in these sections was developed based on early vehicle cg estimates. The vehicle weights data in this volume shows that the cg is further aft then that used in the aerodynamic analysis, and the design loop has not been closed to bring these analyses together. While this cg problem is serious, it is not uncommon during this stage of configuration defintion.

Potential aerodynamic solutions that should not add any weight include:

a. Increasing V-tail rollout.

b. Deflecting bottom surface trimming surface.

c. Reducing nose camber.

d. Reducing body side slope at V-tail.

The FR-3 and FR-4 orbiters can be retrimmed by further deflection of the 10-degree trimming surface. The V-tail sizing analysis showed that the vertical tail area could be reduced so that V-tail rollout can be increased to improve longitudinal stability and control. The FR-4 booster has the more severe problem, and some reshaping of the body to reduce nose camber pitch-up and side slope reduction to increase V-tail effectiveness might have to be done. The possibility of moving equipment forward would be examined at the same time to see if the cg can be moved back toward its initial location.

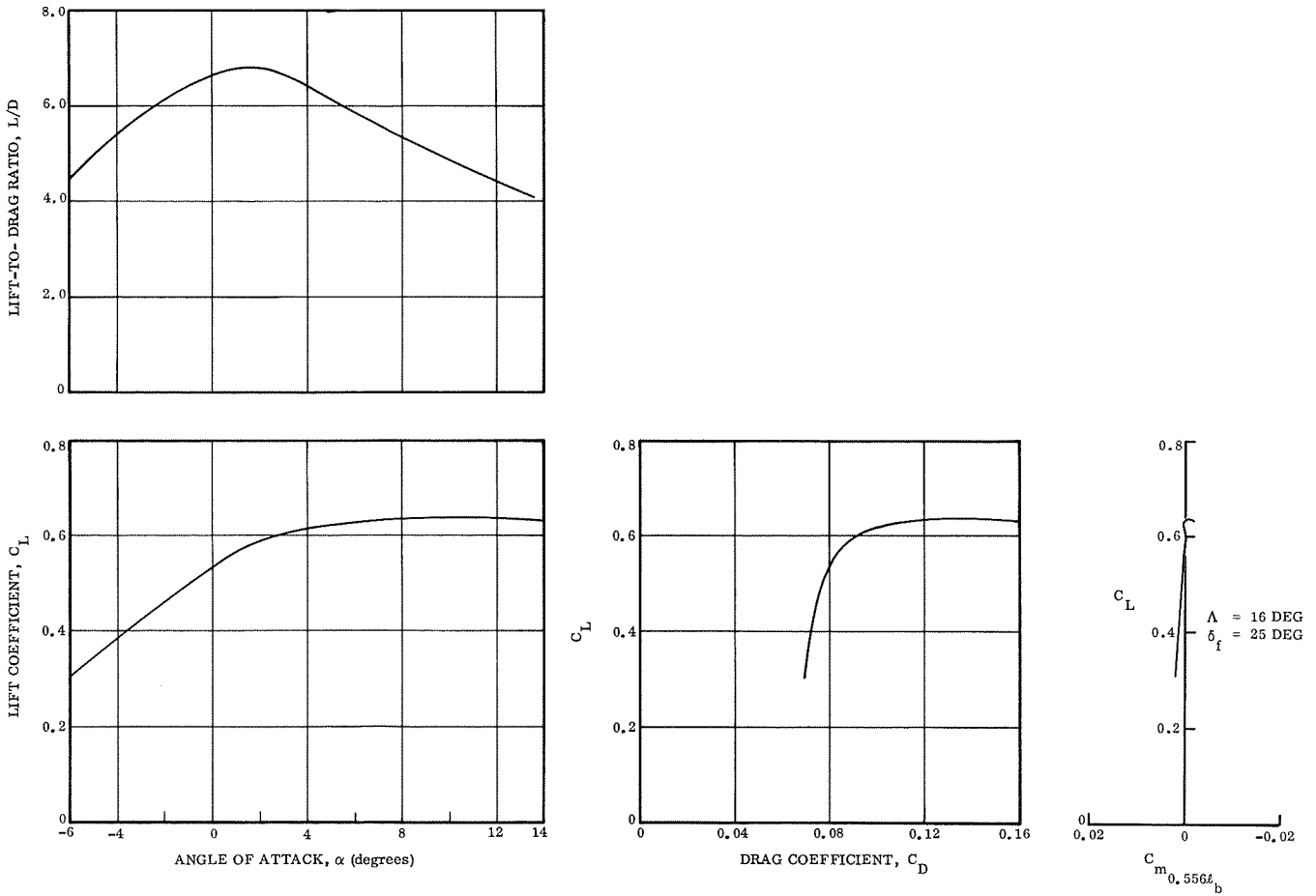

FOLDOUT FRAME

Figure 2-31. FR-3 Subsonic Longitudinal Aerodynamic Characteristics

FOLDOUT FRAME 2

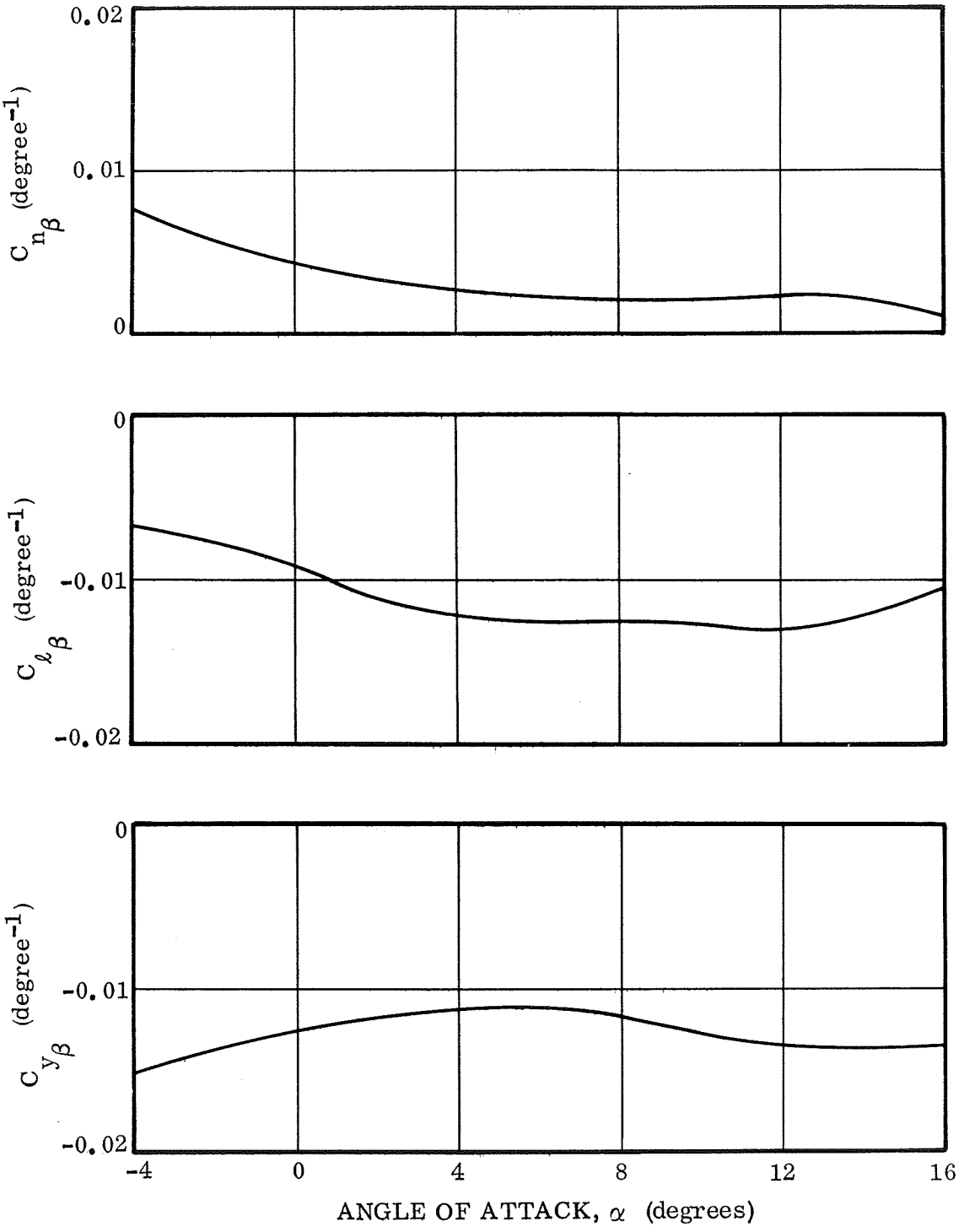

Figure 2-32. FR-3 Subsonic Lateral Direction Aerodynamic Characteristics

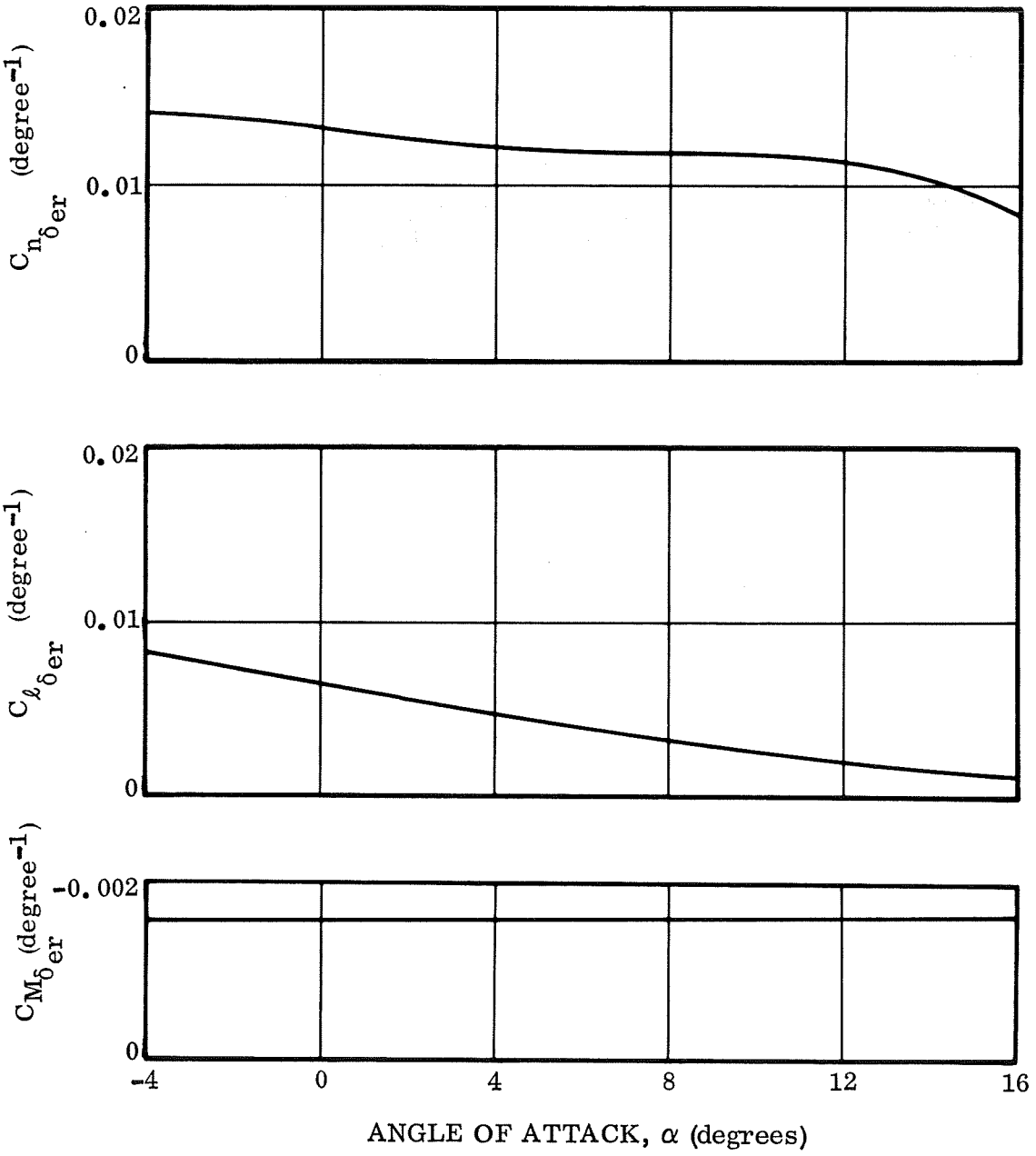

Figure 2-33. FR-3 Ruddervator Control Effectiveness

2.4 REFERENCES

2-1 A Preliminary Compilation of Triamese Aerodynamic Test Data, Convair Aeroballistics Technical Note TN-69-AE-10, August 1969.

2-2 Preliminary IPD Aerodynamic Description, J. R. Raush, Convair Aeroballistics Technical Note TN-69-AE-15, September 1969.

2-3 Subsonic Longitudinal and Lateral-Directional Characteristics of a Number of Tail and Body Configurations of the Triamese Vehicle as Tested in the Princeton Wind Tunnel, K. S. Coward, Convair Aeroballistics Technical Note TN-69-AE-03, March 1969.

2-4 "Viscous Effects on Hypersonic L/D of Three Classes of Manned Spacecraft," J. N. Mueller and R. M. Winebarger, J. of Spacecraft and Rockets, Vol 4, pp 1394-1395 (1967).

2-5 Alvarez - Calderon, United States Patent 3126173.

SECTION 3

FR-3 AND FR-4 PERFORMANCE

This section presents performance and trajectory data for the FR-3 and FR-4 configurations, based on the seven-day space station logistics mission. The mission profile, discussed in Volume II, Section 4.3, consists of the following phases.

Ascent trajectory and Booster return

Injection into 43- by 100-n.mi. transfer orbit

100-n.mi. phasing orbit

Transfer to 270-n.mi. orbit and rendezvous

On-orbit maneuver

Retro, entry, and orbiter glide to launch site

A delta velocity of 2000 ft/sec was allowed for all maneuvers after the transfer orbit injection: 1800 ft/sec from the main engines and 200 ft/sec from the ACS subsystem. Figure 3-1 shows the trajectory profile.

The synthesis program and methodology used throughout the study are described in Section 3.1. The synthesis method, coupling the weight/sizing and trajectory computations in one computer program, provides a proper interface between vehicle design parameters and the trajectory throughout trade studies. The performance data is then presented in the chronological sequence in which the configurations were investigated: FR-4, then FR-3. The topics treated are nominal ascent, abort, entry, landing, and ferry. For alternative mission performance, refer to Volume II, Section 4.3.

3.1 SPACE SHUTTLE SYNTHESIS PROGRAMS

Convair has developed, under company-sponsored efforts, two vehicle and mission synthesis programs for space shuttle configurations: the three-element synthesis program (TSP) and the two-stage recoverable synthesis (TSRS) program. These synthesis programs have been used extensively to generate the tradeoff and sensitivity data presented in Volume III. Both programs were assembled by interfacing Convair's general trajectory simulation module and weight/volume program, References 3-1 and 3-2.

3.1.1 THREE-ELEMENT SYNTHESIS PROGRAM (TSP). The TSP provides vehicle sizing, trajectory simulation, and performance determination for the FR-1 and FR-4 configurations. Vehicle sizing can be accomplished within the common envelope constraint of the booster and orbiter elements, or the elements can be sized independently.

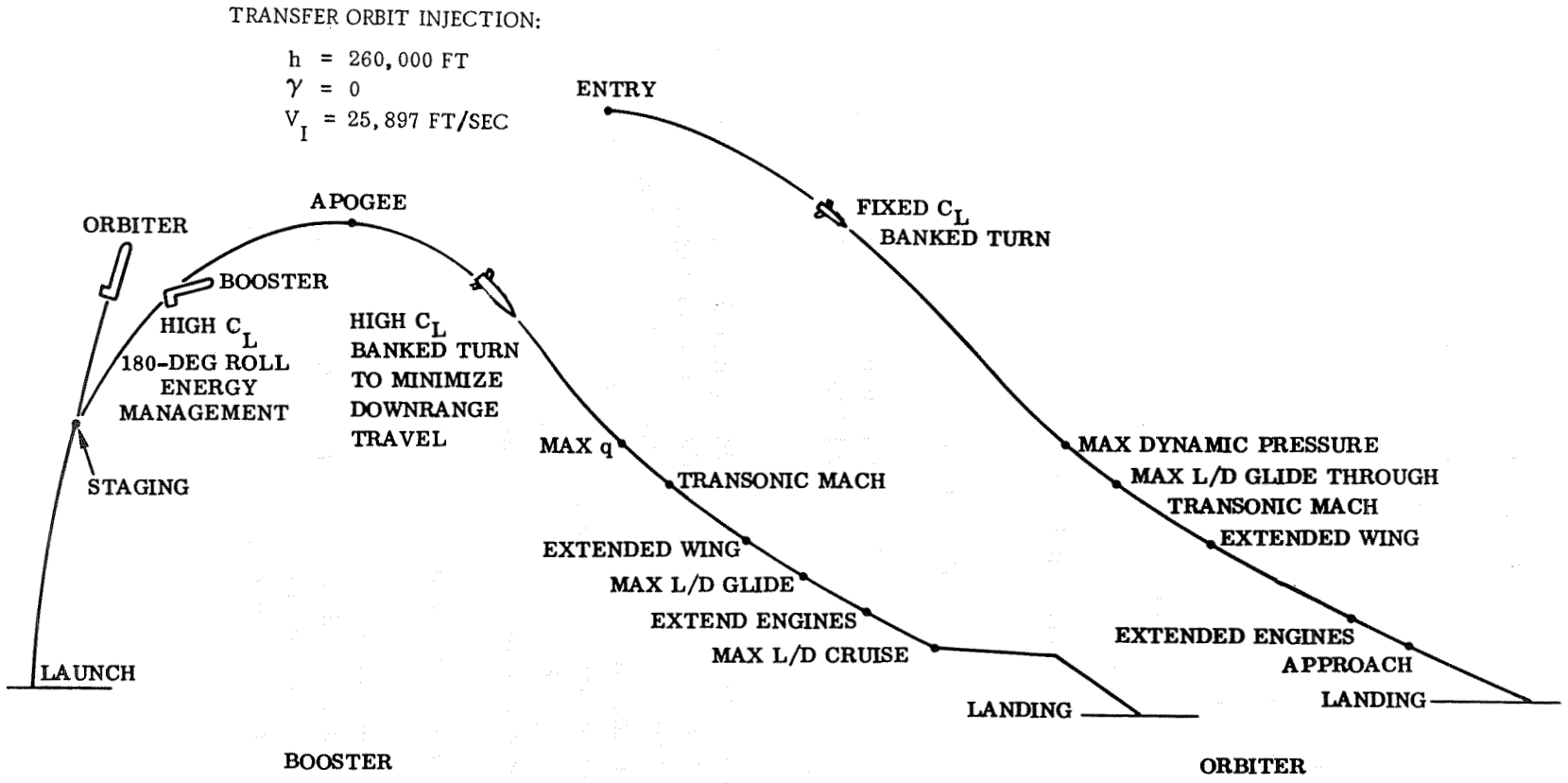

Figure 3-1. Boost and Entry Mission Profiles

Numbers of engines on all booster and orbiter elements are TSP input parameters. Booster/orbiter staging and orbital injection conditions are iteratively satisfied by TSP control logic using trajectory pitch control and element mass ratios. Booster flyback fuel is determined and included in the total configuration sizing. Each TSP run yields a space shuttle configuration sized to perform the specified mission for a given payload within specified constraints, while satisfying given staging and orbital injection conditions. Included in the output are the trajectory history, weight, volume and design data, flight sequence weights, and a summary page with significant weight, volume, geometry, propulsion, and trajectory data.

Organization of the TSP is indicated in Figure 3-2. Trajectory and weight/volume calculations (indicated within the outlined blocks) are performed by program modules from existing programs. The iteration and synthesis logic indicated as Mass Ratio Estimator provides an efficient means of iteratively sizing both the boosters and orbiter to satisfy specified trajectory and vehicle constraints. Typical constraints included are:

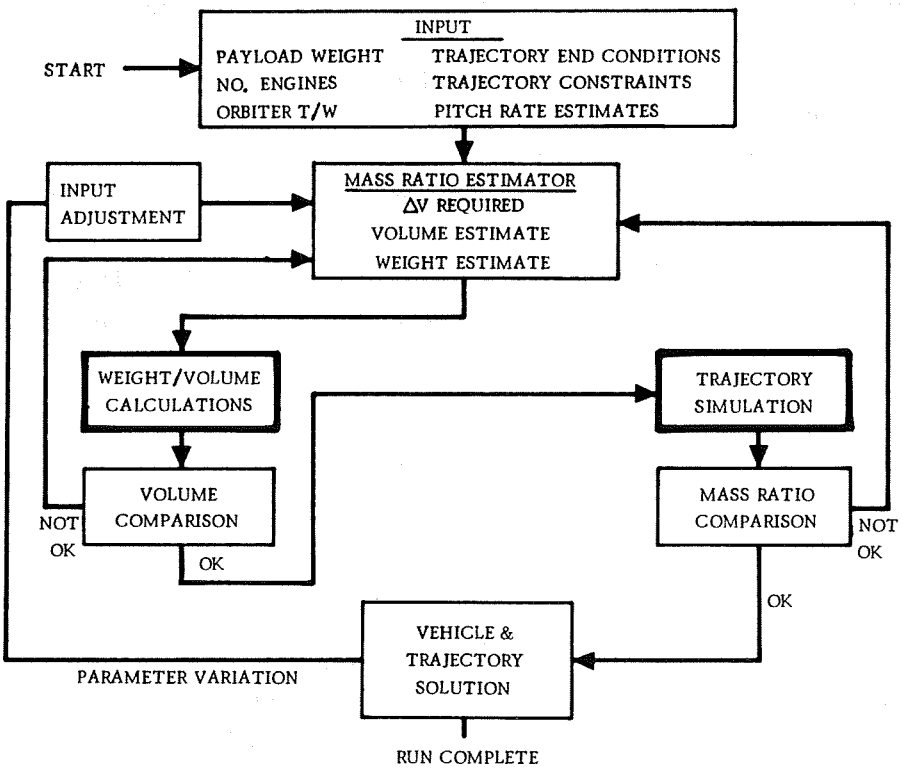

Figure 3-2. TSP Organization

a. Specified terminal conditions for transfer orbit injection.

b. Specified dynamic pressure at stage separation.

c. Axial load limit, requiring thrust throttling.

d. Hardware commonality, including an option for equal volumes for booster and orbiter.

The ascent trajectory is simulated by numerical integration, with simplified aerodynamics and propulsion models and a simple parameterized pitch attitude control program. The booster return flight is accounted for by builtin empirical performance equations that yield flyback range and fuel requirements as functions of the trajectory conditions at separation (dynamic pressure, flight path angle, and velocity) and the vehicle characteristics (L/D, specific fuel consumption, and cruiseback speed). These empirical equations result from previous Convair research in entry configurations. The orbital maneuver and retropropellant requirements are accounted for by ideal velocity computations.

Configuration flexibility provided by TSP input options includes changing the numbers of engines per vehicle element, changing the specification of common-hardware items (i.e., items for which the booster subsystem weights and volumes are set equal to those from the orbiter instead of being scaled with booster size independently of corresponding orbiter subsystems), and changing the propulsion and propellant-feed modes.

An important feature of the synthesis program is its detailed printout of vehicle and trajectory data. First is a weight breakdown, by subsystem, of the orbital element. Next are a volume summary and various design data, and a weight summary according to the flight sequence. Similar data is repeated for the boost elements. Finally, the ascent trajectory listing and a synthesis summary output are presented. A typical sample of this summary sheet is included in Section 3.1.2.

3.1.2 TWO-STAGE RECOVERABLE SYNTHESIS (TSRS). Convair's TSRS provides trajectory and performance simulation for two-stage space shuttle configurations together with stage sizing and weight determination. The program organization is quite similar to that of the TSP described in Section 3.1.1.

TSRS can accommodate sequential or parallel burning of the booster and orbiter elements. Engine throttling to satisfy axial load factor limitations can be simulated, as in TSP. The aerodynamic force coefficient models permit side-by-side or end-to-end configurations to be treated.

The major difference between TSRS and TSP is that TSRS has no option for a volume constraint relating booster and orbiter elements. Whereas staging in TSP is primarily controlled by the common volume constraint, TSRS uses specification of the booster mass ratio. Staging dynamic pressure and orbital injection conditions are satisfied with trajectory pitch schedules and with orbiter mass ratio, just as in TSP.

Output of the TSRS is quite similar to that of the TSP except, of course, that only one booster element is considered.

TSRS provides, in each synthesis run, a two-stage space shuttle sized for the specified parameters together with the associated trajectory and performance histories and weight, volume, geometry, and propulsion determination.

3.2 FR-4 PERFORMANCE

3.2.1 ASCENT. To provide a consistent basis for vehicle synthesis, a baseline ascent trajectory profile was established as shown in Figure 3-3. The important features and constraints are:

a. Eight-second vertical rise.

b. Sixteen-second pitchover, with pitch rate iterated to satisfy staging q = 50 psf constraint.

c. Gravity turn to booster burnout.

d. Coast during separation (two seconds).

e. Constant angle of attack ($\alpha = \alpha_1$) for approximately half of the orbiter burn followed by a linear angle of attack schedule ($\alpha = \alpha_2 - \alpha_2 t$) to injection. Both α_1 and α_2 are iterated to satisfy injection conditions (h = 260,000 ft, V_I = 25,897 fps and γ = 0 deg).

f. Orbiter ignition after staging.

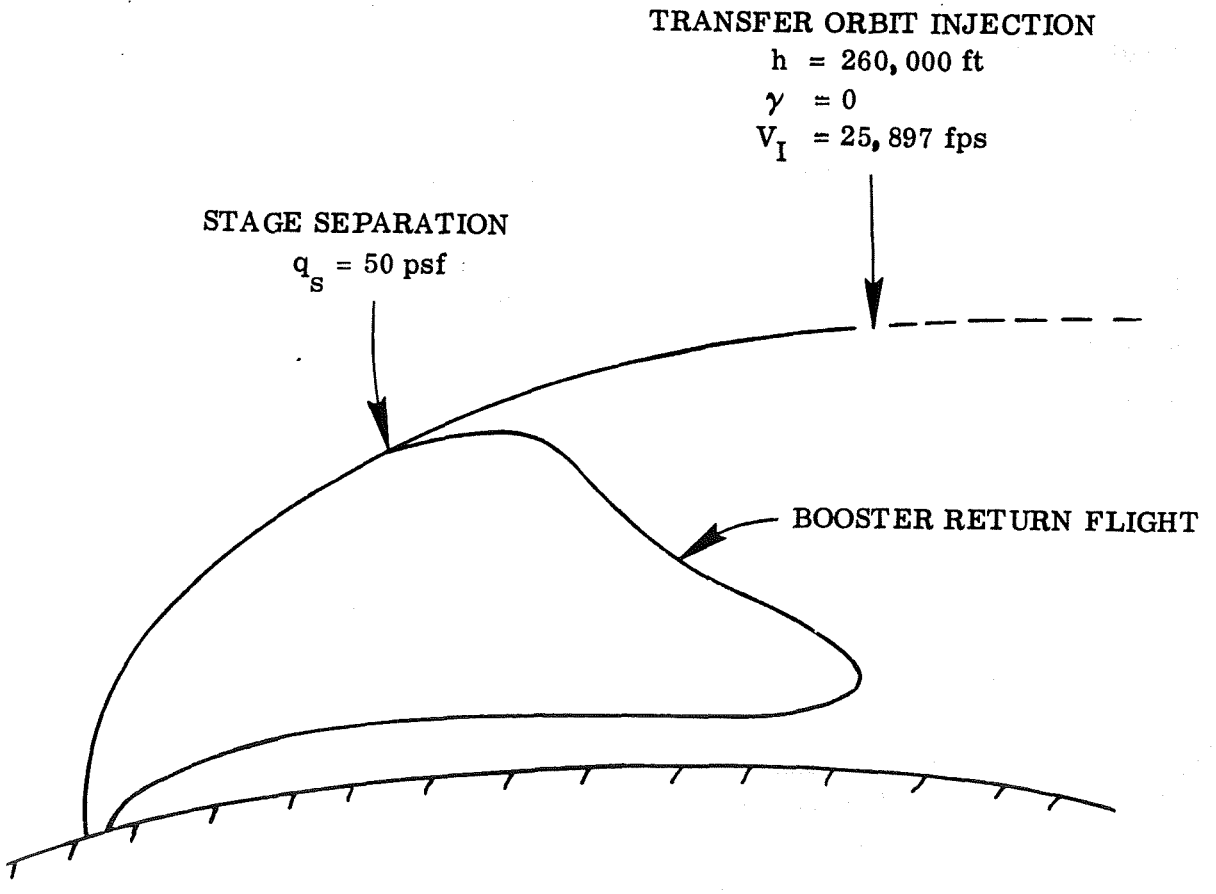

Figure 3-3. FR-4 Launch Trajectory Profile

This trajectory profile is a result of tradeoffs among gross weight minimization, stage separation conditions, booster return and abort requirements, and heating limits. The tradeoff study is discussed in Volume II, where it is shown that the selected staging q (q_s = 50 psf) and injection altitude (h = 260,000 feet) values result in near-optimal performance within reasonable environmental constraints.

Pertinent ascent trajectory parameter time histories for the FR-4 vehicle, taken from the final FR-4 vehicle synthesis, are presented in Figure 3-4. The synthesis summary is given in Table 3-1. The nominal FR-4 launch, liftoff, staging, and injection parameters are:

Launch Site Location	ETR
Launch Azimuth	37.65 deg
Liftoff Thrust	7,199,685 lb
Liftoff Weight	4,915,114 lb
Liftoff Thrust/Weight	1.465
Staging Time	173.11 sec
Staging Altitude	179,326 ft
Staging Relative Velocity	9,400 ft/sec
Staging Dynamic Pressure	50 psf
Staging Relative Flight Path Angle	5.822 deg
Staging Weight	1,901,183 lb
Injection Time	429.41 sec
Injection Altitude	260,000 ft
Injection Inertial Velocity	25,897 ft/sec
Injection Inertial Flight Path Angle	0 deg
Injection Weight	383,325 lb
Injection Orbital Inclination	55 deg
Maximum Longitudinal Acceleration	3 g

3.2.2 FR-4 ABORT. The most critical abort situation from a performance standpoint is an engine failure with the resulting loss of thrust. The abort approach adapted for the FR-4 in the event of an engine failure during any phase of the ascent trajectory is that the orbiter element continues to orbit and goes once around the earth before returning to the launch site. To fulfill this requirement, the orbiter needs sufficient velocity at burnout for injection into a ballistic path having the appropriate entry angle

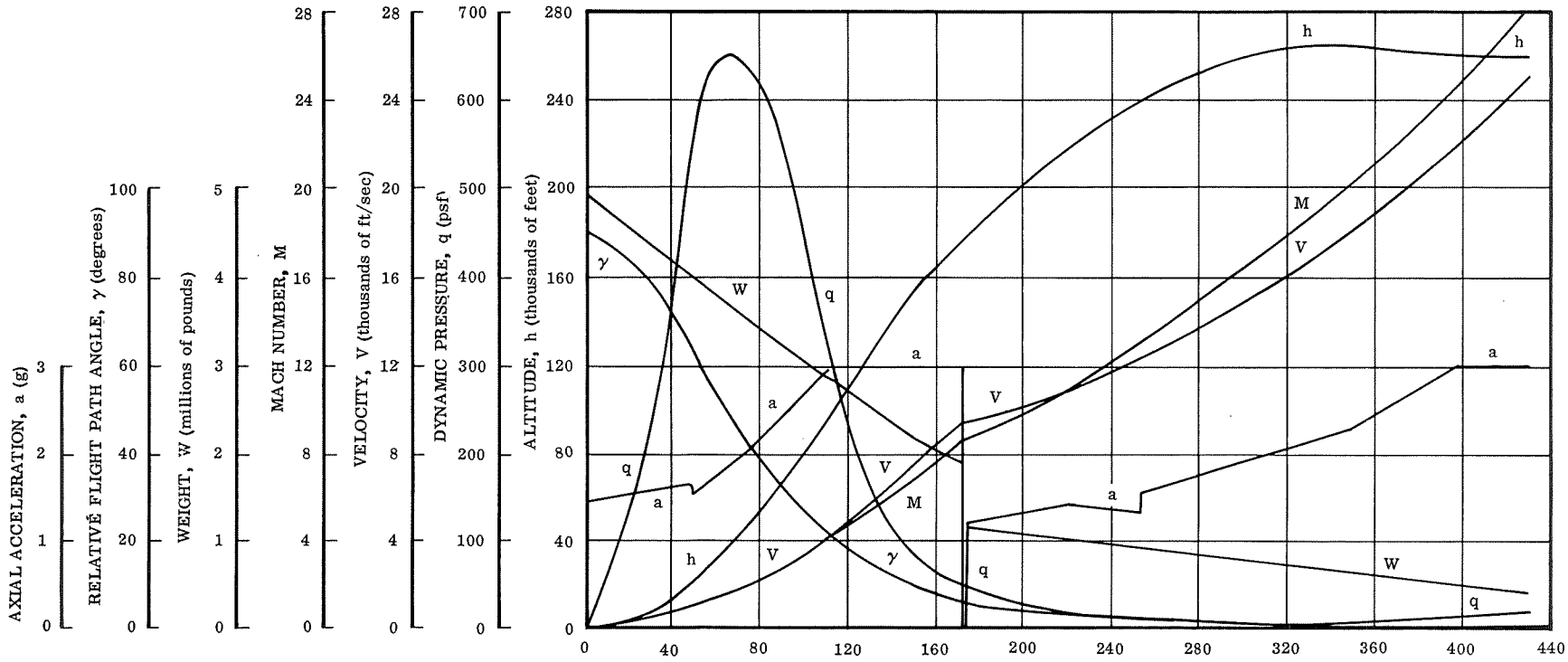

FOLDOUT FRAME

Figure 3-4. FR-4 Ascent Trajectory

FOLDOUT FRAME 2

Table 3-1. FR-4 Synthesis Summary

10/13/69

NASA FR-4, 50K P/L, 9-3-9 ENG 400K, DELTA VOL = +15K

	BOOSTER ELEMENT	ORBITER	VEHICLE
WEIGHT			
PROPELLANT, ASCENT	1506966	783165	
PROPELLANT, ORBIT MANEUVER		42129	
PROPELLANT, TOTAL	1506966	825293	
FLYBACK FUEL	30729	3226	
PAYLOAD		50000	
STRUCTURE	294901	247014	836816
CONTINGENCY	29490	24701	
OTHER	14959	10789	
TOTAL	1877045	1161024	4915114
IN ORBIT		383659	
RETURN CONDITION	370079	373050	
ENTRY	355726	327263	
LANDING	324730	322562	
VOLUME			
FUEL	49835	19141	
OXIDIZER	19382	10074	
PROPELLANT	69217	29215	
PAYLOAD		10638	
OTHER	53115	67590	
TOTAL	122332	107443	
GEOMETRY			
LENGTH	199.2	190.8	
BODY WETTED AREA	18417.5	16891.1	
BODY PLANFORM AREA	6067.1	5564.2	
ENTRY PLANFORM LOADING	58.6	58.8	
PROPULSION			
THRUST-TO-WEIGHT		1.21858	1.46481
NO. OF ENGINES	9	3	
SL THRUST/ENG NOM/UR	399986/ 399986	238369/	7199739/ 7199739
VAC THRUST/ENG NOM/UR	461838/ 461838	471600/	8313082/ 8313082
SL ISP NOM/UR	389.3/389.3	232.0/	389.3/389.3
VAC ISP NOM/UR	449.5/449.5	459.0/	449.5/449.5
TRAJECTORY			
MASS RATIO	2.58529	3.02882	
MAXIMUM DYNAMIC PRESSURE			657.9
STAGING DYNAMIC PRESSURE			50
STAGING VELOCITY (RELATIVE)			9400
STAGING ALTITUDE			179326
STAGING FLIGHT PATH ANGLE (RELATIVE)			5.822
INJECTION VELOCITY (INERTIAL)		25897	
INJECTION ALTITUDE		259993	
INJECTION FLIGHT PATH ANGLE (INERTIAL)		-.000	
INJECTION INCLINATION		54.95	
FLYBACK RANGE	255.6		

and downrange distance values during glide following reentry. To achieve both large downrange and crossrange capabilities with low temperatures, a ballistic path passing through 400,000 feet at a minus one degree flight path angle is used. Figure 3-5 illustrates the once-around geometry.

The additional velocity above the nominal trajectory necessary to achieve the once-around abort maneuver can be described by two velocity increments. The first is associated with the engine-out ascent trajectory and is due to the additional gravity, drag, and misalignment losses encountered in meeting the required burnout conditions. The second velocity increment is the additional injection velocity necessary to achieve the required downrange distance after entry. This second velocity increment is small, typically less than 100 ft/sec. These two additional velocity increments must be less than the orbital maneuver main propulsion velocity allowance for the mission being considered (1800 ft/sec for the baseline mission).

For each burnout velocity (at injection), there is a resulting downrange entry path requirement for landing at the launch site. The downrange distance required after entry, θ_{re}, and the flight path angle at injection, γ_{bo}, were determined for each value of V_{bo}, the injection velocity, from standard Keplerian equations. Figure 3-6 presents the results of these calculations. The effect on the injection velocity requirement of small changes of γ_{re} or of small changes of entry downrange available can be obtained from this figure.

To determine the trajectory effects of engine-out conditions, the ascent trajectory losses for various fractions of booster and orbiter thrust were evaluated with a series of trajectory simulations. The baseline trajectory profile was used for the analysis.

The engine-out (reduced thrust) trajectories were constrained to the same terminal conditions (ballistic injection at 260,000 feet altitude, 25,897 ft/sec) and to the same dynamic pressure at stage separation as the baseline. It was assumed that the orbital maneuver propellant could be used to offset the additional velocity losses due to thrust reduction.

For each trajectory, the total ideal velocity at injection was tabulated and compared to the baseline to determine the additional velocity losses. The results are presented in Figure 3-7. The number of engines on each element can be considered variable, determining the fraction of thrust lost when an engine fails. Once-around capability is satisfied if the sum of additional velocity losses and the injection velocity required for once-around (Figure 3-6) is less than the orbital maneuver propellant allowance.

The data in Figure 3-7 is approximate due to simplifications used to facilitate calculations:

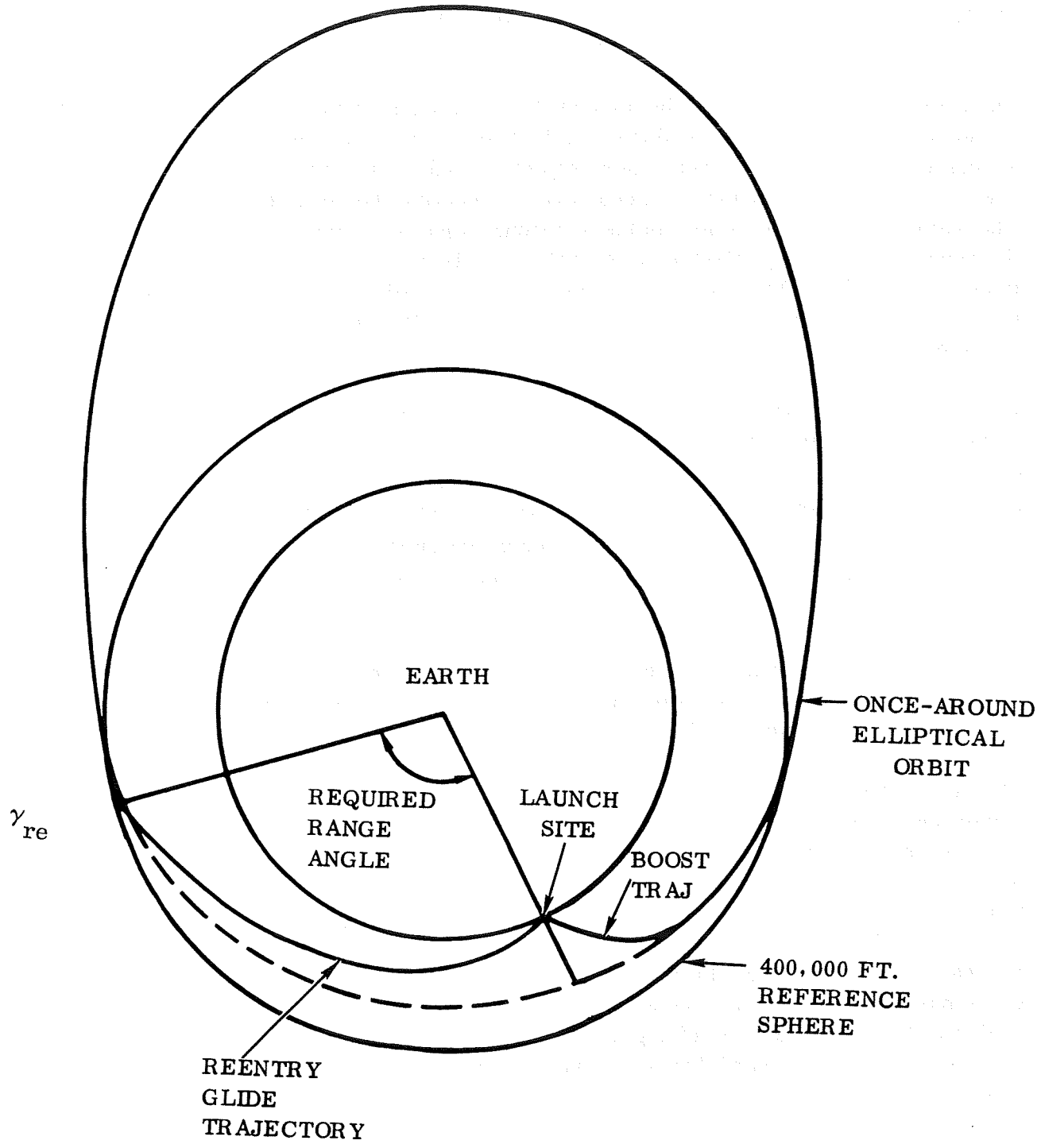

Figure 3-5. FR-4 Once-Around Trajectory

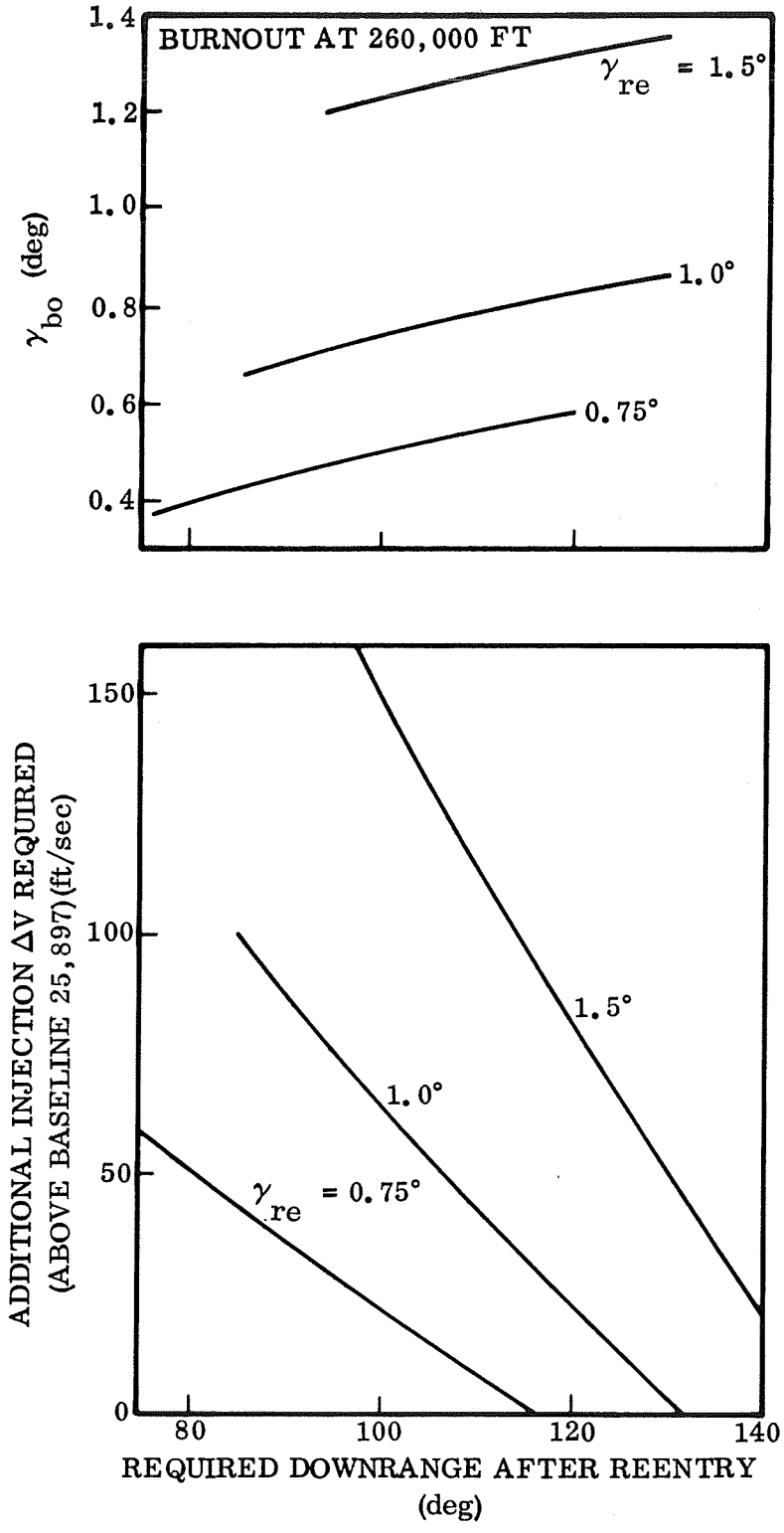

Figure 3-6. FR-4 Once-Around Burnout Requirements

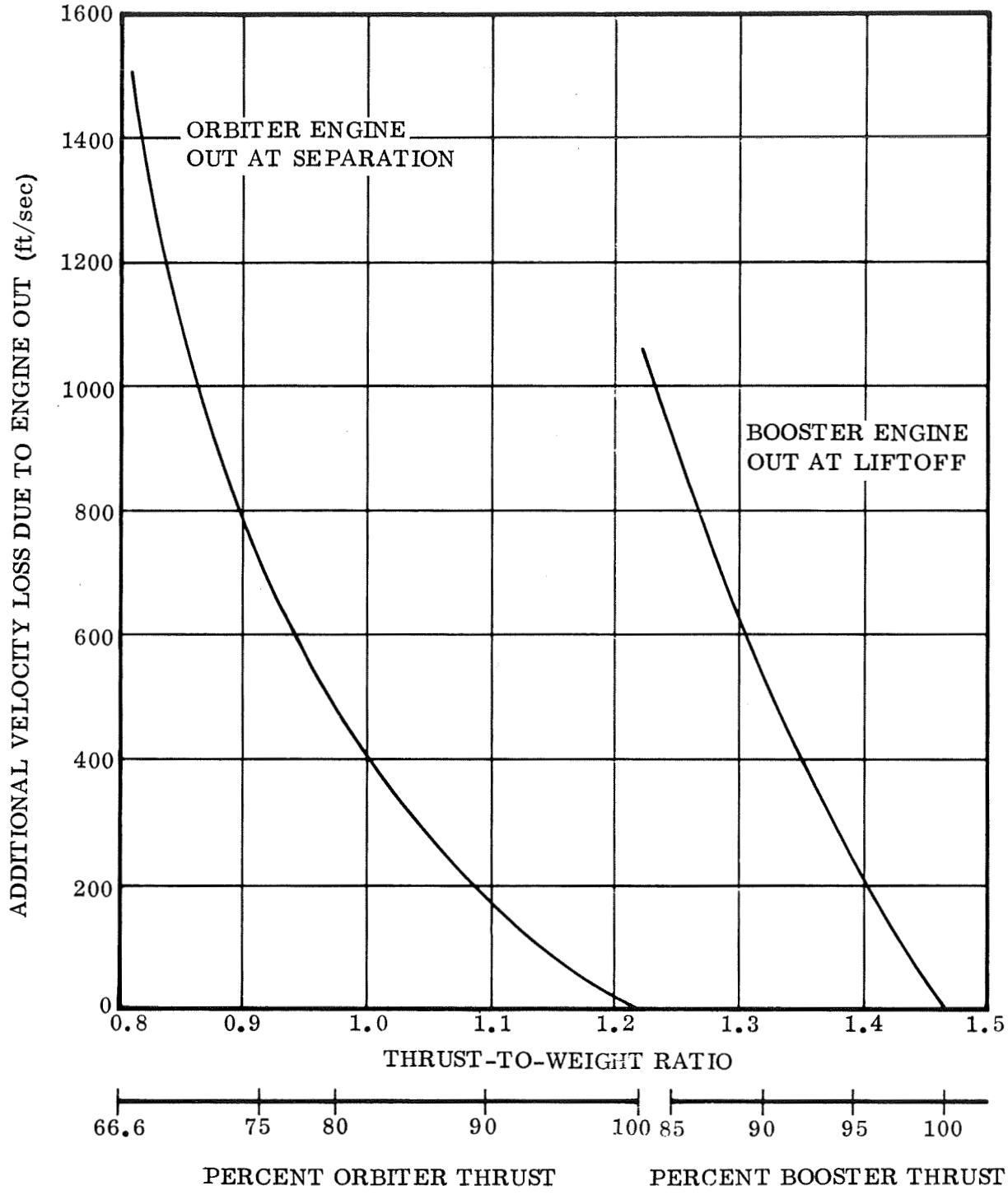

Figure 3-7. FR-4 Engine-Out Trajectory Losses

a. The simplified trajectory profile used throughout (instead of detailed pitch program optimization) results in 20 to 50 ft/sec additional velocity losses. This estimate is based on spot-checking data points with more detailed simulations.

b. Constraining the abort trajectories to the same staging dynamic pressure and terminal altitude results in losses of up to approximately 100 ft/sec. These losses probably cannot be eliminated in practice, however, because staging at lower q to improve orbiter performance would probably result in excessive booster entry temperatures.

c. The performance advantage associated with using the 0-degree burnout flight path angle for the ascent trajectories, instead of 0.8 degree as required for the 1-degree entry condition, is less than 25 ft/sec.

d. The assumption that an engine loss is sensed and compensated for instantly results in the data being optimistic.

e. The penalties due to engine gimballing and aerodynamic effects of the associated angles of attack were not considered.

The errors resulting from these assumptions are in offsetting directions, so conclusions drawn from the data should be reasonably accurate and reliable.

No effort was made to assess guidance, control, or thermal problems. Extension of the data to configurations with different baseline T/W ratios is straightforward by extrapolation and interpretation of the T/W contours in Figure 3-7.

3.2.3 ENTRY PERFORMANCE. Figure 3-1 shows a typical mission profile illustrating the booster return maneuver and the orbital vehicle entry trajectory.

3.2.3.1 Booster Entry. The booster return trajectory is shown in Figures 3-8 and 3-9. Figure 3-8 shows the energy management maneuver (180-degree roll) through apogee and then the rollout to a bank angle (55 degrees) to turn without exceeding the structural load factor at maximum dynamic pressure. When this point is reached, a 90-degree bank is performed to keep the turn load factor as high as possible but still below the structural limit. This turn is held until the flight path angle reaches that of the entry configuration (L/D = 2), where the turn is continued at maximum L/D until Mach 1.0 is reached and wing deployment is initiated.

The vehicle has turned 90 degrees from its initial launch heading at this point, and the turn is stopped until the wing extension is complete and a maximum L/D (7.8) glide has been established. The wing-extension maneuver has not been analyzed in detail, but past Convair analyses indicate that the wing extension is a stable aerodynamic maneuver and presents no unusual control problem. The wing extension is assumed to be completed and an L/D = 7.8 glide established at the altitude where the glide dynamic pressure (100 psf) corresponds to a Mach 0.6 glide. The remaining turn is then made and the glide is continued until 25,000 feet. This glide achieves approximately 40 n.mi. back toward the recovery site.

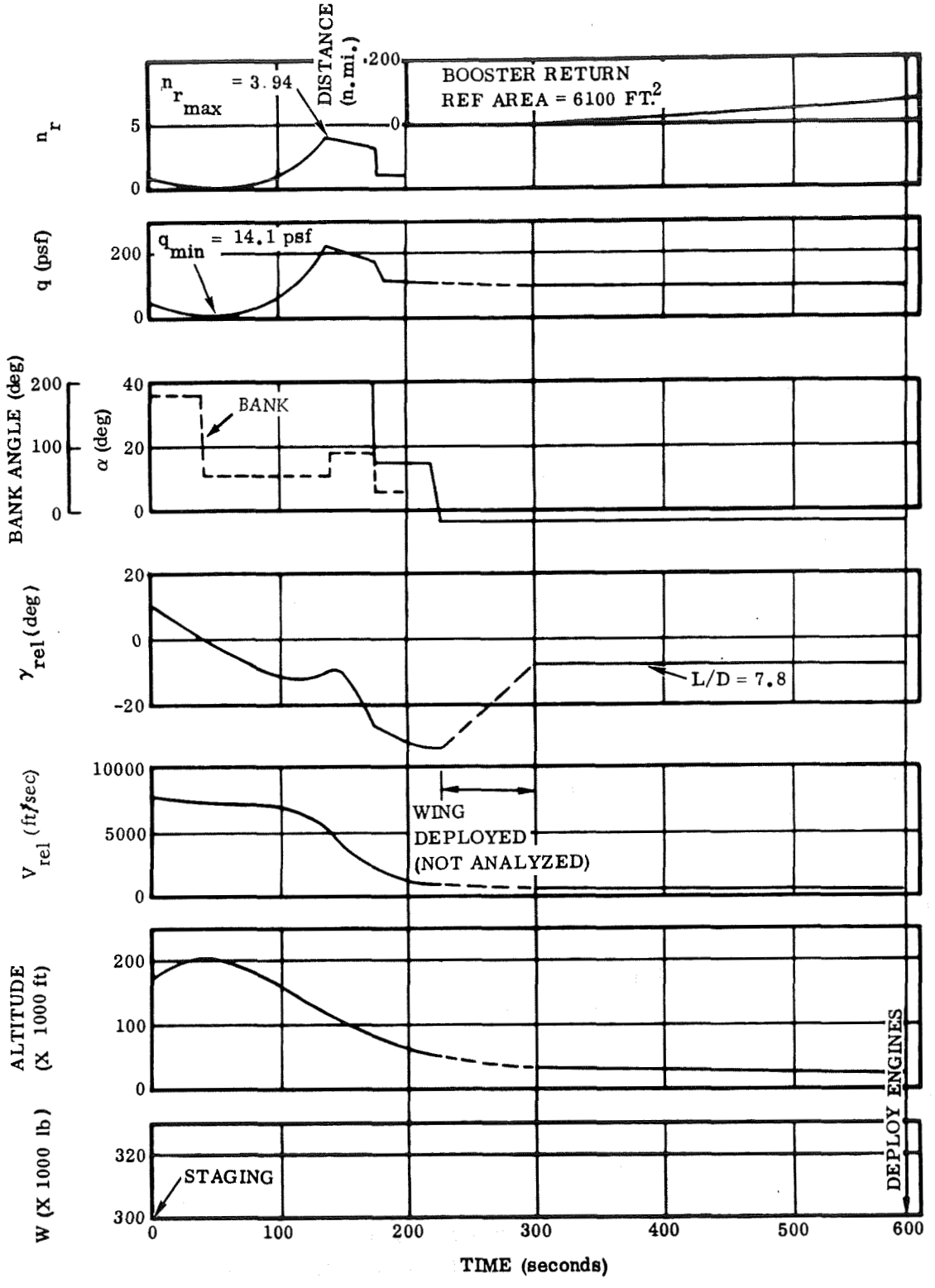

Figure 3-8. FR-4 Booster Return Trajectory - Staging to Engine Deployment

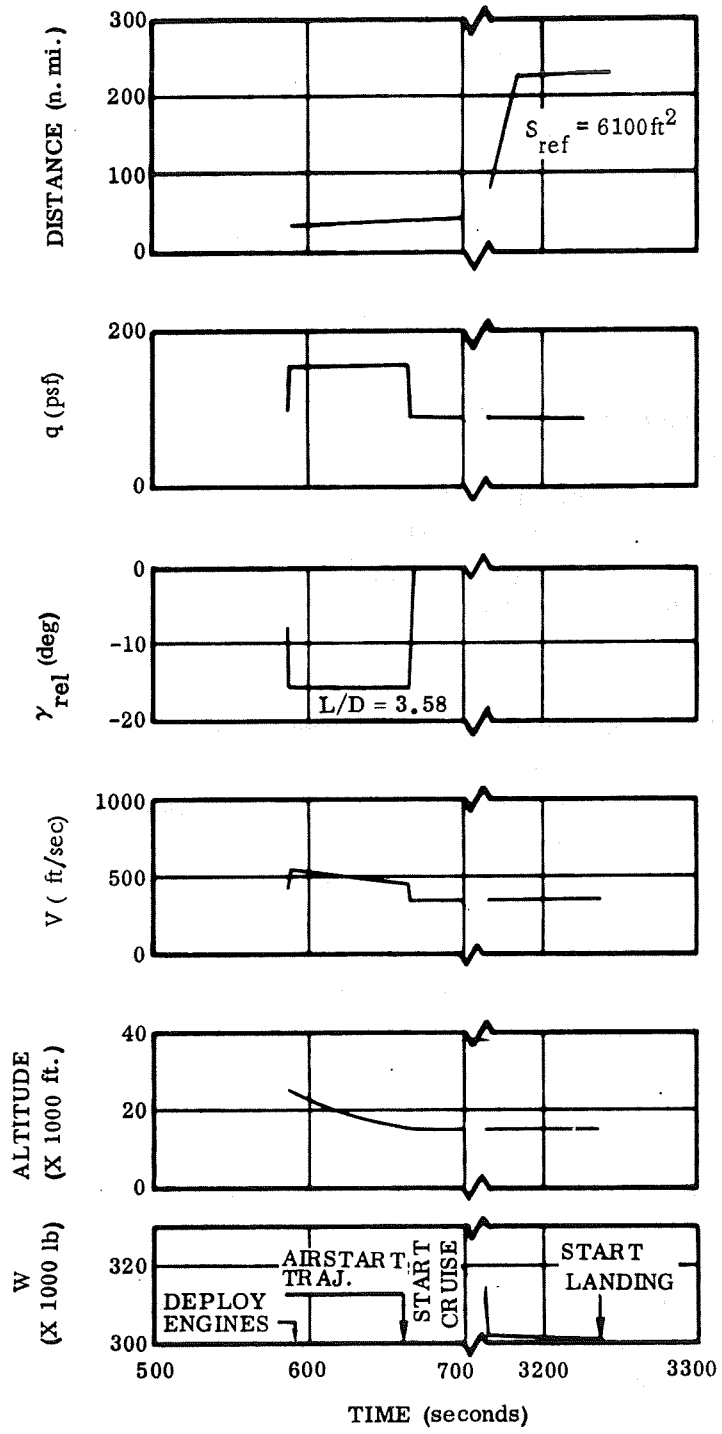

Figure 3-9. FR-4 Booster Return Trajectory - Engine Deployment to Landing

At 25,000 feet (Figure 3-8), the engines are extended and an L/D = 3.5 glide is established to fly the vehicle down an airstart trajectory to 15,000 feet, which takes 77 seconds. The maximum L/D with engines extended and windmilling is 6.5, and could be flown if starters are used. The required cruise distance back to launch point is 189 n.mi. because of the 46 miles of useful glide obtained in this trajectory. Landing performance will be discussed in the next section.

3.2.3.2 Orbiter Entry. The orbiter entry was simulated by a point mass trajectory program starting from a 55-degree orbit with the following starting conditions:

Entry altitude = 400,000 ft

Entry velocity (inertial) = 25,970 ft/sec

Entry flight path angle = -1.0 deg

The entry is made at a constant angle of attack at zero bank angle until the vehicle attains level flight. When the flight path angle reaches zero (level flight), the vehicle rolls to the bank angle that will maintain level flight. As velocity is reduced at this constant altitude, the vehicle rolls back to the final bank angle selected as input. At this point, the flight continues down the equilibrium glide path to reach the desired crossrange. The entry planform loading varies from 50 psf (no payload returned) to 58.5 psf (if a 50,000-pound payload is returned).

A schematic of the landing footprint is shown in Figure 3-10. The 800-n.mi. lateral range is accomplished by maintaining a 37-degree angle of attack and a 20-degree bank, as shown in Figure 3-11. Figure 3-12 presents the history for a 300-n.mi. lateral range. The final glide sequence is shown, but is essentially the same as that for the booster except that the vehicle has no cruise capability.

The wing is extended to allow final corrections in approach to landing site. The engines are extended at 15,000 feet and started during landing approach to allow go-around if necessary. At the orbital velocity, for a 270-n.mi. orbit, of 24,945 ft/sec, the longitudinal miss distance is 4.11 n.mi. per second of retro time error.

3.2.4 LANDING. Three-degree-of-freedom landing trajectories, both powered and unpowered, were generated for the orbital vehicle. A standard -3 degree flight path approach was assumed for the powered landings. Figure 3-13 presents a landing history with an approach speed of 1.2 of power-off stall speed; the flare was initiated at 50 feet, and the sink rate at touchdown was 2.7 ft/sec. This approach speed corresponds to a lift coefficient of 0.486, which is less than that of maximum L/D. Touchdown speed is 186 knots.

Figure 3-14 presents a maximum L/D approach, which results in a 4.2 ft/sec sink rate at touchdown. The flare maneuver requires larger angle of attack changes because of the decline of lift curve slope above maximum L/D. The touchdown speed for this maneuver is 165 knots.

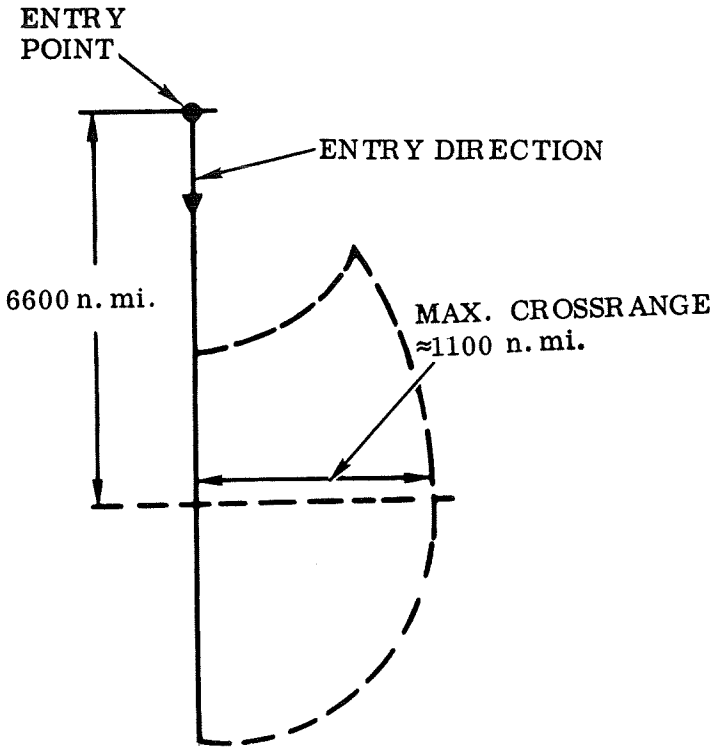

Figure 3-10. Footprint Schematic

Figure 3-15 presents a power-off approach at 320 ft/sec, which results in a -8.1 degree glide slope. The flare maneuver was initiated at 150 feet and the sink rate at touchdown was 7.5 ft/sec. The oscillations during this landing show that further work is needed on the stability augmentation subsystem. The power-off approach must be made at this speed to allow reasonable maneuverability without thrust.

3.2.5 FERRY PERFORMANCE. While there is no specific ferry requirement, performance was analyzed to determine potential ferry range of these vehicles. The wing is mounted at a high angle of incidence on both the booster and orbiter vehicles to maximize cruise and landing performance. This affects the take-off performance of both vehicles in two ways:

a. A B-52 type takeoff is performed (no rotation prior to liftoff).

b. Since the wing has considerable lift, the induced drag must be accounted for during takeoff acceleration (ignoring ground effect on induced drag).

The takeoff performance was computed assuming:

a. Sea level standard day.

b. No wind.

c. Thrust model as shown in Figure 3-16.

d. No rotation.

e. Takeoff speed = 1.2 power-off stall speed.

f. Vehicle $C_L = 0.486$ during takeoff.

g. Rolling friction drag = $0.03\ (W - C_L\ qS)$.

h. Aerodynamic drag = $(C_{D_O} + C_L^2/\pi\ AR_W)qS$

i. SFC = 0.49.

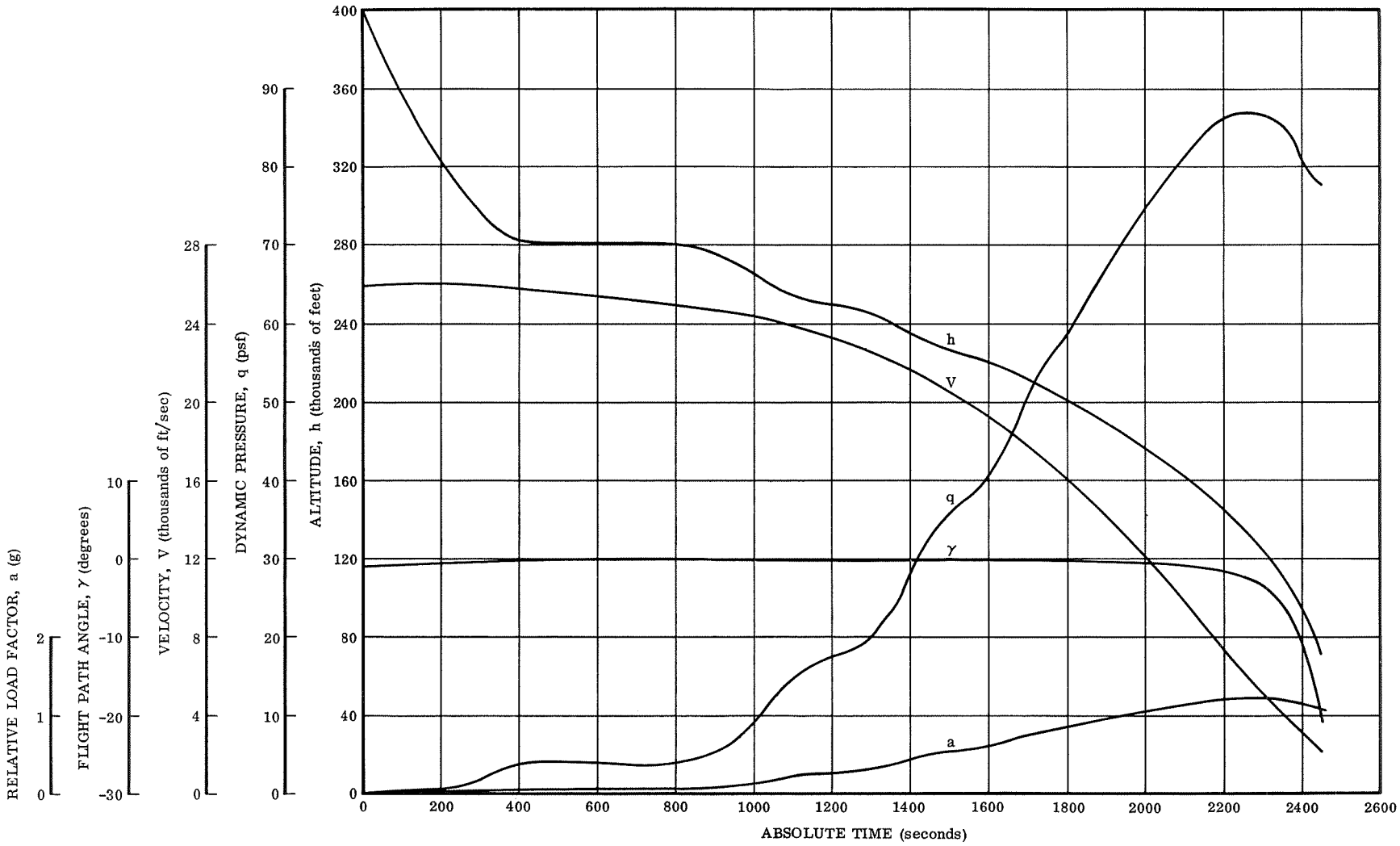

Figure 3-11. 800-n.mi. Crossrange Time History

FOLDOUT FRAME

FOLDOUT FRAME 2

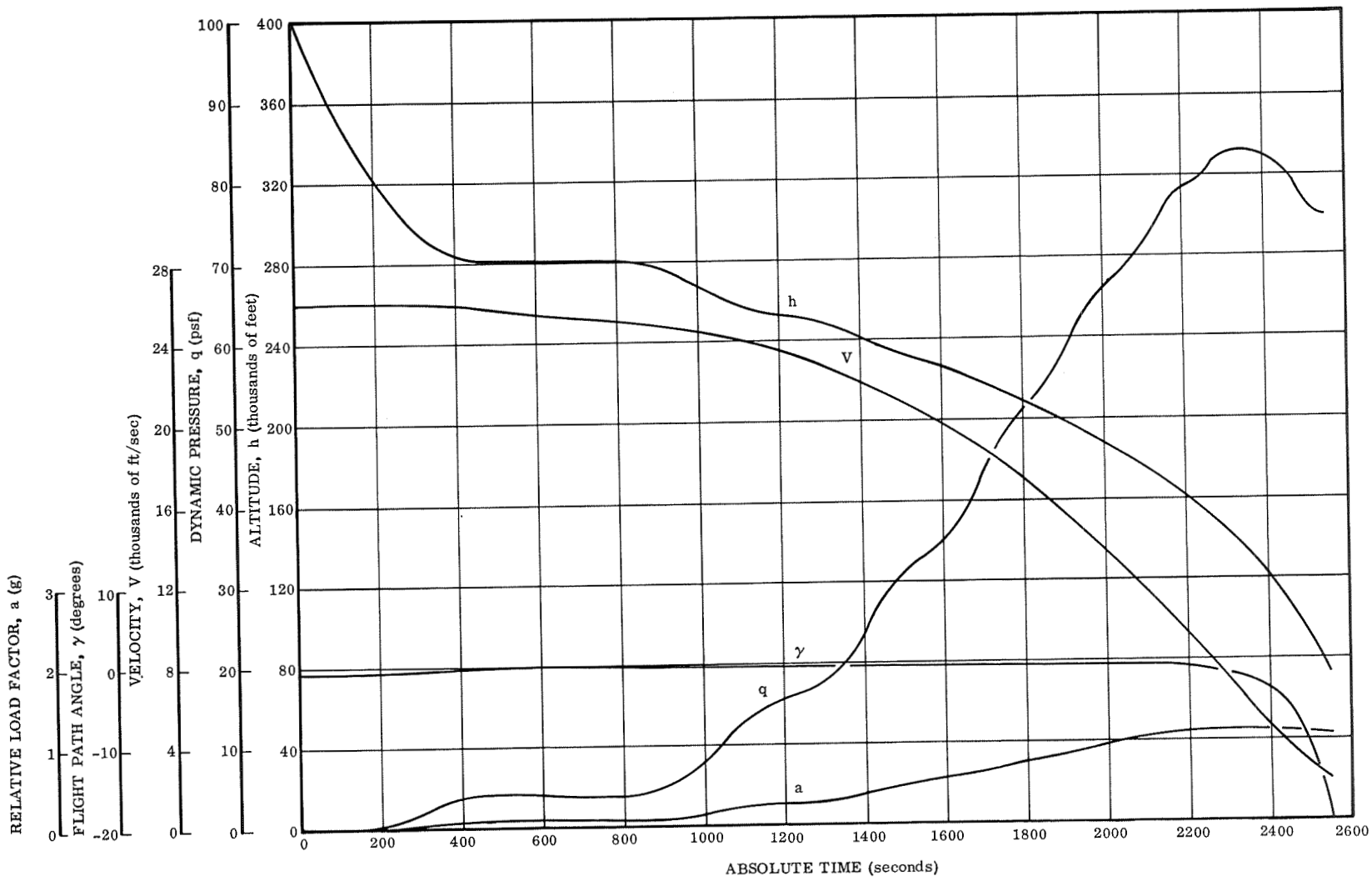

FOLDOUT FRAME

Figure 3-12. 300-n.mi. Crossrange Time History

FOLDOUT FRAME 2

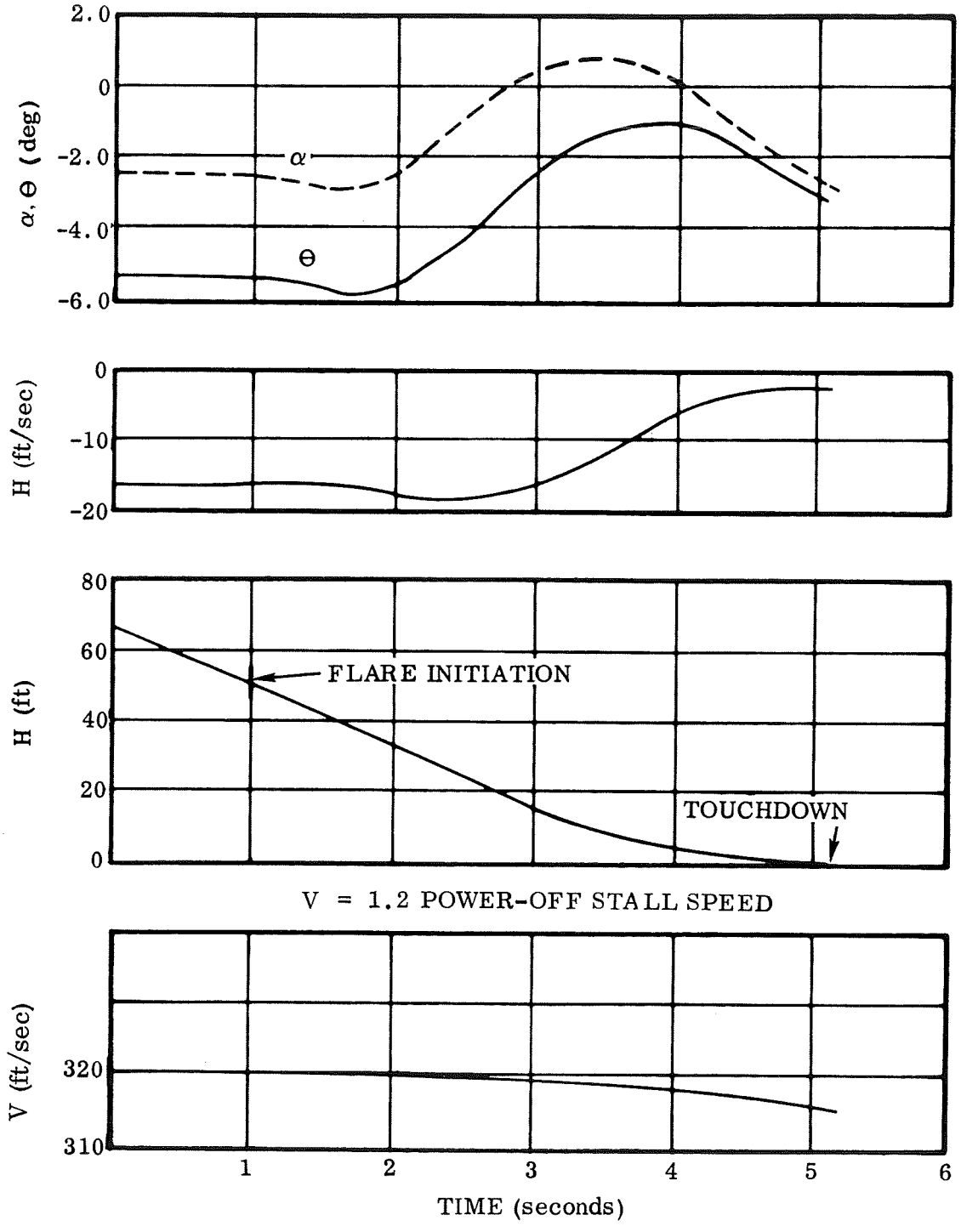

Figure 3-13. FR-4 Flare (V = 320 ft/sec, γ = -3 degrees)

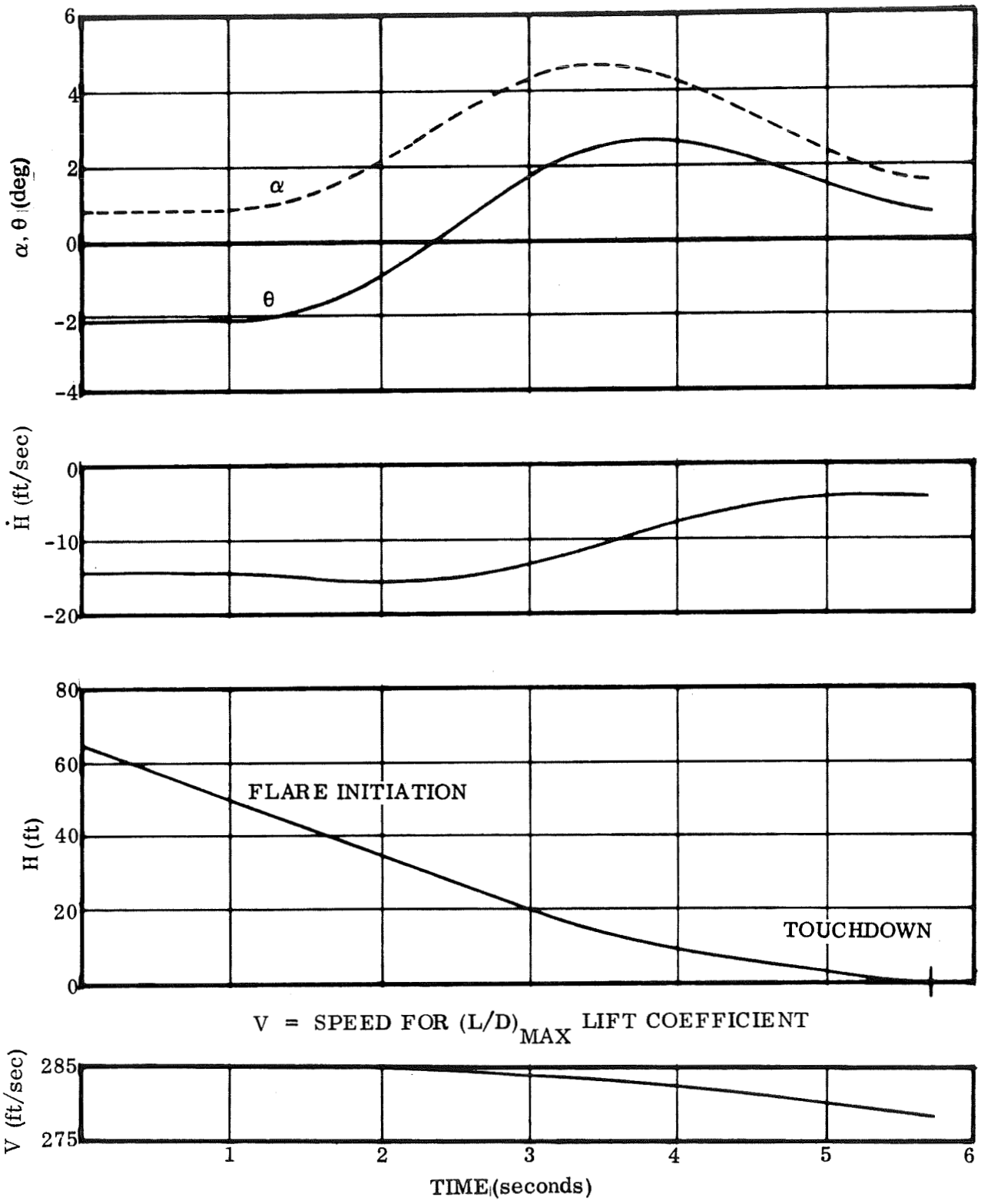

Figure 3-14. FR-4 Flare (V = 285 ft/sec, γ = -3 degrees)

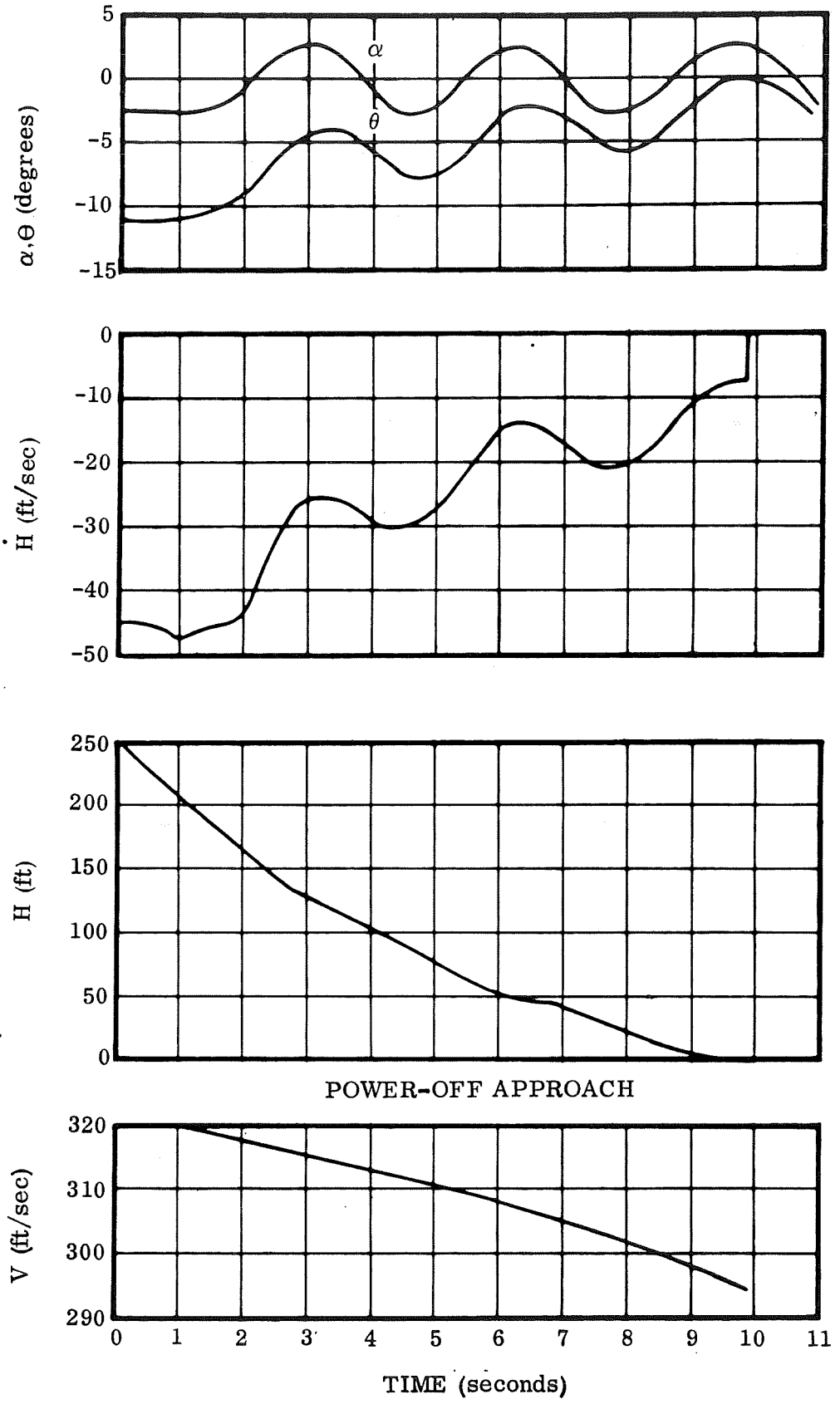

Figure 3-15. FR-4 Flare (V = 320 ft/sec, γ = -8.1 degrees)

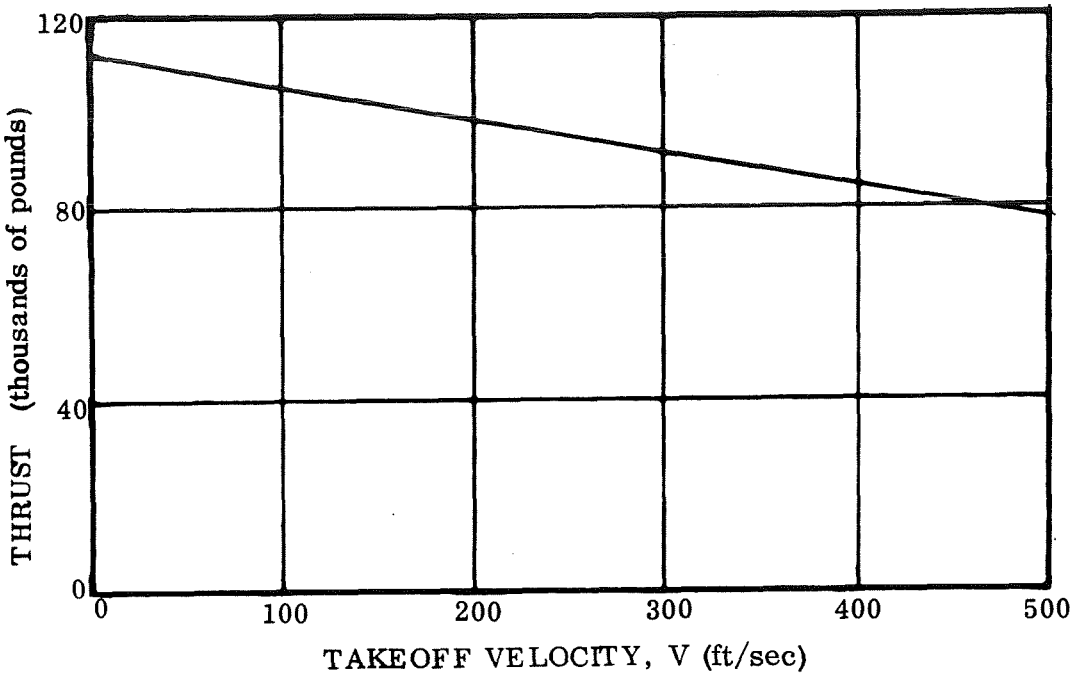

Figure 3-16. FR-4 Takeoff Thrust Model - Five Minute Limit

Distance over a 50-foot obstacle was computed assuming:

a. Five seconds to start climb.

b. Fifty-foot steady climb at maximum L/D.

A very small attitude change is required to go from the takeoff lift coefficient to that of maximum L/D (C_L = 0.55), so that arbitrary five-second delay should be sufficient. The takeoff performance resulting from the preceding assumptions is shown in Figure 3-17, which shows that a maximum takeoff weight to clear a 50-foot obstacle at 10,000 feet is approximately 350,000 pounds. The incremental distance to clear the obstacle after takeoff is due principally to the five-second delay prior to the start of the climb; reduction in this delay could result in sizable increases in takeoff weight. Approximately 625 pounds of fuel are consumed during the takeoff. Figure 3-18 shows a time history of the climb to 14,000 feet to start the cruise. This climb is based on:

a. Maximum L/D climb.

b. Maximum thrust for 5 min., climb thrust for remaining climb.

c. W = 345,000 lb

d. SFC = 0.52

The 14,000-foot altitude for the start of cruise was arbitrarily chosen because of the five minutes of additional climb thrust required to climb to 15,000 feet and because 15,000 feet is the absolute ceiling at maximum continuous cruise power. Approximately 5,600 pounds of fuel are consumed during the climb.

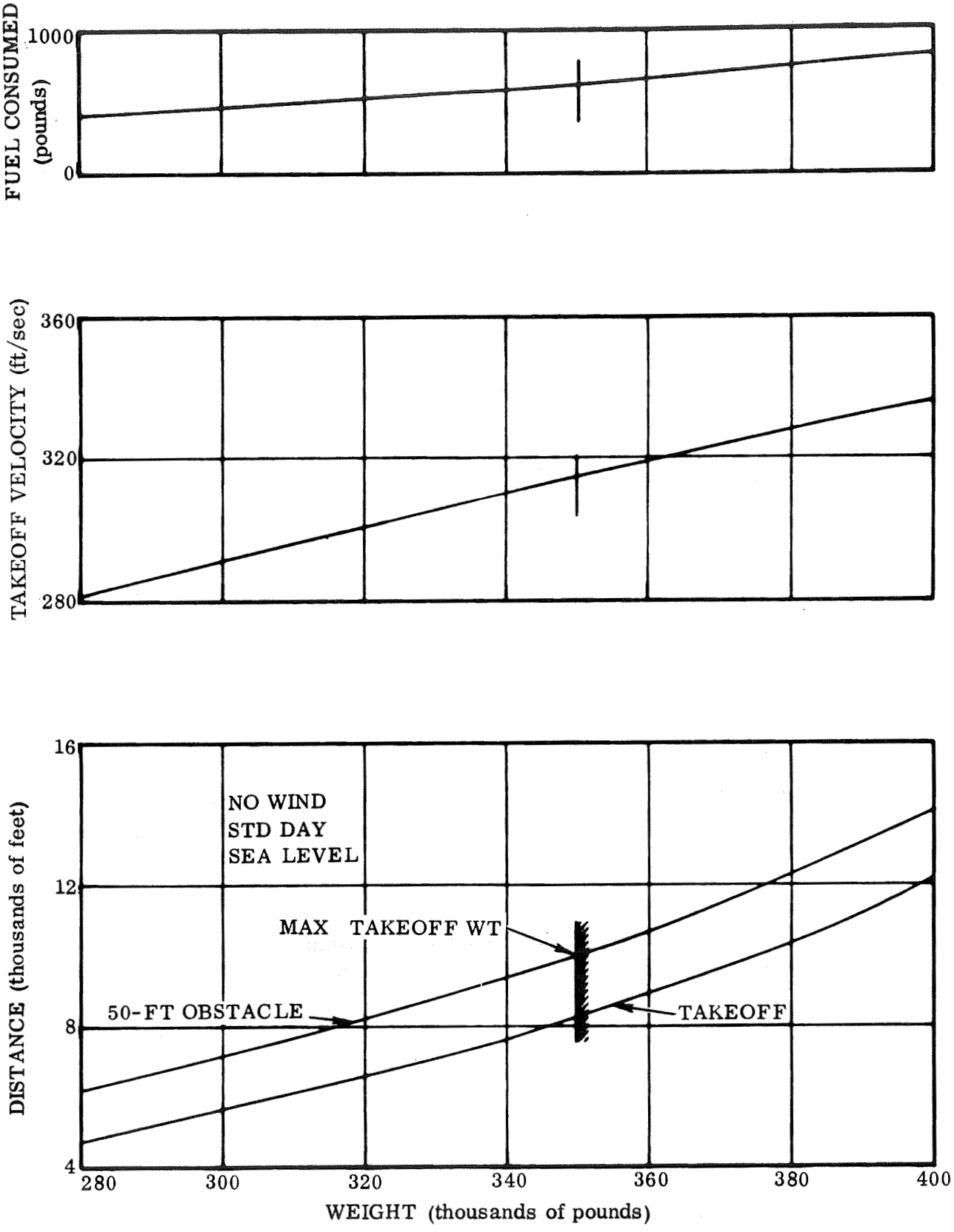

Figure 3-17. FR-4 Takeoff Performance

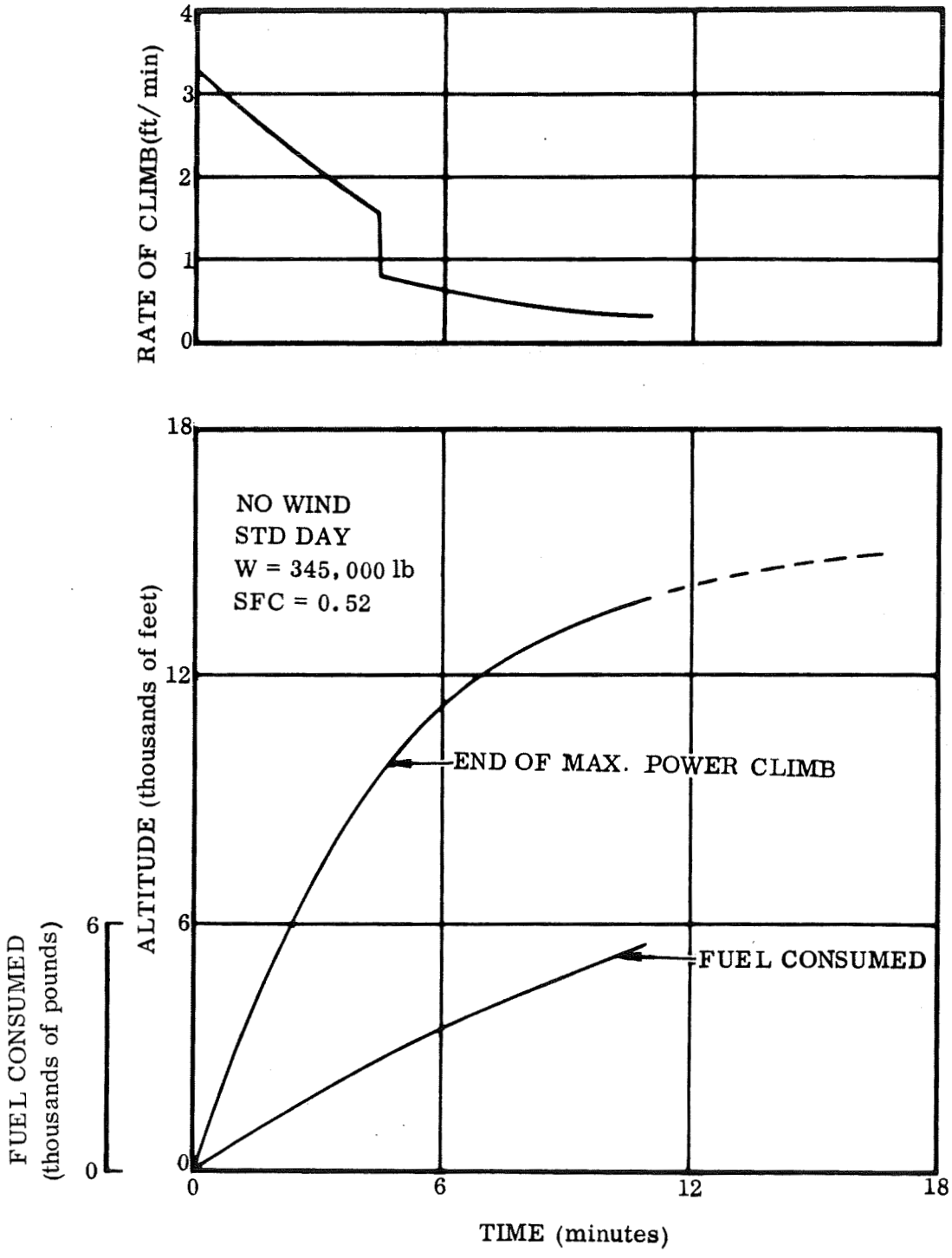

Figure 3-18. FR-4 Climb Performance

Cruise range computation for the orbiter and booster assume:

a. Standard day

b. Zero wind

c. SFC = 0.51

d. $(L/D)_{cruise} = 7.8$

e. Fuel reserve for descent and go-around = 4000 lb

f. Booster dry weight = 300,000 lb + 0.1 (fuel weight - 20,000)

g. Orbiter dry weight = 300,000 lb + 0.1 (fuel weight - 4000)

The added increment to the dry weight represents a penalty for bladder tanks installed in the vehicles to carry the excess fuel above their normal capacity.

Figure 3-19 presents cruise range as a function of cruise fuel weight. Thus for the booster:

a. Fuel weight = 47,300 lb

b. Dry weight = 302,700 lb

c. Takeoff fuel = 625 lb

d. Climb fuel = 5,600 lb

e. Descent fuel = 4,000 lb

f. Cruise fuel = 37,075 lb

g. Cruise range = 380 n.mi.

The orbiter breakdown includes:

a. Fuel weight = 45,800 lb

b. Dry weight = 304,200 lb

c. Takeoff fuel = 625 lb

d. Climb fuel = 5,600 lb

e. Descent fuel = 4,000 lb

f. Cruise fuel = 35,475 lb

g. Cruise range = 350 n.mi.

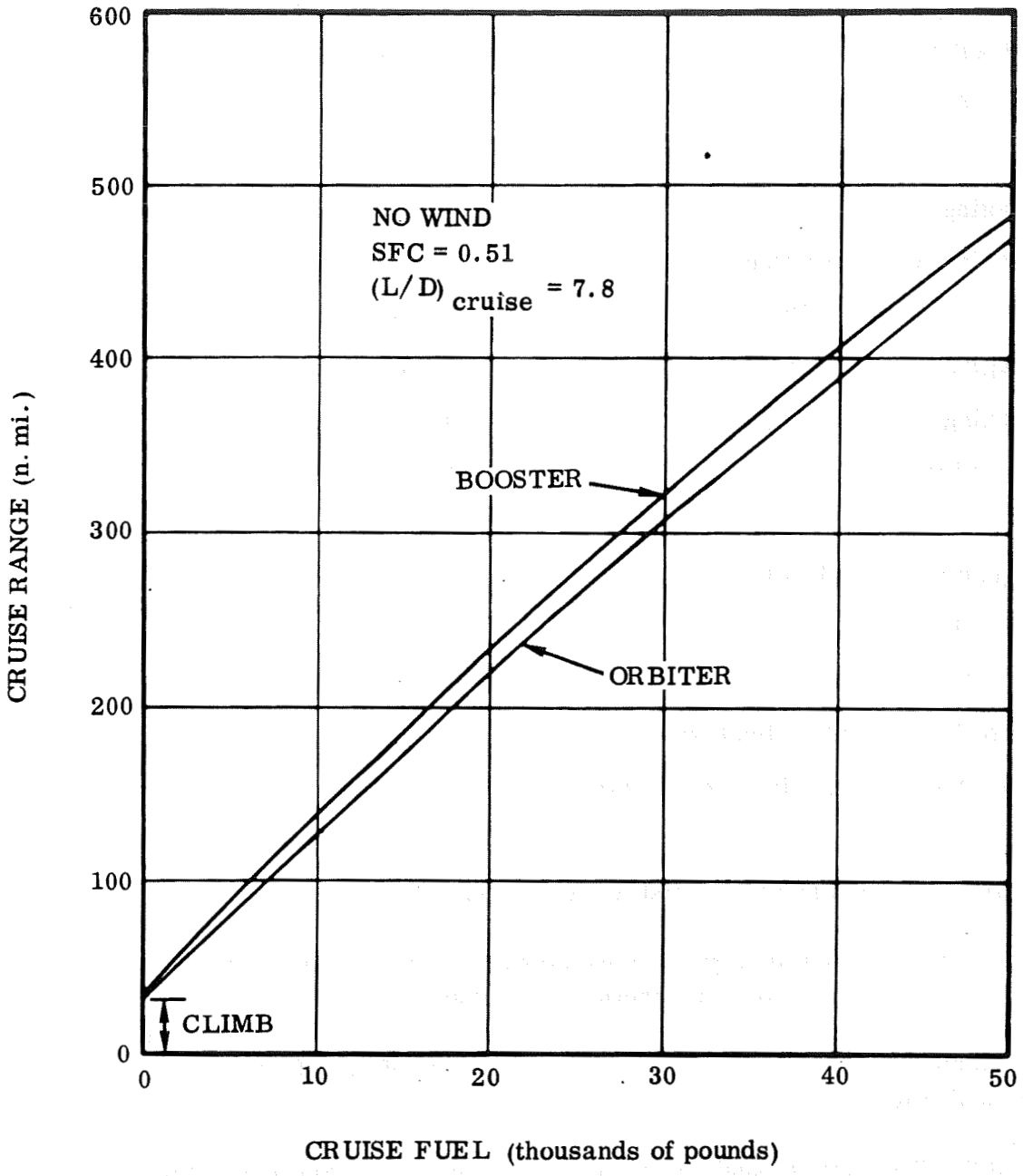

Figure 3-19. FR-4 Cruise Performance

3.3 FR-3 PERFORMANCE

3.3.1 ASCENT. The baseline ascent trajectory profile is essentially identical to that of the FR-4 vehicle discussed in Section 3.2. The orbiter did not fire its engines until after staging. Launch, liftoff, staging and injection parameters for FR-3 are:

Launch Site Location	ETR
Launch Azimuth	37.65 deg

Liftoff Thrust	5,999,905
Liftoff Weight	4,325,501 lb
Liftoff Thrust/Weight	1.387
Staging Time	196.31 sec
Staging Altitude	187,476 ft
Staging Relative Velocity	10,913 ft/sec
Staging Dynamic Pressure	50 psf
Staging Relative Flight Path Angle	2.24 deg
Staging Weight	1,515,895 lb
Injection Time	396.94 sec
Injection Altitude	260,000 ft
Injection Inertial Velocity	25,897 ft/sec
Injection Inertial Path Angle	0 deg
Injection Weight	339,162 lb
Injection Orbital Inclination	55 deg
Maximum Longitudinal Acceleration	3 g

The synthesis summary is presented in Table 3-2. Pertinent ascent parameter trajectory time histories are presented in Figure 3-20.

The FR-3 ascent trajectory is slightly more depressed than optimal. With redesign of the TSP and addition of a booster reaction control system, a more lofted boost trajectory could be used with small performance improvement. This trade is discussed in Volume II; here, the staging dynamic pressure of 50 psf was maintained for consistency with FR-4.

3.3.2 ABORT. The once-around abort approach discussed in Section 3.2 for FR-4 was also adapted for FR-3. In case of an engine failure on the booster or orbiter, the vehicle proceeds to injection into a ballistic path that allows the orbiter to land at the launch site after orbiting the earth once. The orbital maneuver propellants are used to compensate for the additional velocity losses that result from the reduced thrust-to-weight ratio. Figure 3-21 presents these velocity losses parametrically. Ample thrust is available for once-around (for a single engine failure) due to the relatively large thrust-to-weight ratio of the three-engine orbiter. The orbiter can go once-around with two engines out on the booster. With one engine out, the booster incurs a velocity loss of approximately 350 ft/sec; it may therefore be able to perform the logistics mission with a minimal reduction in mission velocity requirement.

Table 3-2. Two Stage Synthesis Summary

NASA FR-3, 50K L 15-3 ENGINES (400K) 10/17/69 SEPARATE BULKHEAD

	BOOSTER ELEMENT	ORBITER	VEHICLE
WEIGHT			
PROPELLANT, ASCENT	2809606	591346	
PROPELLANT, ORBIT MANEUVER		37300	
PROPELLANT, TOTAL	2809606	628646	
FLYBACK FUEL	46937	2867	
PAYLOAD		50000	
STRUCTURE	469708	213030	682738
CONTINGENCY	46971	21303	
OTHER	26647	9786	
TOTAL	3399869	925632	4325501
IN ORBIT		339416	
RETURN CONDITION	590263	330293	
ENTRY	0	289521	
LANDING	517286	286655	
VOLUME			
FUEL	92882	15017	
OXIDIZER	36124	7607	
PROPELLANT	129007	22624	
PAYLOAD		10638	
OTHER	106806	55677	
TOTAL	235812	88939	
GEOMETRY			
LENGTH	210.1	179.1	
BODY WETTED AREA	26598.8	14891.2	
BODY PLANFORM AREA	8165.8	4905.5	
ENTRY PLANFORM LOADING	69.1	59.0	
PROPULSION			
THRUST-TO-WEIGHT		1.52847	1.38709
NO. OF ENGINES	15	3	
SL THRUST/ENG NOM/UR	399994/ 399994	238369/	5999905/ 5999905
VAC THRUST/ENG NOM/UR	461847/ 461847	471609/	6927710/ 6927710
SL ISP NOM/UR	389.3/389.3	232.0/	389.3/389.3
VAC ISP NOM/UR	449.5/449.5	459.0/	449.5/449.5
TRAJECTORY			
MASS RATIO	2.85343	2.72917	
MAXIMUM DYNAMIC PRESSURE			670.5
STAGING DYNAMIC PRESSURE			50
STAGING VELOCITY (RELATIVE)			10913
STAGING ALTITUDE			187476
STAGING FLIGHT PATH ANGLE (RELATIVE)			2.243
INJECTION VELOCITY (INERTIAL)		25897	
INJECTION ALTITUDE		260003	
INJECTION FLIGHT PATH ANGLE (INERTIAL)		-.000	
INJECTION INCLINATION		54.91	
FLYBACK RANGE	281.1		

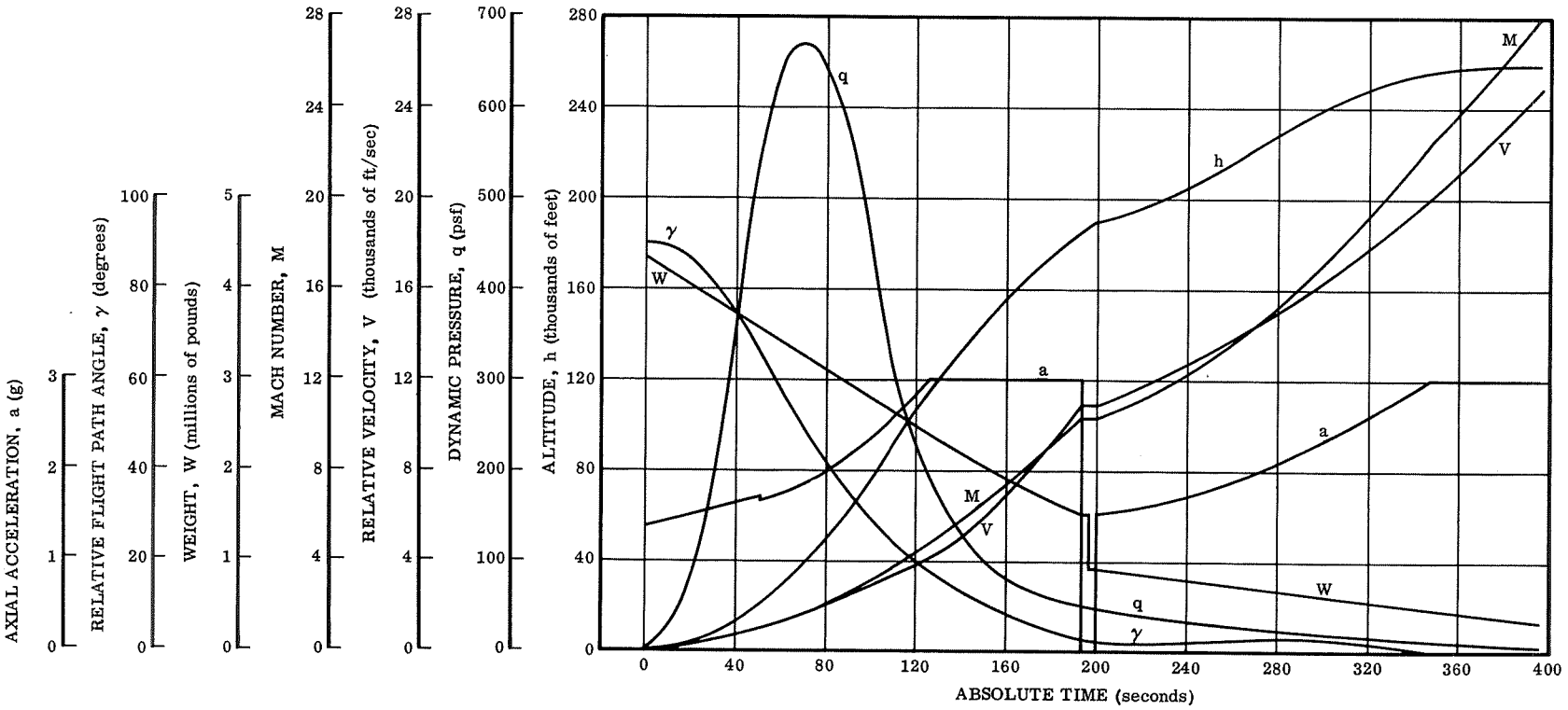

FOLDOUT FRAME

Figure 3-20. FR-3 Ascent Trajectory

FOLDOUT FRAME 2

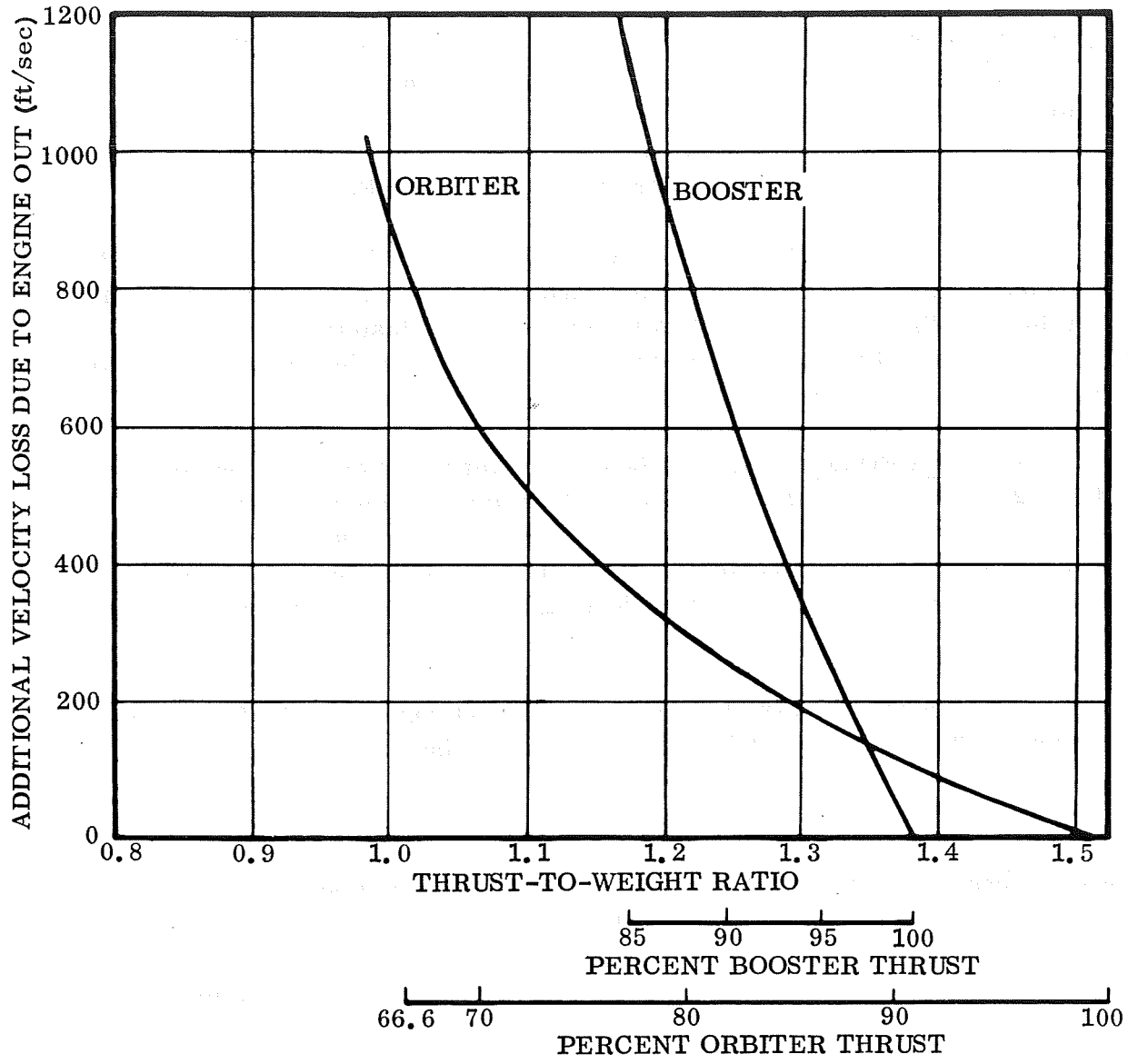

Figure 3-21. FR-3 Engine-Out Trajectory Losses

As in the FR-4 study, the ascent trajectories with engine failures were constrained to the same trajectory profile as the baseline (e.g., $q_{staging}$ = 50 psf). This approach is conservative, since reshaping the trajectory (assuming instantaneous diagnosis of an engine failure) would yield moderate performance improvements. In general, a more lofted baseline trajectory would yield less severe orbiter engine-out velocity penalties, allowing consideration of a two-engine orbiter. This would require considerable redesign of the booster (e.g., addition of a reaction-control system, augmentation of the TSP, and enlargement of the flyback propellant). This tradeoff is discussed in Volume III.

3.3.3 ENTRY. The FR-3 orbiter is essentially the same as that of the FR-4 and the performance presented in Section 3.2.3 also applies to the FR-3 orbiter. The staging condition occurs at much higher velocity for the FR-3, but this is largely compensated by the low flight path angle at staging with the net result of small differences between the FR-3 booster entry (Figure 3-22) and that of the FR-4 (Figure 3-11).

3.3.4 LANDING PERFORMANCE. The data presented in Section 3.2.4 should be representative of the FR-3 orbiter landing characteristics, since it is essentially the same vehicle. Figure 3-23 presents a power-on landing history for the FR-3 booster. The figure shows that a slightly larger flare is required for this heavy vehicle compared to the FR-4, but that the landing presents no problem.

3.3.5 FERRY PERFORMANCE. The takeoff and ferry performance presented in Section 3.2.5 are representative for the FR-3 orbiter. While a complete ferry mission was not run for the FR-3 booster, an analysis was made of its takeoff performance to see if any ferry performance was possible using the same ground rules as defined in Section 3.2.5 (except that the drag was reduced to account for ground effect). The thrust model is shown in 3-24.

Figure 3-25 shows that the vehicle can clear a 50-foot obstacle in 10,000 feet with approximately 26,000 pounds of fuel for climb and cruise.

3.4 REFERENCES

3-1 "General Trajectory Simulation Module," L. G. Tramonti, Convair report GDC-DCD-68-005, September 1968.

3-2 Weight and Size Analysis of Advanced Cruise and Launch Vehicles, Convair report GDC-DCB-66-008, March 1966.

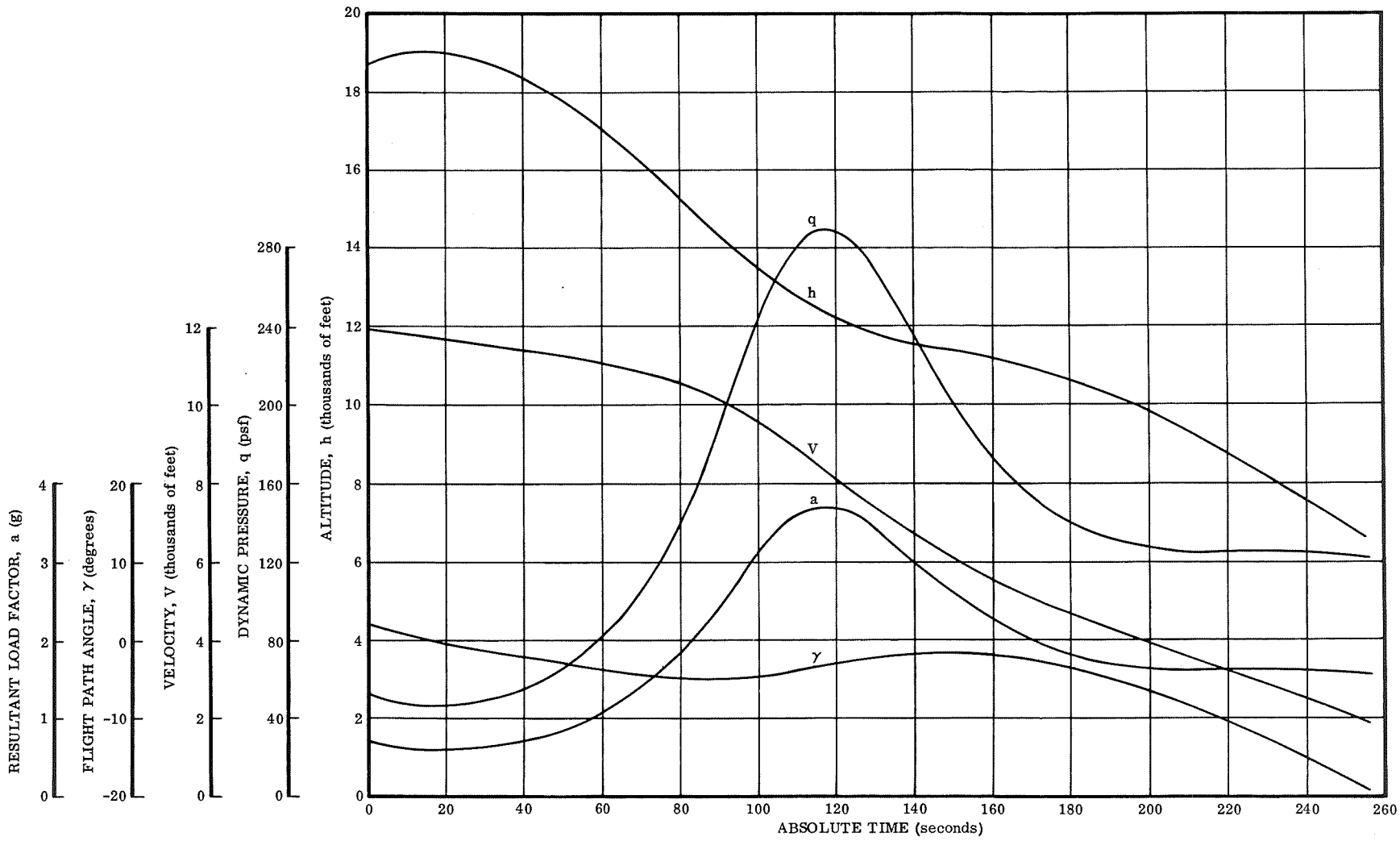

FOLDOUT FRAME

Figure 3-22. FR-3 Booster Entry

FOLDOUT FRAME

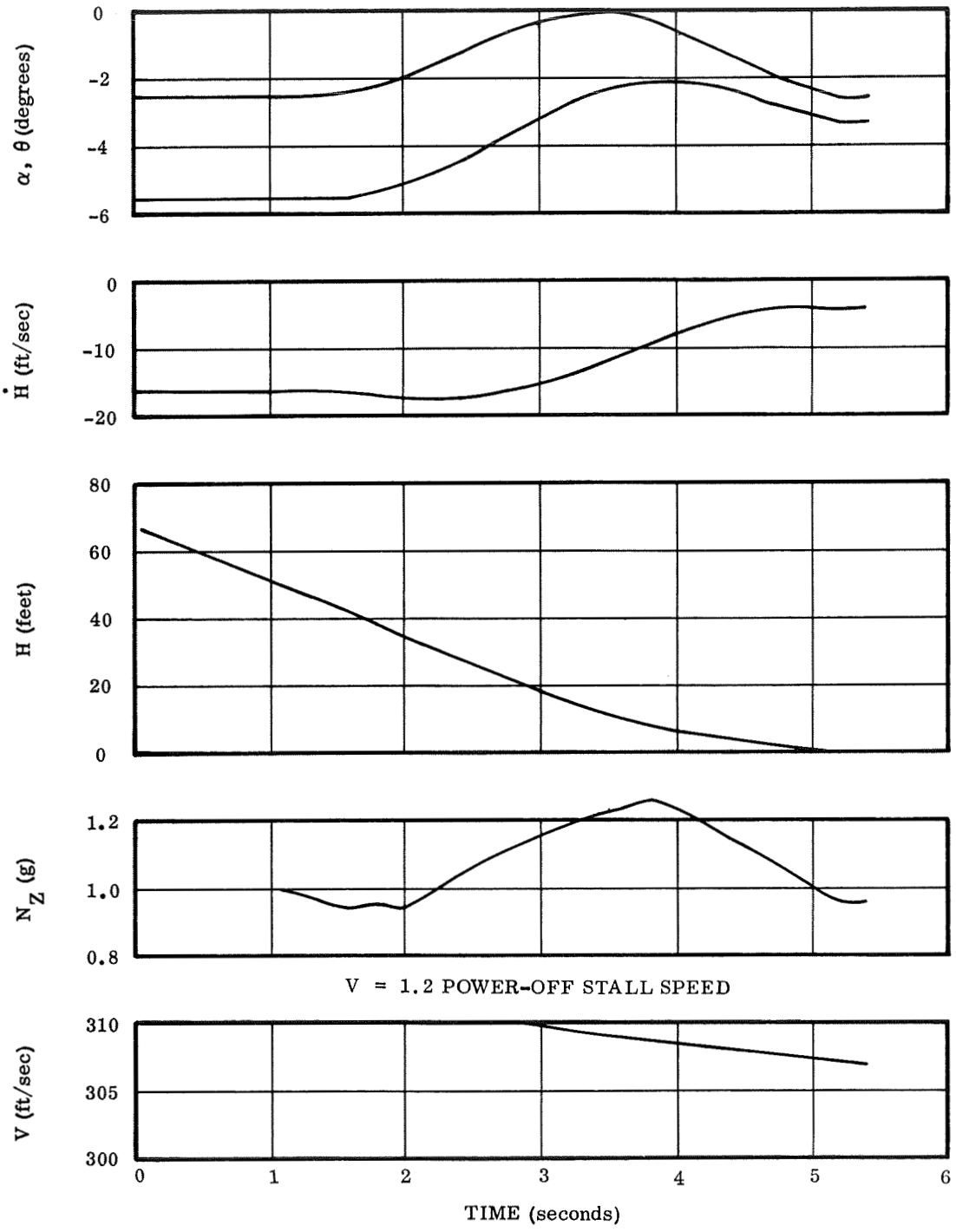

Figure 3-23. FR-3 Booster Landing Flare

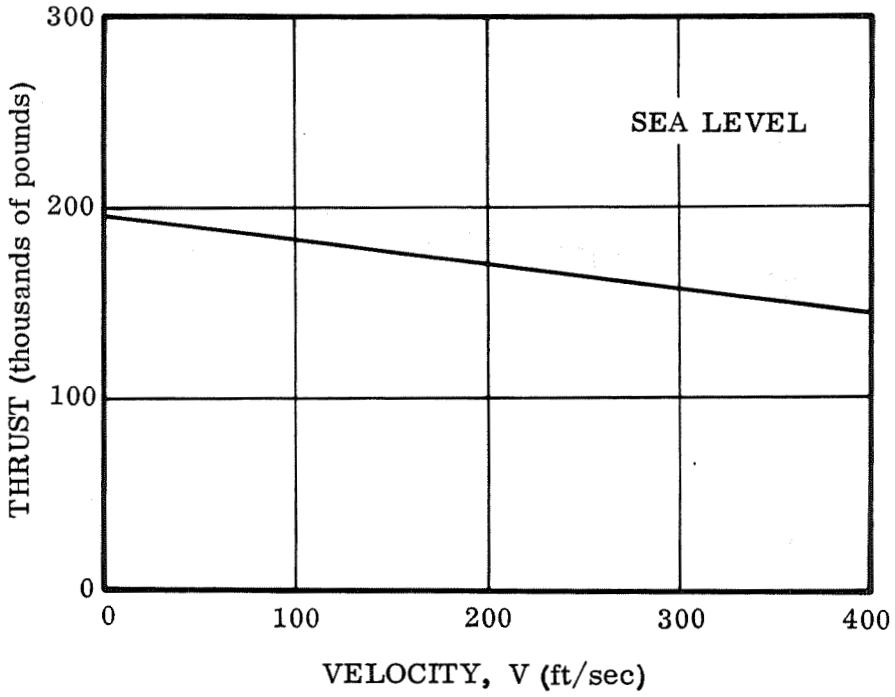

Figure 3-24. FR-3 Takeoff Thrust

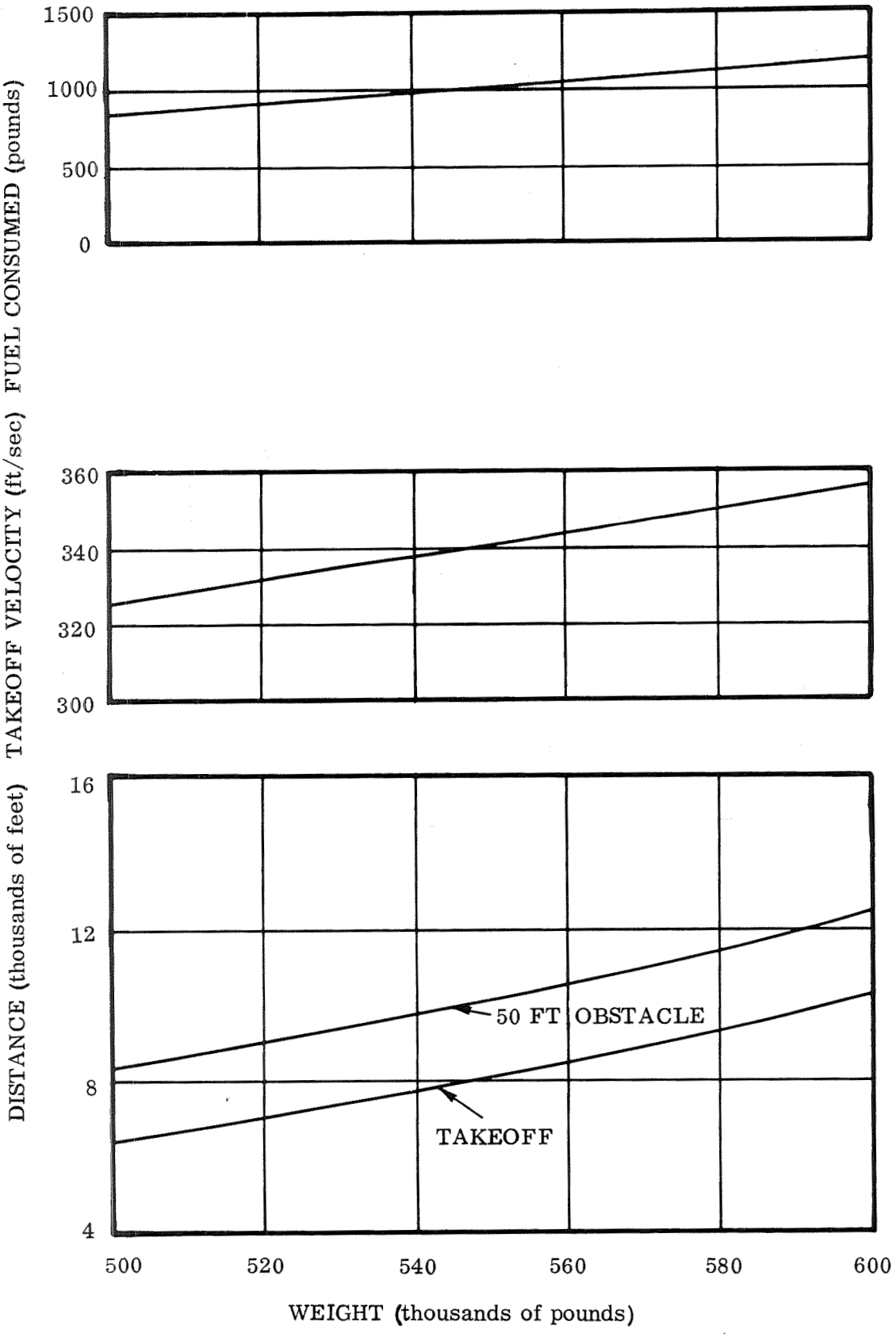

Figure 3-25. FR-3 Takeoff Performance

SECTION 4

AEROTHERMODYNAMICS

A reusable space shuttle system is unique in that it must operate over a thermal environment that ranges from cryogenic temperatures at launch to the high heating rates and high temperature associated with entry from earth orbit and be reusable with a minimum of refurbishment. The problems of thermodynamic analysis and the resultant problems of designing a reusable structure and thermal protection subsystem (TPS) are the most significant problem areas associated with the design of such a subsystem.

This section discusses the aerothermodynamic analysis of the space shuttle systems. The aerothermodynamic results presented herein were used in the design of the structure and TPS as discussed in Volume I, Section 5.3; Volume II, Sections 4.6 and 4.7; Volume III, Sections 3.6 and 6.4; and Volume VI, Section 1.1.9. In addition, this section presents the results of a cryogenic thermal control analysis of the propellant system.

4.1 AEROTHERMODYNAMIC ANALYTIC METHODS

Design of a reusable space shuttle system requires prediction of aerodynamic heating and the resulting thermal response of the vehicle structure. Material selection, structural design, and insulation sizing are all founded on the aerothermodynamic analyses. This section presents the analytic methods in two parts. First, the prediction of aerodynamic heat transfer to vehicle elements is described. Second, techniques for computing the thermal response of the structural members to the aerothermal environment are discussed.

4.1.1 AERODYNAMIC HEAT TRANSFER. Stagnation-point heat transfer was calculated by the method of Kemp and Riddell (Reference 4-1). Equilibrium air properties from Hansen (Reference 4-2) and 1962 ARDC standard atmospheric data were used. This solution technique uses a Newtonian velocity gradient for a spherical body. Numerical computations of stagnation heating were conducted with the Convair 3020 aerodynamic heating computer program (Reference 4-3).

Heating rates to the stagnation line of leading edges were computed by considering the leading edges as infinite swept cylinders subjected to the free-stream flow conditions. Verification of the swept-cylinder analogy has been obtained experimentally (Reference 4-4) for highly swept leading edges at angles of attack such as encountered by the space shuttle configurations. Heat transfer rates, q_{sphere}, to the stagnation point of a sphere of the same radius as the cylindrical leading edge were calculated by the Kemp and Riddell method. These spherical heating rates were transformed to swept cylinder rates, $q_{cyl,\ \Lambda}$, by an equation of the form:

$$q_{cyl,\Lambda} = C_1 (\cos \Lambda_{eff})^{C_2} q_{sphere}$$

where Λ_{eff} is the effective sweepback angle resulting from the geometric sweepback angle, Λ, and the angle of attack, α:

$$\Lambda_{eff} = \sin^{-1} (\cos \alpha \sin \Lambda)$$

In the present Convair 3020 program formulation, the value of C_1 is 0.75 and C_2 is 1.50. This procedure has been used to predict aerodynamic heating to vehicle body and fin leading edges.

Vehicle lower surface aerodynamic heat transfer has been evaluated using the tangent wedge shock layer flow field approximation with ARDC 1962 standard atmospheric data. Real-gas effects in the shock layer are taken into account through the use of a set of empirical equations for determining the thermodynamic properties at the boundary layer edge. Transport properties in the shock layer are determined from curve-fit equations of the data of Hansen (Reference 4-2).

For laminar flow, the boundary layer properties are computed using the Eckert reference enthalpy, i*, where

$$i^* = i_s + 0.5 (i_w - i_s) + 0.22 (i_r - i_s)$$

Enthalpy is represented by i in this equation and the subscripts refer to wall conditions, w, shock layer conditions, s, and recovery conditions, r. The laminar recovery factor for evaluating the recovery enthalpy is 0.84. Laminar skin friction is determined from the Blasius solution for an incompressible boundary layer. The use of a Reynolds number based on reference conditions transforms this solution into a compressible skin friction solution. Application of the Colburn-Reynolds analogy yields the laminar Stanton number.

Turbulent boundary layer heat transfer is evaluated using the Schultz-Grunow solution for the local skin friction coefficient. As in the laminar case, the modified Reynolds analogy is employed to obtain the Stanton number. Most significant to the discussion of turbulent heat transfer prediction is the method of computing the reference properties for use in the skin friction and Stanton number calculations. The Eckert reference enthalpy method with an adiabatic wall was used for all baseline design aerodynamic heat transfer predictions in this study. Adiabatic wall reference enthalpy, i_{aw}^*, is calculated from:

$$i_{aw}^* = i_s + 0.72 (i_r - i_s)$$

where the symbols retain the meanings defined previously. This equation is identical to the Eckert reference enthalpy method, with the wall enthalpy set equal to the recovery enthalpy (adiabatic wall assumption). Flight test data obtained during the X-15 program (Reference 4-5) indicated that the adiabatic wall assumption leads to more realistic predictions of the turbulent boundary layer aerodynamic heat flux than does the Eckert reference enthalpy solution. These two methods are compared with other prediction techniques in Section 4.5. A value of 0.89 was used for the turbulent recovery factor. A turbulent boundary layer Reynolds number run from the nose of the vehicle has been assumed.

For both laminar and turbulent flow, strip theory was used at low angles of attack. With increasing angle of attack, lower surface heat-transfer rates were corrected for crossflow effects by application of the data shown in Figure 4-1. This data, from Reference 4-6, has been incorporated into the Convair 3020 computer program for more rapid, accurate calculation of the crossflow influence on heat transfer. Any effects of inflow at low angles of attack have been neglected.

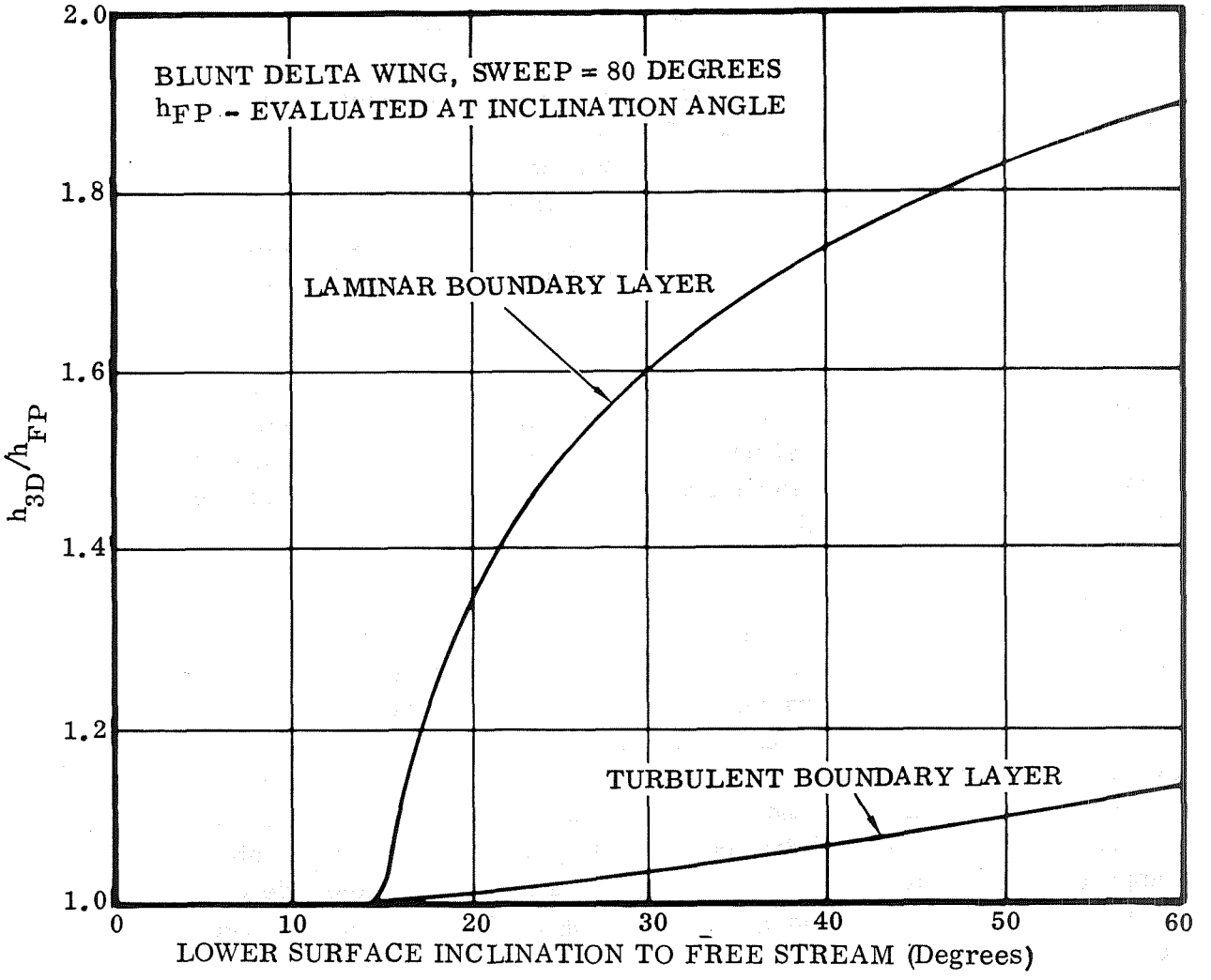

Figure 4-1. Heat-Transfer Correction Due to Three-Dimensional Flow Effect on Lower Surface Centerline

Boundary layer transition from laminar to turbulent flow has been predicted based on a Reynolds number computed using shock layer properties and the distance from the nose of the vehicle. Initiation of transition was assumed to occur when the Reynolds number reached 1×10^6. A finite transition zone was postulated between the laminar and fully turbulent regions, as suggested by the work of Masaki and Yakura (Reference 4-7). Transition to fully turbulent flow was considered complete at a Reynolds number of 2×10^6. In the transition zone, the boundary layer parameters were assumed to increase linearly from the laminar values at the beginning of transition to the turbulent values at the end. Comparisons of the results of predictions based on the finite transition zone with results based on instantaneous transition from laminar to turbulent flow at a shock layer Reynolds number of 1×10^6 are discussed in Section 4.3. Also discussed in Section 4.3 is the influence on peak heating prediction of variations in the transition Reynolds number.

During the launch phase, boundary layer transition from turbulent to laminar flow is expected to occur. For this study, instantaneous reverse transition has been assumed to occur when the shock layer Reynolds number drops to 1×10^6.

Aerodynamic heat transfer to the upper surface and sides of the vehicle has been determined using essentially the techniques described for the lower surface. Forward portions of the upper surface are conical; boundary layer parameters in this region were evaluated using tangent cone theory as long as the flow inclination angle between the surface and the free-stream velocity vector was positive. At zero or negative flow inclination angles, the surfaces were considered to be flat plates aligned parallel to the flow.

Aft of the conical section, upper surface aerodynamic heat transfer was calculated based on flat plate at zero angle of attack flow. Reference properties, solution techniques, and the boundary layer transition criterion were identical to those used in the lower surface analysis. All upper surface design aerodynamic heat transfer predictions were made using this approach.

Unpublished experimental work by Convair at the NASA Langley wind tunnel facility has indicated that at certain angles of attack a vortex flow develops from the juncture of vehicle leading edge and side wall. The location of the vortex is a function of the vehicle angle of attack. Preliminary data reduction has shown that the upper surface aerodynamic heat transfer film coefficients can be three to four times the predicted flat-plate values in the local regions where the vortical flow reattaches to the vehicle surface. Design calculations reported in this study do not reflect this increased heating on the side walls. Detailed data on the heating levels were not available in time to support design predictions. The heating levels indicated on the side walls suggest that more detailed vehicle analyses, including the increased heating rates, be conducted.

Vertical fin aerodynamic heating was evaluated assuming the fin was isolated from the body and exposed to the free-stream flow. Fin leading edges were treated as infinite swept cylinders using the previously discussed methods of analysis. Fin side panels were analyzed using tangent wedge techniques similar to the lower surface analysis. Reynolds number run lengths were measured from the fin leading edge.

Aerodynamic heating of the bell rocket nozzles during launch and entry was computed. The bottom surface extended far enough aft to protect the retracted nozzles from experiencing impingement heating on the vehicle windward side during entry. During launch, the extended nozzles will receive impingement heating and during entry the retracted nozzles may experience impingement of leeward side flow. A conservative assumption was adopted regarding the magnitude of this impingement heating. Heating rates to the nozzles (assuming attached flow), were computed using the methods discussed previously. Separated flow was then considered with reattachment on the nozzle; a reattachment heating factor of five was applied to the attached flow heating rates. The resulting heat-transfer rates are felt to represent upper limits for the nozzle heating.

Base region heat-transfer rates have been estimated for space shuttle vehicles from a consideration of Atlas and Saturn flight test experience coupled with plume data generated by the rocket engine manufacturers. Predicted heating rates for the vehicle base region are therefore very preliminary and will require further verification by test and more detailed analysis.

4.1.2 STRUCTURAL THERMAL RESPONSE. External surfaces of the designs considered in this study are composed of thin metallic skins. Thermal masses of these skins are quite low; additionally, behind the skin panels, layers of low density insulation serve to limit internal heat conduction to low values. Under these conditions, the surface panels respond quite rapidly to imposed aerodynamic heating and reach temperatures very close to radiation equilibrium. The slightly lower temperatures are a result of the fact that some energy is conducted into the insulation and structure.

For establishing peak temperature levels for material selection, radiation equilibrium temperature assumptions are entirely satisfactory. All design temperature data for surface cover panels provided in this report is for radiation equilibrium temperatures. The Convair 3020 program (Reference 4-3) has an internal subroutine for calculating these temperatures using the aerodynamic heating methods discussed previously.

Solution is obtained by an iterative procedure in which the assumed surface temperature at each point in the trajectory is varied until the aerodynamic heating influx equals the radiant outflux.

Sizing insulation thickness requirements involves a more complex analytical treatment. One-dimensional thermal models of the vehicle TPS and structure were developed for selected locations on the vehicle. These models included the surface

cover panel, the layers of low density insulation, and the supporting structure. Transient thermal responses of these thermal models to the applied aerodynamic heat transfer were then evaluated using the Convair 3020 program. The critical parameter in sizing insulation thickness is the temperature limit of the vehicle structure. For each location being considered, the insulation thickness was varied parametrically to yield the minimum thickness required to maintain the structure below the required temperature limit. TPS insulation materials were Dynaflex adjacent to hot cover panels and Microquartz in areas where the temperatures were lower. Both insulation materials have thermal conductivities that are strong functions of the temperature and the air pressure in the insulation. The 3020 program includes matrices of the properties of both materials as functions of temperature and pressure. At each time step in the calculation, properties are evaluated using the insulation layer temperature and the external shock layer pressure.

Because of the nature of a cover panel, low-density insulation TPS, energy is stored in the TPS during the entry trajectory. Conductivities of the insulation are so low that some of this energy does not reach the structure until after the vehicle has completed the landing. Insulation thicknesses for the design configuration were sized to limit the structural temperatures to 200°F (660°R) after landing without supplemental cooling. In all cases, the internal structure was assumed adiabatic. An analysis of alternative approaches to limiting structural temperature after landing is presented in Section 4.8.

Certain structural and TPS elements could not be satisfactorily simulated by one-dimensional thermal models where only internal conduction was considered. Cover panel supports and posts represent breaks in the insulation barrier and provide heat leakage paths to the underlying structure. Only a three-dimensional thermal model can adequately represent the energy flow in the area surrounding such an element. For some support configurations, internal radiation plays a significant role in the thermal energy distribution. Detailed analyses of these localized problem areas were conducted using the Convair Variable Boundary II Heat Conduction, computer program 2162 II (Reference 4-8). This program allowed the formulation of three-dimensional thermal models, including conduction and internal radiation among the model elements. Transient solutions of the temperature responses of the thermal models to aerodynamic heating were obtained. Using this approach, thermal performance of structural support concepts was evaluated to assist in design concept selection.

An analysis of structural cooling concepts to supplement the baseline passive insulation TPS was made and is discussed in Section 4.6.2.

4.2 ORBITER AEROTHERMODYNAMIC ANALYSIS

The analytic procedures discussed in Section 4.1 were used to predict the aerodynamic heating characteristics of the orbiter. The nominal orbiter entry mission for initial operational capability has a crossrange requirement of 800 n.mi.

The design entry trajectories used for the orbiter temperature predictions and insulation sizing are presented in Section 3. Surface emissivities were assumed to be 0.85 for all cover panels except the nose cap and leading edges, which were assumed to be 0.8. The nominal orbiter entry was the design trajectory for the orbiter TPS.

4.2.1 800-n.mi. AND 300-n.mi. CROSS RANGE ENTRIES. Figure 4-2 presents the heat transfer rate histories calculated for the orbiter nose and leading edges for the 800-n.mi. crossrange entry using the design prediction methods described in Section 4.1. Figures 4-3 and 4-4 show the heat transfer-rate histories calculated for the orbiter lower surface at Stations 5, 40, and 165 (measured from the vehicle nose).

Figure 4-5 presents the upper and lower surface centerline maximum temperature distribution calculated using the design prediction method. Both the 300-n.mi. and the nominal 800-n.mi. crossrange entry trajectory distributions are shown. Nose and body leading edge peak temperatures for both entry trajectories are also listed.

Figure 4-6 shows peak radiation equilibrium temperatures on fin surfaces for the 800- and 300-n.mi. crossrange entries.

Figure 4-7 gives radiation equilibrium temperature histories for the nose and body at Stations 5, 40, and 165 aft of the nose on the lower surface for the 800-n.mi. crossrange entry using the design prediction method. Shock-layer pressures at Stations 5 and 165 aft of the nose on the lower surface are also presented. Figure 4-8 shows the temperature histories under the same conditions for the body leading edge, fin leading edge, and upper surface 10 feet aft of the nose.

Insulation TPS thermodynamic models used for sizing orbiter insulation requirements for various vehicle locations are presented schematically in Figure 4-9. Figure 4-10 shows the peak orbiter structural temperatures during the 800-n.mi. crossrange entry as a function of insulation thickness for lower surface Stations 10, 60, and 165 feet aft of the nose. The upper surface structural temperature is also given for Station 10 feet. Figure 4-11 presents the similar parameters for the 300-n.mi. crossrange entry.

The upper surface thermal model used was identical to that of the lower surface at 60 feet (shown in Figure 4-9), except that Microquartz alone was used as the insulator because of the lower temperature levels predicted for upper surface cover panels. The required design insulation thicknesses to limit structural temperatures to 200°F (660°R) at representative locations are:

	STATION LOCATION (feet)	THICKNESS (inches)
Lower Surface	10	3.7
	60	2.9
	165	2.8
Upper Surface	10	2.1

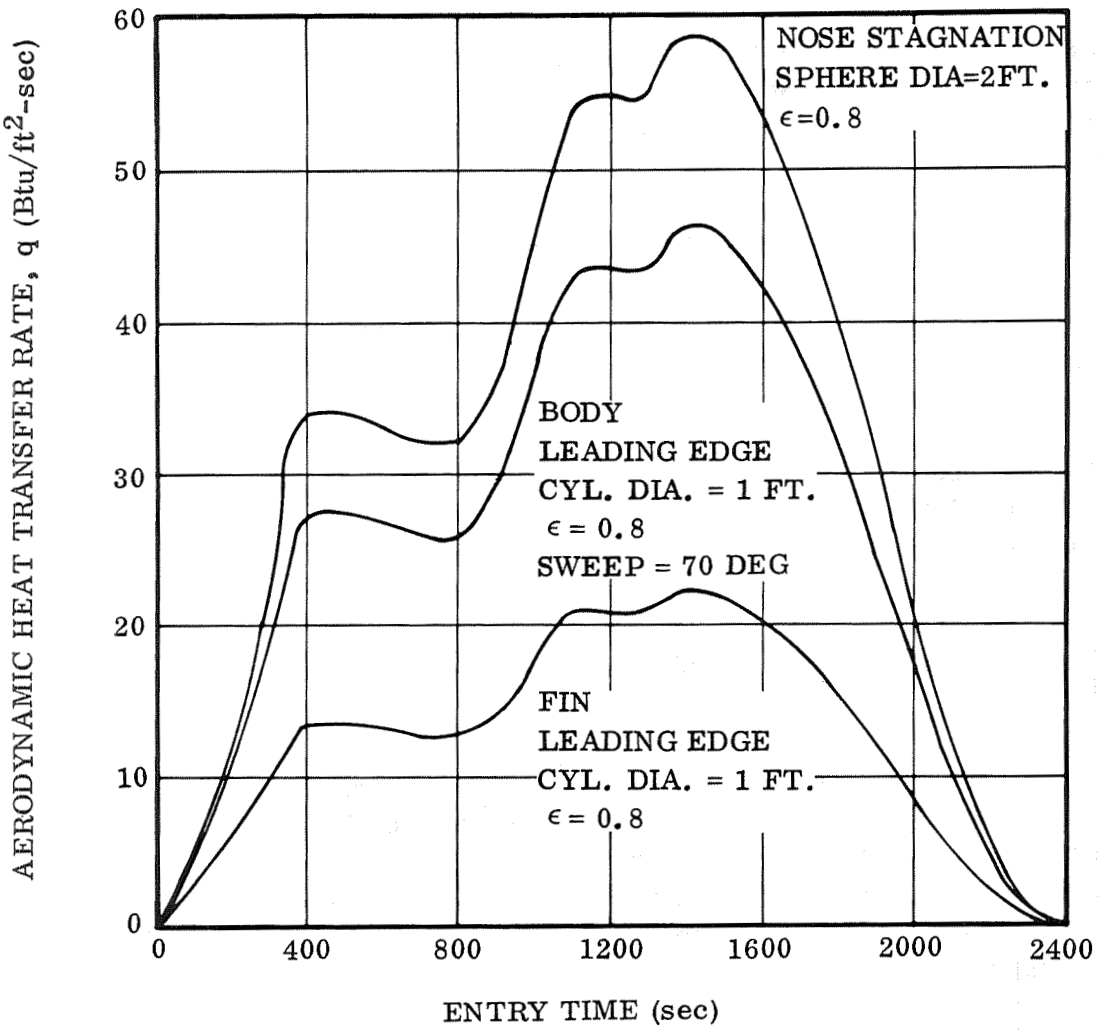

Figure 4-2. Orbiter Body Stagnation and Leading Edge Hot Wall Heat Transfer Rates, Trajectory 353, 800-n.mi. Crossrange

4.2.2 500 n.mi. CROSSRANGE ENTRY. A 500 n.mi. entry studied during the Air Force space transportation system (STS) study is compared with the NASA entries in this section. The entry trajectory for the two missions differed in the following areas. The STS entry flight path is from a polar orbit and approaches the United States from the south. Then, with a left bank, the flight path continues toward the western United States.

This action adds relative air velocity and results in increased heating during entry. The space shuttle approaches the United States from the southwest on a 55-degree inclination flight path and the right bank required results in decreased relative air velocity during entry. Higher temperatures, therefore, can be expected for the STS polar mission.

Figure 4-12 presents the STS upper and lower surface centerline maximum temperature distribution calculated using the design prediction method (adiabatic wall

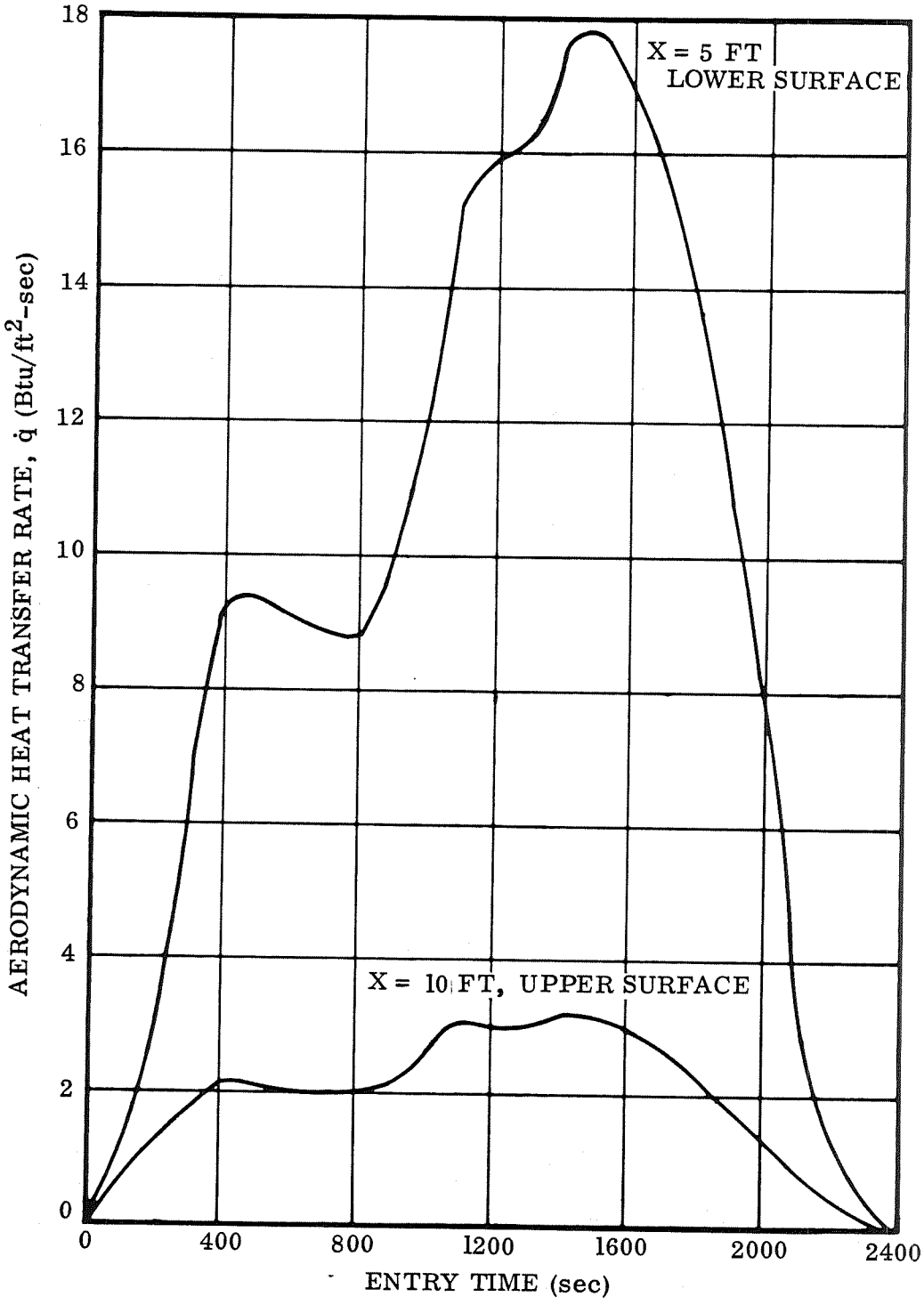

Figure 4-3. Orbiter Body Hot Wall Heat Transfer Rates, Trajectory 353, 800-n.mi. Crossrange

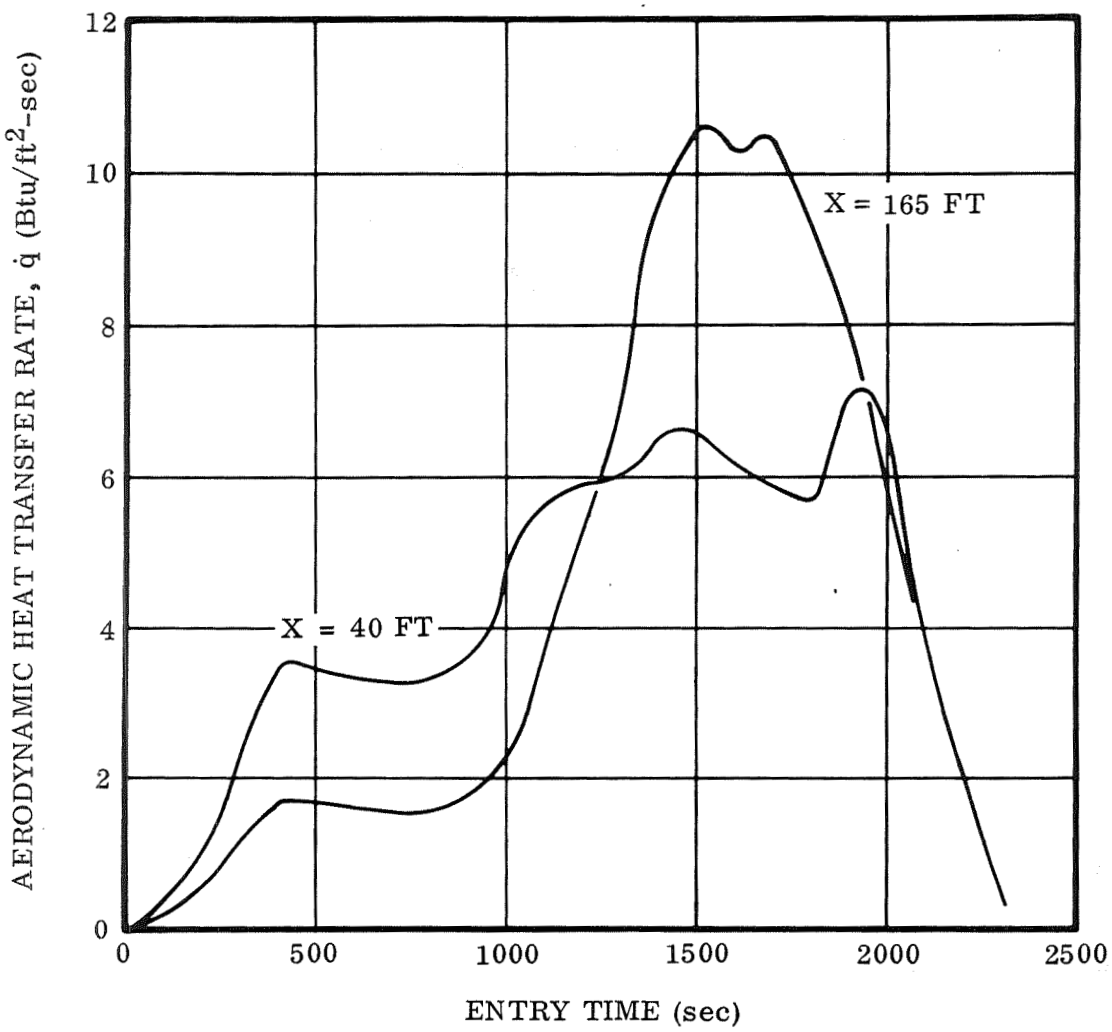

Figure 4-4. Orbiter Body Lower Surface Aerodynamic Heat Transfer Rate, Trajectory 353, 800-n.mi. Crossrange

prediction method with gradual transition). The Eckert prediction method with instantaneous transition will be discussed later in Section 4.4.

4.3 BOOSTER AEROTHERMODYNAMIC ANALYSIS

The nominal ascent trajectory and the booster reentry trajectory are presented in Section 3. Figure 4-13 gives the radiation equilibrium temperature history for the booster vehicle lower surface centerline at Station 10 feet for ascent and entry. Aerodynamic heat transfer was predicted using the design prediction methods discussed in Section 4.1. Surface emissivities of 0.85 were used for all booster cover panels, including the nose and leading edges. Peak radiation equilibrium temperatures for the nose, body leading edge, fin leading edge, fin surface at 10 feet aft of the leading edge, body lower surface Stations 10 and 80 feet aft of the nose, and upper Stations 10 and 70 feet aft of the nose are also shown in Figure 4-13.

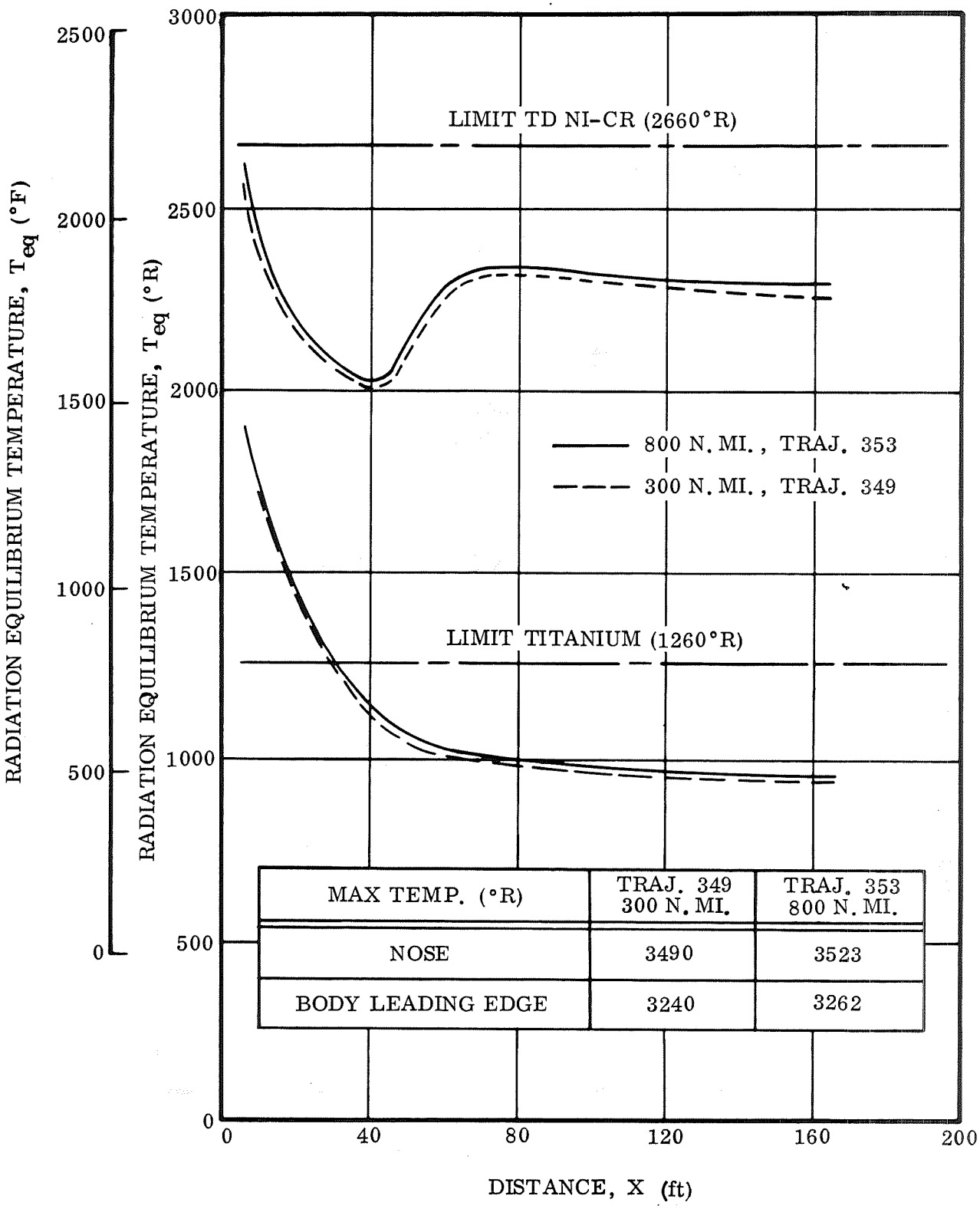

MAX TEMP. (°R)	TRAJ. 349 300 N. MI.	TRAJ. 353 800 N. MI.
NOSE	3490	3523
BODY LEADING EDGE	3240	3262

Figure 4-5. Maximum Orbiter Radiation Equilibrium Temperatures for the 300- and 800-n.mi. Crossrange

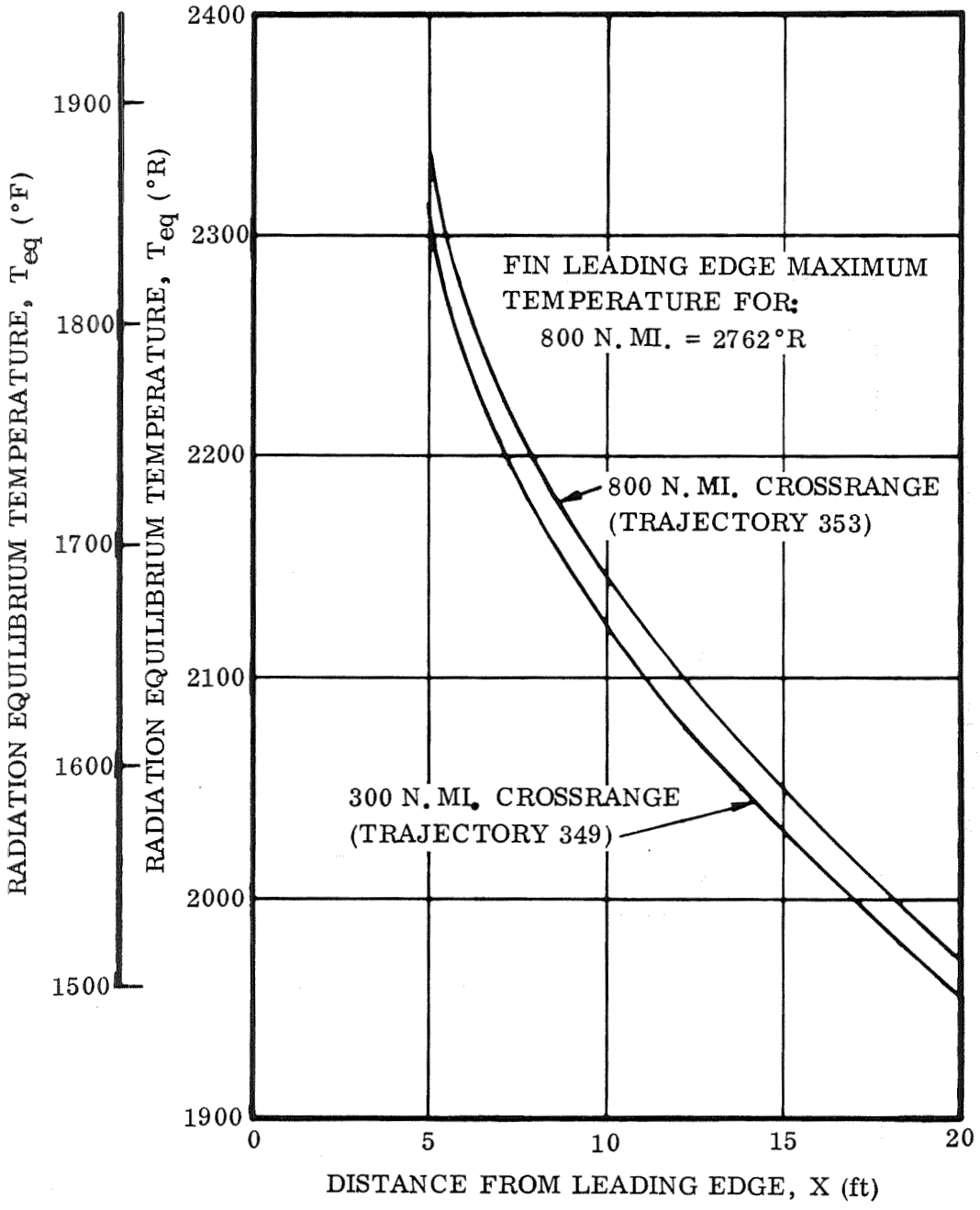

Figure 4-6. Orbiter Fin Maximum Temperature Versus Fin Station for 300- and 800-n.mi. Crossrange

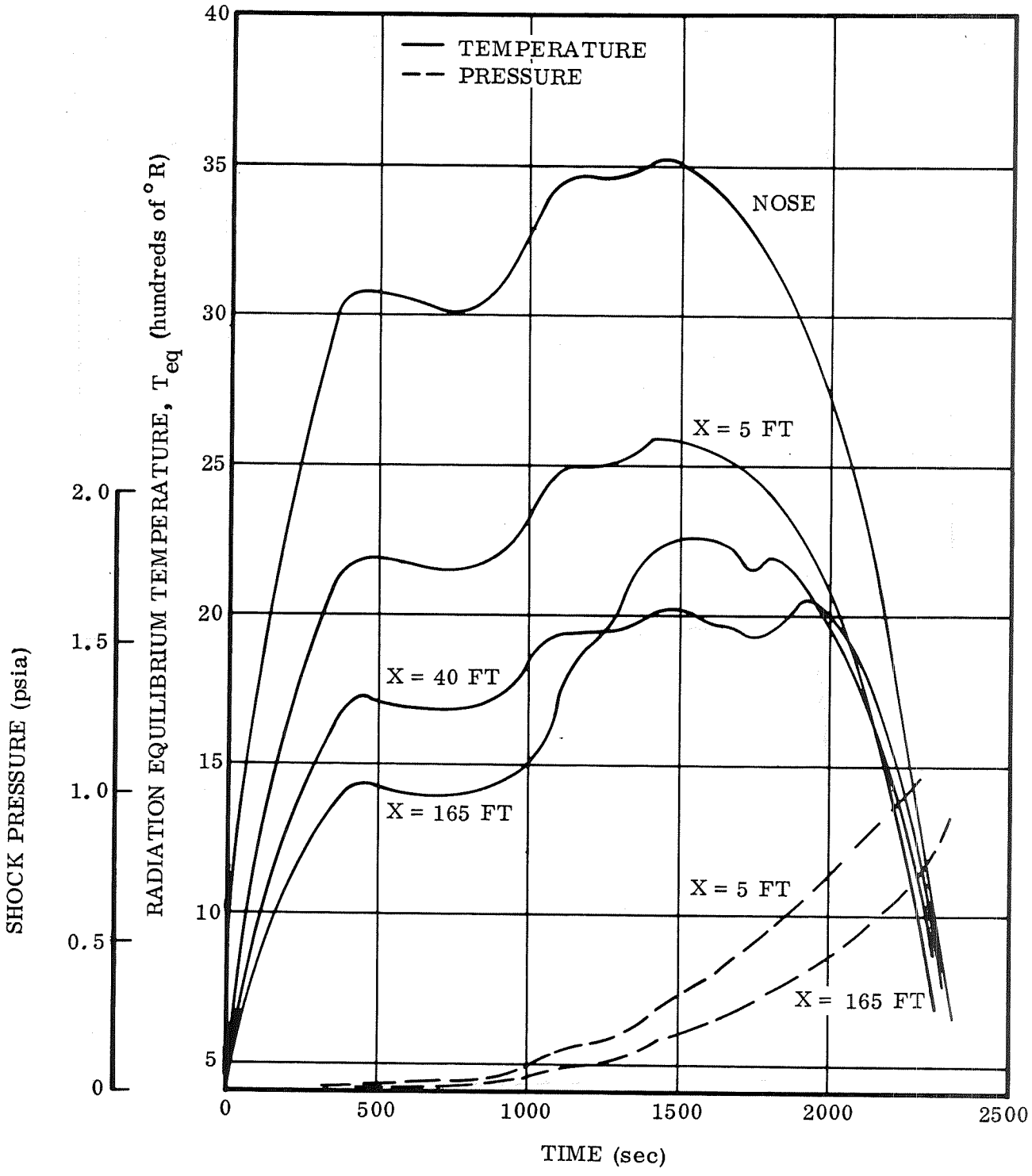

Figure 4-7. Temperature and Pressure Histories at Various Orbiter Stations on the Lower Surface, Adiabatic Method and Gradual Transition, Trajectory 353, 800-n.mi. Crossrange

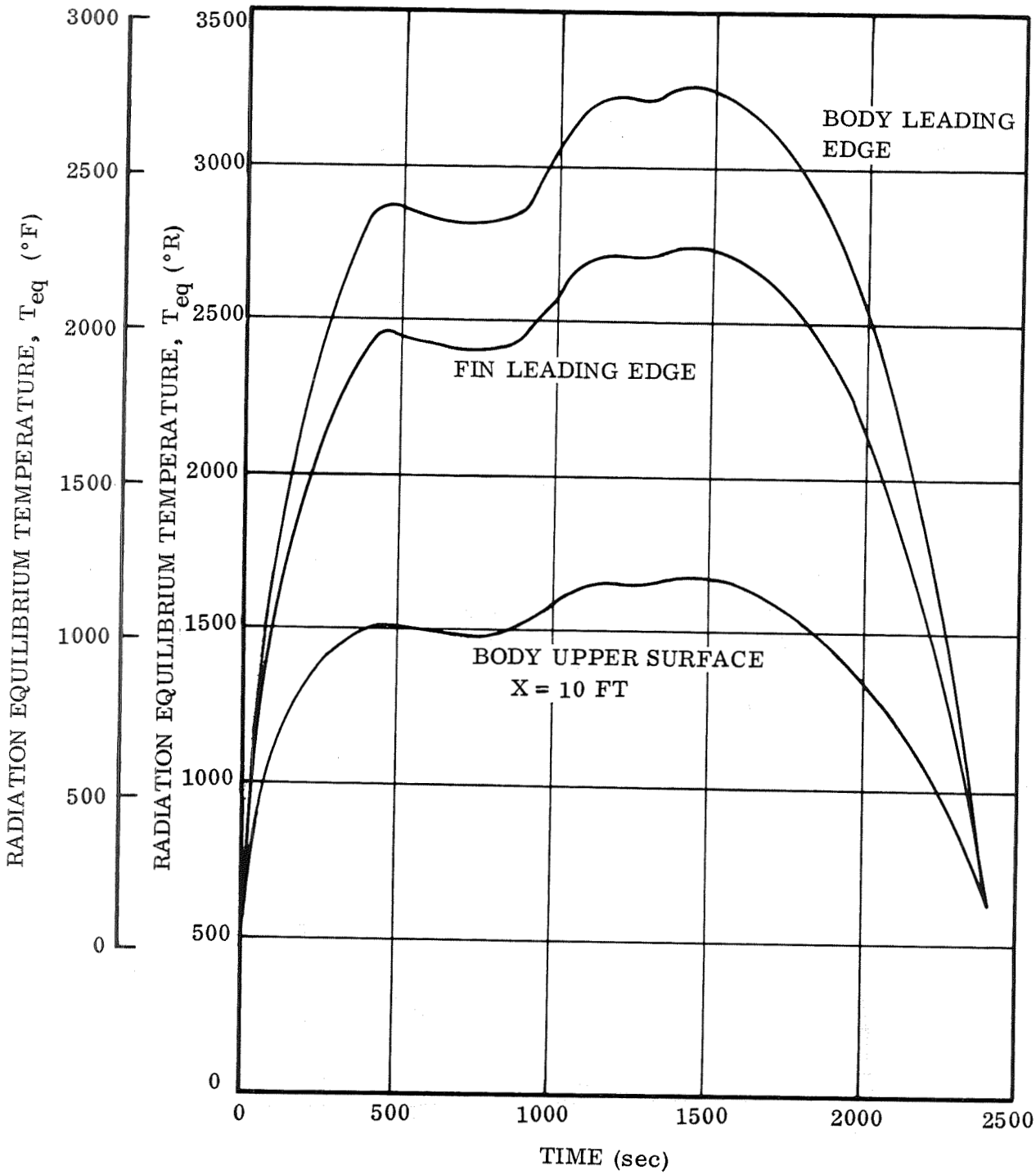

Figure 4-8. Temperature Histories at Various Orbiter Locations Using Adiabatic Method and Gradual Transition, Trajectory 353, 800-n.mi. Crossrange

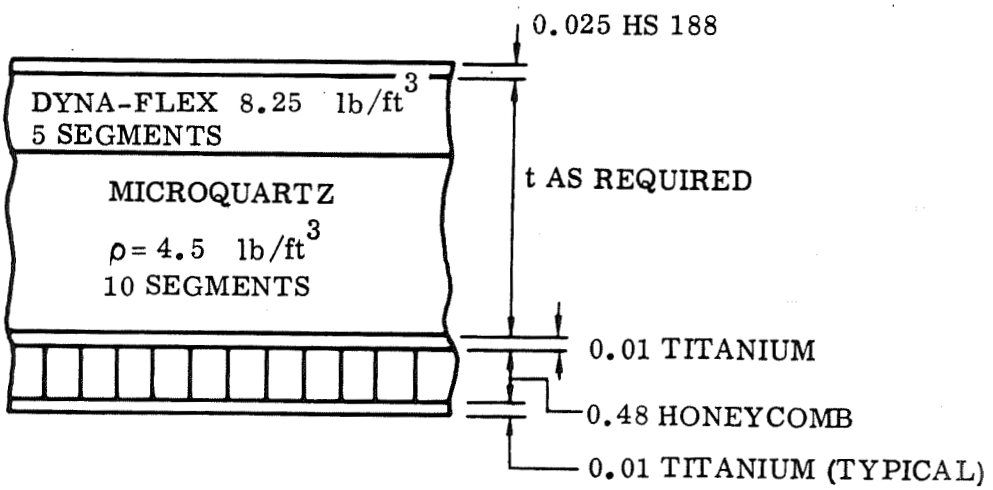

X = 10 ft

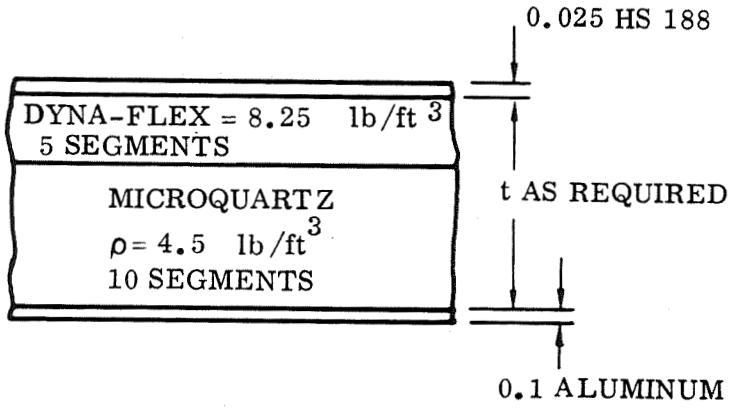

X = 60 ft

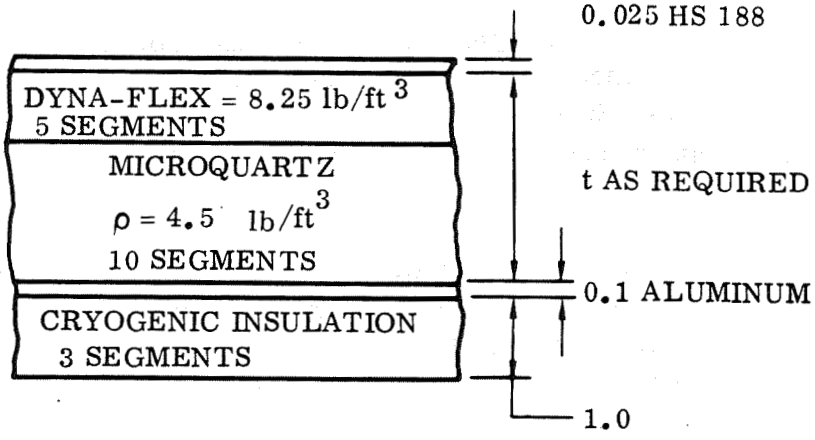

X = 165 ft

Figure 4-9. Insulation TPS Thermodynamic Model

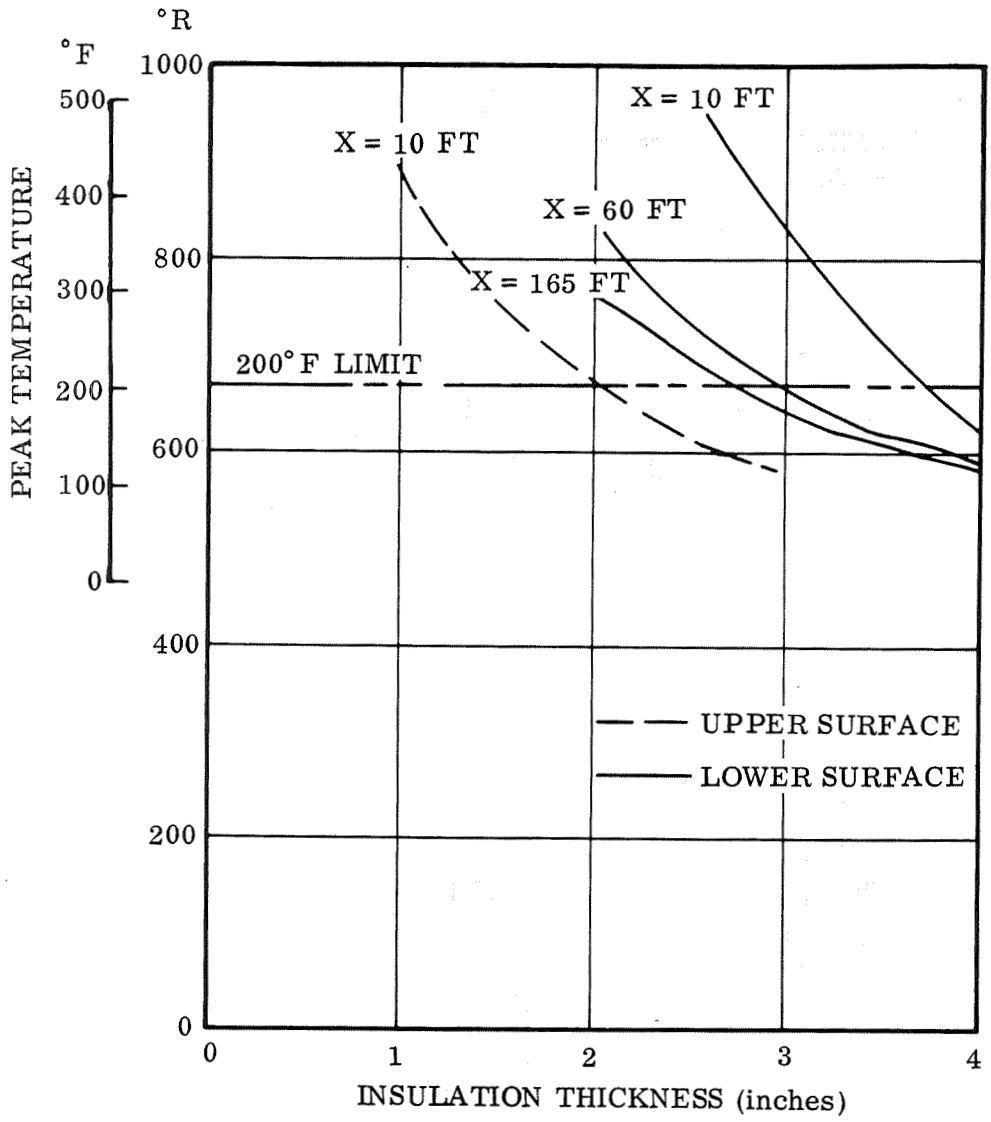

Figure 4-10. Orbiter Lower and Upper Surface Insulation Requirements at Various Stations, Trajectory 353, 800-n.mi. Crossrange

Figure 4-14 shows radiation equilibrium temperature data for the orbiter during ascent. This data was compiled to check orbiter entry design conditions against the ascent conditions. All areas of the orbiter vehicle are subjected to critical design temperatures during entry except the forward area on the upper surface, which is most critical during ascent.

Figure 4-15 shows the temperature distribution in the orbiter insulation material during ascent, during post-ascent coast, and at 5600 seconds as measured from lift-off. Review of the energy distribution shown in Figure 4-15 shows that more energy is dissipated through radiation from the TPS during orbital coast than is absorbed during ascent.

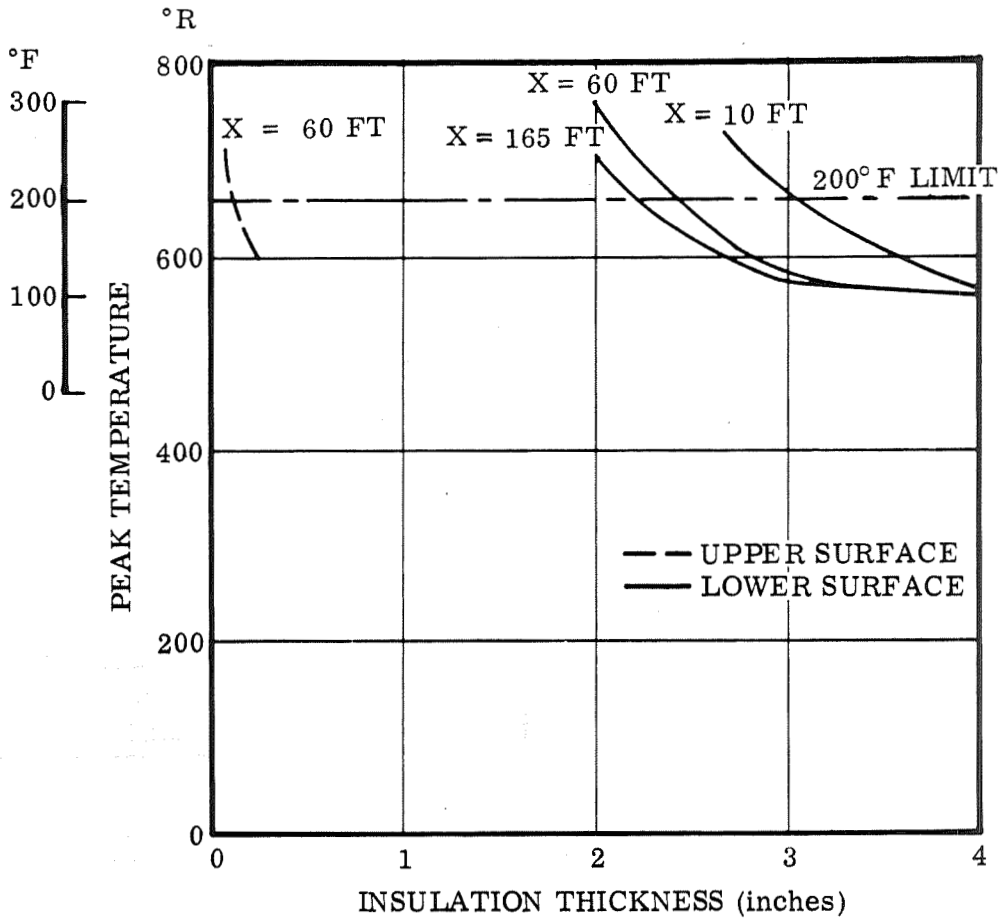

Figure 4-11. Orbiter Lower and Upper Surface Insulation Requirements at Various Stations, Trajectory 349, 300-n.mi. Crossrange

4.4 AEROHEATING UNCERTAINTIES

Evaluation of aerodynamic heat transfer in hypersonic flow is subject to a number of uncertainties. The inability of existing test facilities to simulate hypersonic entry flight conditions coupled with the scarcity of appropriate flight data suggests that prediction of aerothermodynamic performance in the hypersonic regime be made with caution. Several problem areas have been particularly troublesome. Among these, the most significant uncertainties lie in the prediction of the transition from laminar to turbulent flow and of the behavior of the resulting turbulent boundary layer. The magnitude of the uncertainties associated with these predictions is discussed in the following paragraphs.

4.4.1 TURBULENT HEATING PREDICTION. Four turbulent boundary layer heat transfer prediction methods are currently in common use. Two of these, the Eckert reference enthalpy method and the reference enthalpy method with an adiabatic wall, have been discussed in Section 4.1. The adiabatic wall reference enthalpy method based on X-15 flight test data was used for all design aerodynamic heating predictions in this study. Eckert's reference enthalpy method was felt to be conservative for the hypersonic regime of interest. Two other techniques, the modified Spalding-Chi

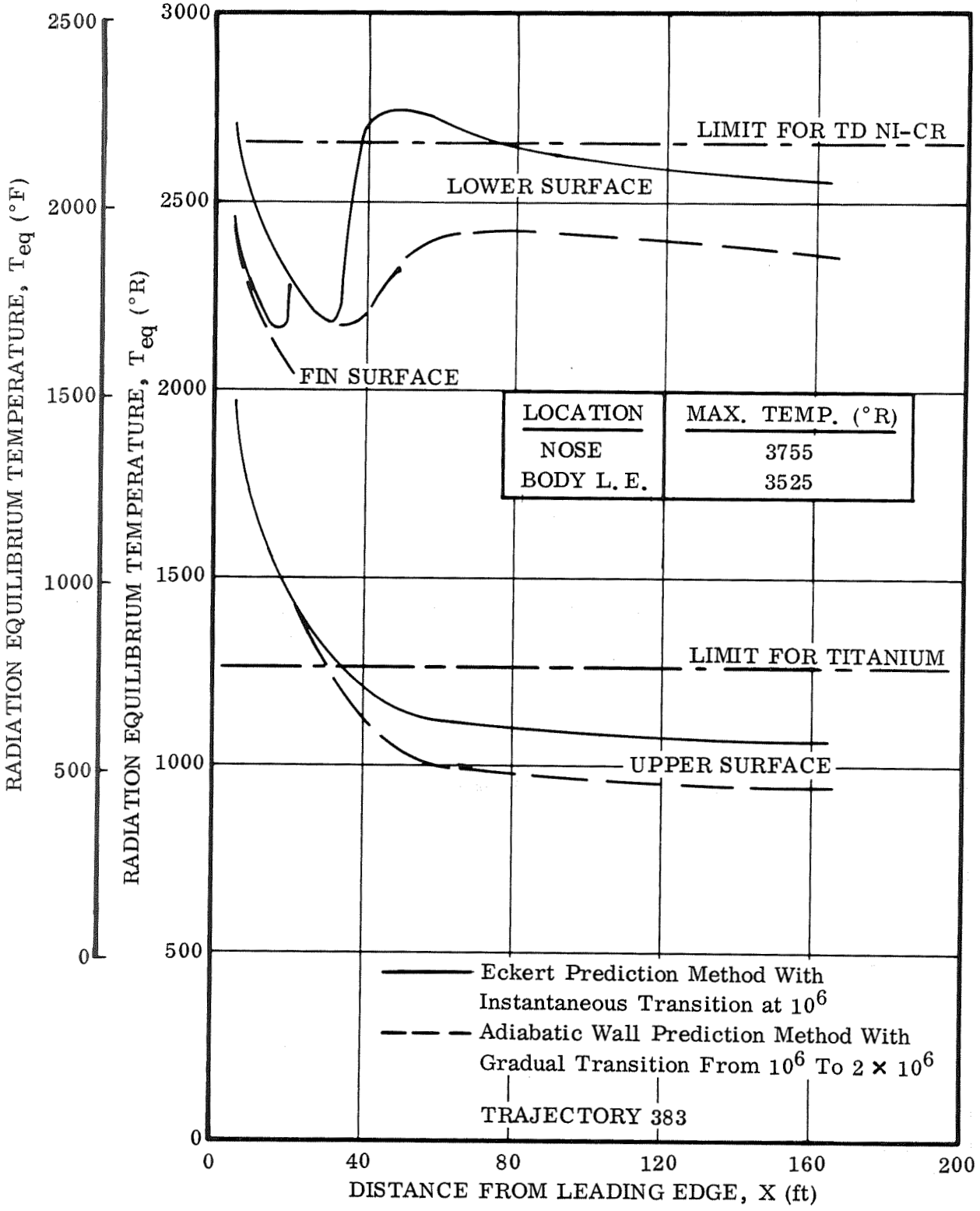

Figure 4-12. STS Orbiter Maximum Temperature Versus Station for 500-n.mi. Crossrange

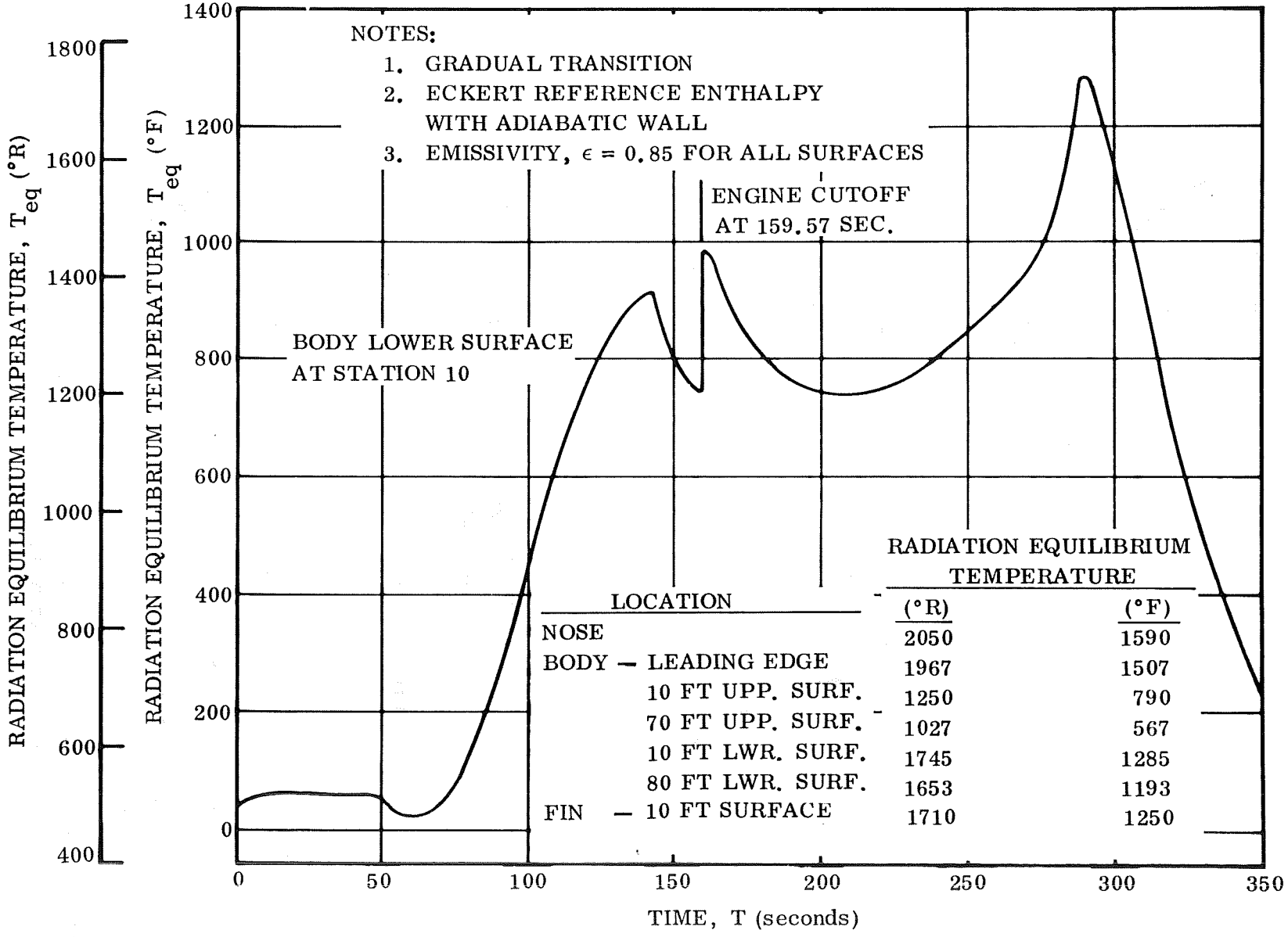

Figure 4-13. Maximum Booster Temperatures at Selected Locations

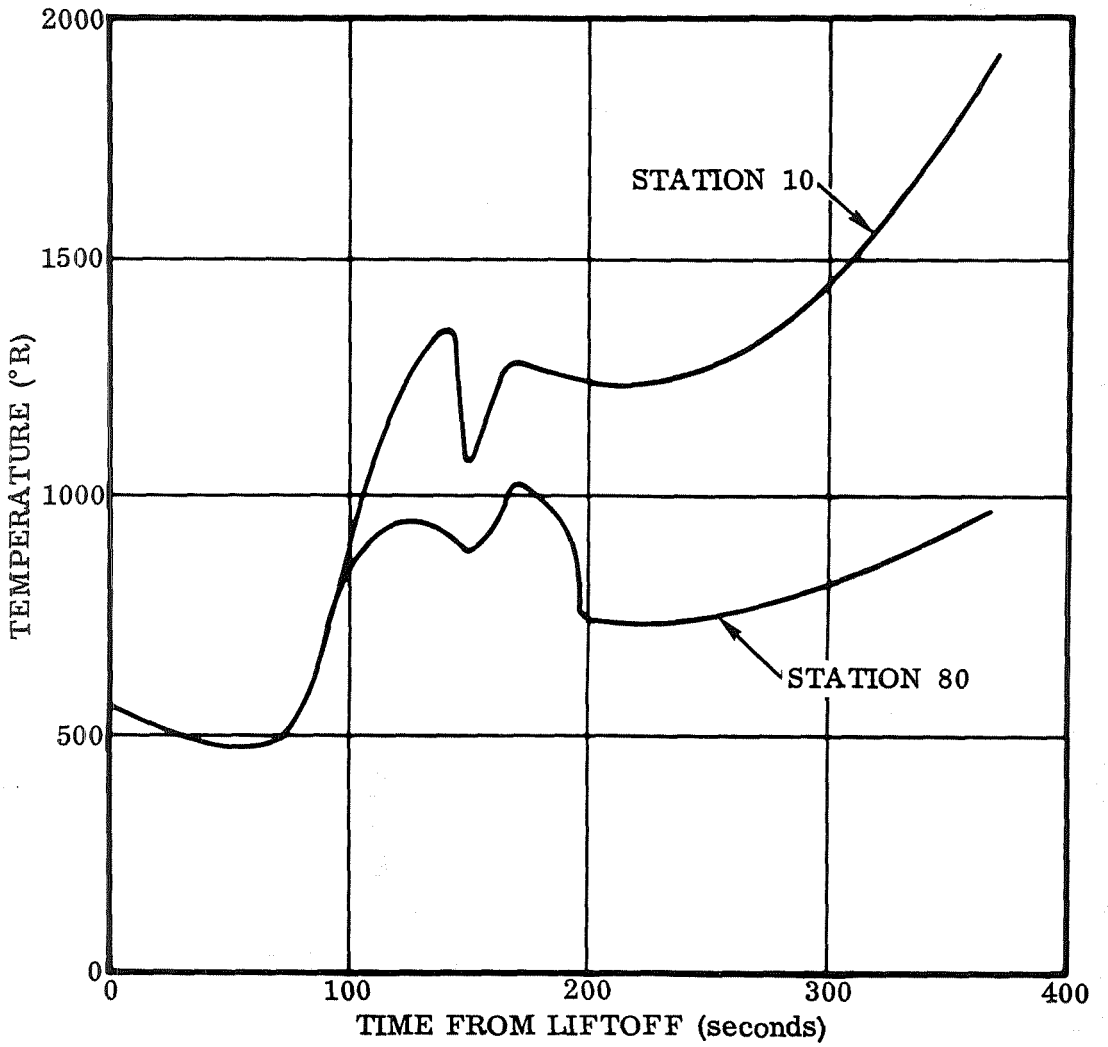

Figure 4-14. Orbiter Ascent Temperatures

methods (Reference 4-9) and the $\rho_r \mu_r$ method (Reference 4-10), have also been used for predicting entry aerodynamic heating characteristics.

For the range of flight conditions covered by this study, there is a significant variation in predicted aerodynamic heating among the four methods. Because of this variation and the sensitivity of material selection to peak surface temperatures, a comparison of the prediction methods was made.

Comparison of the aerodynamic heat transfer predictions and resulting radiation equilibrium temperatures for the four methods were made for lower surface locations on the orbiter vehicle using a number of available entry trajectories to investigate the effects of entry parameters. Surface emissivity was set at 0.85 for these calculations. Instantaneous boundary layer transition at a shock layer Reynolds number of 1×10^6

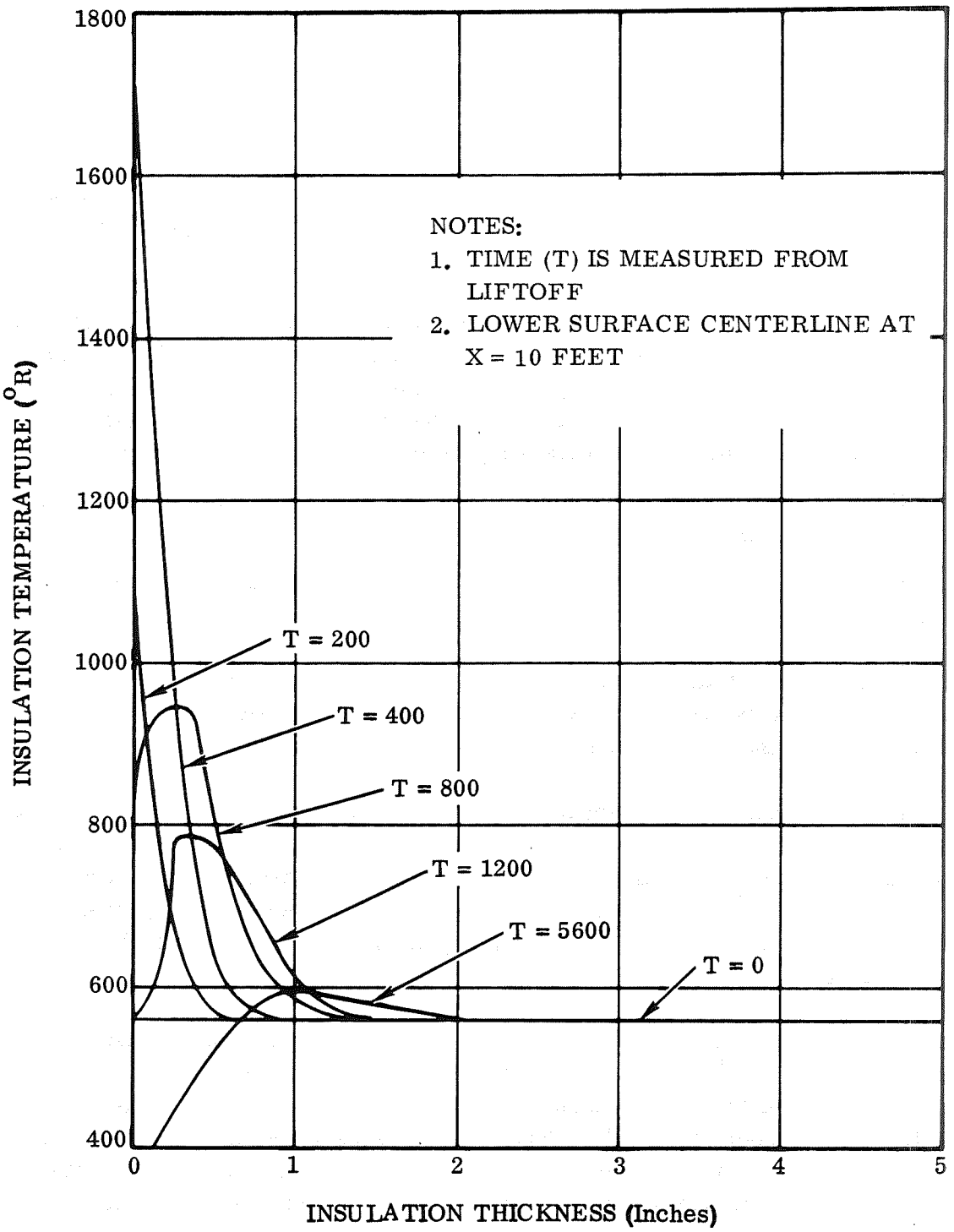

Figure 4-15. Orbiter Insulation Temperature Profiles During and After Ascent

was assumed. Table 4-1 presents the peak surface radiation equilibrium temperatures computed by the various methods for the locations and trajectories noted. Angle of attack for each trajectory is also shown.

The spread between the highest and lowest temperature predictions is as great as 458°R, although a spread of 350°R appears to be nearer the average.

An evaluation of these results shows that the Eckert reference enthalpy method with an adiabatic wall is quite close to the average value of all prediction methods in each case. The Eckert reference enthalpy method predicts the highest temperatures in each case.

4.4.2 BOUNDARY LAYER TRANSITION. Selection of the criteria for boundary layer transition from laminar to turbulent flow can have significant effect on TPS material selection. Unfortunately, no universally reliable analytical procedure has been developed for predicting the onset, duration, and heating levels of the transitional process. The two most common criteria for predicting the initiation of transition are:

a. Transition upon reaching a selected value of shock layer Reynolds number based on run length from the vehicle nose.

b. Transition upon reaching a selected value for the ratio of boundary layer momentum thickness Reynolds number to local Mach number.

Both techniques represent attempts to infer the microscopic transitional process from macroscopic flow parameters. As such, neither is on particularly solid theoretical ground; rather each depends on empirical justification.

In addition to the difficulties attendant to predicting transition onset, the extent of the transitional region must be considered. It is well established that transition does not occur instantaneously. For lifting entry vehicles, the transitional region may occur over a significant portion of the vehicle surface for a considerable period of time during entry. For some vehicle locations, peak heating will occur in the transitional region as the entry trajectory is traversed.

Comparisons have been made between instantaneous transition at a shock layer Reynolds number of 1×10^6 based on run length from the vehicle nose and transition in a finite zone starting at a Reynolds number of 1×10^6 and reaching fully turbulent flow at a Reynolds number of 2×10^6. These comparisons were made by evaluating the peak radiation equilibrium temperatures obtained using both methods for a number of the orbiter entry trajectories. Emissivities of the surfaces were 0.85.

Both the Eckert reference enthalpy method and Eckert reference enthalpy with an adiabatic wall were used. In the finite transition region method, boundary layer parameters were assumed to vary linearly from the laminar values at the onset of transition to the turbulent values at the end. Table 4-2 shows the resulting peak temperatures for vehicle lower surface locations.

Table 4-1. Comparison of Turbulent Heating Prediction Methods — Peak Temperatures With Instantaneous Transition

Trajectory Number	364 (Abort) α = 25 deg (°R)	383 (Nominal) α = 37 deg (°R)	382 α = 60 deg (°R)	353 α = 37 deg (°R)	360 α = 25 deg (°R)	357 α = 20 deg (°R)
Eckert Reference Enthalpy						
X = 30 feet	2960					
X - 80 feet	2680	2630	2100	2530	2665	2605
Eckert Reference Enthalpy with Adiabatic Wall						
X = 30 feet	2740					
X = 80 feet	2440	2430	1965	2330	2445	2375
Modified Spalding-Chi						
X = 30 feet	2595					
X = 80 feet	2222	2296	1913	2197	2289	2253
$\rho_r \mu_r$						
X = 30 feet	2753					
X = 80 feet	2463	2430	1951	2331	2450	2388
Average						
X = 30 feet	2757					
X = 80 feet	2451	2447	1982	2347	2462	2405
Maximum Spread						
X = 30 feet	365					
X = 80 feet	458	334	187	333	376	352

Variations in peak temperatures of up to 190°R can be observed between the instantaneous and finite transition zone models. The significance of the difference in prediction models is strongly dependent on trajectory parameters and on the time in the trajectory when transition occurs at a particular location.

Figure 4-16 shows the effect on peak surface temperature of variation in the Reynolds number assumed for the start of transition. Gradual transition was used. Reynolds number values at the end of transition were assumed to be two times the Reynolds number at the start of transition. Eckert reference enthalpy with an adiabatic wall was used. This data reflects the peak temperature observed on the lower surface aft of a point five feet from the vehicle nose. The effect of transition Reynolds number, like the choice of instantaneous or gradual transition, is strongly dependent on trajectory. For the $C_{L_{max}}$ entry, the peak lower-surface temperatures occur in the laminar boundary layer; the L/D_{max} trajectory shows a 360°R variation between values of transition Reynolds number of 1×10^6 and 3×10^6.

Evaluating the data in Table 4-2 and Figure 4-16 shows that selection of transition criteria can influence the predicted peak surface temperatures by over 300°R.

Table 4-2. Boundary Layer Transition Criteria Comparison — Peak Lower Surface Radiation Equilibrium Temperatures

Trajectory	364 α = 25 deg (Abort) X = 30 ft (°R)	383 α = 37 deg (Nominal) X = 80 ft (°R)	364 α = 25 deg (Abort) X = 80 ft (°R)
Eckert Reference Enthalpy with Adiabatic Wall			
1. Gradual Transition $Re_{TR} = 1\times10^6$ to 2×10^6	2595	2425	2440
2. Instantaneous Transition $Re_{TR} = 1 \times 10^6$	2740	2430	2440
Eckert Reference Enthalpy			
1. Gradual Transition $Re_{TR} = 1\times10^6$ to 2×10^6	2770	2625	2680
2. Instantaneous Transition $Re_{TR} = 1 \times 10^6$	2960	2630	2680

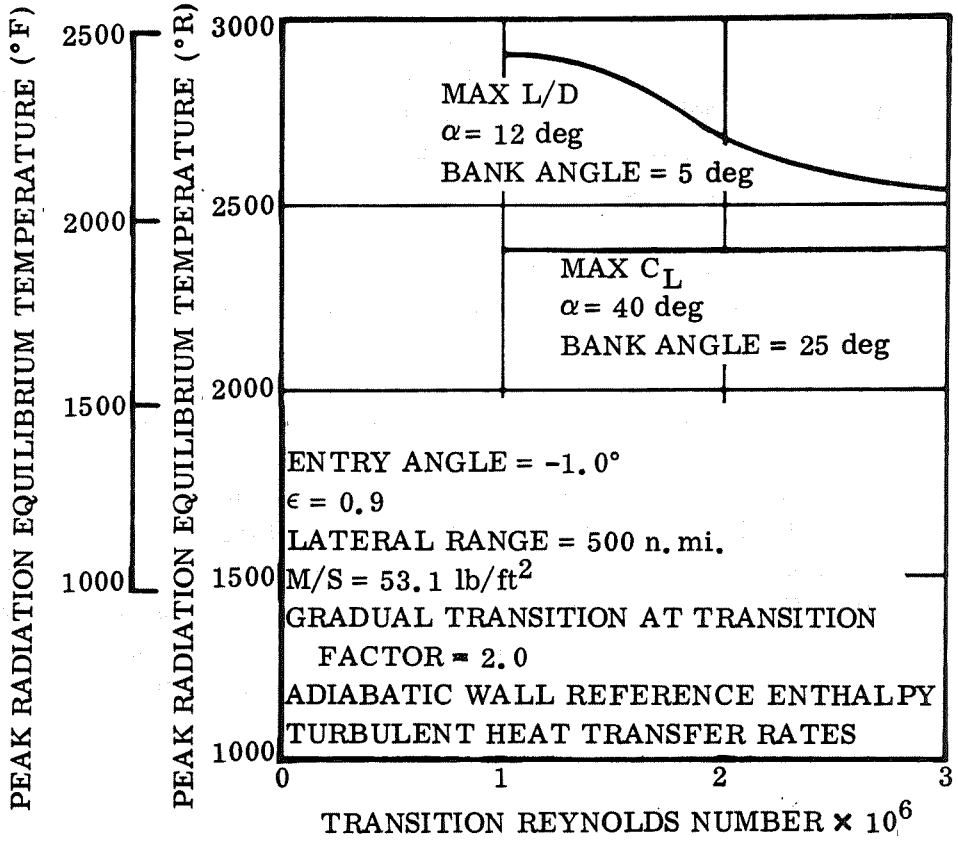

Figure 4-16. Peak Temperature Sensitivity to Transition Reynolds Number

It was concluded that gradual transition from laminar to turbulent flow would be used for design predictions in this study. The criterion selected for initiation of transition was a shock layer Reynolds number (based on run length from the vehicle nose) of 1×10^6. Transition was assumed complete when the Reynolds number reached 2×10^6. For backup material selection, instantaneous transition was assumed to occur at a Reynolds number of 1×10^6.

4.4.3 ATMOSPHERIC DISPERSIONS. An analysis of the effect of atmospheric dispersions on the aerodynamic heating characteristics was made. The assumption was made that the ascent trajectory would be a fixed altitude-velocity-trajectory and during entry the vehicle would fly a velocity-density trajectory. Under these assumptions, the ascent trajectory heating would be influenced by atmospheric dispersions but they would have little effect on entry heating.

The effect of a 3σ dispersion in atmospheric density increased the peak nose temperature by about 175°R and the lower surface temperature by about 80°R.

4.5 CROSSRANGE EFFECT ON THERMAL PROTECTION REQUIREMENTS

Figure 4-17 shows TPS insulation requirements as a function of orbiter entry crossrange for several vehicle locations. Insulation was sized to limit structural temperatures to a maximum of 200°F. The crossrange influence on insulation thickness is shown to be minor between 300 and 800 n. mi. Crossrange has no influence on cover panel material selection or structural design. Thus, the TPS weight is relatively insensitive to crossrange requirements. The 300-n. mi. TPS weight is 6.7 percent less than required for 800 n. mi.

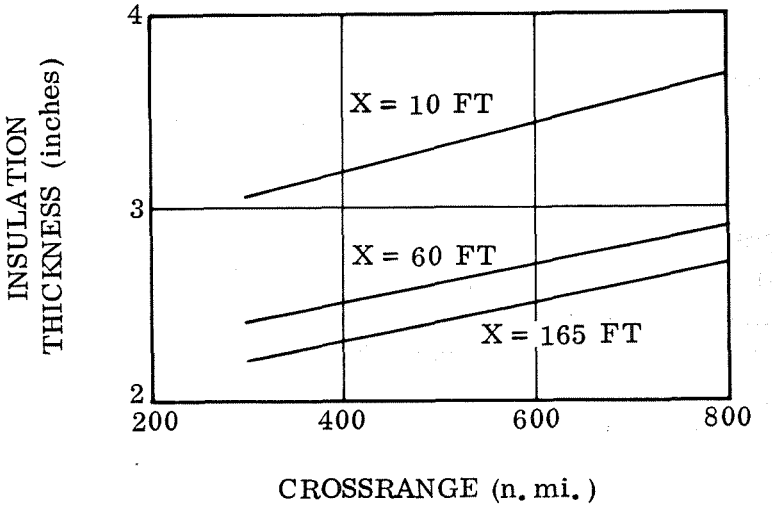

Figure 4-17. Lower Surface Insulation Requirements

4.6 CRYOGENIC THERMAL CONTROL

Orbiter cryogenic propellant tanks, particularly the LH_2 tankage, require an insulation system that will eliminate cryopumping and minimize heat leak into the tank. The insulation must be capable of operating within the ground hold, launch, space, and entry environments for up to 100 flights. It must also be structurally compatible with the propellant tank design. An internal insulation system is most desirable because 1) it is inside the tank and more accessible for inspection and servicing and is less subject to service and handling damage, 2) the tank structure remains "warm" when filled with cryogenics and is subjected to lower thermal stresses, and 3) helium purge is not required.

The recommended approach to the main propellant tank insulation for a reusable system is the simultaneous development of 1) an open-cell internal cryogenic insulation and 2) the installation and qualification of the Saturn S-IVB 3D foam in a large-scale tank of flight-weight design and construction.

The open-cell concept is an internal tank insulation with small open cells such as honeycomb or stacked tubing. One end of the cell is bonded to the tank wall and the other end is open to the liquid. The cells are sized so that liquid surface tension prevents liquid entry into the cells. The open-cell matrix forms an insulating gas layer between the liquid surface and tank wall. The advantage of this concept is that it has no bonded and sealed inner liner subjected to cryogenic temperatures and pressure cycling due to cryopumping then heating. Materials are becoming available that make this insulation potentially capable of temperatures up to 500° to 600°F.

The internal 3D polyurethane foam insulation used on the Saturn S-IVB stage is a candidate material for a reusable launch vehicle. It has been subjected to numerous cryogenic tanking cycles during static ground tests of the S-IVB vehicle. Failures that occurred are considered repairable. This concept is probably compatible with a 200°F maximum temperature limit. Since it has a bonded inner liner which is subjected to cyclic temperatures down to liquid hydrogen, it will be subjected to embrittlement and thermal stress failures. The S-IVB insulation is installed in one ft^2 panels within the rib pattern of the integrally stiffened tank skins. This block-type installation provides stress relief and tends to prevent crack propagation through the foam. This is an example of a compatible insulation/structure design. It is possible that this insulation would not be so successful in a different structural concept. It must be demonstrated to be reusable by cyclic life testing through the structural load, vibration, and thermal environments.

4.6.1 ORBITER MAIN PROPELLANT TANKS, VENT AND PRESSURE SCHEDULES.

The LH_2 is internally insulated and will be self-pressurized about two minutes prior to launch. The tank pressure will be increased to about 25 psia prior to staging by

bleeding hydrogen from the engines. The pressure schedule is designed to supply the necessary pump NPSH and to minimize the effect of liquid stratification.

The LO_2 tank is assumed to be uninsulated but protected from wind and moisture condensation by nitrogen purge in the space between the heat shield and the tank. The tank will be pressurized prior to launch to about 20 psia with a ground helium supply. LO_2 has a fairly high collapse factor (condensation rate when self-pressurized). The helium pressurant will minimize the development of a large stratified or boiling layer of LO_2 at the top of the tank. Ullage pressure will be maintained after staging by pressurizing with gaseous oxygen bled from the engines, eliminating the need for an onboard helium supply. LO_2 tank pressure is required only to prevent two-phase flow at the tank outlet into the propellant transfer line. The hydrostatic head in the long propellant line will provide the required NPSH at the pump.

The vent and pressure schedules for the launch are shown in Figure 4-18. These pressures are considered a minimum requirement to prevent cavitation in propellant lines and to maintain the necessary NPSH. Structural considerations and vent control component tolerances may dictate higher pressures. Venting may occur after burnout to maintain 25 psia, to pressurize the maneuvering tanks, or to operate the ACS engines. Tank pressure schedules in orbit will be determined by the orbital maneuvering propulsion subsystem design requirements.

4.6.2 ORBITER MAIN PROPELLANT TANKS, PROPELLANT LOSSES. Propellant losses for the orbiter element were determined assuming a one-inch-thick internal cryogenic insulation. Main tank losses were determined for chilldown during ground hold. Aluminum tank structure weights were estimated from the corresponding propellant weights using:

$$LH_2 \text{ Wt} = 0.12\ W_H$$

$$LO_2 \text{ Wt} = 0.12\ W_O$$

The tanks were assumed to be purged externally by dry nitrogen gas to eliminate moisture condensation and to disperse leaking propellants. Skin temperatures of the LH_2 and LO_2 tanks during ground hold were -5 and +10°F, respectively. The propellants were assumed to be saturated at their normal boiling points so that no liquid temperature increase was assumed. The resulting propellant losses are: hydrogen 3.7 percent of the tanked mass and oxygen 0.6 percent of the tanked mass.

4.6.3 ORBITAL MANEUVERING PROPELLANT TANKS. The orbital maneuvering propellant tanks were thermally analyzed to determine the boiloff losses and tank pressures for various amounts of insulation. The thermal model for the orbital case is illustrated in Figure 4-19. The external surface is assumed to have a radiative α/ϵ= 1.0, which results in an approximate average surface temperature of 535°R (75°F).

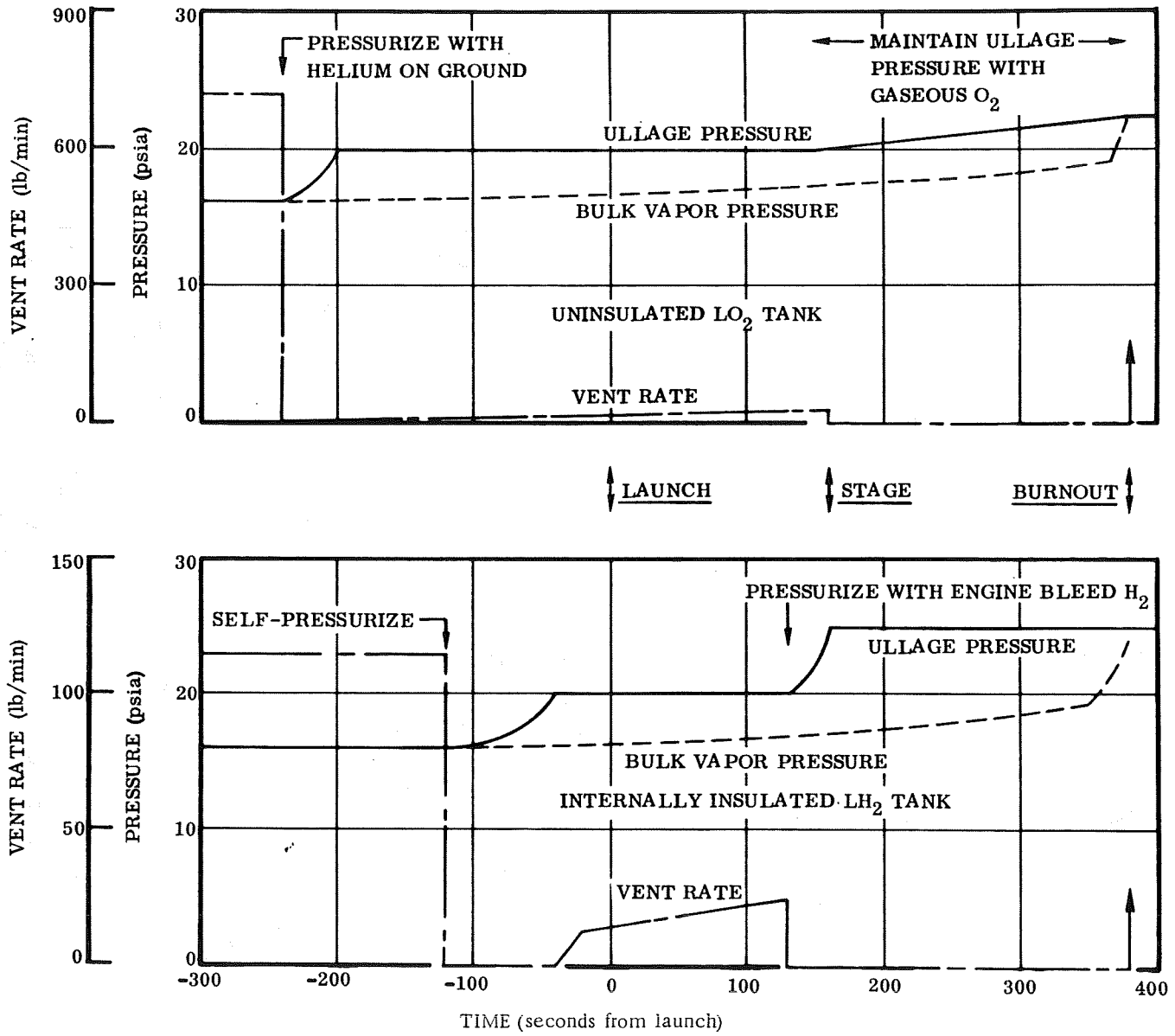

Figure 4-18. Orbiter Vent and Pressure Schedules

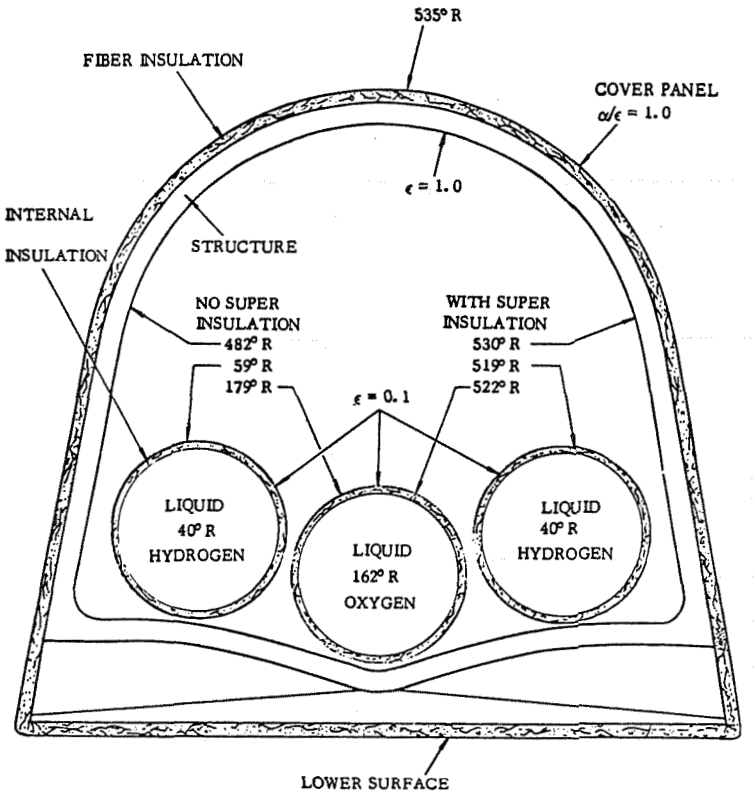

Figure 4-19. Orbiter Cryogenic Thermal Model

Two inches of fiber insulation for high-temperature thermal protection of the structure has been assumed under the cover panel. The tanks will be coated with a reflective surface $\epsilon = 0.1$. Heat transfer to the tanks in orbit is by radiation, with a representative amount added for conduction through supports and penetrations.

During ground hold and launch, the area around the tanks is assumed to be purged with room temperature dry nitrogen gas. The heat transfer coefficient to the tanks is assumed to be h = 2 Btu/hr-ft^2°R. A sufficient quantity of nitrogen purge should be used to keep the external fiber insulation around the payload bay above 32°F or the local dew point whichever is higher. Under these conditions, the external surface of the maneuvering propellant tanks will be 425°R (-35°F) with one inch of internal insulation.

The maneuvering tanks are full during ground hold and launch and the first five hours in orbit. The tanks are assumed to be 2/3 full with the propellant settled for a seven-day orbital coast period. The tank sizes and wetted areas used for this analysis are given in Table 4-3(a).

Table 4-3. Orbital Maneuvering Propellant Tanks

		LO_2	LH_2				
(a) Tank Geometry							
Sizes							
Diameter	(in.)	85	85				
Cylinder Length	(in.)	84	300				
Volume	($in.^3$)	798,000	2,024,000				
Surface Area	($in.^2$)	45,000	103,000				
Initial Mass	(lb)	10,417	65,974				
Wetted Area (ft^2)		(One Tank)	(Two Tanks)				
Ground Hold and Launch		626	1,426				
Orbit to 270 n.mi.		626	1,426				
Orbit, 7-Day Coast		401	940				
		Quantity Super Insulation					
		None		4 Layers		40 Layers	
		LO_2	LH_2	LO_2	LH_2	LO_2	LH_2
(b) Heat Flux to Propellants							
Ground Hold and Launch	$Btu/hr\text{-}ft^2$	112	154	112	154	112	154
Orbit	$Btu/hr\text{-}ft^2$	7.3	8.4	0.65	0.86	0.065	0.086
Penetrations	Btu/hr	500	250	500	250	500	250
(c) Integrated Heat Input to Propellants (Btu)							
Ground Hold and Launch	21 min	24,700	77,090	24,700	77,090	24,700	77,090
Orbit to 270 n.mi.	5 hr	25,350	61,140	4,530	7,380	2,700	1,860
Orbit, 7-Day Coast	168 hr	575,790	1,368,500	127,790	177,810	88,380	55,580
	Total	625,840	1,506,730	157,020	262,280	115,780	134,530
(d) Boiloff and Insulation Mass							
Internal Insulation		376	856	376	856	376	856
Super Insulation		0	0	6	13	60	130
Boiloff	15 psia	7,277	7,815	1,825	1,333	1,345	669
	50 psia	3,020	6,620	0	231	0	0
	150 psia	0	4,660	0	0	0	0

Varying quantities of superinsulation from none up to 40 layers were evaluated. The superinsulation has no effect on the heat transfer during ground hold and launch. Heat flux to the propellants, including that through penetration, is shown in Table 4-3(b). The integrated total heat input to the propellants for the trajectory segments is shown in Table 4-3(c). The quantity of propellant that boils off can be reduced by varying the storage pressure, thus allowing the liquid to absorb heat. The insulation and boiloff masses are shown in Table 4-3(d).

The tanking pressure is 15 psia; if held at this pressure, all the heat input results in boiloff. As the pressure is increased, the boiloff is reduced. The heat input and boiloff are also reduced by adding superinsulation for thermal protection in orbit. As indicated in the table, LO_2 boiloff can be eliminated by pressurizing to 50 psia and using four layers of superinsulation. About 10 layers of superinsulation would eliminate hydrogen boiloff at 50 psia.

4.7 NOZZLE HEATING

Radiation equilibrium temperature histories for the rocket nozzle external surfaces have been calculated for launch and entry. Nozzles were considered to be extended during launch and retracted during entry. Heating rates were calculated with the 3020 computer program, Reference 4-3, using the Eckert adiabatic wall reference enthalpy method for turbulent flow. Gradual transition from laminar to turbulent flow was assumed; transition from turbulent to laminar flow was assumed to occur instantaneously. Surface emissivities were 0.80.

Figure 4-20 shows the surface temperatures for the side and upper nozzles during the launch and injection phase. Temperatures were calculated for attached flow and for flow reattached on the nozzle after separation from the base of the vehicle. A very conservative reattachment heating ratio of five times the attached heating was used. The peak temperature, 830°F (1290°R), is on the side nozzle at 135 seconds.

Figure 4-21 presents similar data for the lower nozzle during launch. The nozzle is extended beyond the bottom surface during this period. Again, both attached and separated/reattached flow heating effects were considered. No effects attributable to recirculated exhaust gases or the normal nozzle flow were included in this analysis. A peak temperature of 1060°F (1520°R) is shown.

Figure 4-22 shows temperature histories for the side nozzles during entry from orbit, using the 800-n.mi. trajectory. Attached and separated/reattached flow conditions are shown, with a peak reattached temperature of 1130°F (1590°R) attained 1740 seconds into the entry. The lower and upper nozzles will be cooler than the side nozzles if the lower nozzle is retracted so that there is no exposure to the flow.

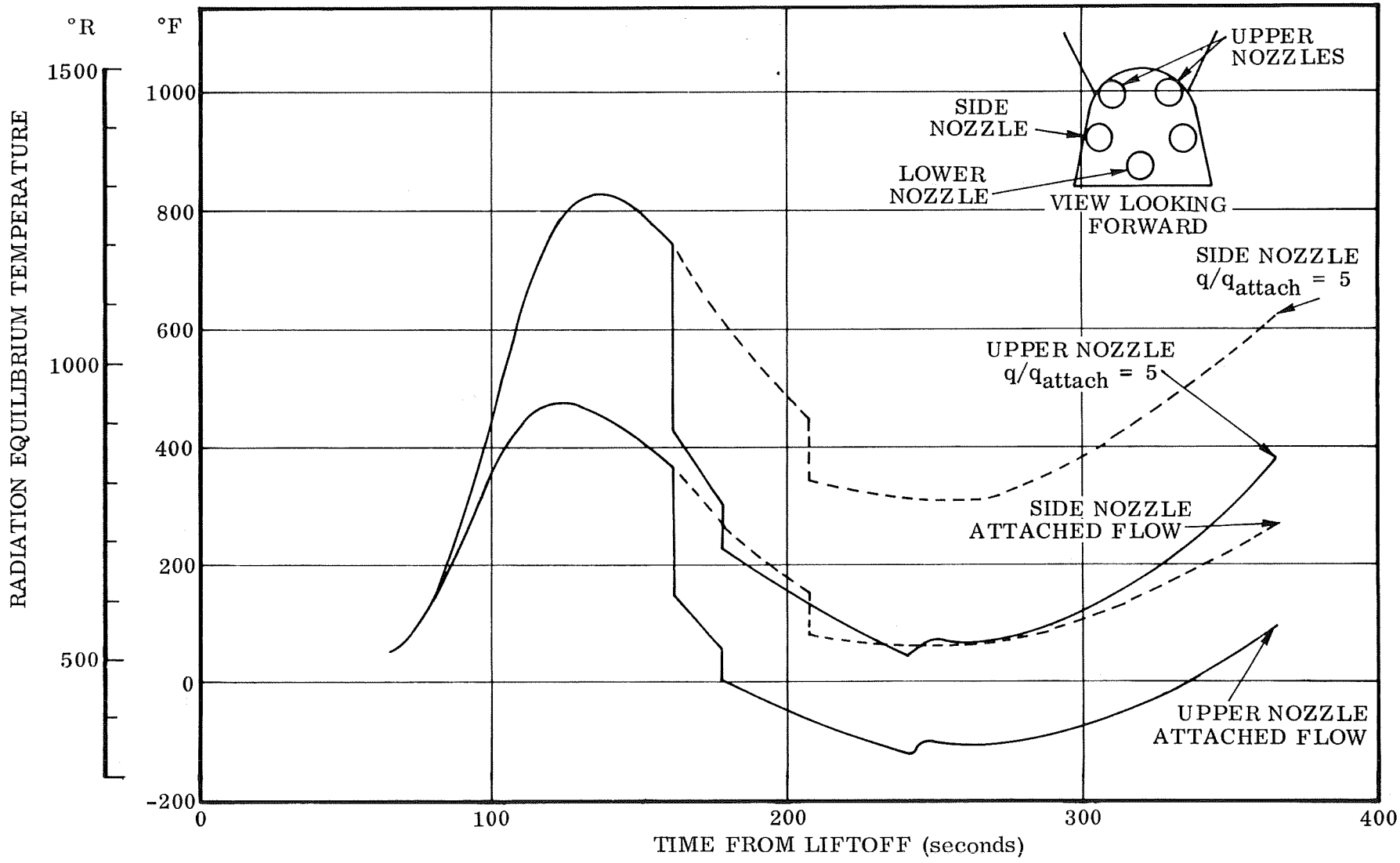

Figure 4-20. Upper and Side Nozzle Temperatures During Launch

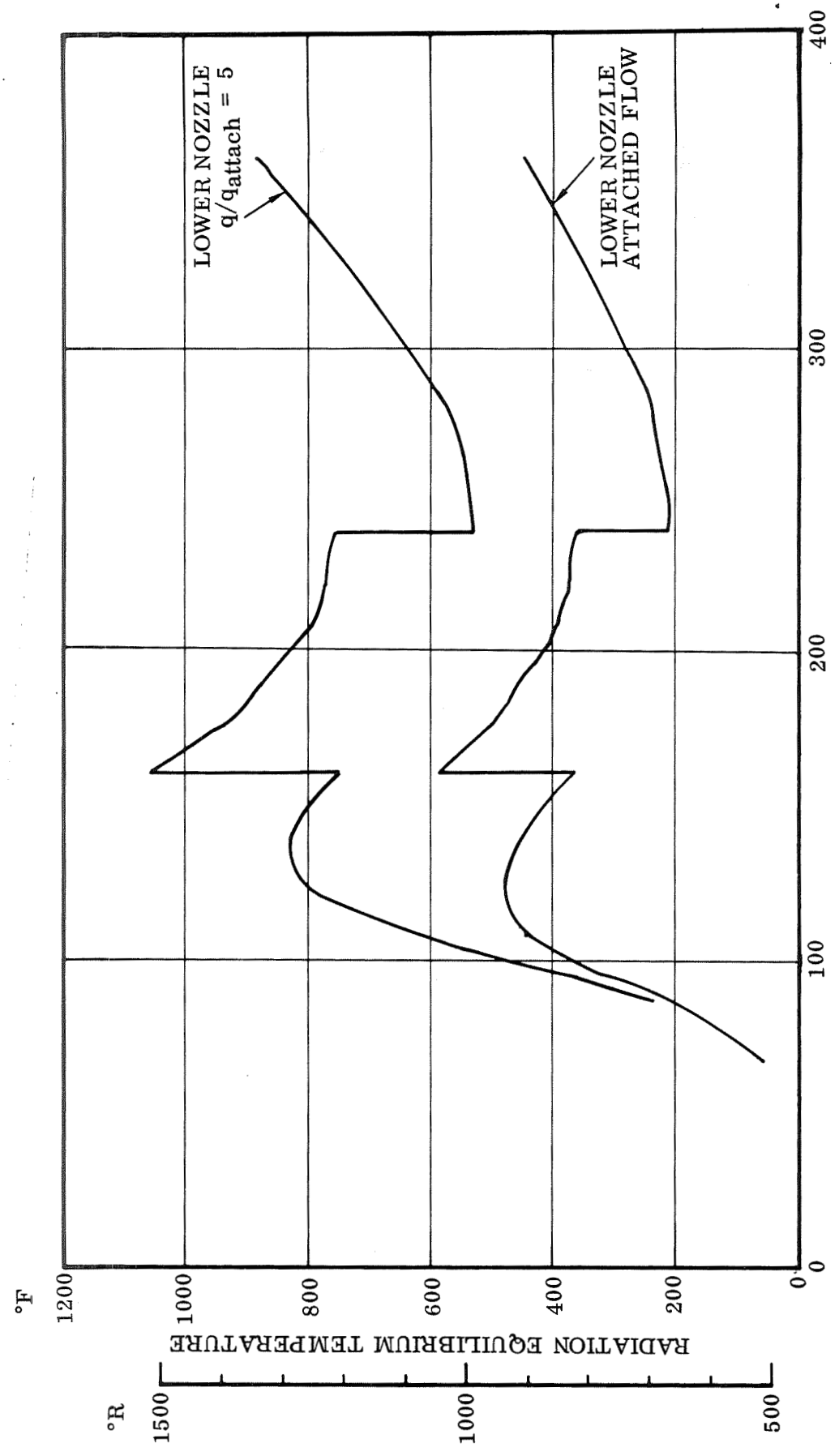

Figure 4-21. Lower Nozzle Temperature During Launch - Nozzle Extended

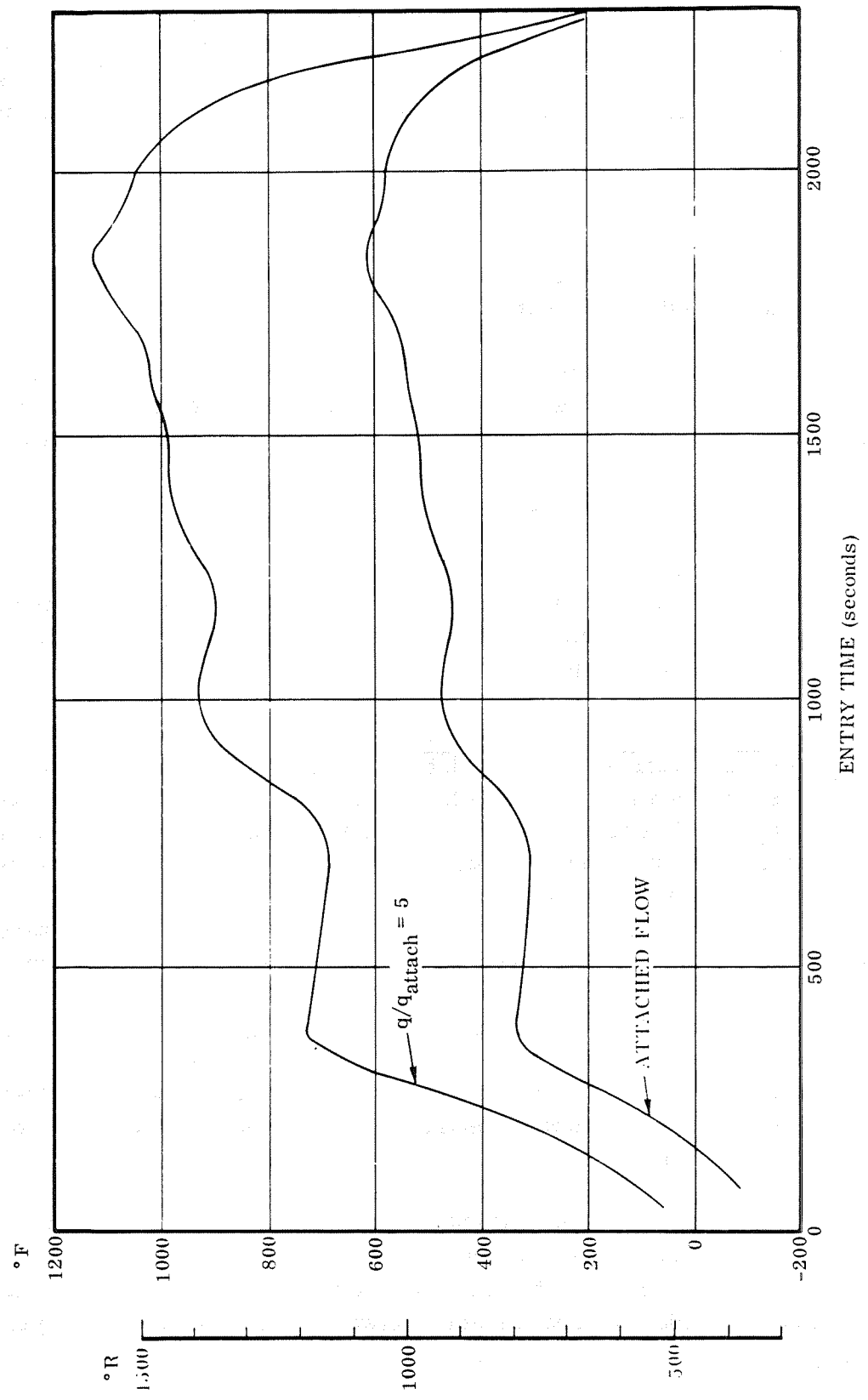

Figure 4-22. Side Nozzle Temperatures During Entry

Figure 4-23 shows the results of an analysis of the heating on a lower nozzle extended during entry for L/D_{max} and $C_{L_{max}}$ trajectories. Peak temperatures of 2300°F were calculated using attached-flow assumptions. If the flow separates from the rear edge of the elevon and reattaches on the extended nozzle during entry, temperatures in excess of this 2300°F value can be expected. Nozzle temperatures for four engine arrangements can be expected to be approximately the same as those shown for five-engine clusters.

4.8 STRUCTURAL THERMAL CONTROL

An analysis of alternative approach to the passive TPS subsystem was conducted, and the results are discussed in this section.

The use of an insulation-only TPS for a lifting entry vehicle presents, in general, a heat soak-back problem due to high internal temperatures in the insulation. Even though the insulation system may keep the structure at an acceptable temperature level during flight, overheating of the structure may occur after landing unless some additional method of heat removal is employed.

In an attempt to solve this heat soak-back problem, and additionally to try to reduce the total weight of the TPS, a number of alternative approaches were considered. These five approahces, with their attendant advantages and disadvantages, are described in the following paragraphs.

4.8.1 INSULATION WITH GROUND AIR COOLING. (See Figure 4-24.) In a pure insulation system, the interior of the insulation is at a high temperature (1000 to 1500°R) at landing. This heat then soaks towards the outside and inside, tending to raise the temperature of the inside structure above acceptable limits. This heat can be removed by blowing air over the primary structure. Preliminary calculations indicate that the required air flow to maintain the primary structure at 200°F would be approximately 0.017 lb/ft^2-sec. The motive power required (for 6300 ft^2 bottom surface area) would be approximately 400 hp per psi pressure drop in the distribution system.

A pure insulation approach has the advantages of being simple and safe, as it is completely passive and there are no moving parts to fail during flight. Failure on the ground may lead to overheating of the structure, but crew safety is not involved. This type may not have significant growth potential, which precludes the insertion of additional thicknesses of insulation.

4.8.2 LIQUID-TO-VAPOR PHASE CHANGE. (See Figure 4-25.) An approach using insulation combined with a liquid-to-vapor phase change in which the insulation is used to retard the heat flow from the radiative cover panel just as in the pure insulation case has been evaluated. Additional heat capacity between the insulation and the primary structure is provided by phase-change capability.

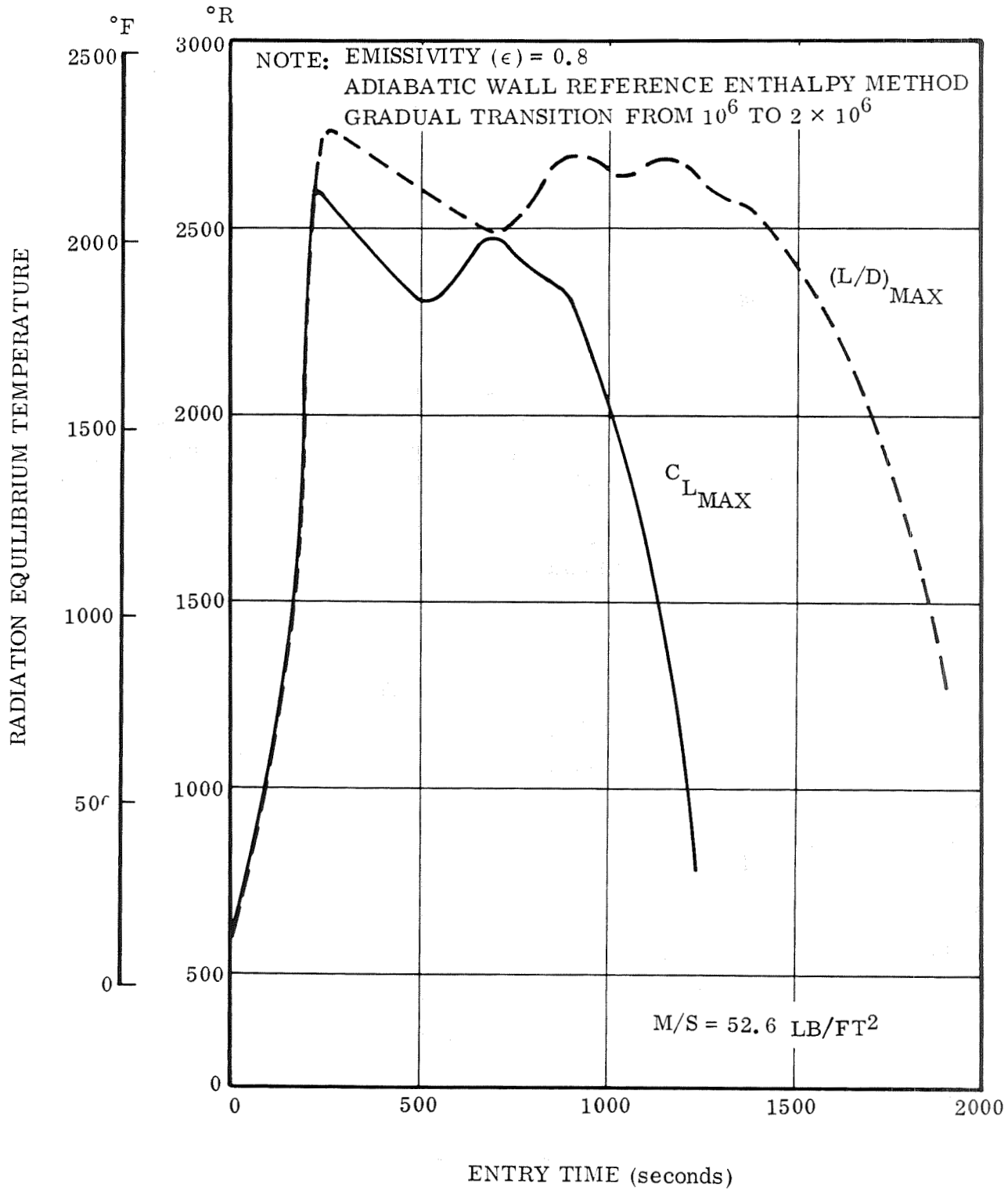

Figure 4-23. Temperature Histories on Nozzle Wall Outer Surface

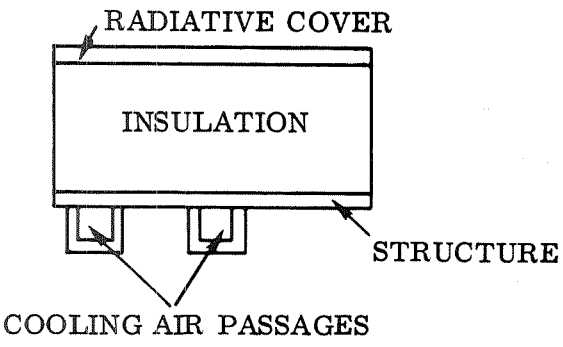

Figure 4-24. Insulation with Ground Air Cooling

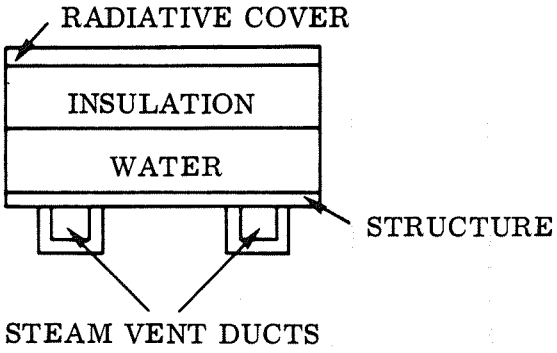

Figure 4-25. Liquid-to-Vapor Phase Change

Preliminary calculations were performed with water as the boiling material (1000 Btu/lb latent heat of vaporization). Table 4-4 shows the total insulation plus water weight required for a typical trajectory. For purposes of comparison, a 4.4-inch-thick insulation system that provides adequate protection to the structure during flight has a weight of 2.08 lb/ft^2. The water container weighs about 0.1 lb/ft^2.

The minimum system weight occurs at about two inches of insulation thickness. Further studies are required to identify the optimum insulation-water combination.

Table 4-4. Total Insulation Weight Plus Water Weight for a Typical Trajectory

	Insulation Thickness (Inches)			
	(4.4)	(3)	(2)	(1)
Dynaflex Weight (lb/ft^2)	1.01	0.86	0.86	0.69
Microquartz Weight (lb/ft^2)	1.07	0.66	0.28	--
Water Weight Required				
Before Landing (lb/ft^2)	0	0.14	0.36	0.91
After Landing (lb/ft^2)	0	0.10	0.05	--
Total Insulation, Water, & Container				
With Ground Air Cooling (lb/ft^2)	2.08	1.76	1.60	1.70
Without Ground Air Cooling (lb/ft^2)		1.86	1.65	1.70
ΔMass	0	-0.22	-0.43	-0.38

In this weight comparison with pure insulation approach, weight of the water-containment material and of the venting ducts required to carry away the water vapor was not included in the insulation-water total.

This approach also has the advantage of being completely passive. Flight safety is enhanced since it cannot fail during flight and cause overheating of the structure. Good growth potential is inherent because one lb/ft^2 of water can be contained in approximately 0.2 inch of thickness. This permits a 400 percent increase in the capacity to absorb heat with only an 0.8-inch increase in system thickness.

4.8.3 SOLID-TO-LIQUID PHASE CHANGE. (See Figure 4-26.) This approach is exactly the same as the liquid-to-vapor phase change, with the exception of the material used to absorb the energy. A preliminary study shows that this concept is less practical due to the relatively low latent heat of melting of materials that melt at the proper temperature (200°F or below). Additionally, the subsystem weights are prohibitive, and it offers no advantages.

4.8.4 ACTIVE COOLING LOOP. (See Figure 4-27.) An active cooling loop would be essentially a fin-tube radiator. Tubes carrying a heat-transport fluid are connected with high conductivity fins. If the primary structure can be used as the fin, with the tubes attached to it, the concept may be feasible. If the fin-tube arrangement must be separate from the primary structure, a severe weight penalty is imposed on the vehicle.

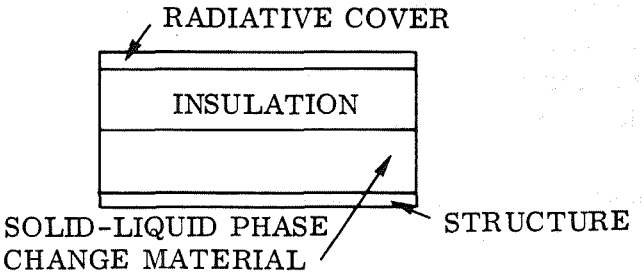

Figure 4-26. Solid-to-Liquid Phase Change

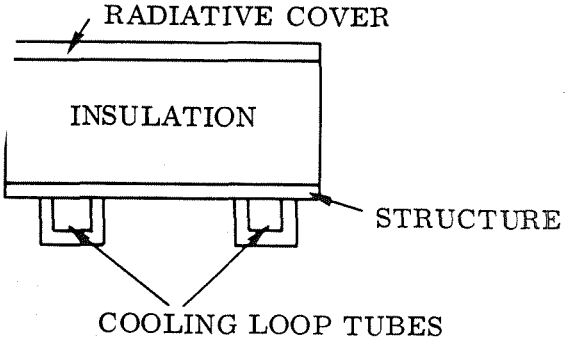

Figure 4-27. Active Cooling Loop

The critical item to be considered in this approach is the heat sink to be used. If propellant residuals can be used as a sink, the scheme remains viable. If a water boiler must be used, the water requirements will be approximately the same as for the liquid-to-vapor phase change approach. A weight tradeoff of pump weight, tube and transport weight, and pumping power versus the weight of the water containment device plus the steam ducting system of the liquid-to-vapor phase change approach

would be needed to determine which was lighter. A preliminary estimate indicates that the active loop concept would probably be heavier.

This approach has limited growth potential in that the tube size is fixed, and an attempt to move a larger volumetric flow through the tube will result in excessive pressure losses. A failure of the pumping subsystem early in entry could lead to dangerous overheating of the primary structure during flight.

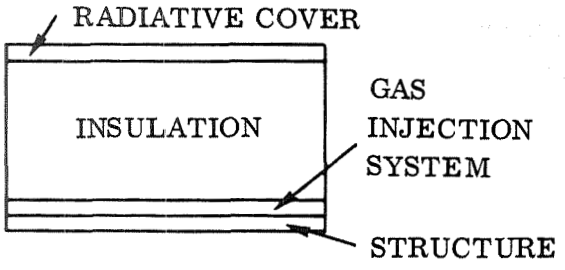

Figure 4-28. Gas Injection Through Insulation Model

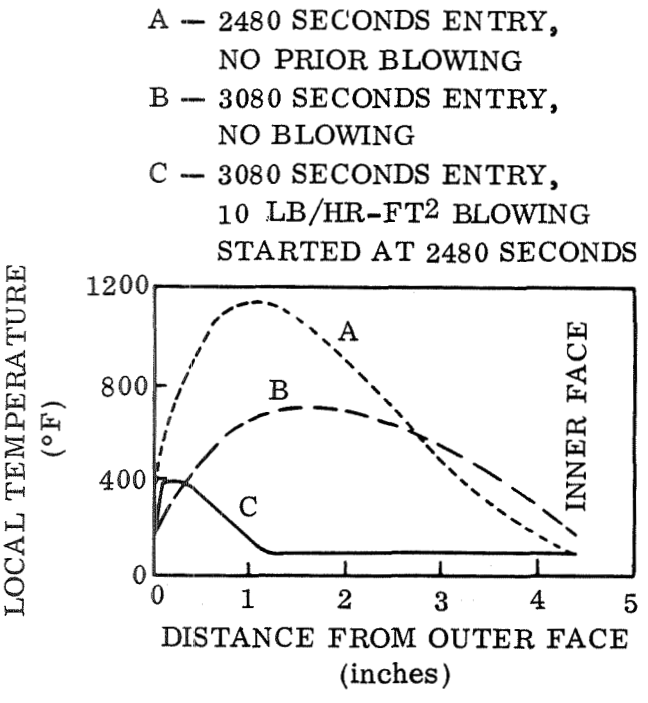

Figure 4-29. Gas Injection Through Insulation

4.8.5 GAS INJECTION THROUGH INSULATION. (See Figure 4-28.) A relatively cold gas can be blown through the insulation, from the inside to the outside, to provide cooling to the insulation and prevent the heat soak-back to the primary structure. Preliminary calculations show that an air blowing rate of 10 lb/ft^2-hr for the last 600 seconds of a typical trajectory (a total gas flow of 1.66 lb/ft^2) cools the insulation sufficiently to prevent heat soak-back to the structure. (See Figure 4-29.)

Ram-air could be used as the injected gas. At the time cooling is required, the recovery temperature of the air is generally low enough to make it attractive as a coolant. Further studies will be necessary to explore the potential of this concept completely.

An approach of this type has excellent growth capability, especially when ram-air is considered as the coolant. If ram-air is used as a coolant, the method is inherently safe.

4.9 ATMOSPHERIC DISPERSIONS

A preliminary analysis of effects of dispersions in atmospheric density on ascent and entry aerodynamic heating was made. Preliminary radiation equilibrium temperatures for several locations on an early orbiter concept are presented for the ascent trajectory.

A peak temperature on the nose of 3680°R (3220°F) was obtained using the 1962 standard atmosphere. The effect of a $+3\sigma$ dispersion in atmospheric density increased the peak temperature to about 3855°R (3395°F), a temperature increase of 175°R(°F).

A velocity/density trajectory will be flown during entry, and normal atmospheric dispersions should have little effect on heating rates. Abnormal local density gradients could cause abrupt changes in heating rates depending on vehicle ability to fly the density gradient. Further work is required in this area to determine the nature and magnitude of these gradients and their effect on vehicle temperature and aerodynamic performance.

4.9.1 ASCENT. The boost trajectory presented in Figure 4-30 was used in calculating radiation equilibrium temperatures for several locations on the orbiter. The vehicle locations used, and the methods used in the computer program, are presented in Table 4-5.

It is expected that the shuttle will fly a fixed velocity/altitude ascent trajectory regardless of the local atmospheric conditions. Using this assumption, radiation equilibrium temperatures were obtained for both the 1962 U.S. Standard Atmosphere and a dispersed atmosphere based on the $+3\sigma$ dispersions presented in Figure 4-31.

The results of these calculations are presented in Figures 4-32, 4-33, and 4-34 for the nose, lower surface, and upper surface respectively. Maximum temperatures occur, of course, at the stagnation point. A peak temperature of about 3680°R (standard atmosphere) occurs at the end of the boost trajectory (365 seconds after launch) as shown in Figure 4-32. Extension of the boost trajectory (i.e., transfer to orbital altitude at essentially constant velocity) would yield decreasing radiation equilibrium temperatures. An increase in temperature of about +175°R occurred at 365 seconds after launch as a result of using the $+3\sigma$ atmospheric dispersions.

Peak radiation equilibrium temperatures for the vehicle lower and upper surface locations used increased by about 80°R when using the dispersed atmosphere as shown in Figures 4-33 and 4-34. Another effect of the dispersed atmosphere was to delay boundary layer transition at a given vehicle station such that it occurred later in the trajectory when compared to the standard atmosphere. Transitional boundary layer heating was assumed to occur at Reynolds numbers between 1.0×10^6 and 2.0×10^6.

4.9.2 ENTRY. During entry, it is expected that the vehicle will fly a velocity/density trajectory. The result of this type of entry will essentially eliminate variations in entry heating rates caused by normal atmospheric dispersions.

Table 4-5. Vehicle Location and Calculation Method

Location	Method*
Nose - Station 0.0 ft	2.0 ft Diameter Sphere, $\epsilon = 0.80$
Lower Surface - Station 10.0 ft	Tangent Wedge, 14.5° Body Angle, $\epsilon = 0.85$
Lower Surface - Station 100.0 ft	Tangent Wedge, 0° Body Angle, $\epsilon = 0.85$
Upper Surface - Station 10.0 ft	14.5° Half-Angle Cone, $\epsilon = 0.85$
Upper Surface - Station 100.0 ft	Flat Plate, $\epsilon = 0.85$

*The low entropy, adiabatic wall turbulent boundary layer solution was used for the tangent wedge, cone, and flat plate problems.

Abnormal density gradients and a slow vehicle response time could conceivably place the vehicle in a local high-density region at higher than normal velocities and thus higher heating rates and temperatures would be experienced. Numerous atmospheric density measurements have been made in the past by using the falling sphere method. Some of these flights have shown local density gradients. A typical case is that presented in Figure 4-35, where the measured density is plotted and compared to the 1962 U.S. Standard Atmosphere. For this flight, a rapid increase in density occurred as the altitude decreased from about 278,000 to 275,000 feet. Unfortunately, the accuracy of the data for altitudes above 250,000 feet is questionable due to possible error of the accelerometers used. Whether the data presented in Figure 4-35 is actually representative of density gradients that could be encountered at these altitudes, or simply data scatter is unknown. Additional effort is required in this area to 1) determine the type and magnitude of the density gradients in the altitude range of interest, 2) set up a model atmosphere including the worst-case density gradients from an aerodynamic heating standpoint, and 3) determine the net effect on vehicle heating.

4.10 BASE HEATING

The configurations have clustered rocket propulsion arrangements which, when operating, produce a severe base heating environment. Preliminary thermal environmental data for the base region is required to establish a base area design configuration that can be integrated into the space shuttle.

A literature survey indicated there is no readily available analytical thermodynamic treatment in the simulation of base heating. Vehicle design data is based on model or full-scale testing. Therefore, since the vehicle base configuration has not been firmly defined, experimental and empirical base heating data from numerous applicable vehicles were investigated. Preliminary design data was estimated.

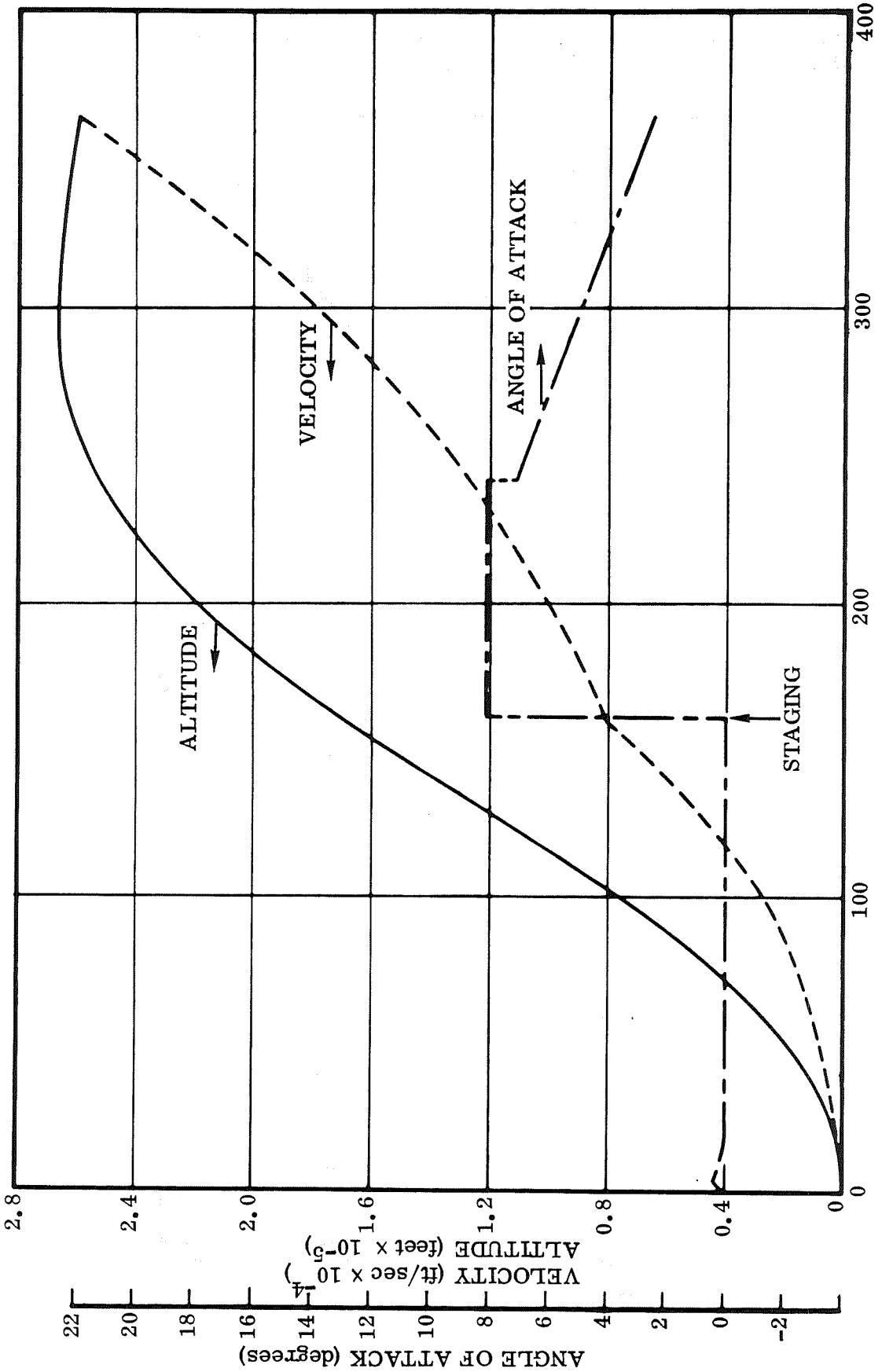

Figure 4-30. FR-1 Boost Trajectory -- Polar Orbit

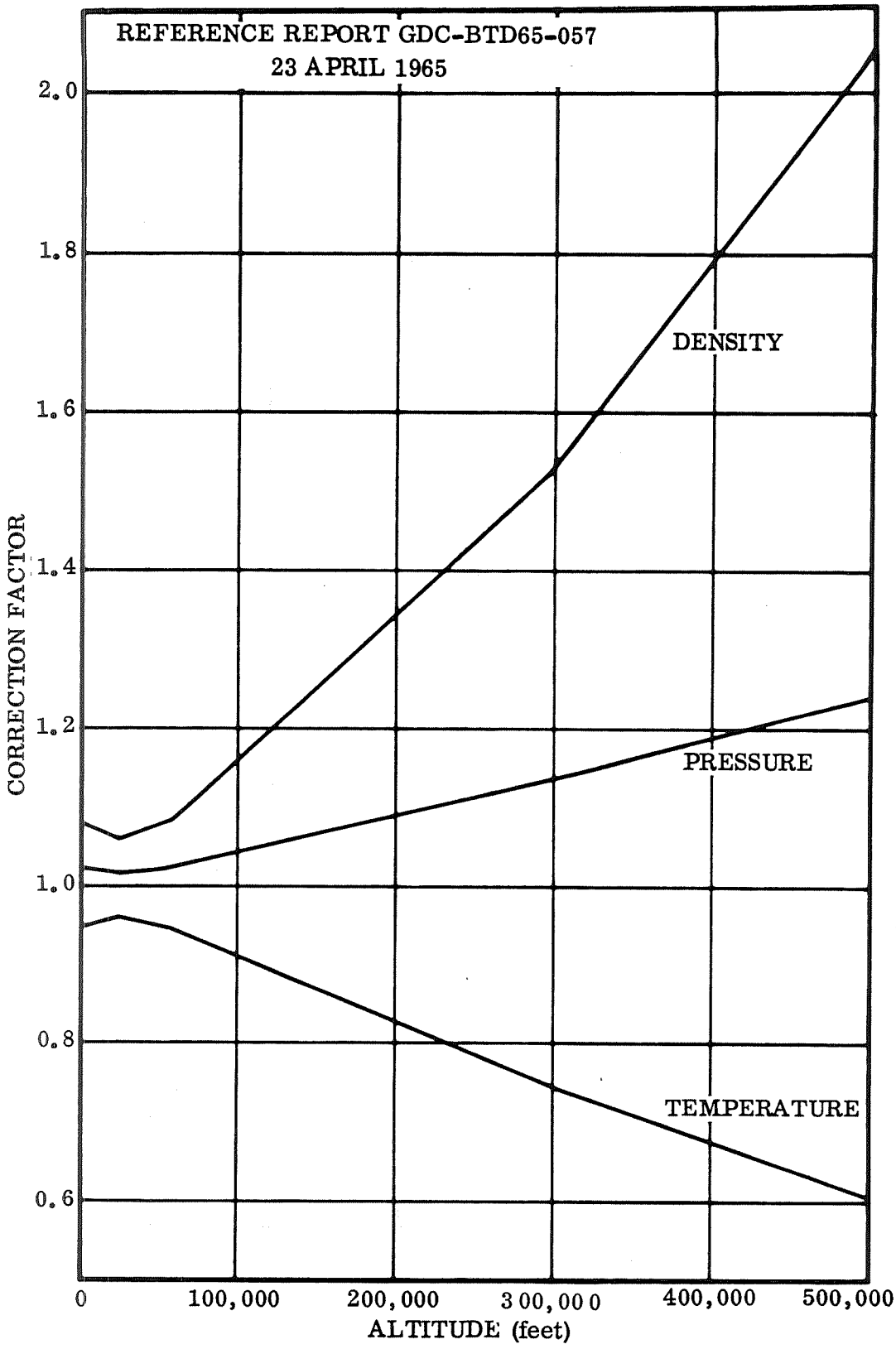

Figure 4-31. Atmospheric Dispersions

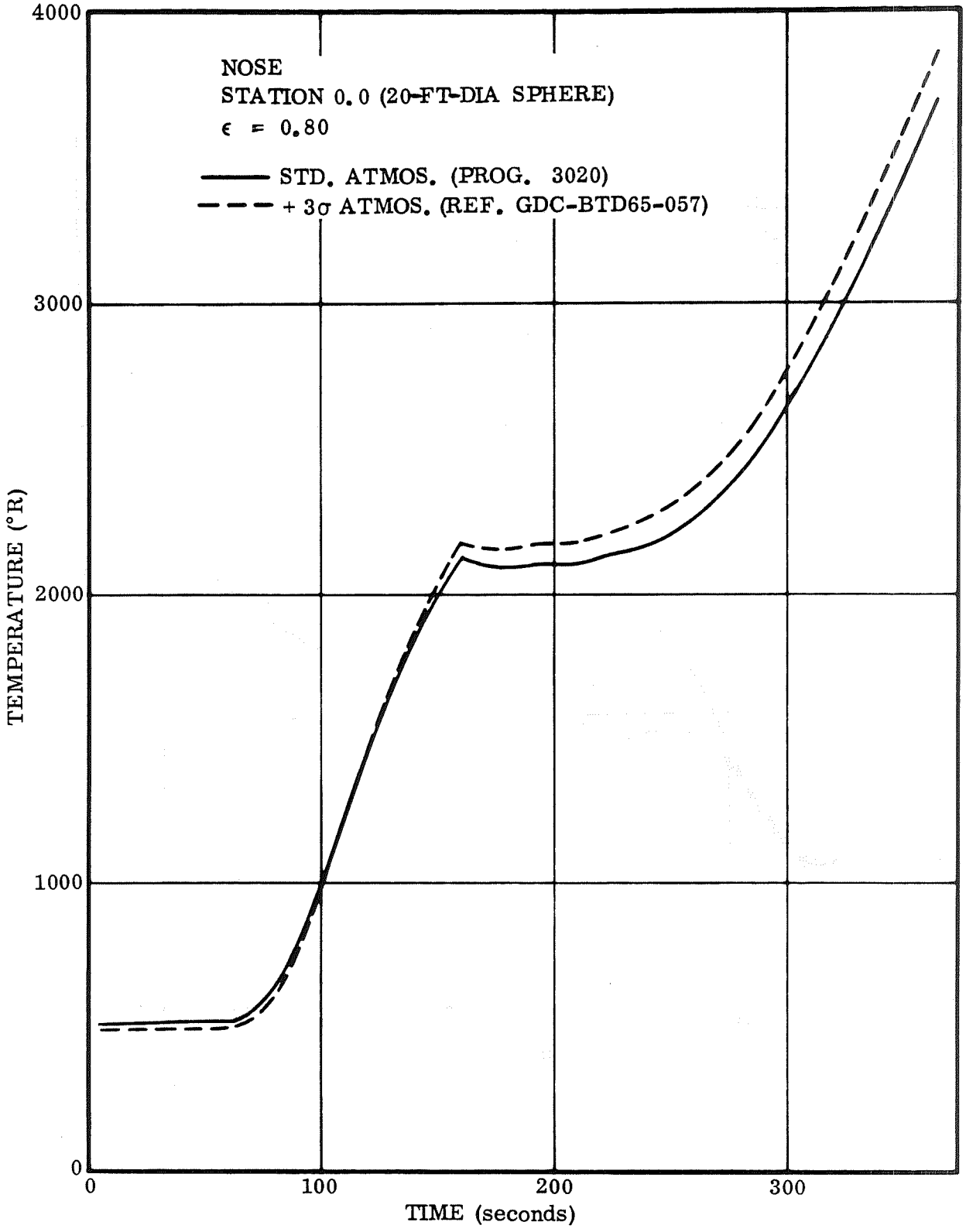

Figure 4-32. Radiation Equilibrium Temperature Versus Time at Nose

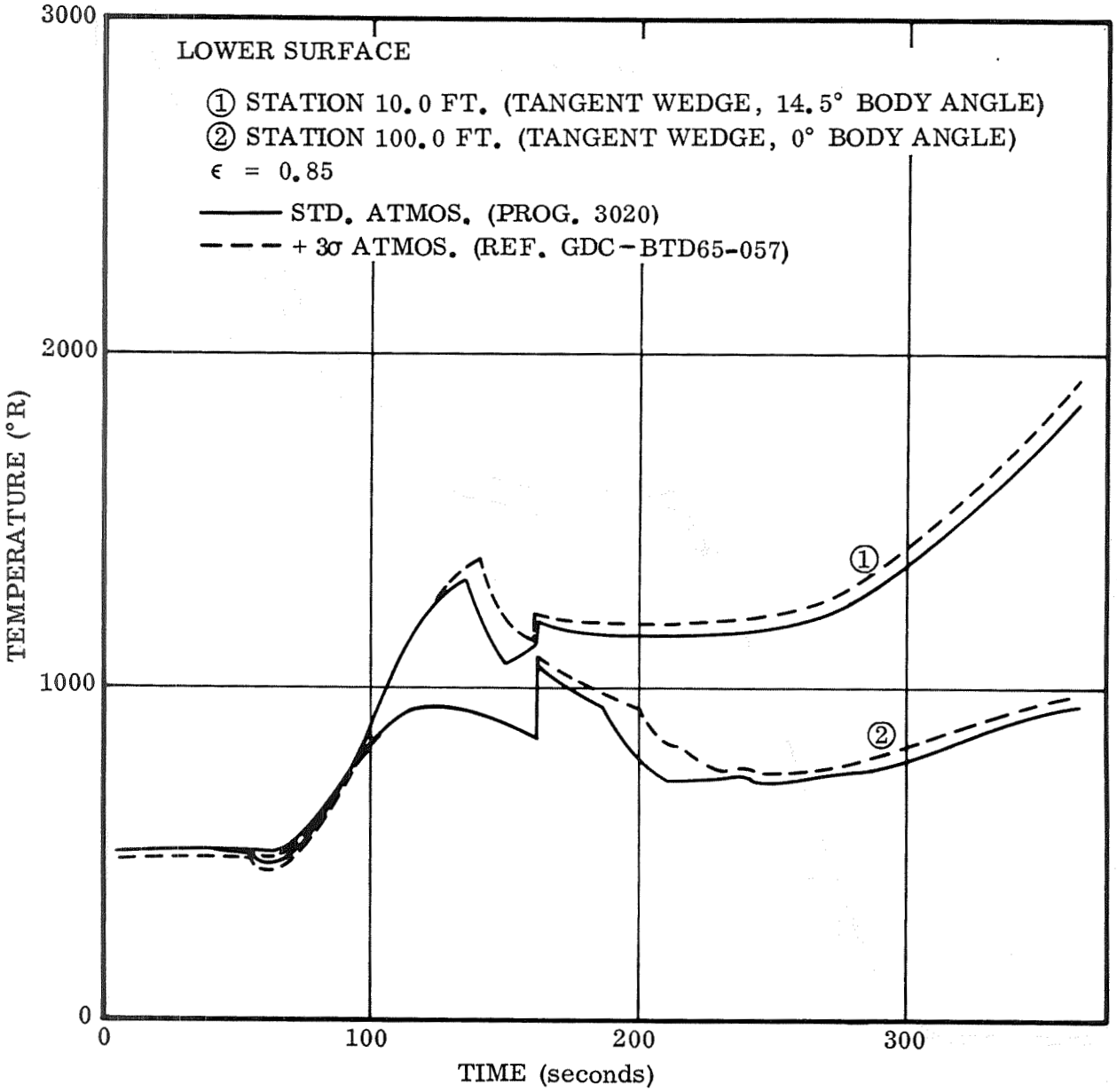

Figure 4-33. Radiation Equilibrium Temperature Versus Time at Lower Surface

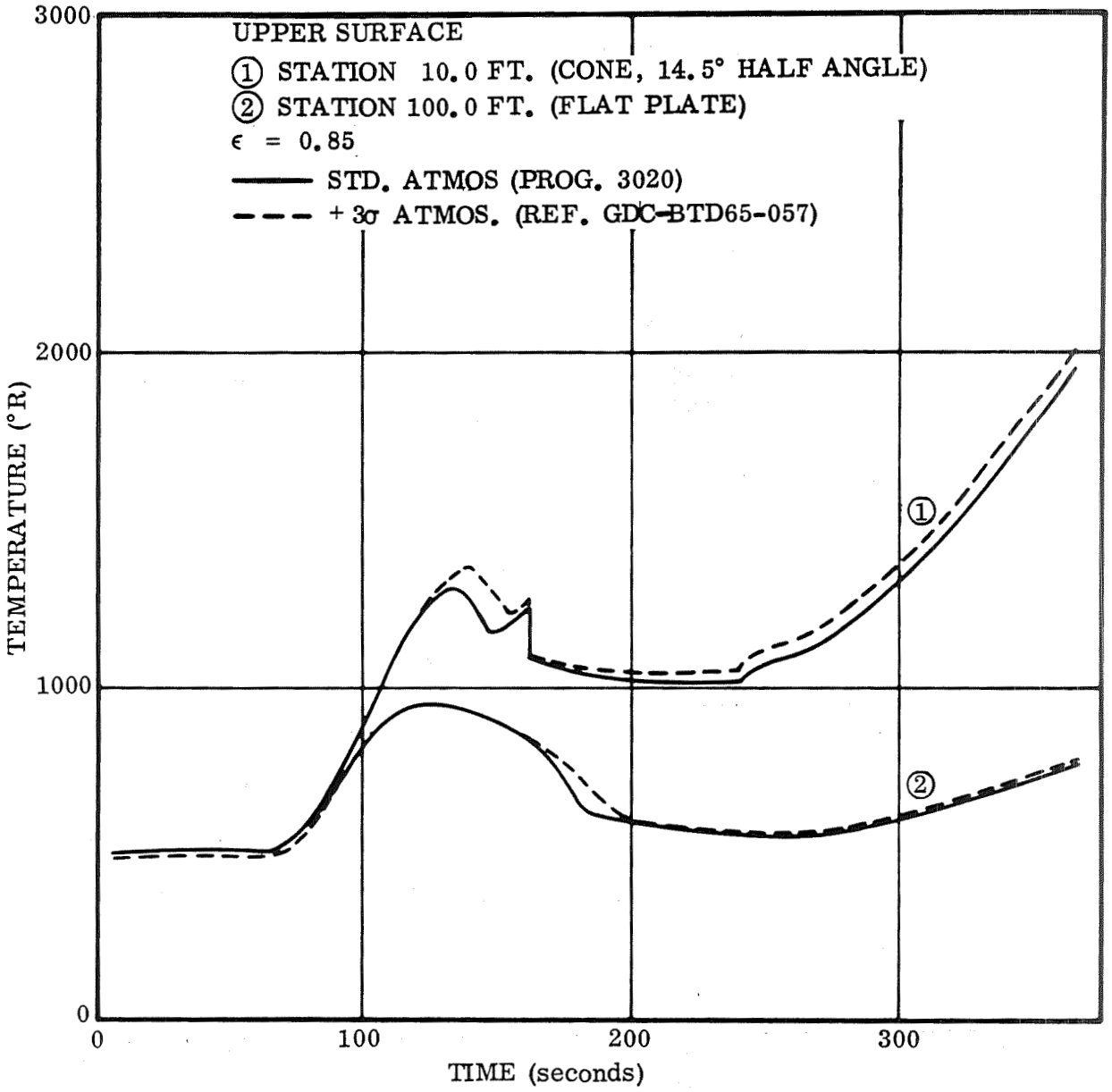

Figure 4-34. Radiation Equilibrium Temperature Versus Time at Upper Surface

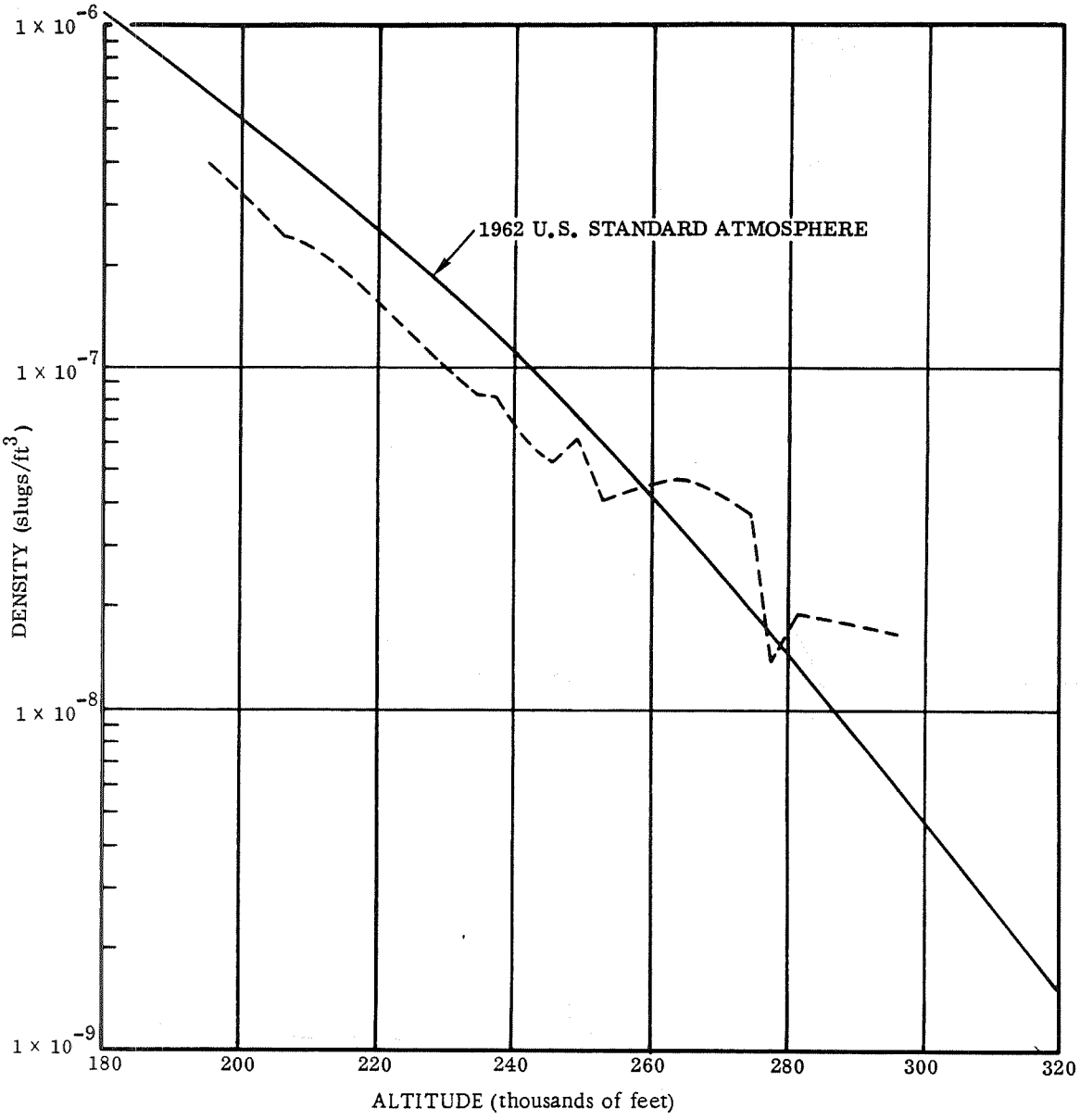

Figure 4-35. Density Versus Altitude

The total base heat rate is composed of convective and radiant heating rates. In a hydrocarbon fuel propulsion system, such as Atlas or Saturn first stage, a significant amount of the base heating is attributed to solid particle radiation and impingement. The space shuttle has a hydrogen fuel propulsion system; therefore, gaseous convection is the primary base heating source because of the absence of the solid carbon particles. The data shows the base heating rate to increase with time because of the exhaust jet expansion with altitude. The maximum heating rate is produced from jet interaction, recirculation, and jet expansion due to the altitude and maximum amount of side flow. At approximately 85 seconds after launch, the maximum heating rate of 25 Btu/ft^2/sec will occur in the base cavity; during the remainder of ascent, this heating rate will be essentially constant.

4.11 REFERENCES

4-1 "Heat Transfer to Satellite Vehicles Reentering the Atmosphere", N. H. Kemp and F. R. Riddell, Jet Propulsion, Vol. 26, No. 12, December 1956.

4-2 Approximations for the Thermodynamic and Transport Properties of High Temperature Air, C. F. Hansen, NASA TR R-50, 1959.

4-3 A Description of the Revised Aerodynamic/Structural Heating and Radiation Equilibrium Temperature Computer Program 3020, R. S. Scullen, Convair report GDC-ERR-1336, December 1968.

4-4 An Experimental Study of the Pressure and Heat Transfer Distribution on a 70° Sweep Slab Delta Wing in Hypersonic Flow, M. H. Bertram and P. E. Everhart, NASA TR R-153, December 1963.

4-5 Comparison of Measured and Calculated Turbulent Heat Transfer on the X-15 Airplane at Angles of Attack up to 19.0°, R. D. Quinn and M. Politz, NASA TM X-1291, September 1966.

4-6 Advanced Re-entry Systems Heat-Transfer Manual for Hypersonic Flight, A. C. Thomas, et al, Air Force Flight Dynamics Laboratory Technical Report HFFDL-TR-65-195, October 1966.

4-7 Transitional Boundary Layer Considerations for the Heating Analysis of Lifting Re-entry Vehicles, M. Masaki and J. Yakura, AIAA Paper 68-1155, December 1968.

4-8 Variable Boundary II Heat Conduction Program, R. F. O'Neill, et al, Convair report GDC-BTD67-004A, 5 September 1968.

4-9 Recent Experiments in Hypersonic Turbulent Boundary Layers, M. H. Bertram and L. Neal, NASA TMX-56335, May 1965.

4-10 Investigations of Turbulent Heat Transfer at Hypersonic Speeds, R. T. Savage and C. L. Jaeck, AFFDL-TR-67-144, Air Force Flight Dynamics Laboratory, December 1967.

SECTION 5

LOAD ANALYSIS

Loads for major FR-1, FR-3, and FR-4 vehicle structural components presented in this section include body, wing, fin, and landing gear loads for various ground and flight conditions. Net body loads were initially determined for an early FR-1 configuration (Convair T-15A), and the final FR-1 net body loads were then derived by conversion factors (since the configurations were very similar). The net loads were determined by computer programs that handle airload and mass distributions, cruise and booster thrust vectors, concentrated loads, and translational and rotational inertias. The vehicle is in quasi-static equilibrium in all cases. Rigid body analysis was used. Details relative to airloads, mass distributions, and net loads are given in the following paragraphs.

5.1 FR-1 AND FR-4 LOADS

Since loads for the FR-1 and FR-4 vehicles are essentially the same, only the FR-1 vehicle will be referred to in the following discussion.

5.1.1 AIRLOADS. Vehicle airloads were obtained for conditions of maximum boost dynamic pressure, subsonic cruise gust, landing, and launch pad ground winds.

The loading distribution for a single vehicle element subjected to a surface wind speed envelope of 99 percentile for Eastern Test Range (ETR) is shown in Figure 5-1 at the end of this section. The surface winds are assumed to act normal to the longitudinal axis of the vehicle on the launch pad and to be from the most critical direction.

Figure 5-2 presents the normal force loading distribution and Figure 5-3 presents the drag load distribution for the maximum dynamic pressure (α q) condition, which occurs during the boost portion of flight. The wind and wind shears encountered by the vehicle represent all-directional 99 percentile conditions at ETR. Loading is for a maximum α q of 4000 psf-deg, which occurs at 34,940 feet in altitude and 70.81 seconds from liftoff. Engine-out conditions were also investigated and yielded α q values smaller than 4000 psf-deg. Since the maximum α q loads were computed for the most severe wind direction condition, the vehicle has an all-azimuth launch capability.

Figure 5-4 presents the normal force loading distribution and Figure 5-5 presents the drag load distribution for the subsonic gust condition. The gust considered was a 50 ft/sec sharp-edge gust as specified in MIL-SPEC-8861. Loadings on the wing, fin, and body are included.

5.1.2 MASS DISTRIBUTIONS. The mass distributions used in the calculation of net body loads for a single element were those for the dry weight and propellant weight corresponding to each of the conditions analyzed.

5.1.3 NET LOADS. Due to similarities in trajectory, aerodynamic shape, and mass distribution between the final FR-1 and the Convair T-15A vehicles, net body loads for the FR-1 vehicles were obtained from the existing T-15A loads multiplied by appropriate conversion factors for each condition. Four basic factors were used for this purpose: vehicle weight ratio (K_W), vehicle length ratio (K_L), vehicle diameter ratio (K_D), and maximum boost dynamic pressure ratio (K_q). Loads for the wing, fin, and landing gear were obtained directly for the FR-1 vehicles.

a. Body Net Loads. Net limit loads for the body were determined for various ground and flight conditions, including ground winds, maximum αq, maximum βq, booster burnout, subsonic gust, and landing. Net axial and shear loads for the FR-1 were obtained by multiplying the T-15A loads by K_W. Torsion and bending moments of the T-15A were multiplied by the products ($K_W K_D$) and ($K_W K_L$), respectively, to obtain FR-1 torsion and bending moments. Peak load intensities N_x due to the combined effects of axial loads and bending moments were multiplied by a factor (K_{N_x}) depending on the four basic factors as shown in Note 4 of Table 5-1. The appropriate conversion factors for each load condition are presented in Table 5-1. These factors were used in conjunction with the T-15A net loads shown in Figures 5-6 through 5-16 and applicable dynamic amplification factors to generate limit design loads for the body structure of FR-1 vehicles. The plots of Figures 5-15 and 5-16 include the effects of internal pressure in the integral tanks; i.e., 23.0 psi in LO_2 tanks, 28.5 psi in LH_2 tanks during boost, and 2.0 psi in all tanks during subsonic gust and landing conditions. These two figures indicate that the critical design conditions for most of the body structure are ground winds (unpressurized tanks), subsonic gust, booster burnout, or maximum αq in combination with the quoted internal pressures. The criticality of the various loading conditions in relation to each major structural component is discussed in more detail in Section 6.

b. Wing Net Loads. The critical design condition for the wing is the subsonic gust condition. The wing used with the FR-1 configuration had the following characteristics (one panel only):

Exposed plan area	880 ft^2
Plan taper ratio	0.8
Structural span	822 in. (pivot to tip)
Thickness ratio	0.21 (root) to 0.18 (tip)
Incidence	6 deg (reference body lower surface)

The wing, with deployed flaps, was used to determine ultimate shear, bending, and torsional loads. Plots of these net ultimate loads along the wing structural span are shown in Figure 5-17 for the orbiter vehicle with payload, which is critical. The torsional moments were conservatively determined by assuming the center of pressure to be ahead of the wing box elastic axis a distance equal to 10 percent of the unflapped wing chord. The subsonic gust loads generate a load factor equal to 2.32 g (limit) at the vehicle's center of gravity.

c. Fin Net Loads. The critical load condition for the FR-1 fins is at maximum αq. Net ultimate shear, bending moments, and torsional moments along the fin's 44 percent chord line are shown in Figure 5-18. The torsional moments were determined conservatively by assuming the airload center of pressure to be behind the elastic axis a distance equal to 6 percent of the chord at each fin station. The rudder airload at maximum αq is 101,500 pounds ultimate, normal to the rudder surface. Since the rudders are used as elevators during landing to maintain a nose-up attitude, down airloads on the tail must equal 98,000 pounds for a two-point landing and 67,000 pounds for a three-point landing.

5.1.4 LANDING GEAR LOADS. Two-point and three-point landing load histories for the FR-1 main and nose landing gears are presented in Figures 5-19 and 5-20. These loads are for a 12 ft/sec touch-down sink speed, using a rigid-body analysis. The fin rudders are used as elevators to maintain a nose-up attitude after touchdown.

5.2 FR-3 LOADS

Net loads were determined for two FR-3 vehicle configurations. These configurations are differentiated by the orbiter position relative to the booster: nose-to-nose or tail-to-tail.

The net loads presented herein are net body shears, bending moments, and axial loads for various ground, flight, and landing conditions. All loads shown in this section are limit. The net loads were determined by computer programs, which handle airloads and mass distributions, cruise and booster thrust vectors, concentrated loads, and translational and rotational inertia loads. Rigid body analysis was used and the vehicles are in quasi-static equilibrium in all cases. Details relative to airloads, mass distributions, and net loads are given in the following paragraphs.

5.2.1 AIRLOADS. Vehicle airloads were obtained for conditions of maximum boost dynamic pressure, subsonic cruise gust, landing, and launch pad ground winds. The surface winds were assumed to act normal to the longitudinal axis of the vehicle on the launch pad and to be from the most critical direction. The winds were 99 percentile surface wind speed envelopes for ETR. The maximum boost dynamic pressure loads were obtained by a three-degree-of-freedom simulation with control system of the vehicle. The vehicle was flown through 99 percentile Marshall synthetic winds for the most critical direction, with the peak gust occurring at maximum dynamic pressure.

The subsonic cruise gust loads were for a 50 ft/sec sharp-edge gust as specified in MIL-SPEC-8861. Airloads on the wing, fin, and body were determined. The landing loads are for a 12 ft/sec touchdown landing speed and a rigid body. Both two-point and three-point attitude conditions were considered.

All airloads are for a rigid body. The maximum dynamic pressure loads were computed for an elastic body and the elastic body amplification factor was found to be 1.026. The first bending frequency for this class of vehicles was found to be between 3.0 and 3.5 cps.

5.2.2 MASS DISTRIBUTIONS. The mass distributions used in the calculation of net loads were those for the dry weight and the propellant weight corresponding to each of the conditions analyzed.

5.2.3 NET LOADS. Net loads for the body were determined for various ground and flight conditions. These include ground wind, maximum αq, booster burnout, subsonic gust, and landing. Plots of net axial loads, shears, and bending moments for these conditions are shown in Figures 5-21 through 5-32 for both the orbiter and the booster of each configuration. Subsonic gust and two-point landing loads shown in Figures 5-29 through 5-32 are typical of all configurations. To visualize the effects of configuration on loads, plots of net axial loads and net bending moments for the maximum αq and booster burnout conditions are presented in Figures 5-33 through 5-38 for both orbiter and booster vehicles. Peak compression load intensities were also plotted for the nose-to-nose and tail-to-tail configurations to enable identification of critical load conditions. These plots include the effects of internal pressure in the orbiter's integral tanks and are shown in Figures 5-39 through 5-42.

5.3 GIMBAL ANGLE REQUIREMENTS

The control of a space shuttle system during launch can be accomplished using thrust vector, aerodynamic surfaces, and thrust modulation. This section is a brief analysis of the advantages and disadvantages of each type of approach. The analysis was performed for the FR-1, FR-3, and FR-4 space shuttle configurations concepts. During the boost phase, the attitude control subsystem corrects for aerodynamic moments produced by winds and for thrust moments produced by off-thrust-axis centers of gravity.

Simulated flights using 99 percentile winds have demonstrated the need for engine gimbaling. Gimbal requirements (in degrees) for each configuration are:

		Requirements				
Configuration	Cant Angle	Gimbal Angle*	Liftoff	Max αq	Burnout	One-Engine-Out
FR-1 and FR-4	0	±5	±0.1	3	±0.1	5
FR-3	8	±5	-3.8	4	3.5	4.5

*Gimbal angle is the engine rotation about the cant angle.

These requirements are dictated by 1) engine-out, 2) center of gravity offset, and 3) maximum αq conditions. A unique feature that heavily influences the gimbal angle requirement is that all vehicles under consideration are aerodynamically stable throughout the boost phase of flight. With an aerodynamically stable vehicle, maximum αq loads can be relieved by limiting the gimbal angle. For the limited gimbal angle conditions at maximum αq, the vehicle weather-cocks (rotates into the wind) to reduce the angle of attack, thereby reducing airloads on the vehicle. The gimbal angle requirements were established by limiting the attitude error (command attitude minus actual attitude) to less than three degrees. This gimbal angle limiting is unconventional when compared to the control subsystems on operational unstable boost vehicles, where a gimbal angle limit can produce a catastrophic failure and load relief can only be provided by sophisticated control subsystem electronics.

Figure 5-43 is a block diagram of the boost phase control subsystem. Rate and attitude feedback were used with provisions for a filter. Since this analysis was for a rigid body, no filter was used. Preliminary bending frequency analysis indicates that the first bending frequencies for these configurations lie between 3.0 and 4.0 cps. In the forward loop, proportional and integral control was used. The gimbal actuator was considered first order with rate and acceleration limits imposed.

Simulated three-degree-of-freedom flights were run for various gimbal angle rate and acceleration limits. The combinations used and the resulting stability states are:

	$\ddot{\delta}$ rad/sec^2				
$\dot{\delta}$ deg/sec	5	10	15	20	25
5	Limit Cycle	Limit Cycle	Limit Cycle	Limit Cycle	Limit Cycle
10	Limit Cycle	Stable			
15	Limit Cycle		Stable		
20	Limit Cycle			Stable	
25	Limit Cycle				Stable

The limit cycle oscillations occurring at the low rates and acceleration are due to the nonlinearities in the second-order system and the displacement errors introduced by wind disturbance. The results of the study show that the minimum gimbal angle rate is 10 deg/sec and the minimum acceleration is 10 rad/sec. These minimums are for no-limit-angle operation.

5.3.1 DIFFERENTIAL THRUST. For the FR-1 and FR-4 booster vehicle, 9.25 percent differential thrust on each engine produces a pitch moment equivalent to that generated by one degree of gimbal angle. For the orbiter element, 33.9 percent differential is equivalent to one degree of gimbal angle. Figure 5-44 presents the geometry used for these computations. Of course, no yaw or roll moments can be produced by differential thrust. For a required five-degree gimbal angle deflection, 46.25 percent differential thrust would be needed for the clustered configuration. The large differential thrust needed makes it impractical to consider differential thrust alone for attitude control. For the FR-3 vehicle, the large offset center of gravity make differential thrust control impractical.

5.3.2 AERODYNAMIC CONTROL. Aerodynamic control surfaces have been sized for entry, cruise, and landing operations. During these phases of operation, the vehicles are in the single element mode and the main LH_2 and LO_2 tanks are empty. Consideration was given to using these surfaces for control during the boost phase of flight. Figure 5-45 presents the time history of the ratio of aerodynamic control surface deflection to an equivalent degree of gimbal angle deflection. At 70 seconds of flight, this ratio is minimum at 5. That is, five degrees of aerodynamic surface is equivalent to one degree of gimbal angle. The surfaces are totally ineffective at launch, and even at 20 seconds the ratio is 37. Aerodynamic control is useful only from 50 seconds after launch to 90 seconds after launch because of the slow rise of dynamic pressure at lower altitudes and the rapid decay of dynamic pressure at the higher altitudes.

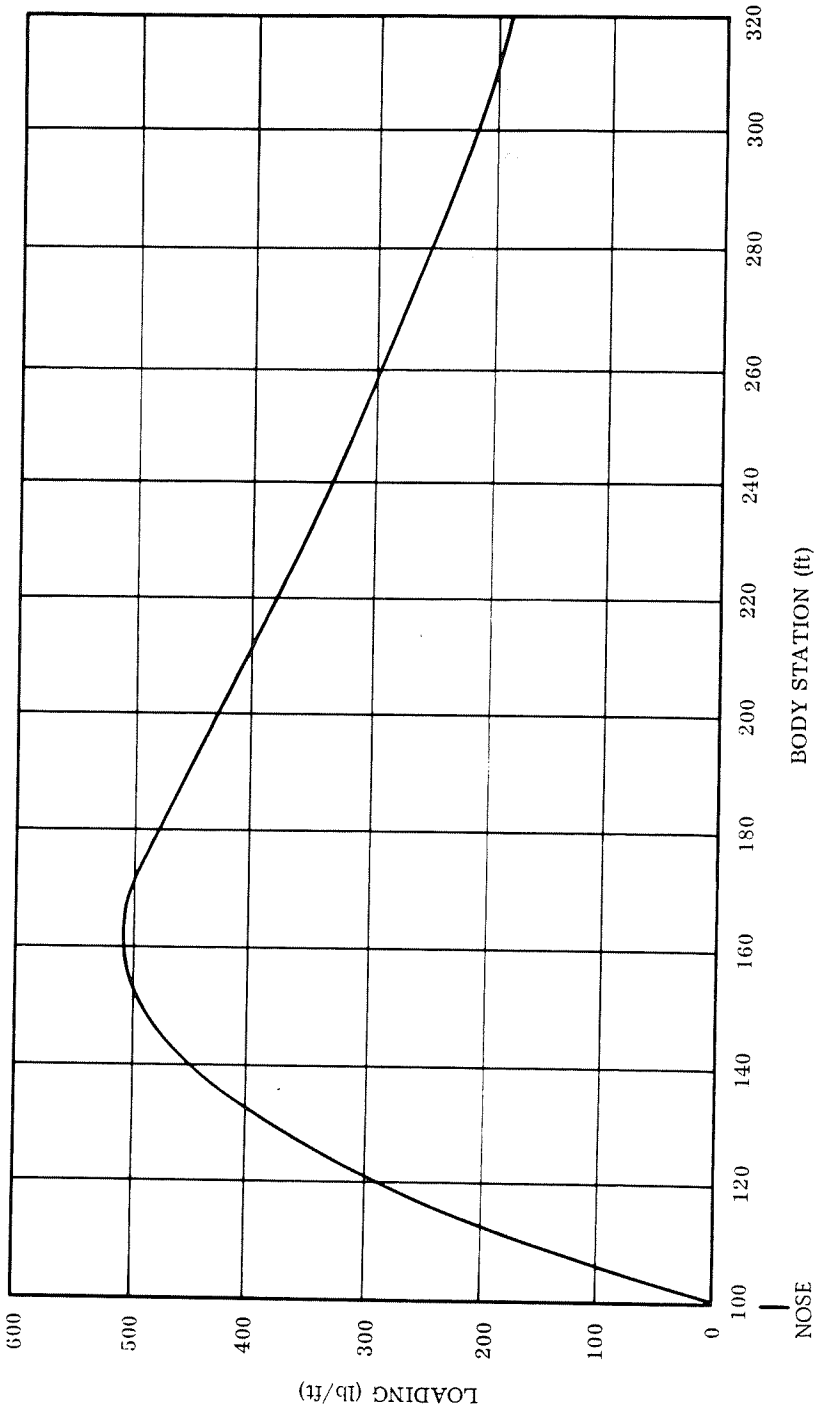

Figure 5-1. Ground Wind Loads

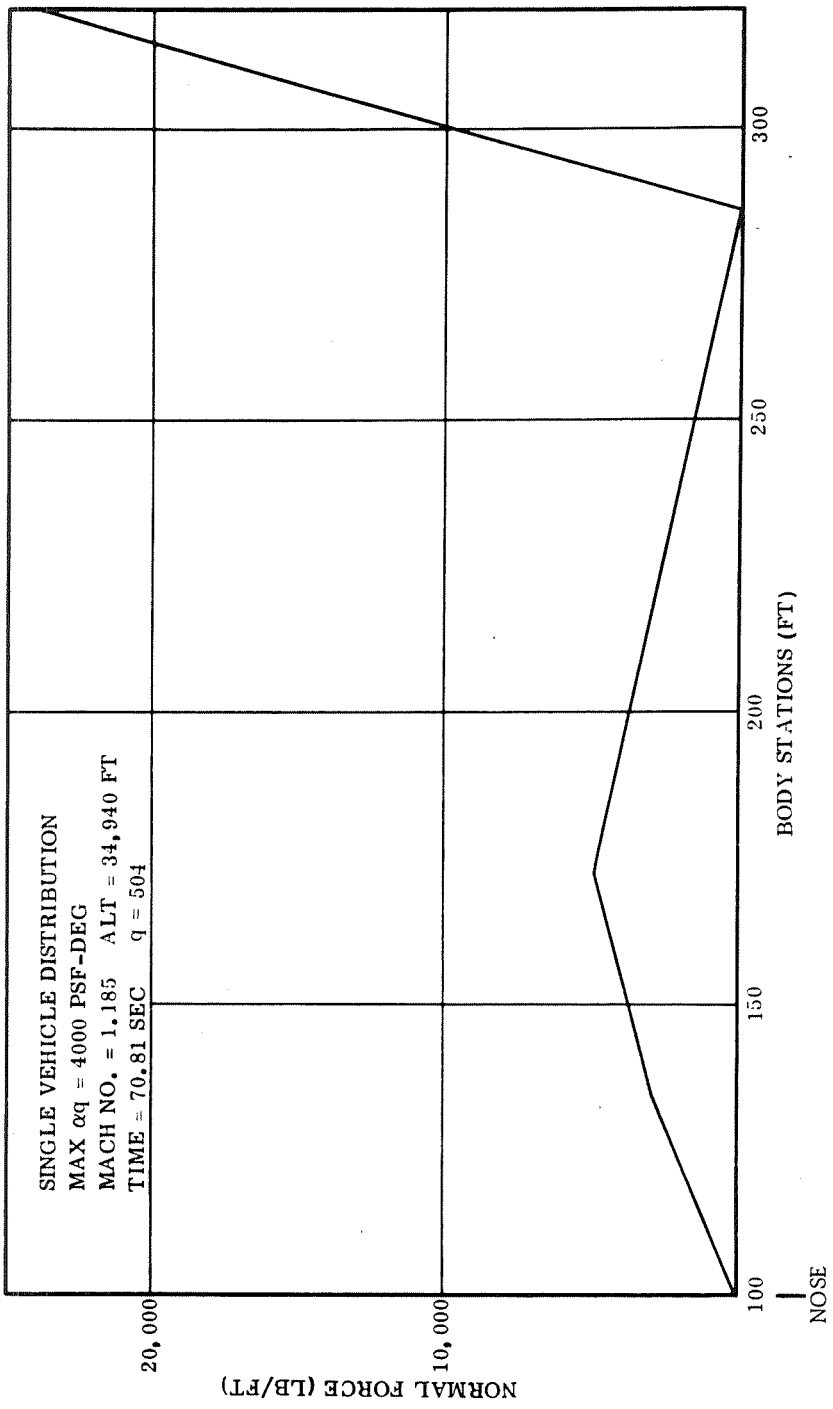

Figure 5-2. Launch Configuration Loads at Maximum α q Condition

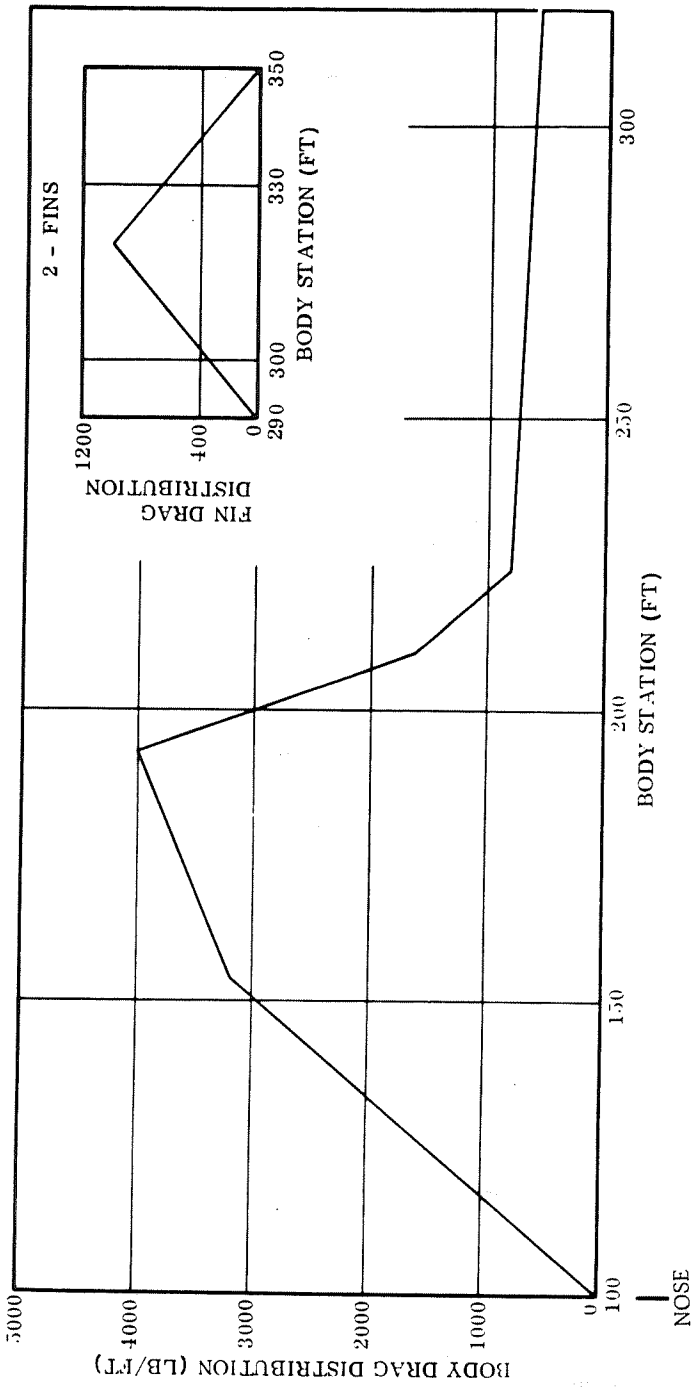

Figure 5-3. Drag Distribution at Maximum αq Condition

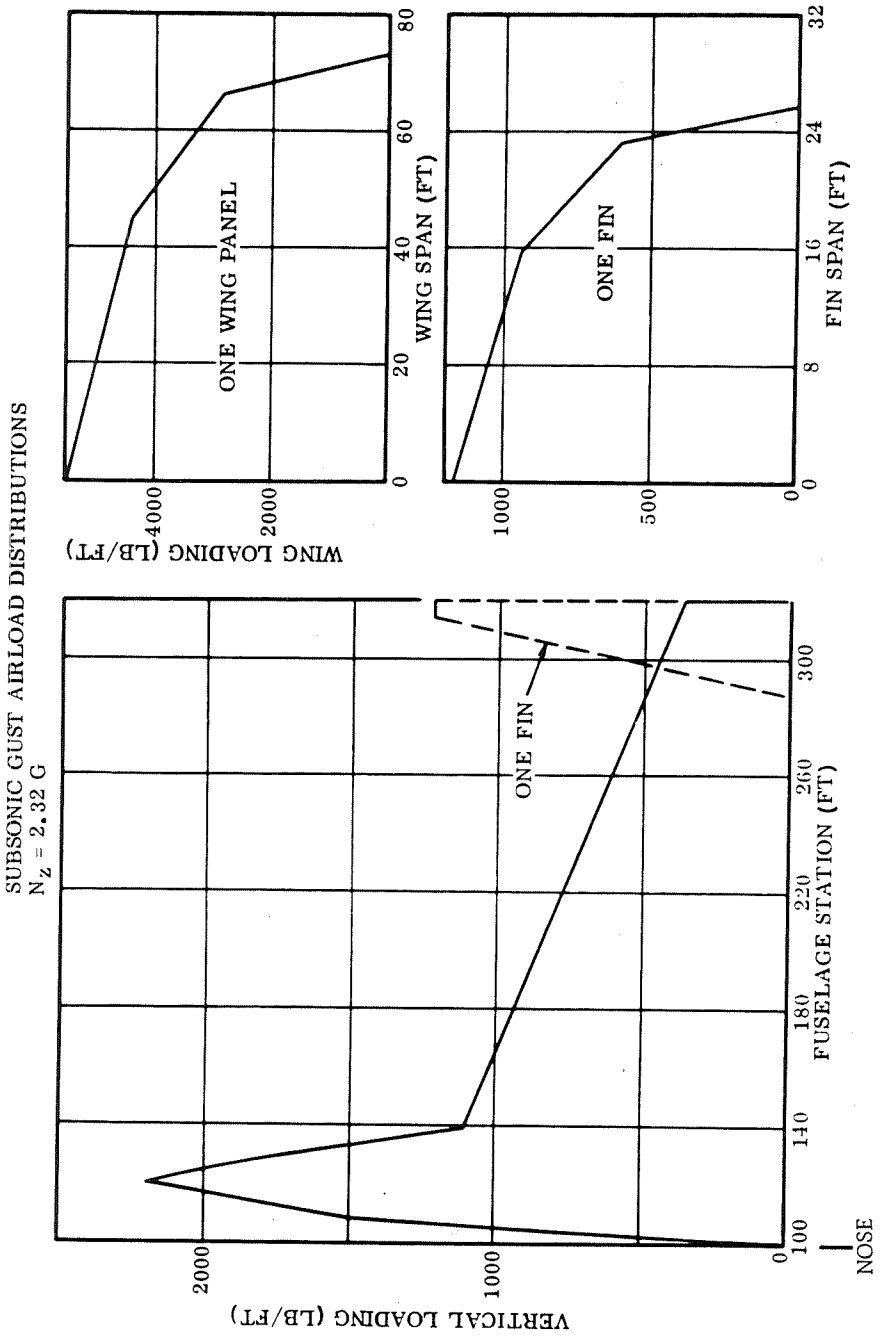

Figure 5-4. Subsonic Gust Airload Distributions (n_z = 2.32g)

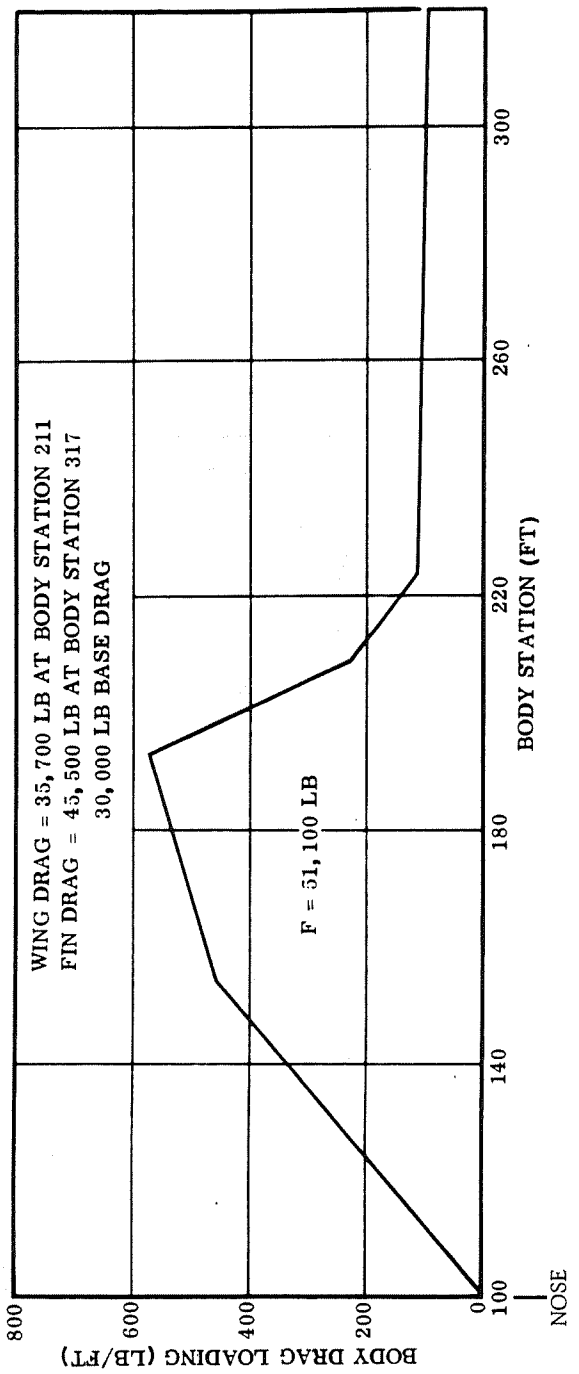

Figure 5-5. Subsonic Gust Body Drag Distribution

Table 5-1. T-15-to-Final-FR-1 Body Net Load Conversion Factors

Condition	Weight (lb)		Basic Factors					Net Load Conversion Factors				
			(2)				(3)	Axial	Shear	Torsion	Bending Moment	Peak Load Intensity
	T-15A W_{15}	FR-1 W_f	K_W	K_L	K_D	K_q	K_M	K_W	K_W	$K_W \times K_D$	$K_W \times K_L$	K_{N_x} (4)
Booster												
Ground Wind	1,962,239	1,708,416	0.871	0.925	0.994	-	0.23	0.87	0.87	0.86	0.81	0.86
Maximum αq	1,259,363	1,091,980	0.867	0.925	0.994	1.036	0.31	0.90	0.90	0.89	0.83	0.88
Maximum βq	1,259,363	1,091,980	0.867	0.925	0.994	1.036	0.16	0.90	0.90	0.89	0.83	0.89
Burnout	382,754	330,164	0.863	0.925	0.994	-	0.50	0.86	0.86	0.85	0.79	0.84
Subsonic Gust	369,754	320,052	0.866	0.925	0.994	-	1.00	0.87	0.87	0.86	0.80	0.81
Landing	340,035	300,249	0.883	0.925	0.994	-	1.00	0.88	0.88	0.87	0.82	0.83
Orbiter												
Ground Wind	1,485,139	1,434,203	0.996	0.925	0.994	-	0.25	0.97	0.97	0.96	0.89	0.96
Maximum αq	1,485,139	1,434,203	0.996	0.925	0.994	1.036	0.43	1.00	1.00	1.00	0.93	0.98
Maximum βq	1,485,139	1,434,203	0.996	0.925	0.994	1.036	0.39	1.00	1.00	1.00	0.93	0.98
Booster Burnout	1,485,139	1,434,203	0.996	0.925	0.994	-	0.00	0.97	0.97	0.96	0.89	0.97
Subsonic Gust (1)	360,279	360,764	0.996	0.925	0.994	-	1.00	1.00	1.00	0.99	0.93	0.93
Landing (1)	355,965	356,486	0.996	0.925	0.994	-	1.00	1.00	1.00	0.99	0.93	0.93

(1) Includes 50 K payload.

(2) $K_W = W_f/W_{15}$

$K_L = \text{Length}_f/\text{Length}_{15} = 204.0/220.6 = 0.925$

$K_D = \text{Diameter}_f/\text{Diameter}_{15} = 26.5/26.67 = 0.994$

$K_q = \sqrt{541/504} = 1.036$ used for maximum αq and maximum βq only.

(3) K_M = Percentage of total peak load intensity, N_x, depending on bending moment.

(4) $K_{N_x} = (K_M K_W K_L / K_D^2) + ((1 - K_M) K_W / K_D)$

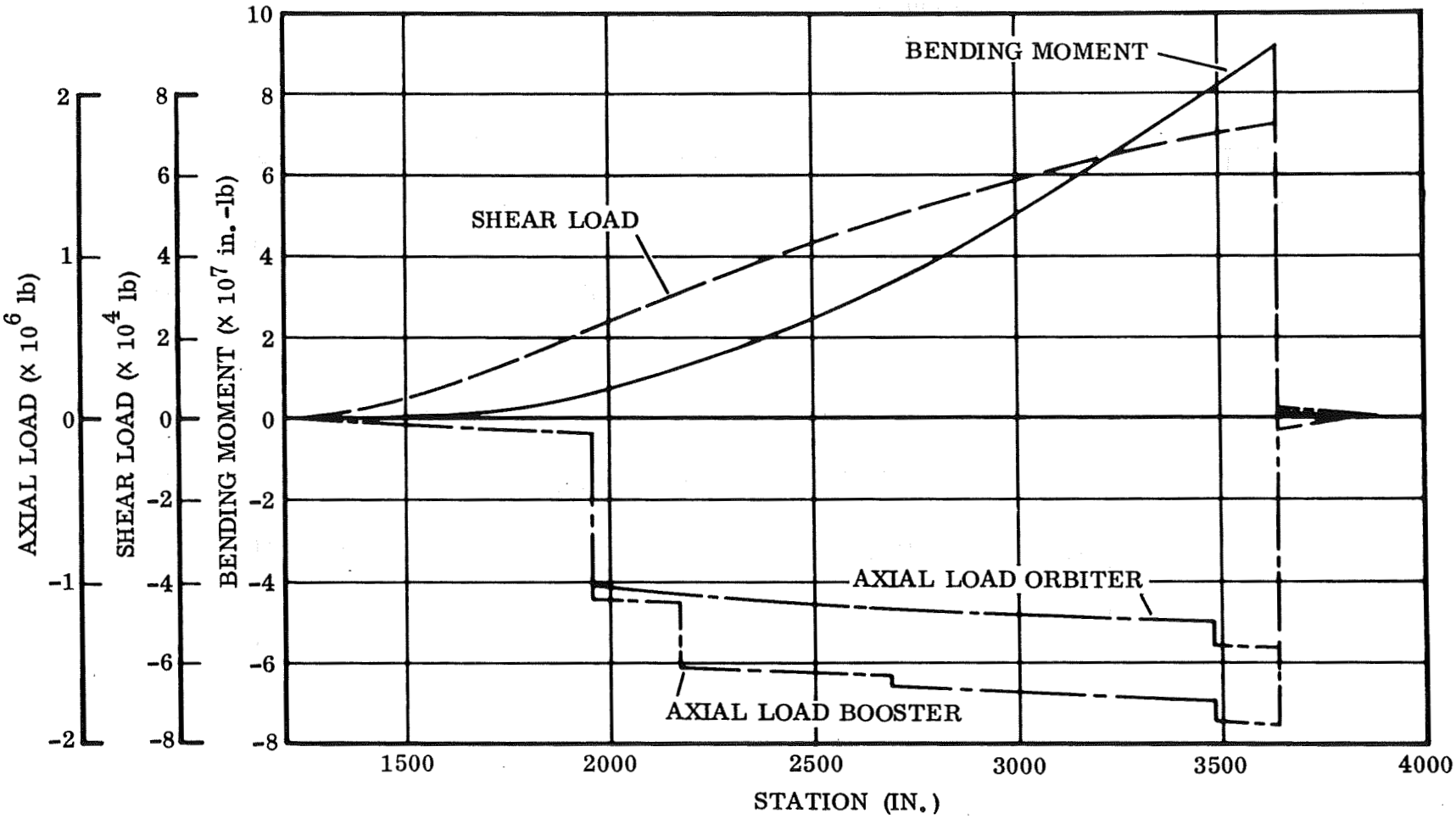

Figure 5-6. Ground Wind Condition

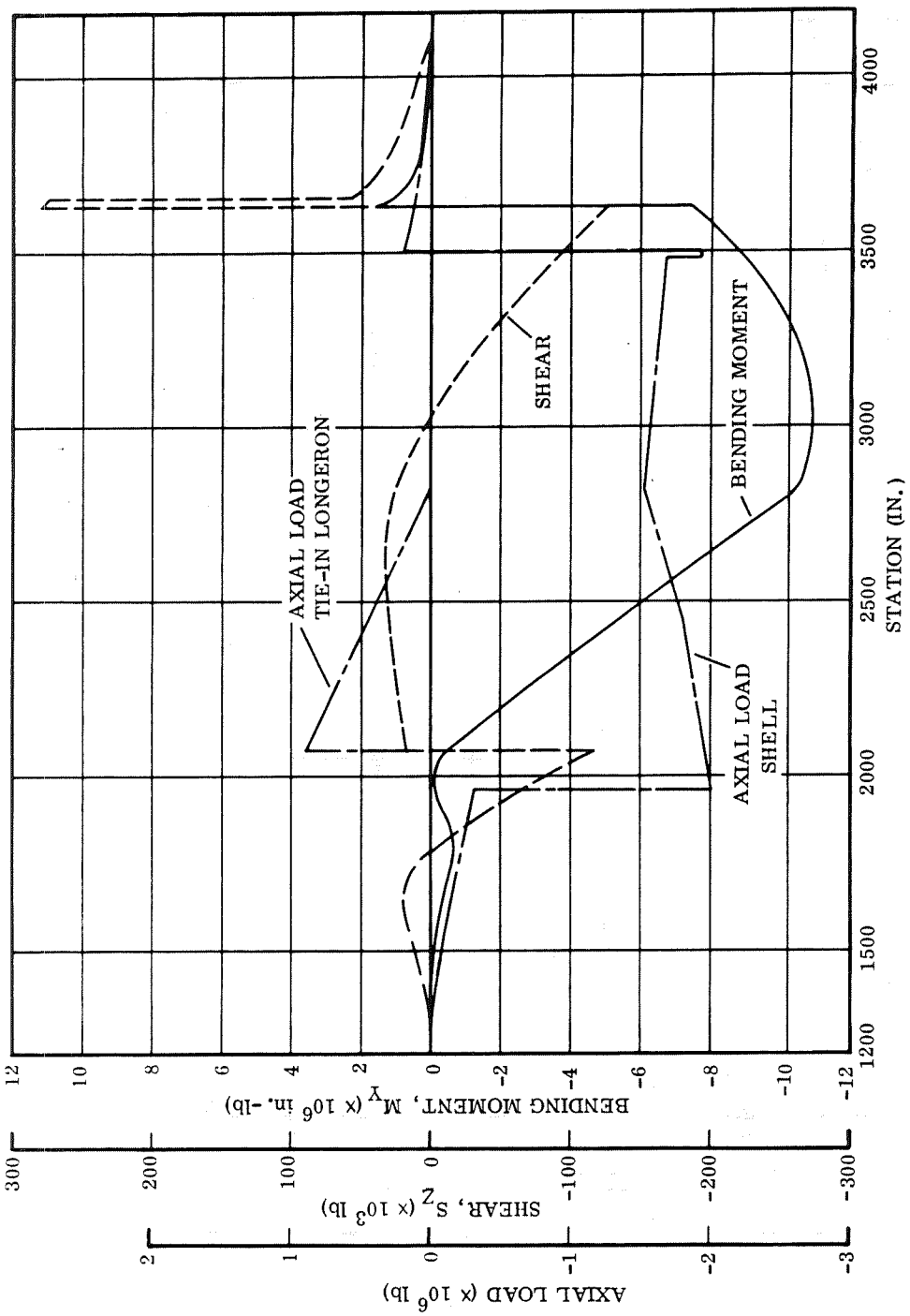

Figure 5-7. Orbiter Loads at Maximum αq

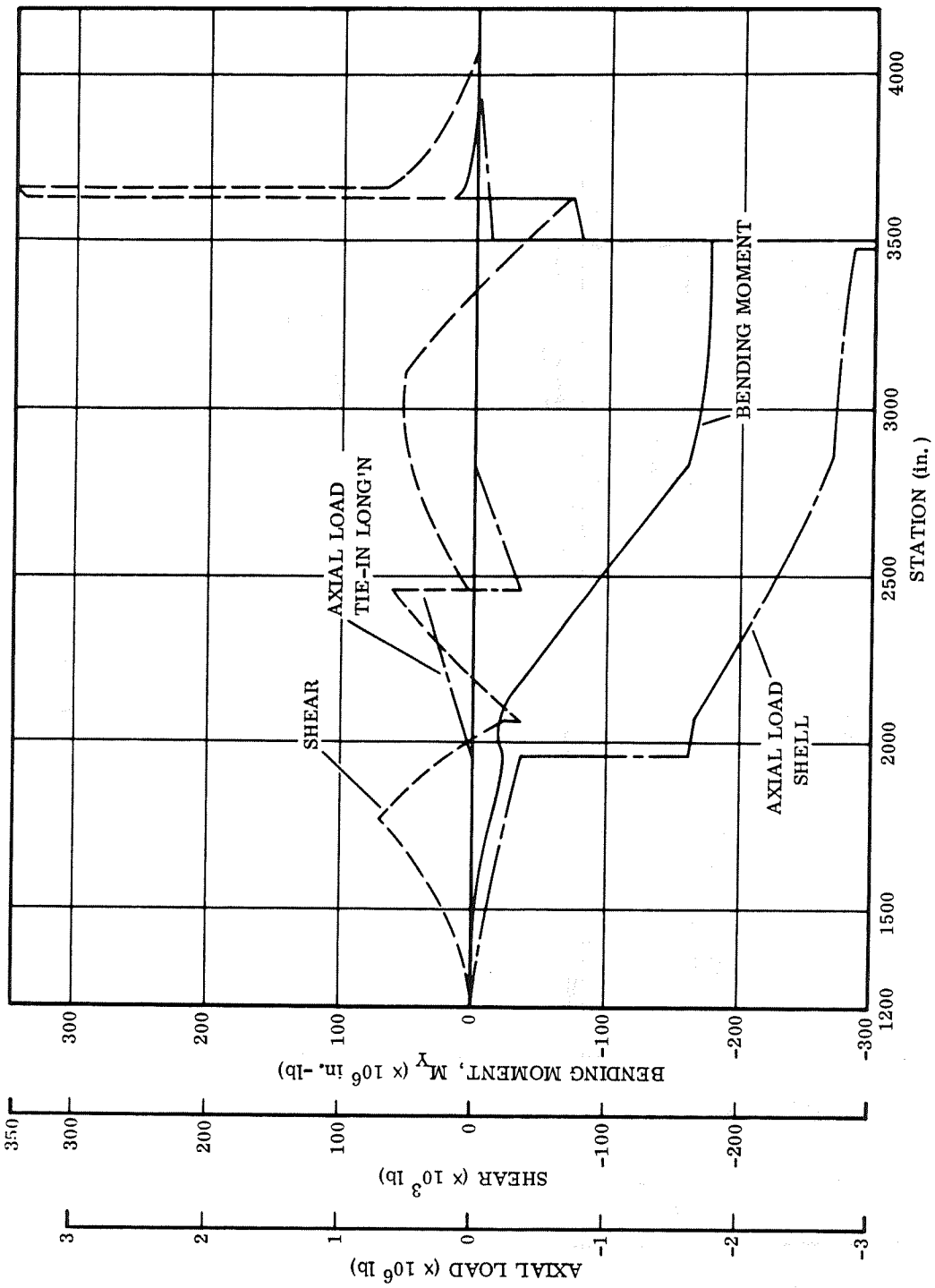

Figure 5-8. Booster Loads at Maximum αq

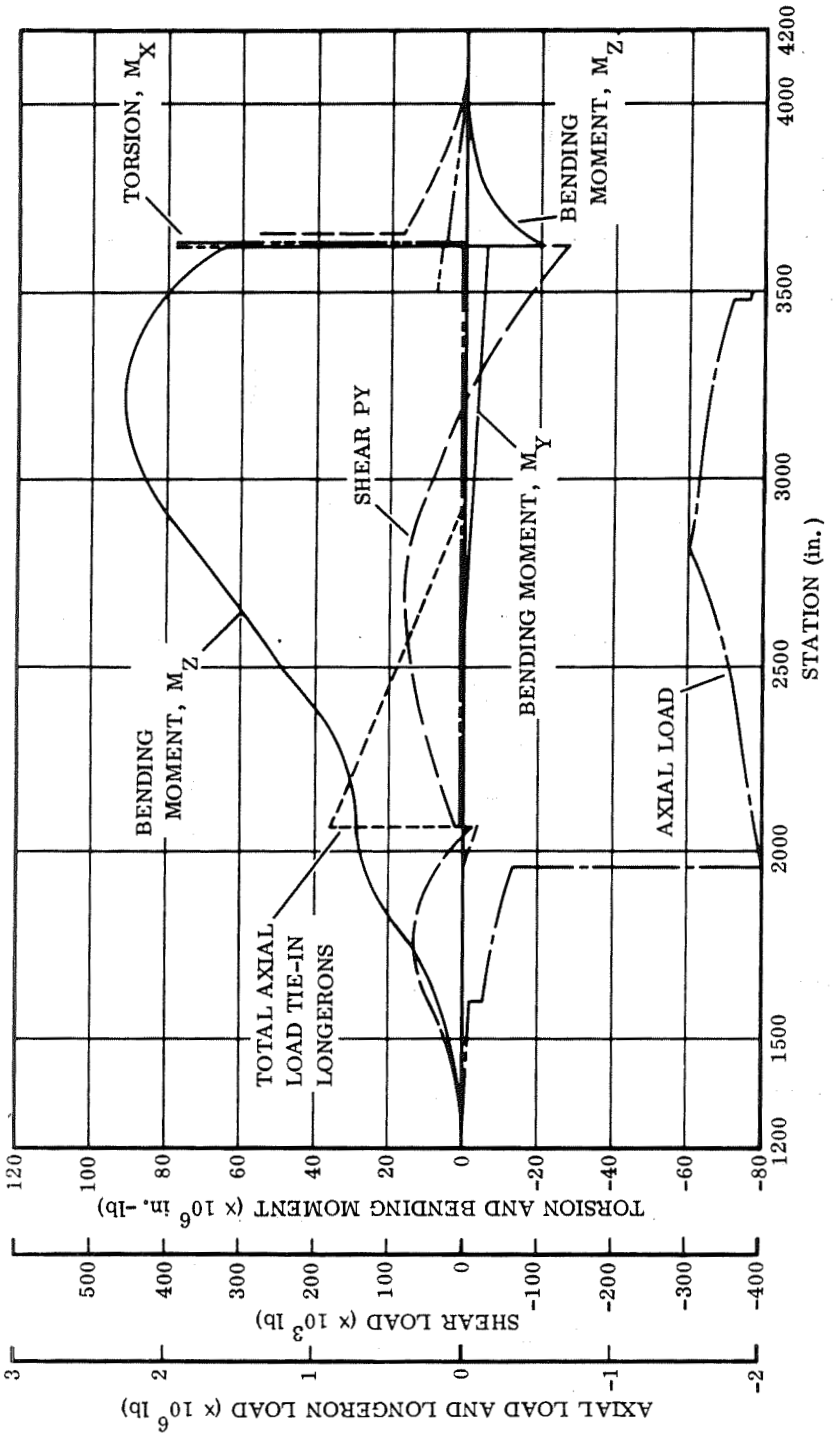

Figure 5-9. Orbiter Loads at Maximum βq

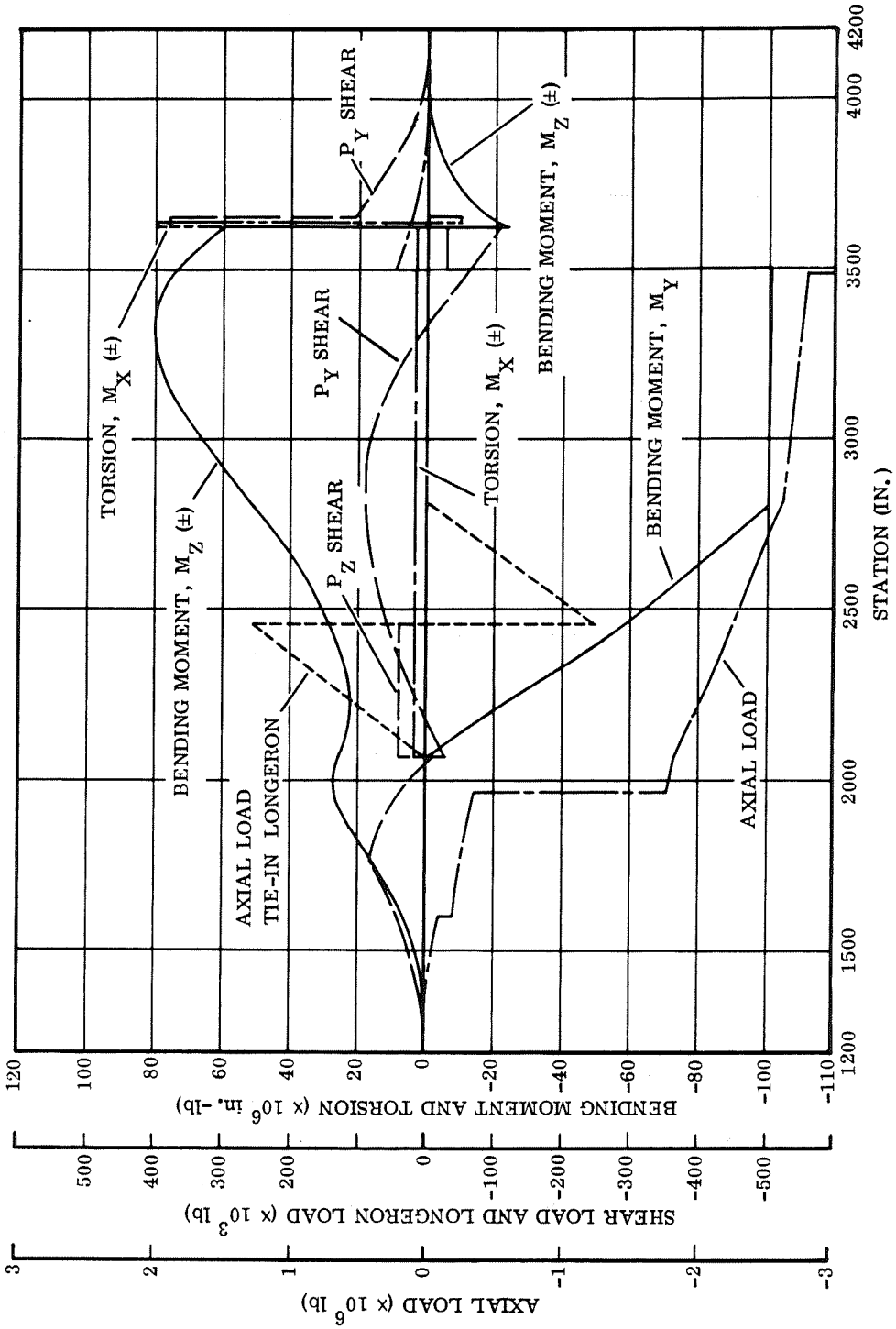

Figure 5-10. Booster Loads at Maximum βq

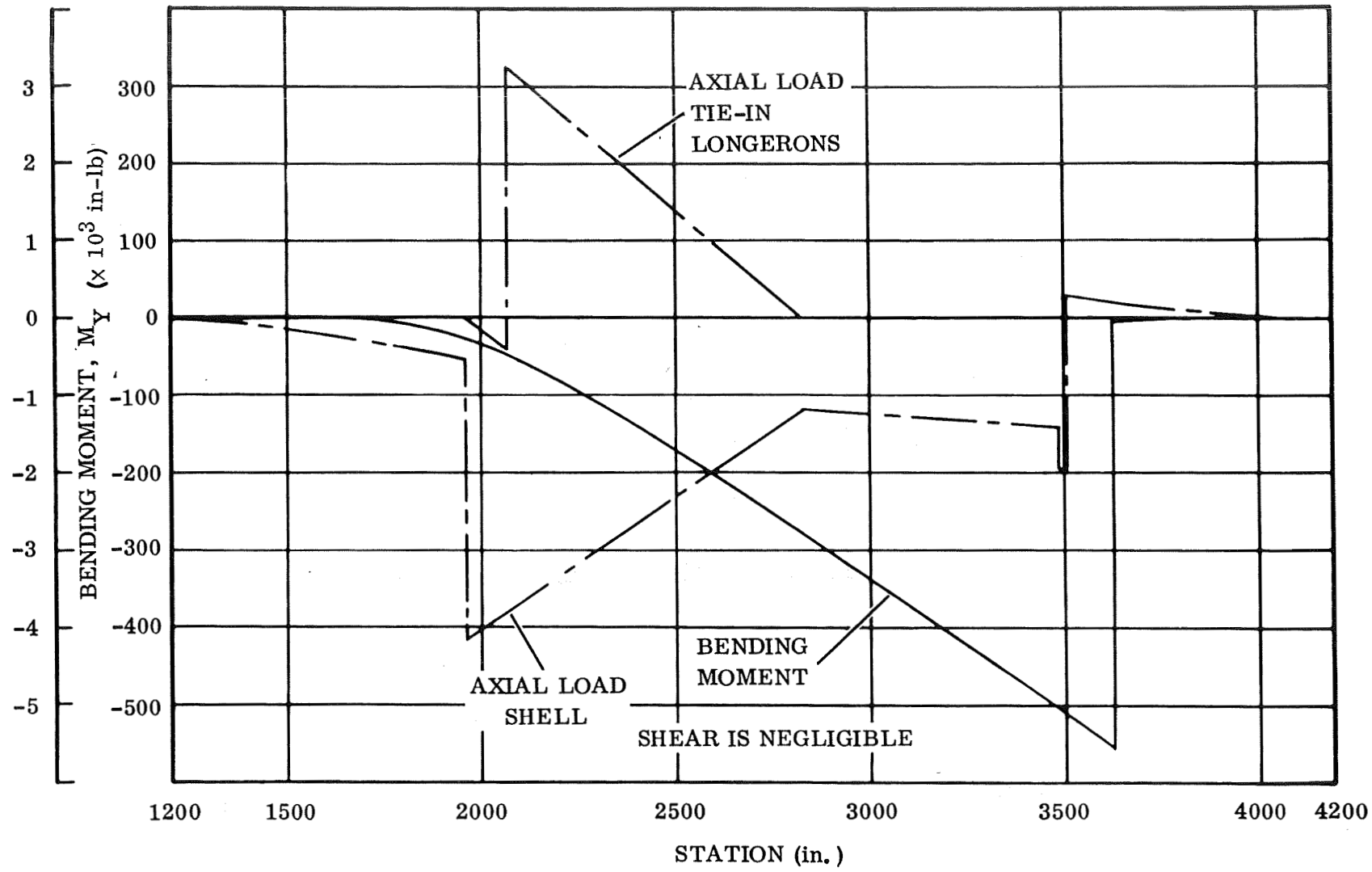

Figure 5-11. Orbiter Loads at Booster Burnout

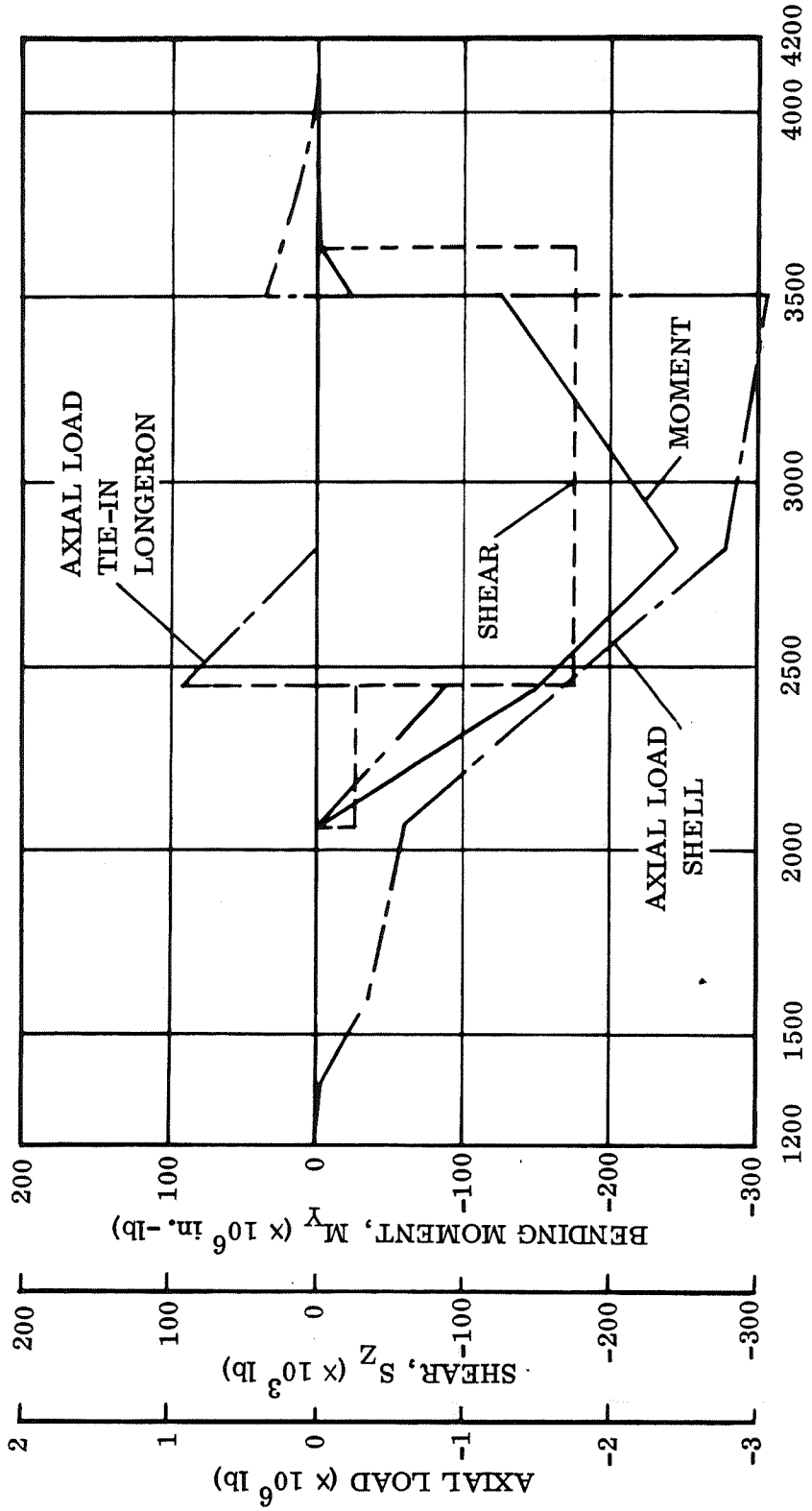

Figure 5-12. Booster Loads at Booster Burnout

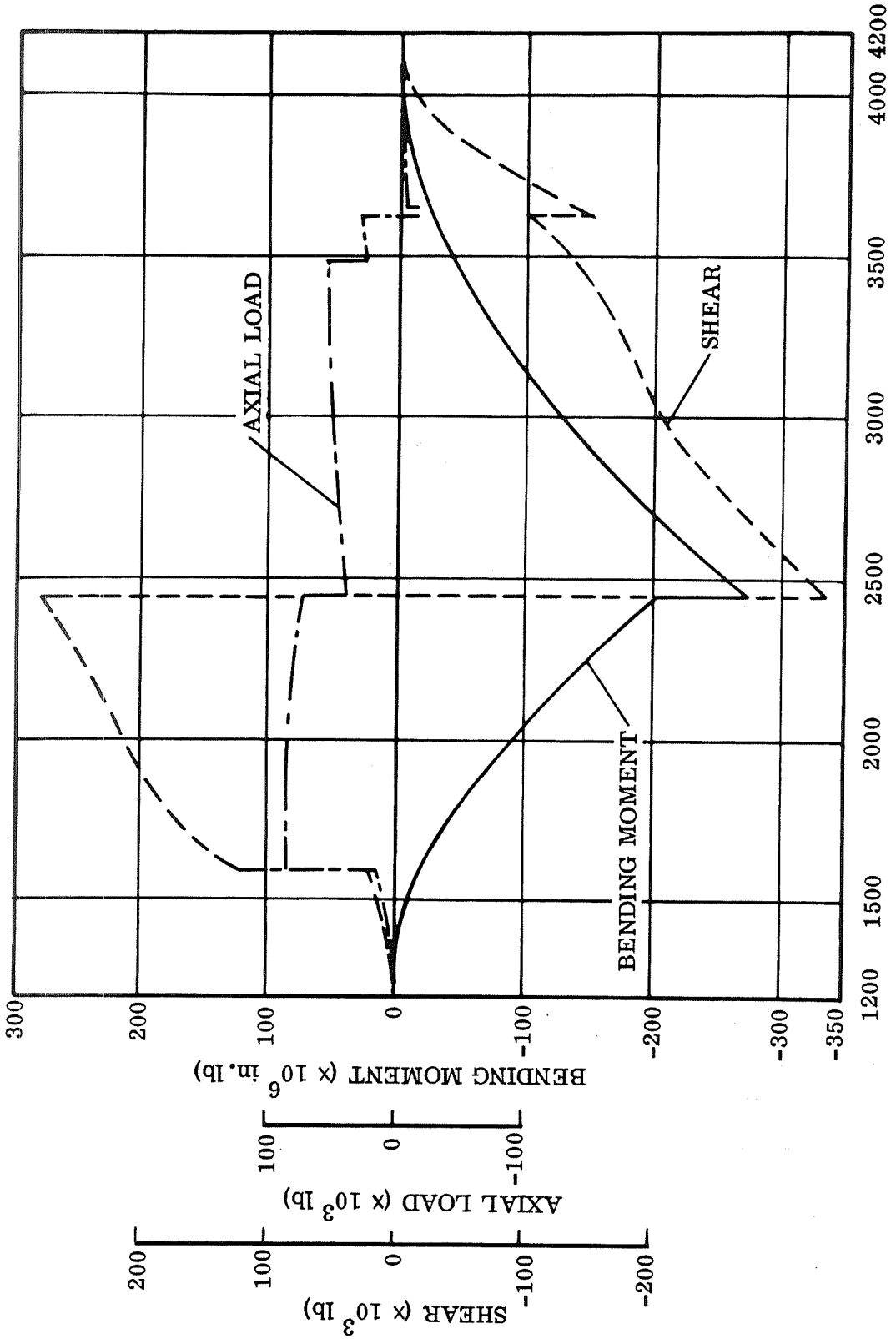

Figure 5-13. Booster Loads at Subsonic Gust

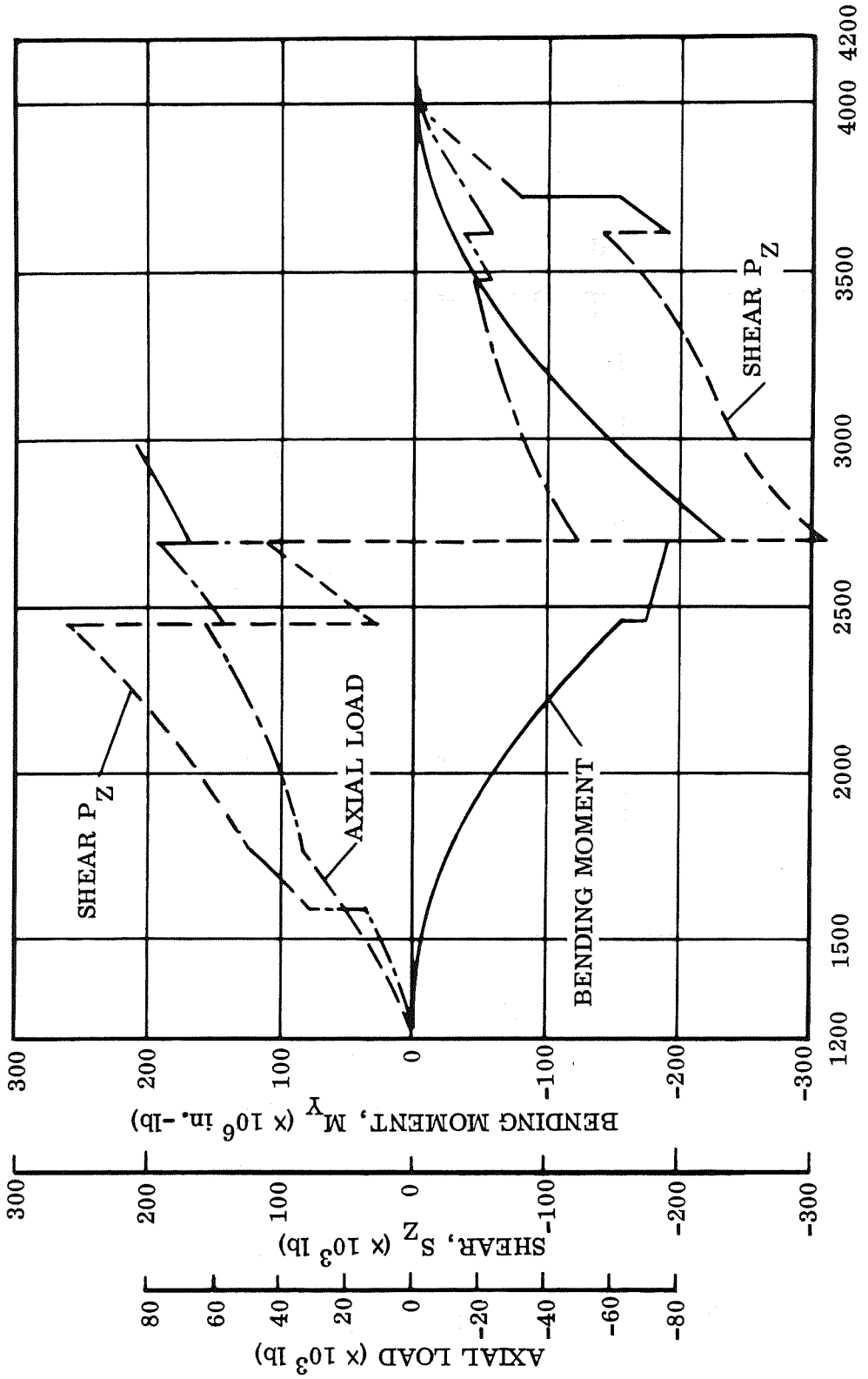

Figure 5-14. Two-Point Landing Loads (Orbiter Plus 50K Payload)

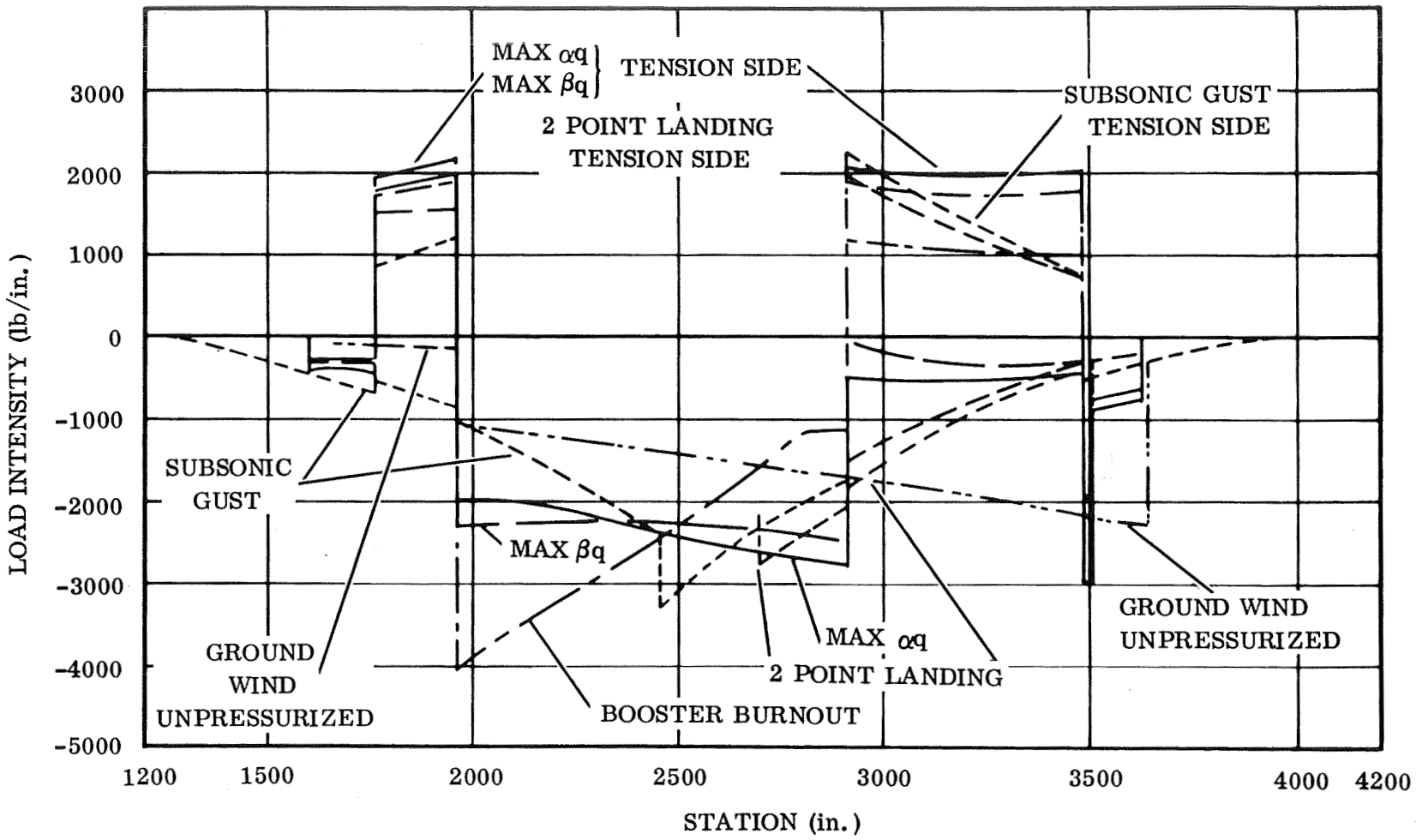

Figure 5-15. Comparison of Orbiter Peak Limit Load Intensities

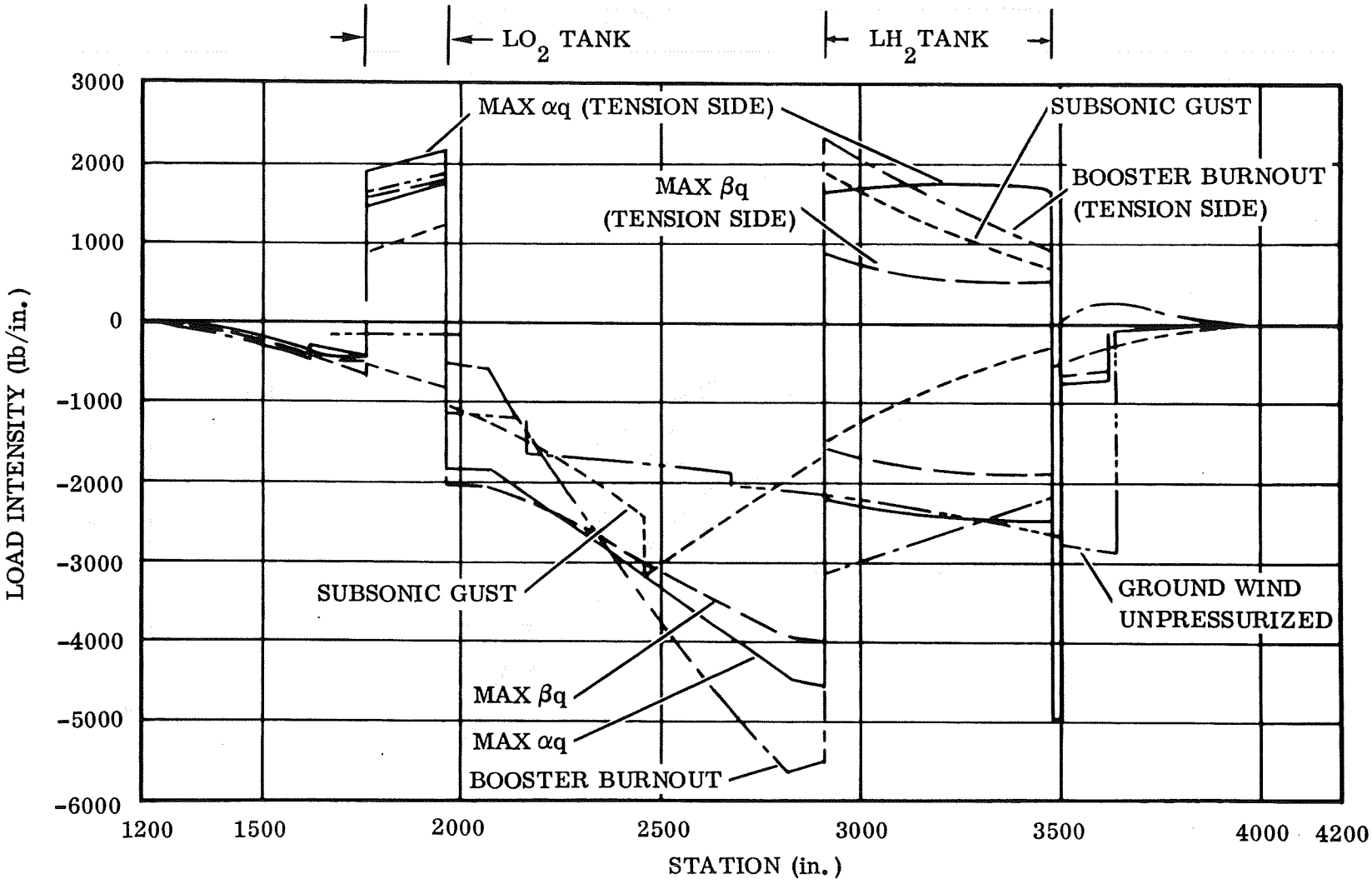

Figure 5-16. Comparison of Booster Peak Limit Load Intensities

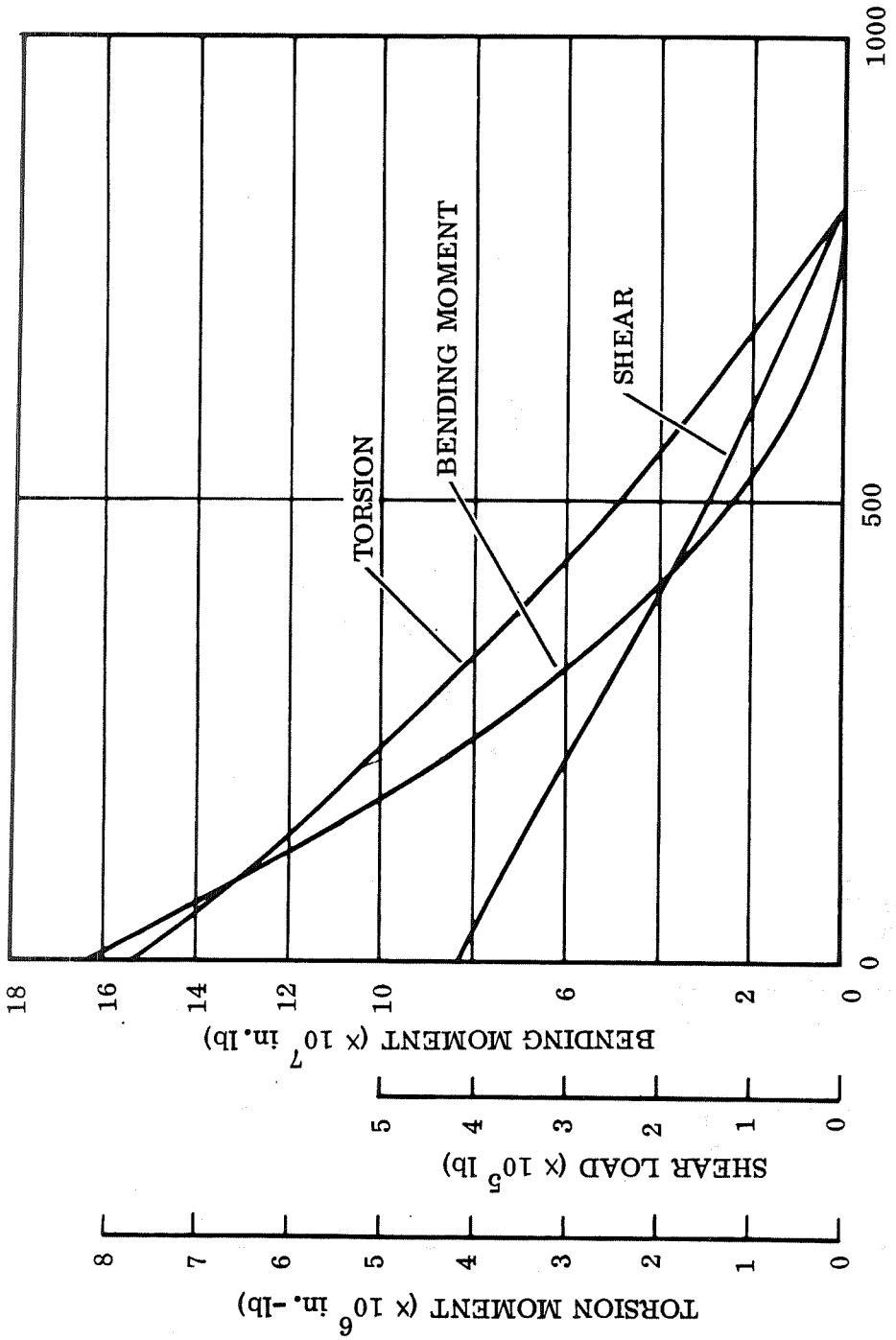

Figure 5-17. FR-1 Wing Net Ultimate Loads at Subsonic Gust Condition

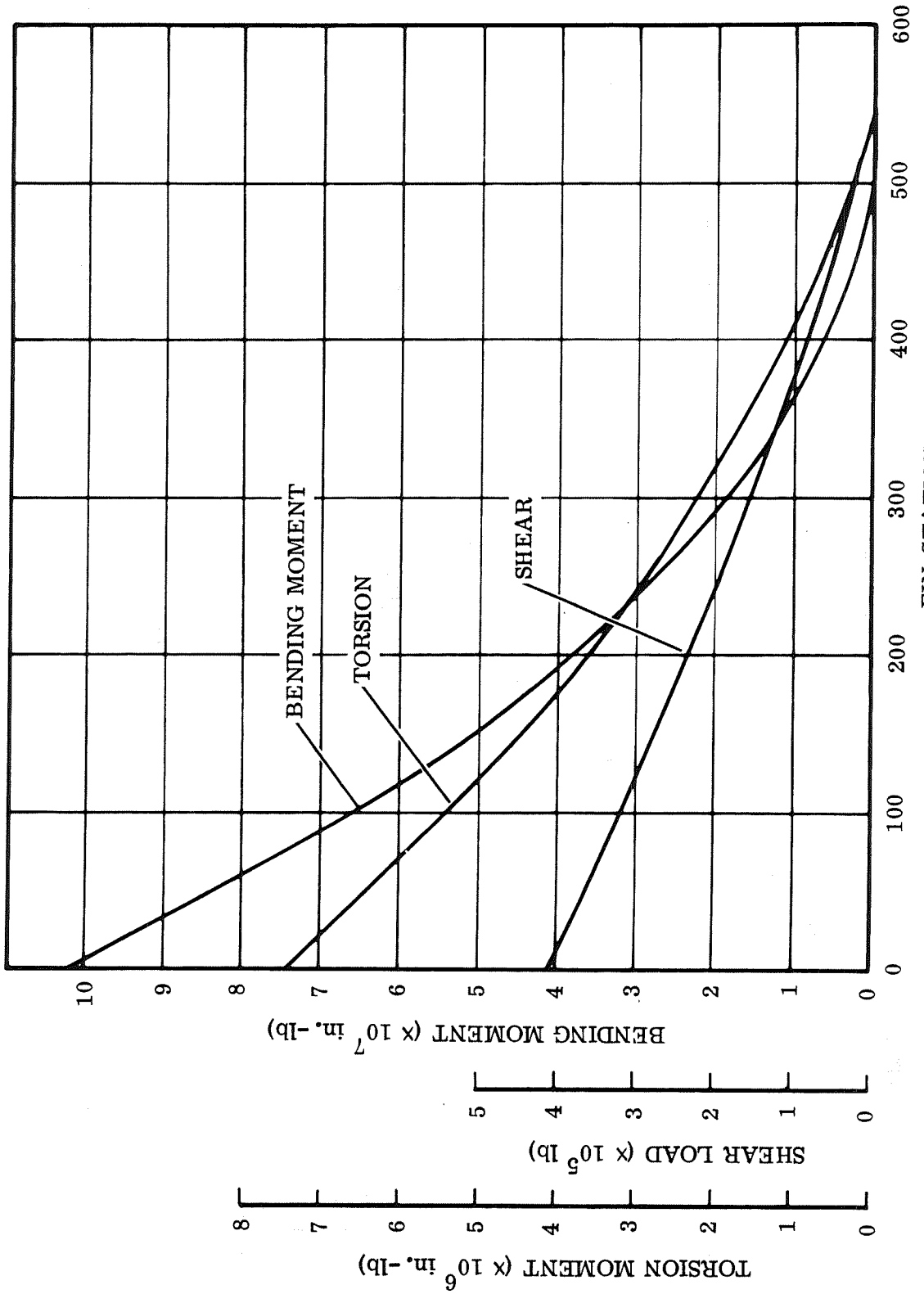

Firug 5-18. FR-1 Fin Net Ultimate Loads at Maximum αq Condition

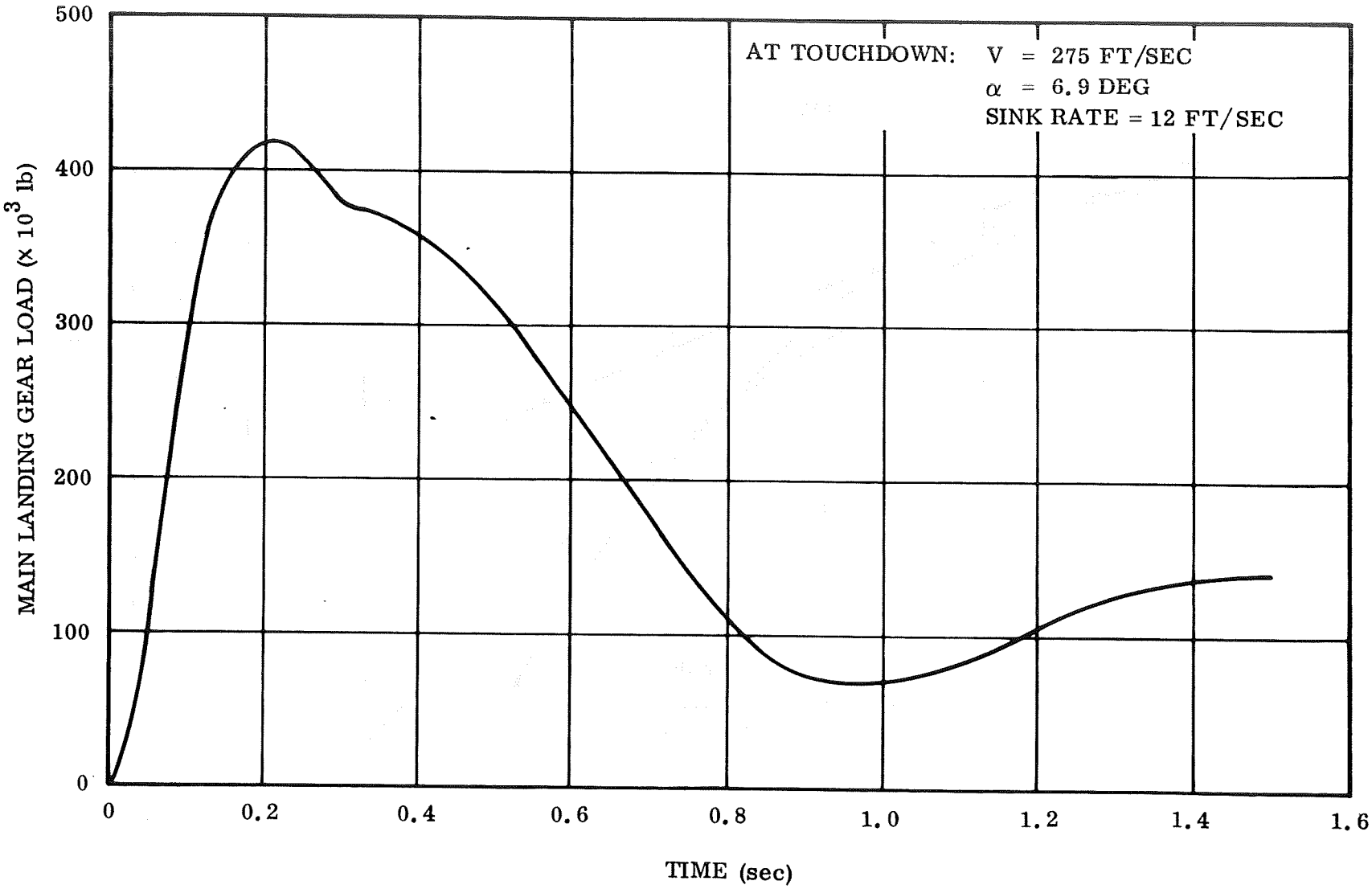

Figure 5-19. FR-1 Two-Point Landing (Power-Off Approach Weight = 356,500 lb)

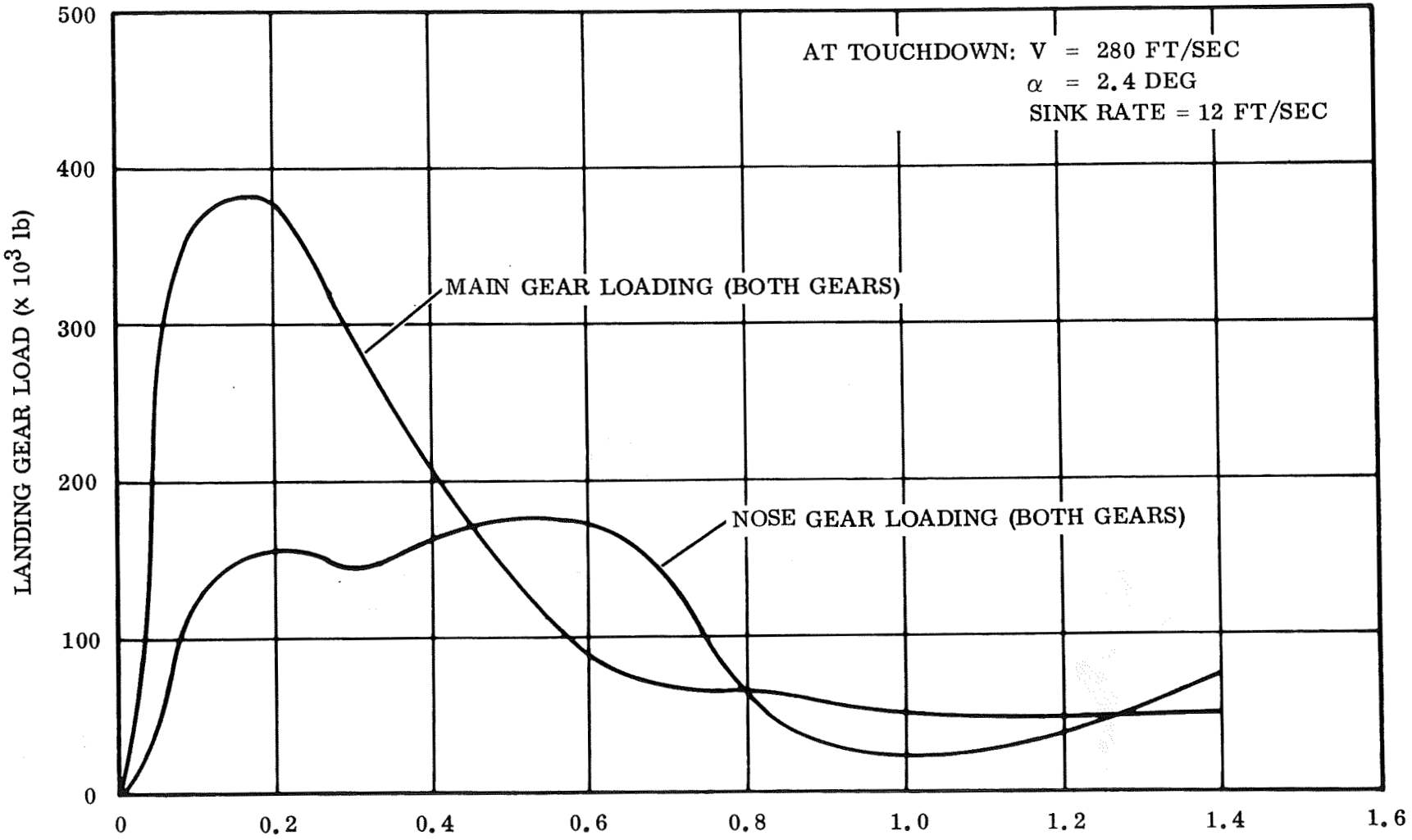

Figure 5-20. FR-1 Three-Point Landing (Power-Off Approach Weight = 356,500 lb)

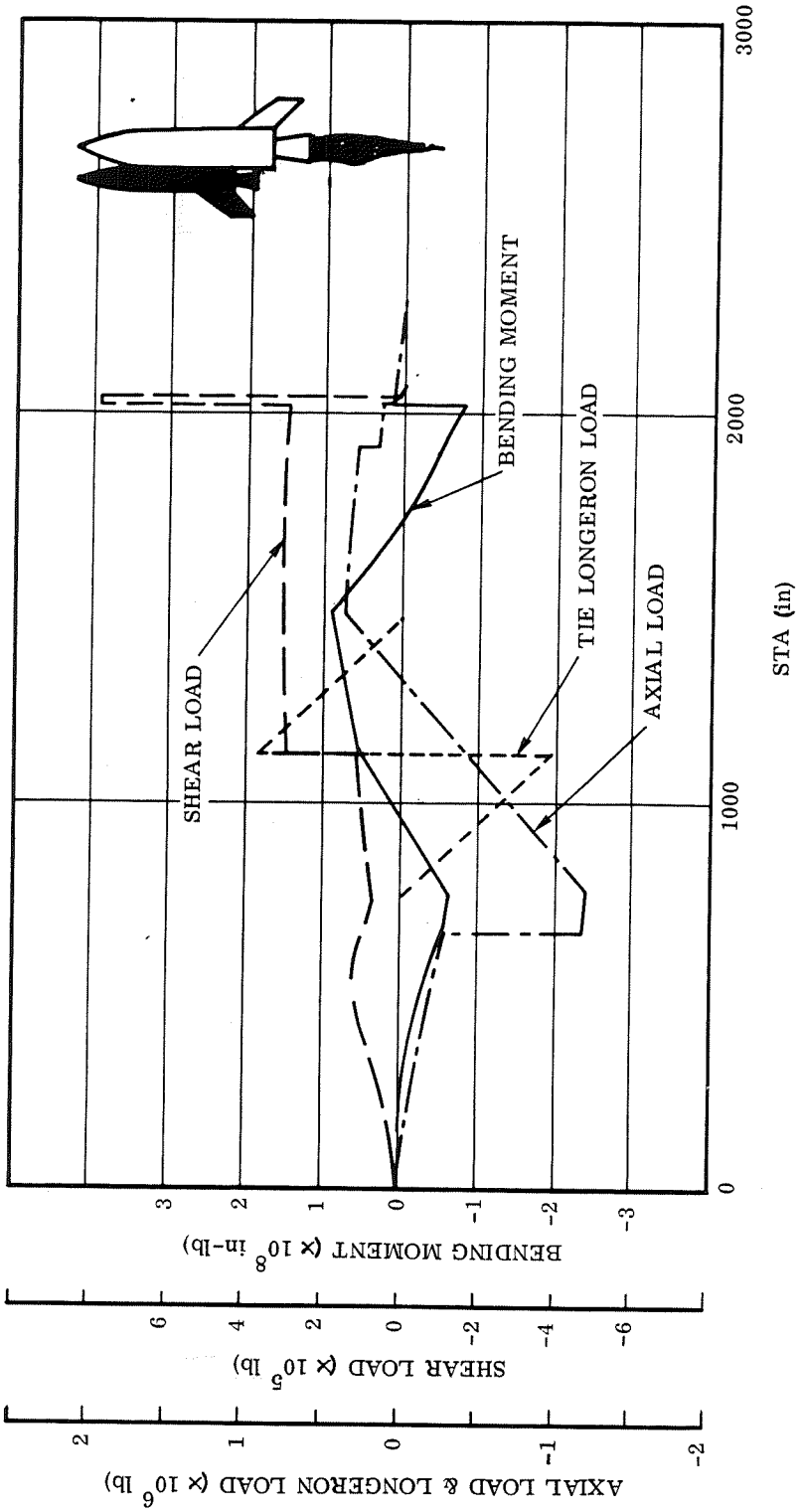

Figure 5-21. FR-3 Orbiter at Maximum αq (Nose-to-Nose)

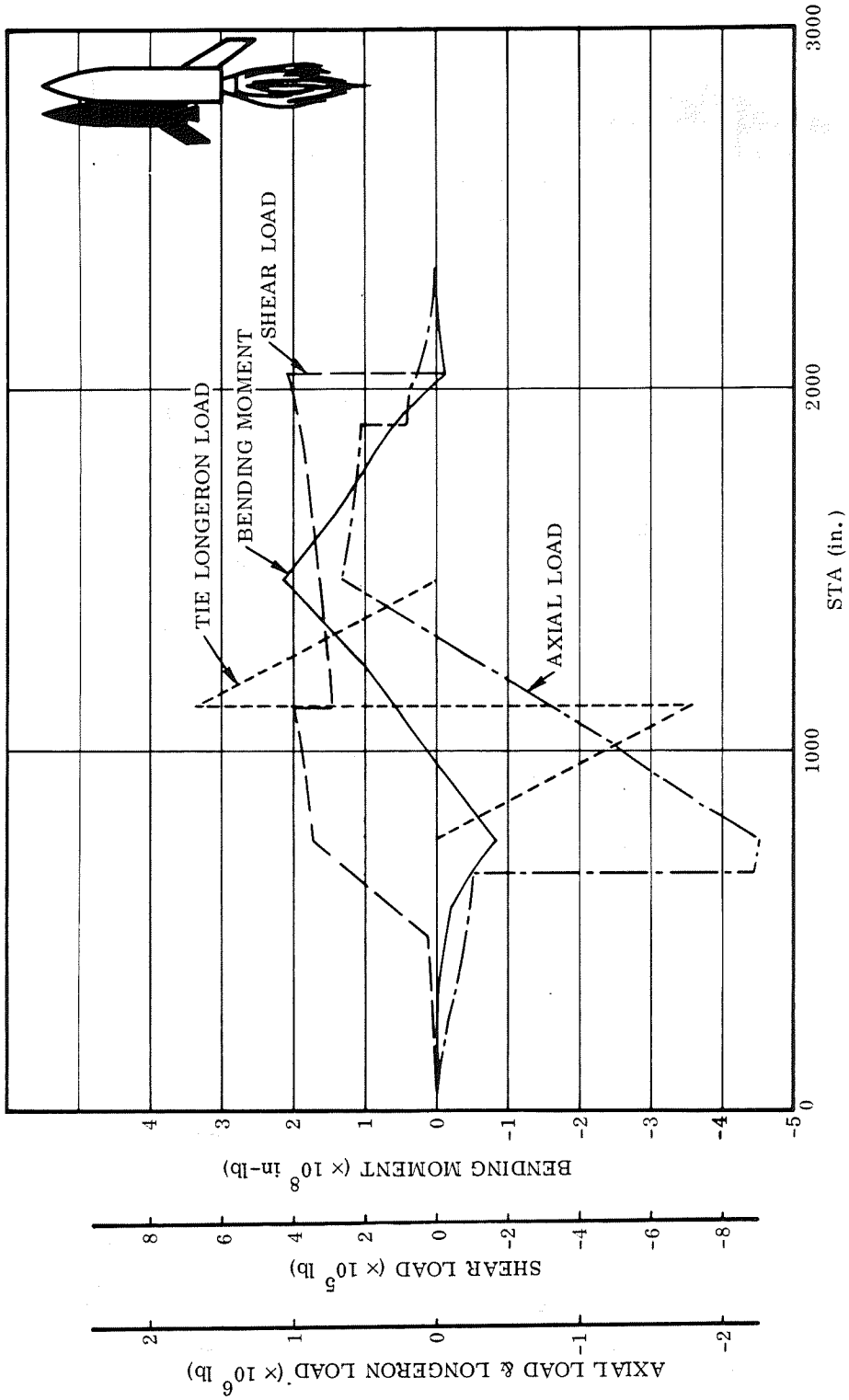

Figure 5-22. FR-3 Orbiter at Booster Burnout, 4g-N_x (Nose-to-Nose)

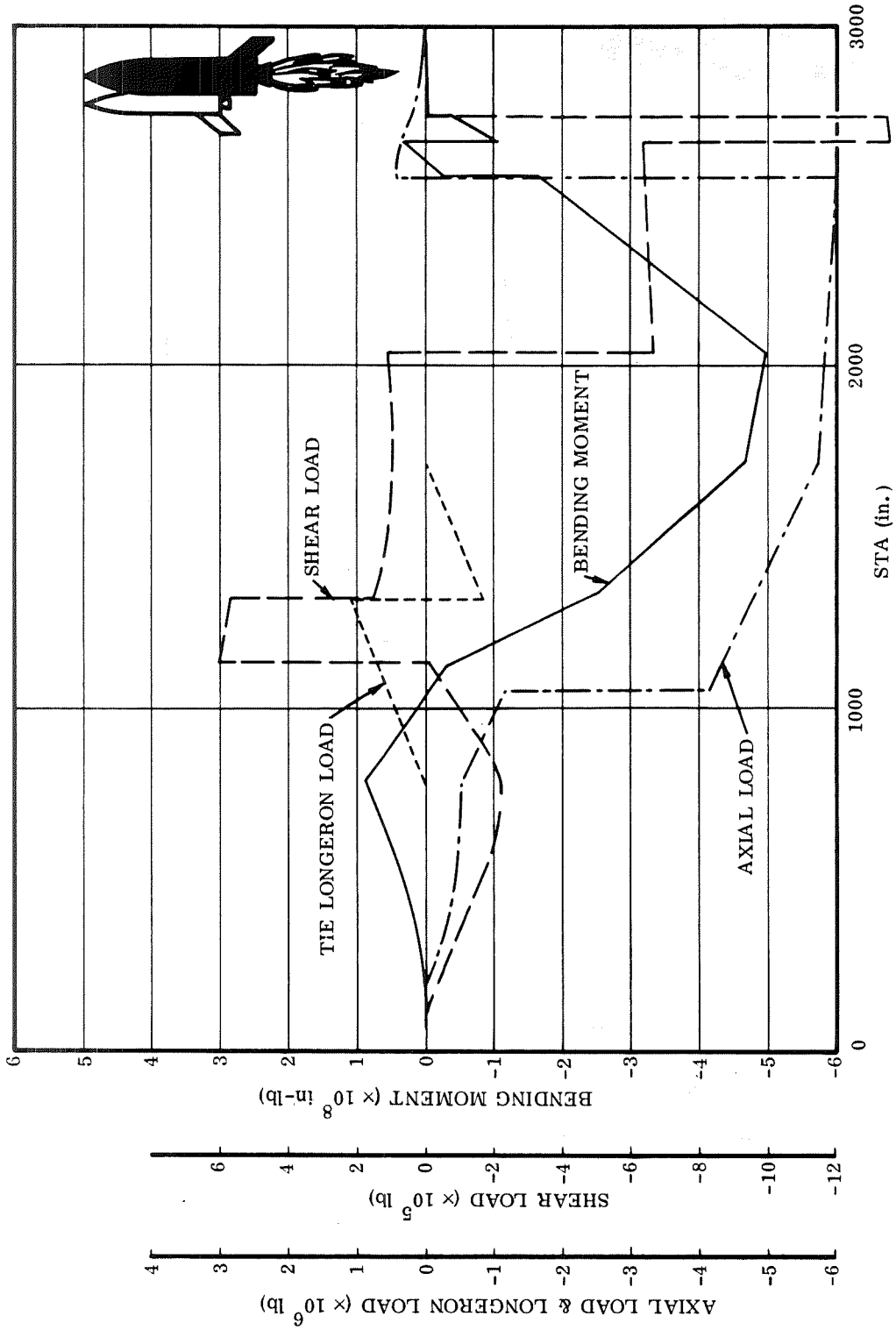

Figure 5-23. FR-3 Booster at Maximum αq (Nose-to-Nose)

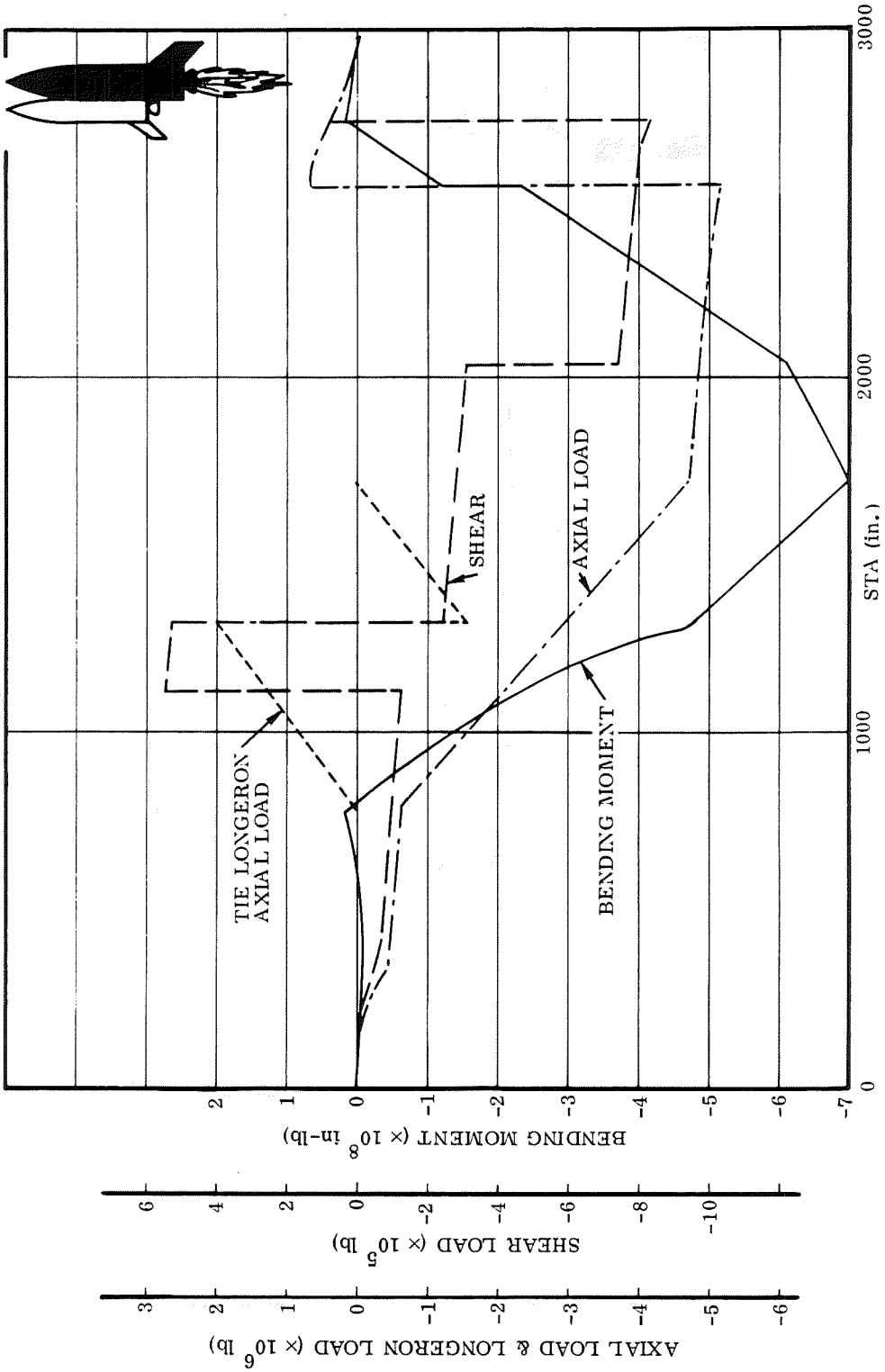

Figure 5-24. FR-3 Booster at Booster Burnout, 4g-N_x (Nose-to-Nose)

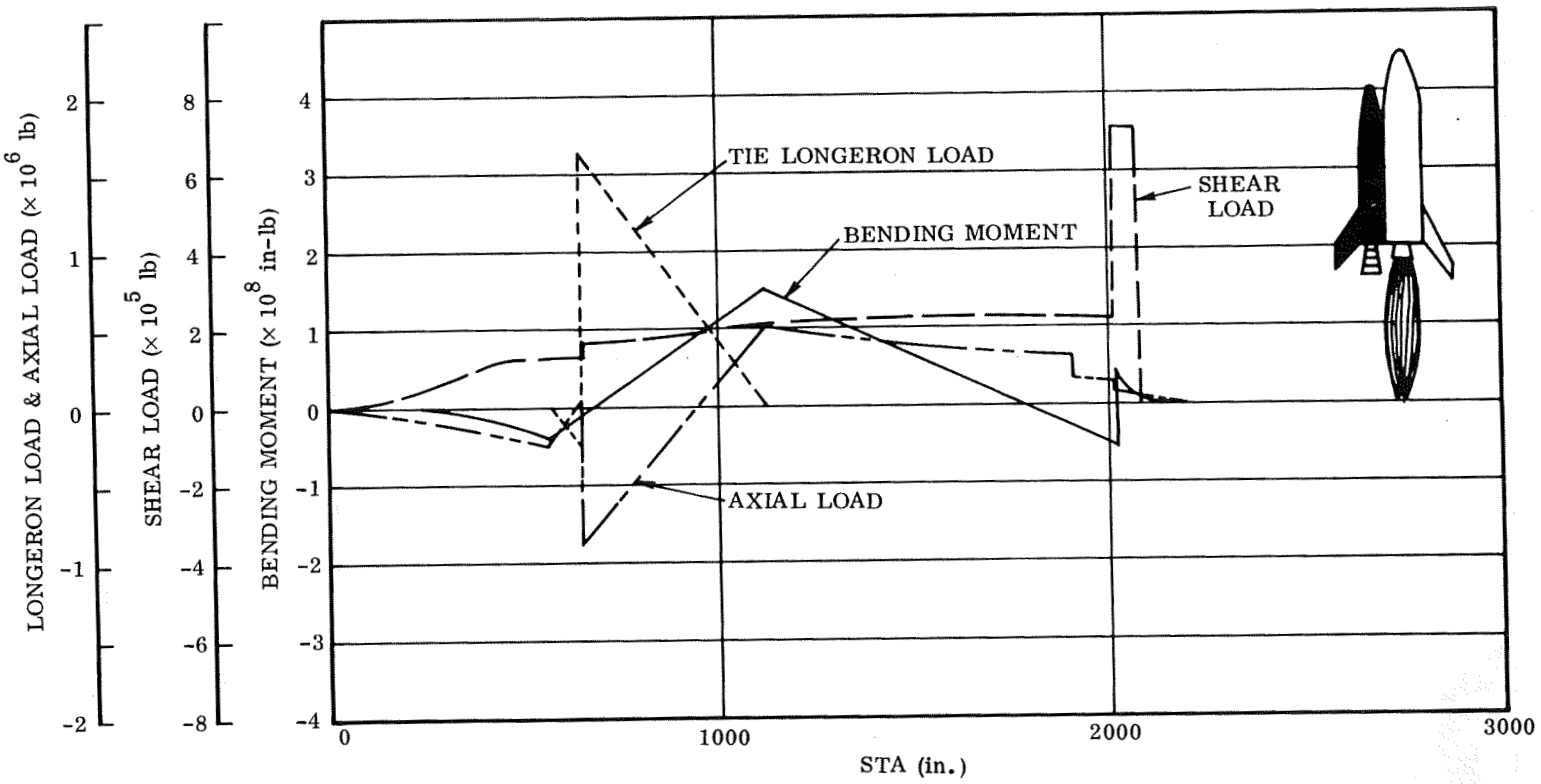

Figure 5-25. FR-3 Orbiter at Maximum αq (Tail-to-Tail)

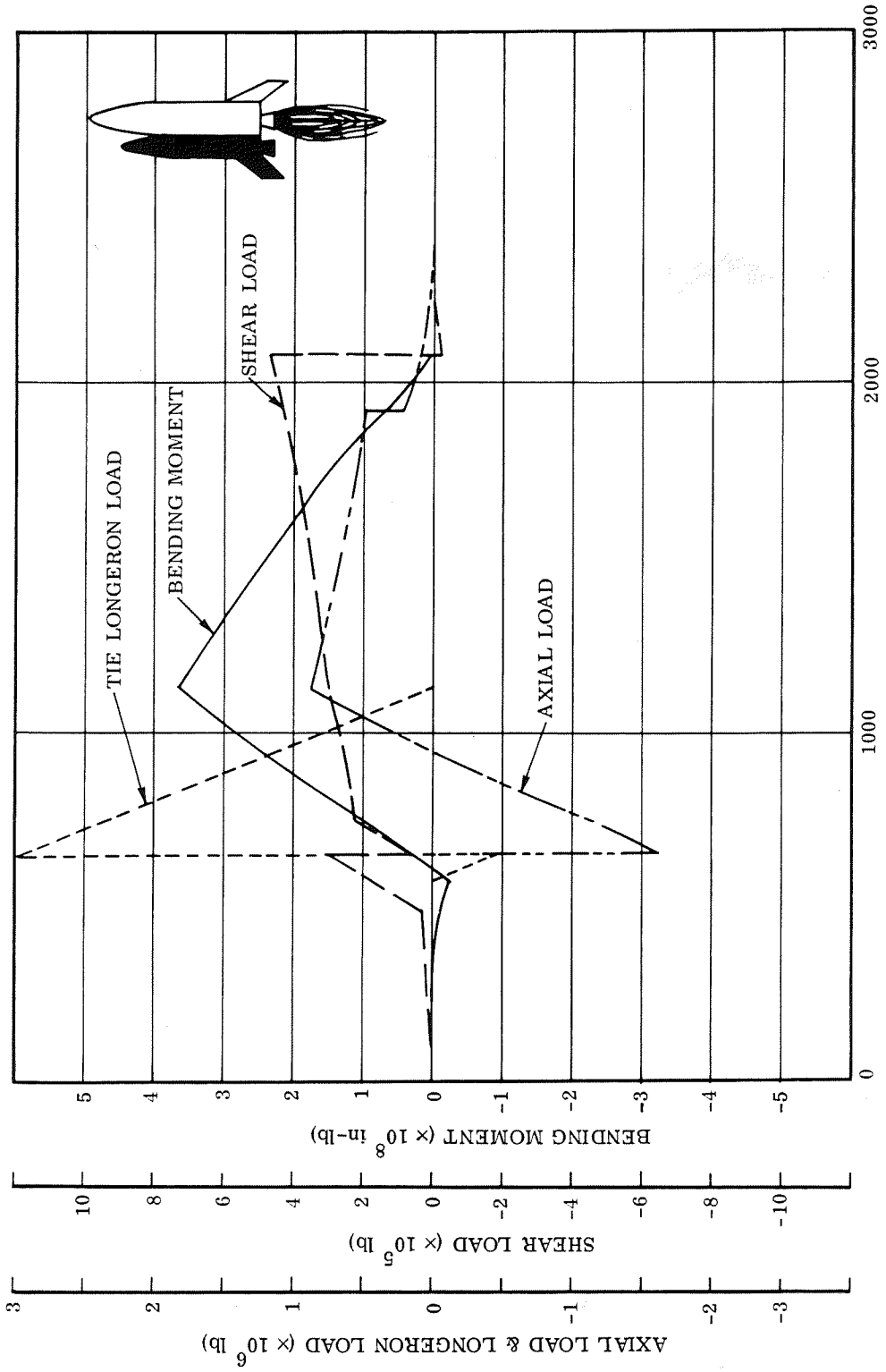

Figure 5-26. FR-3 Orbiter at Booster Burnout, 4g-N_x (Tail-to-Tail)

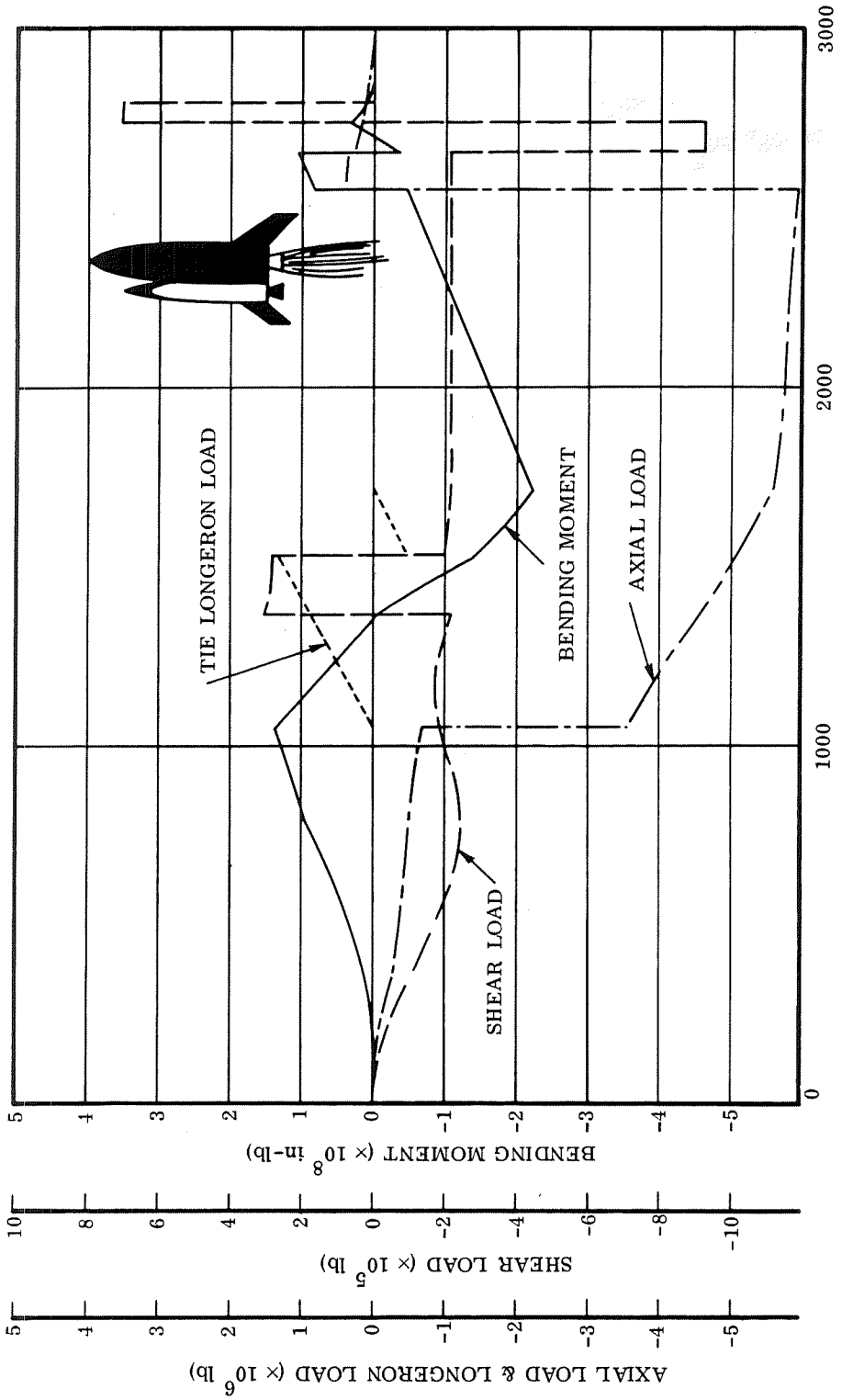

Figure 5-27. FR-3 Booster at Maximum αq (Tail-to-Tail)

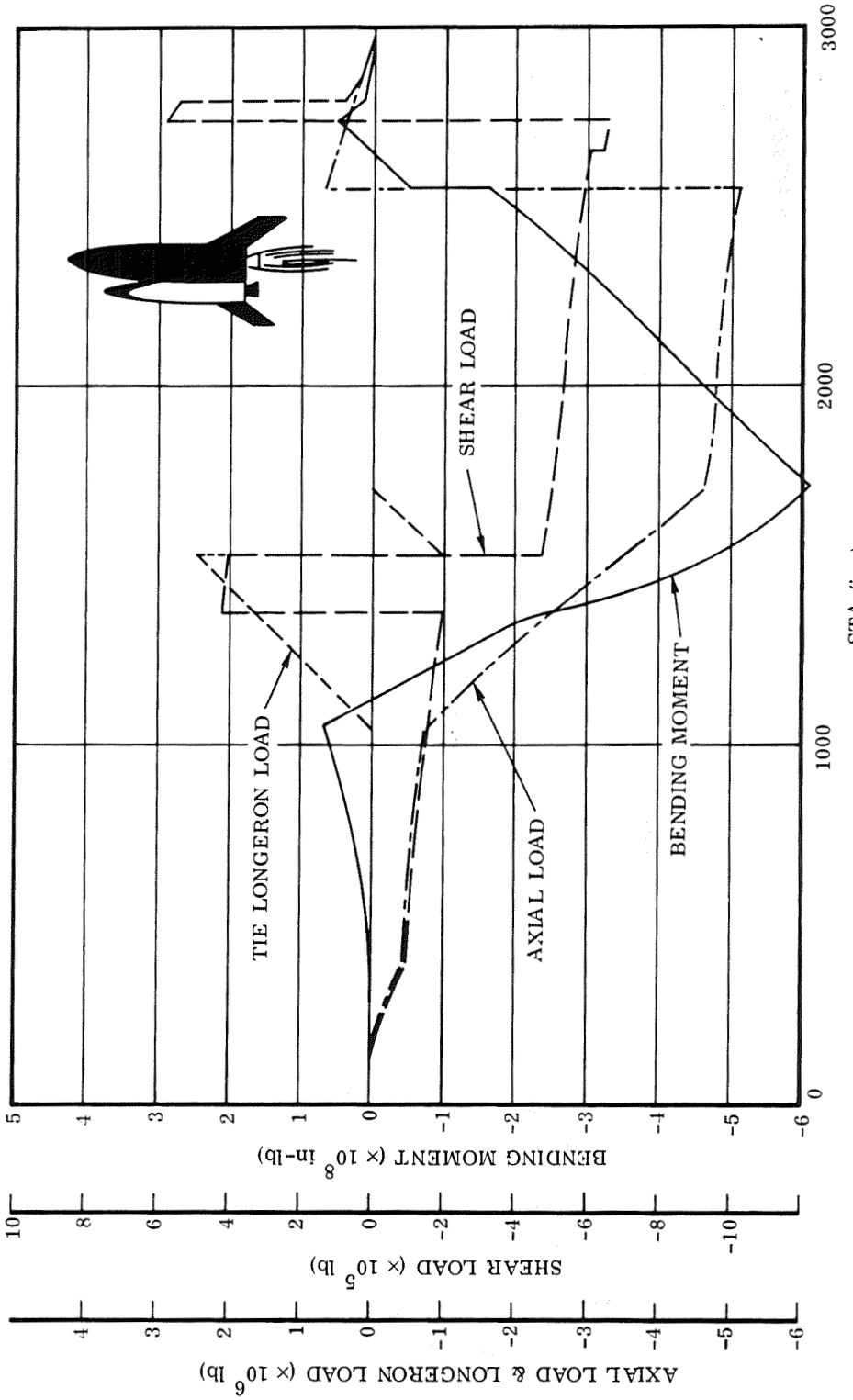

Figure 5-28. FR-3 Booster at Booster Burnout, 4g-N_x (Tail-to-Tail)

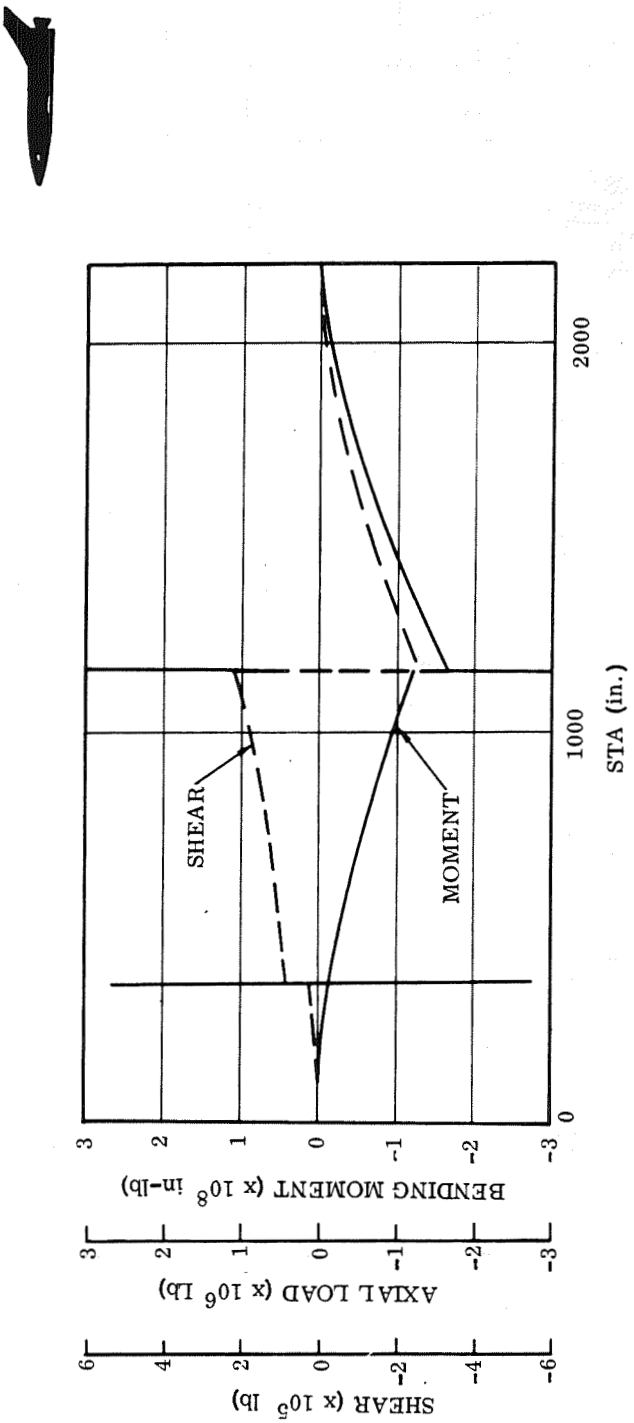

Figure 5-29. FR-3 Orbiter at Subsonic Gust

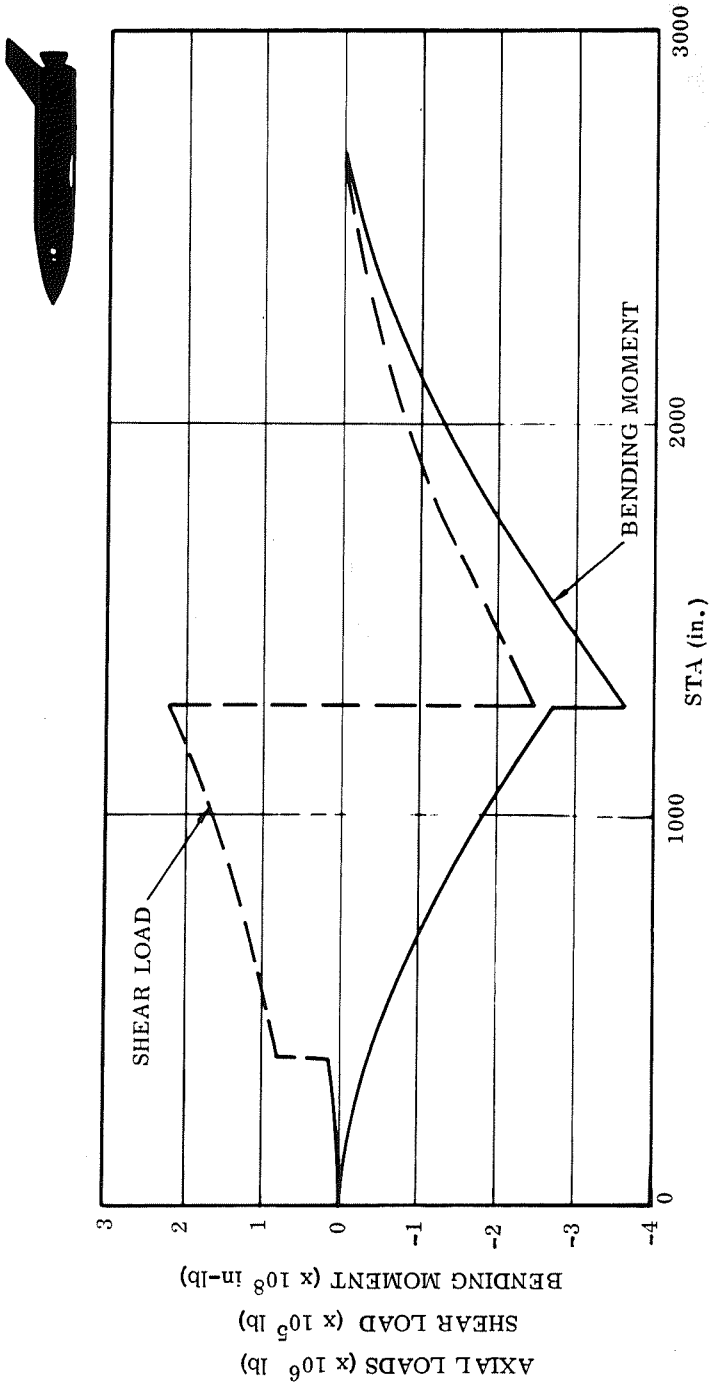

Figure 5-30. FR-3 Booster at Subsonic Gust

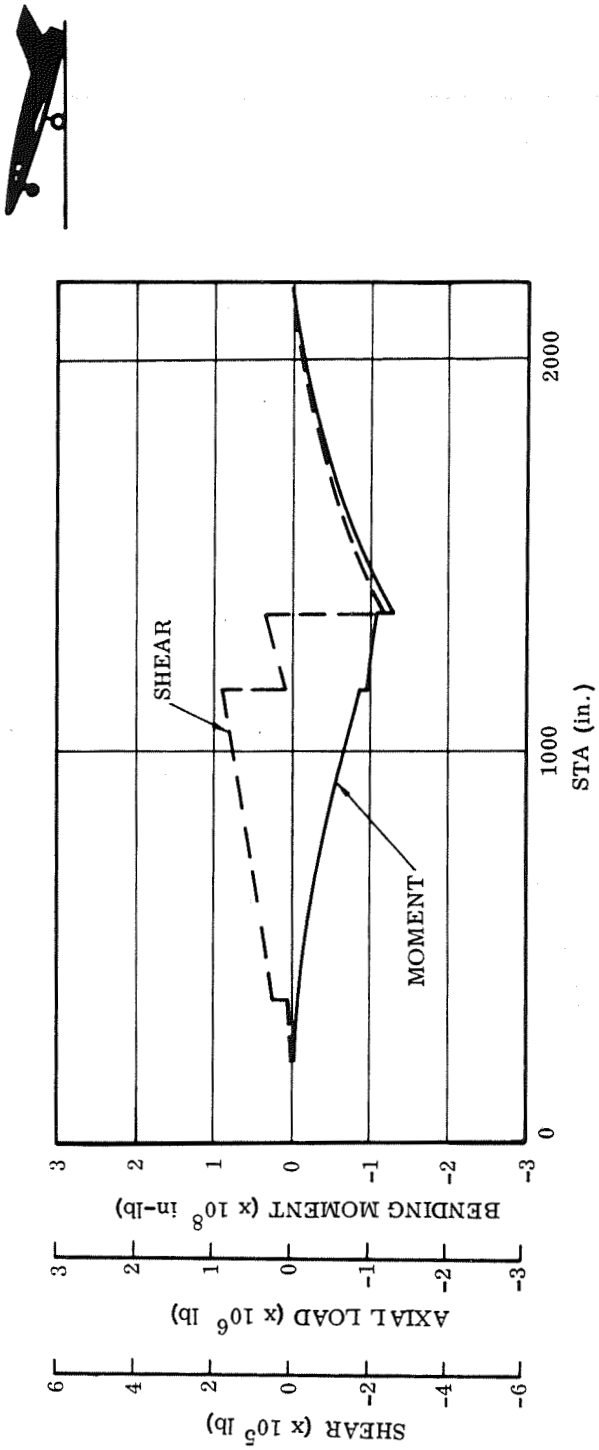

Figure 5-31. FR-3 Orbiter Two-Point Landing

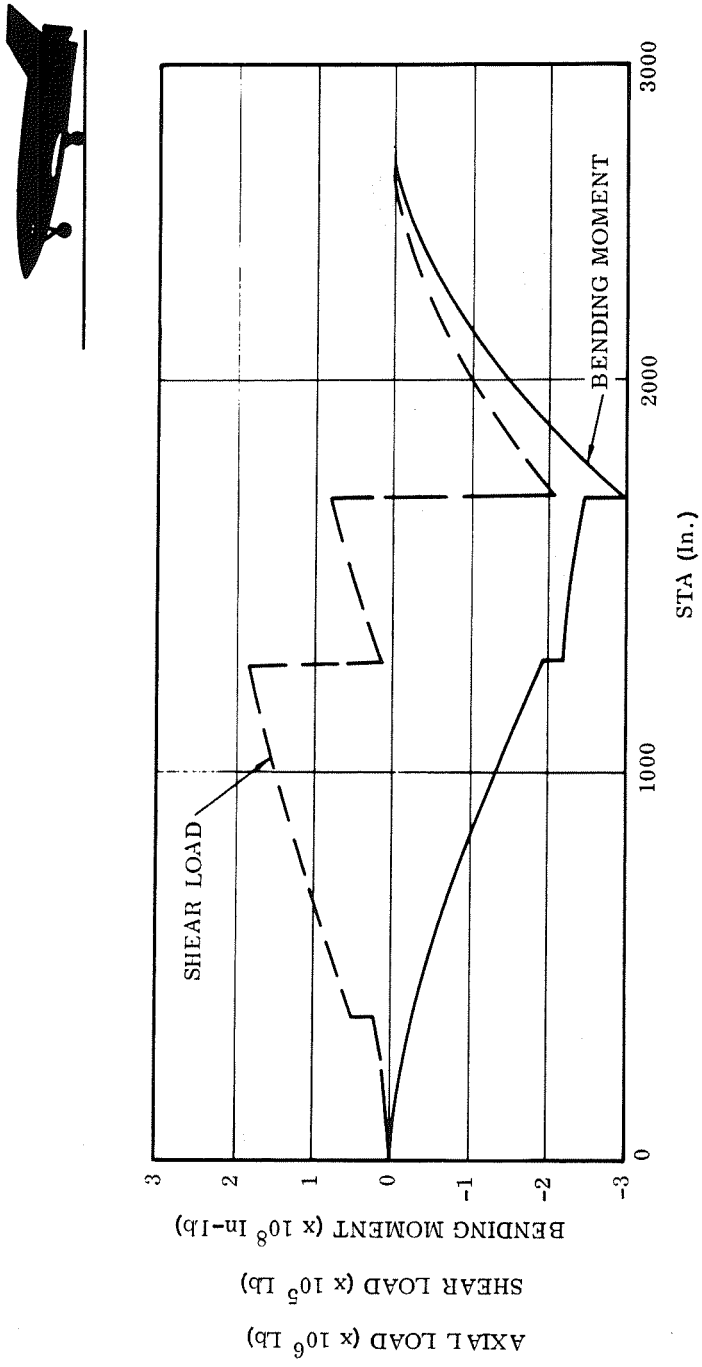

Figure 5-32. FR-3 Booster Two-Point Landing

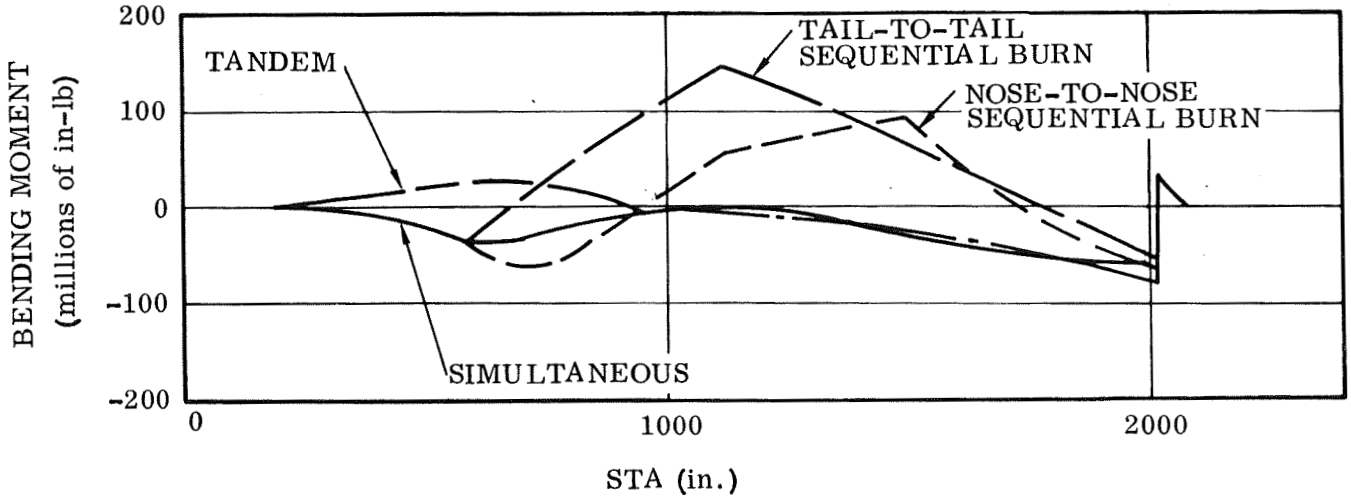

Figure 5-33. FR-3 Orbiter Axial Loads at Maximum αq

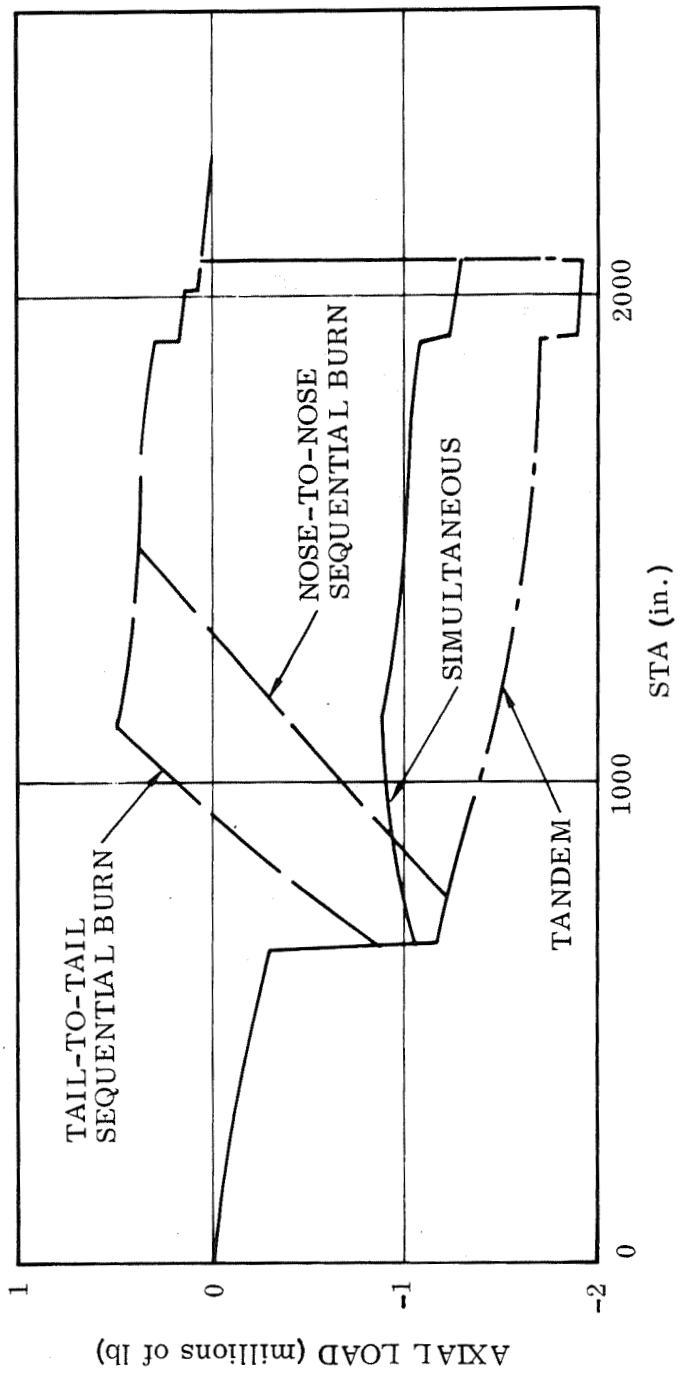

Figure 5-34. FR-3 Orbiter Bending Moments (Booster Burnout)

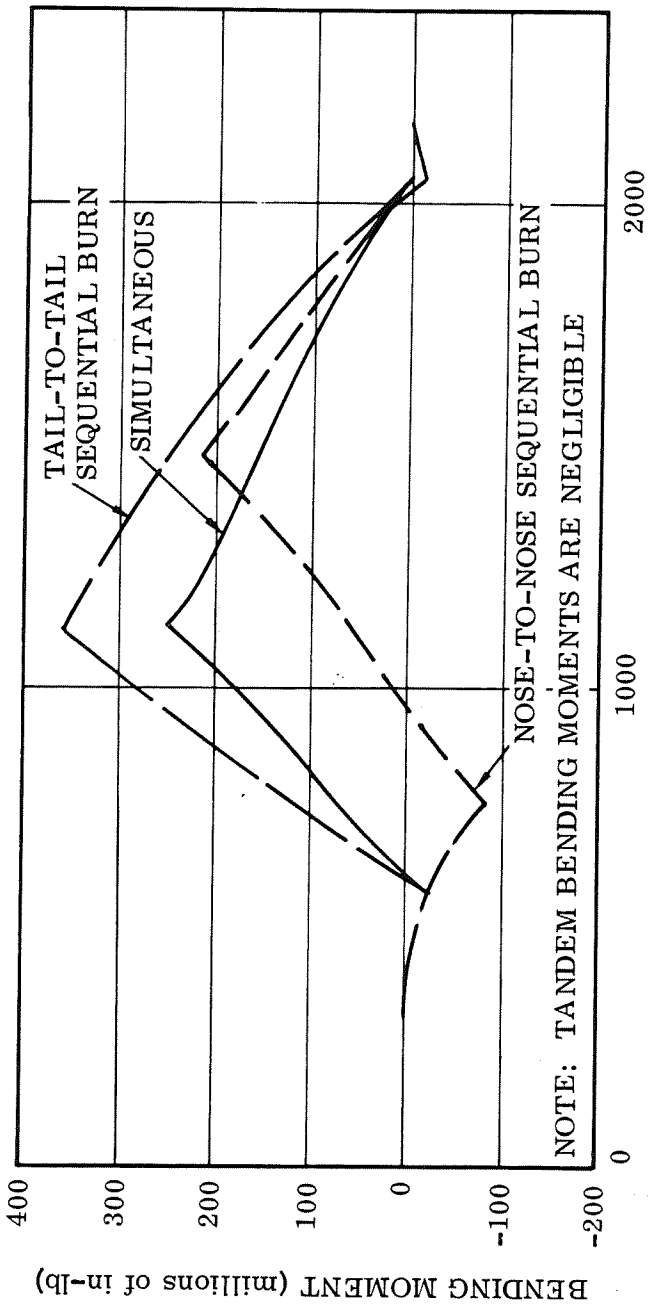

Figure 5-35. FR-3 Orbiter Bending Moments (Booster Burnout)

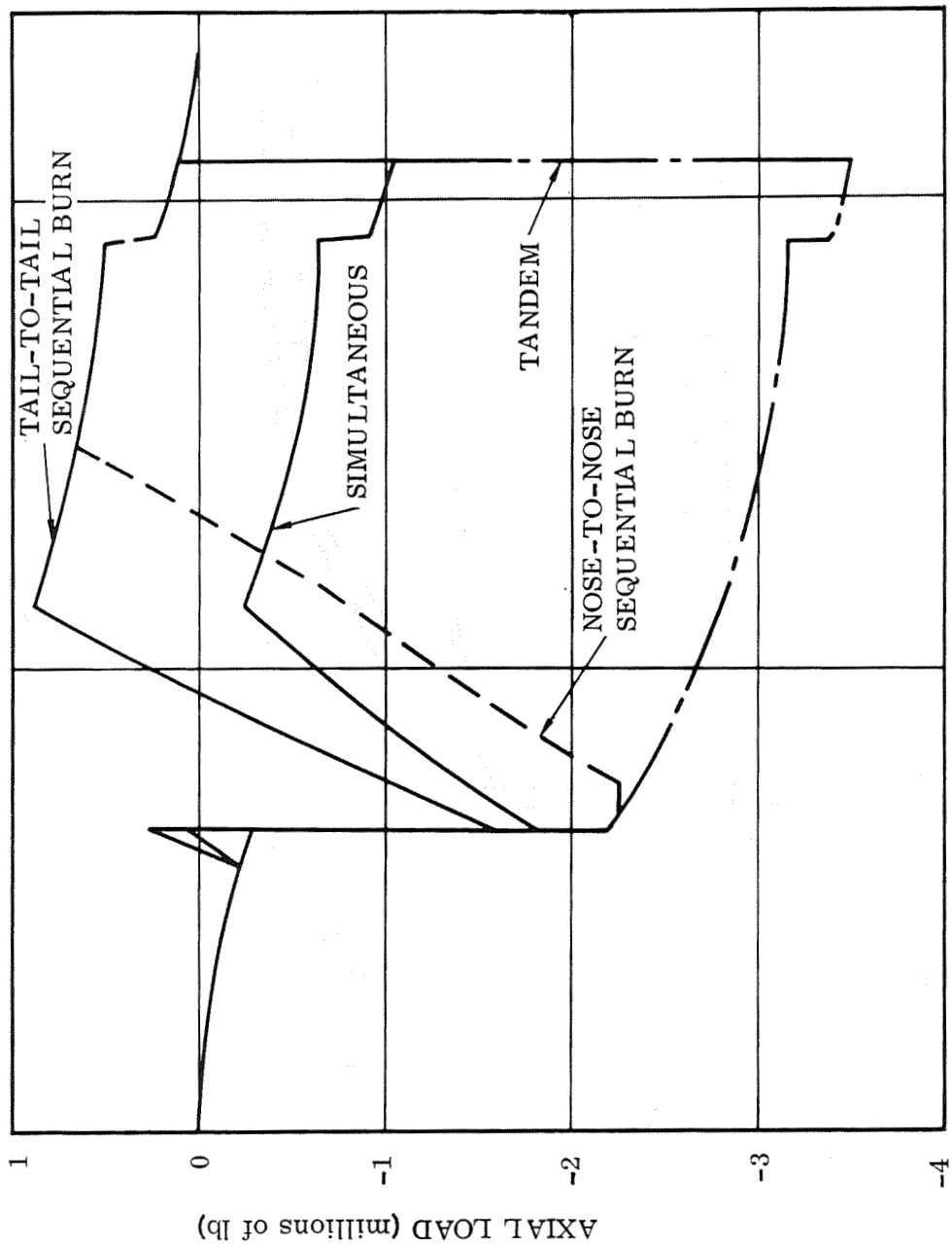

Figure 5-36. FR-3 Orbiter Axial Loads 4g (Booster Burnout)

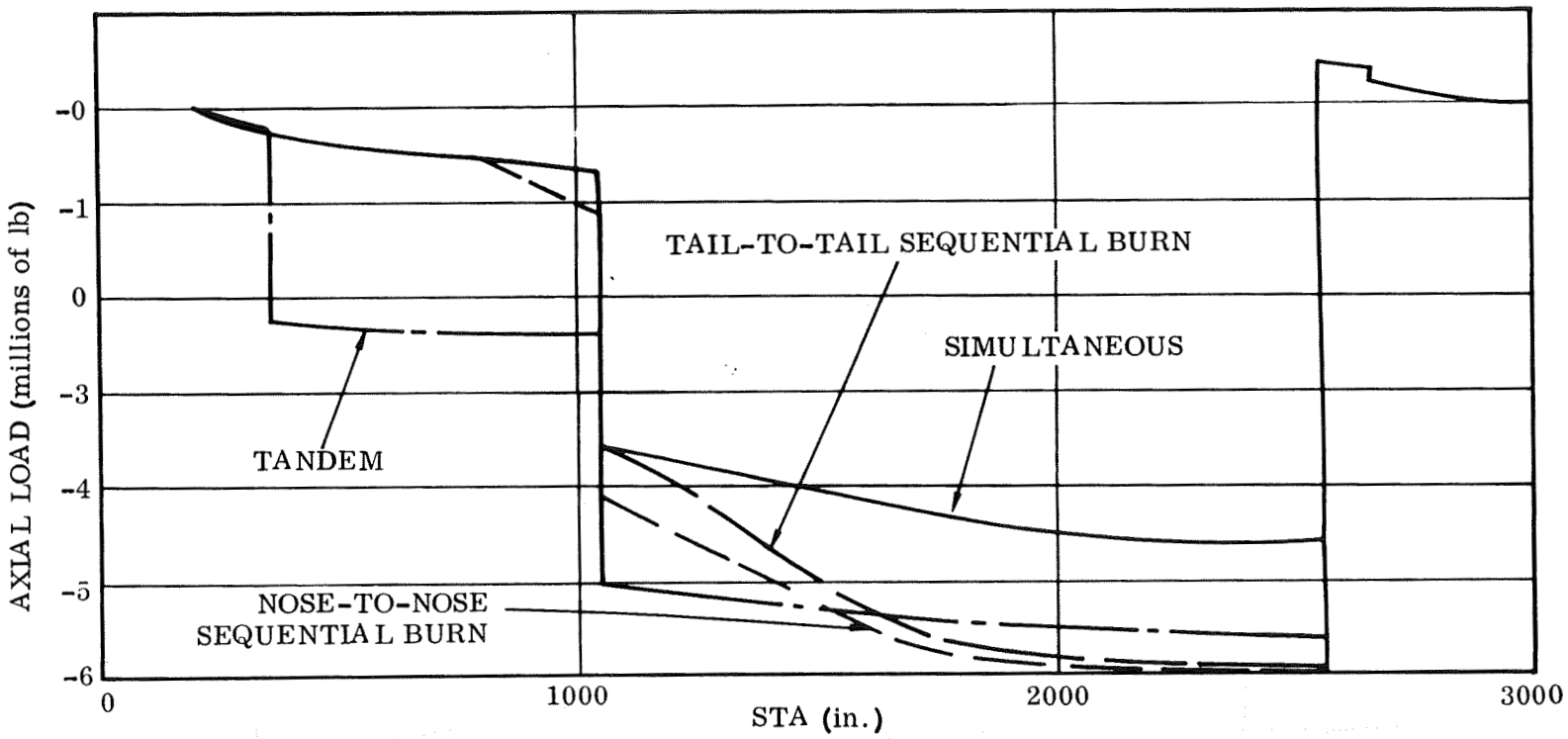

Figure 5-37. FR-3 Booster Axial Loads Maximum αq

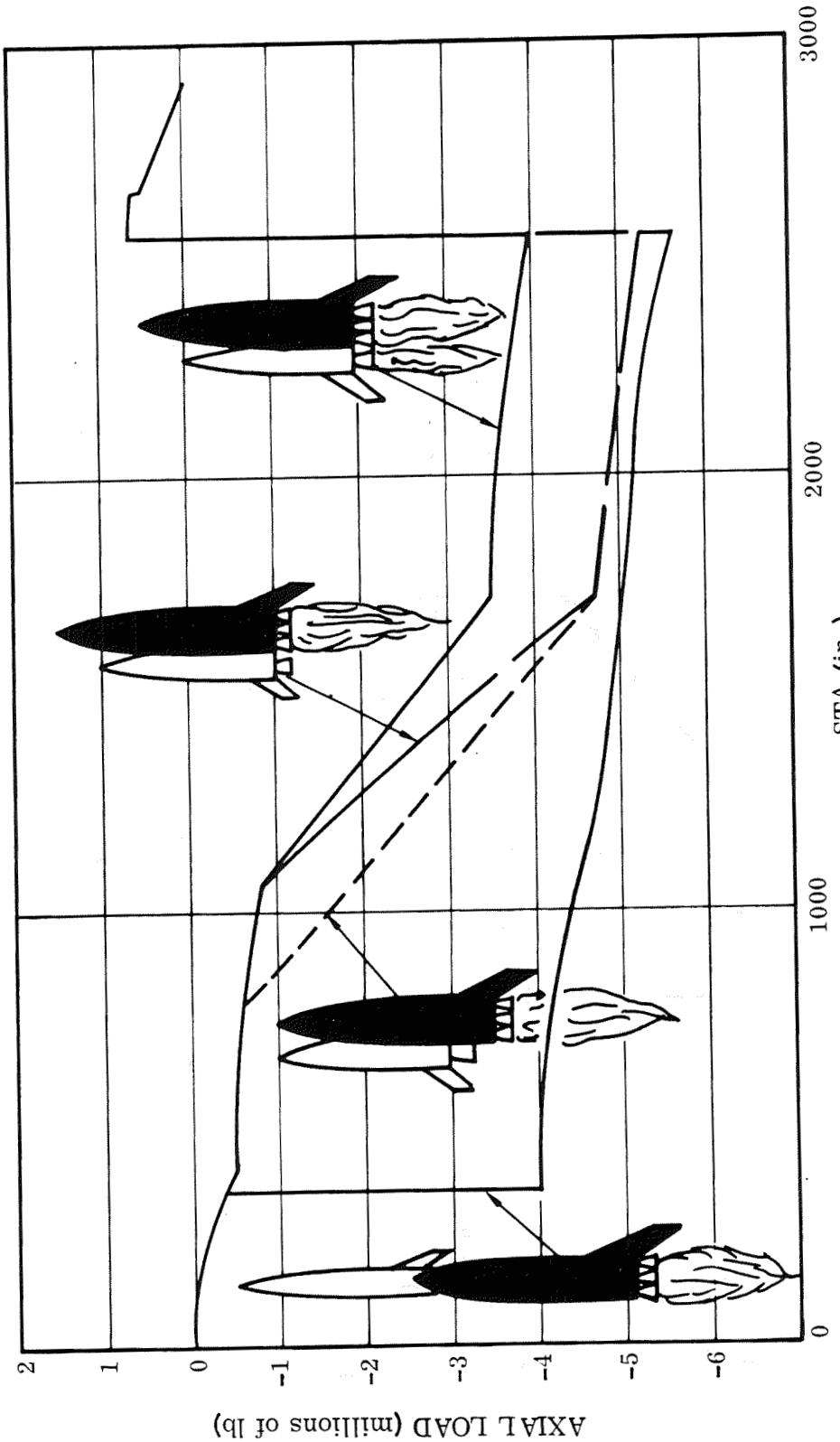

Figure 5-38. FR-3 Booster Axial Loads 4g (Booster Burnout)

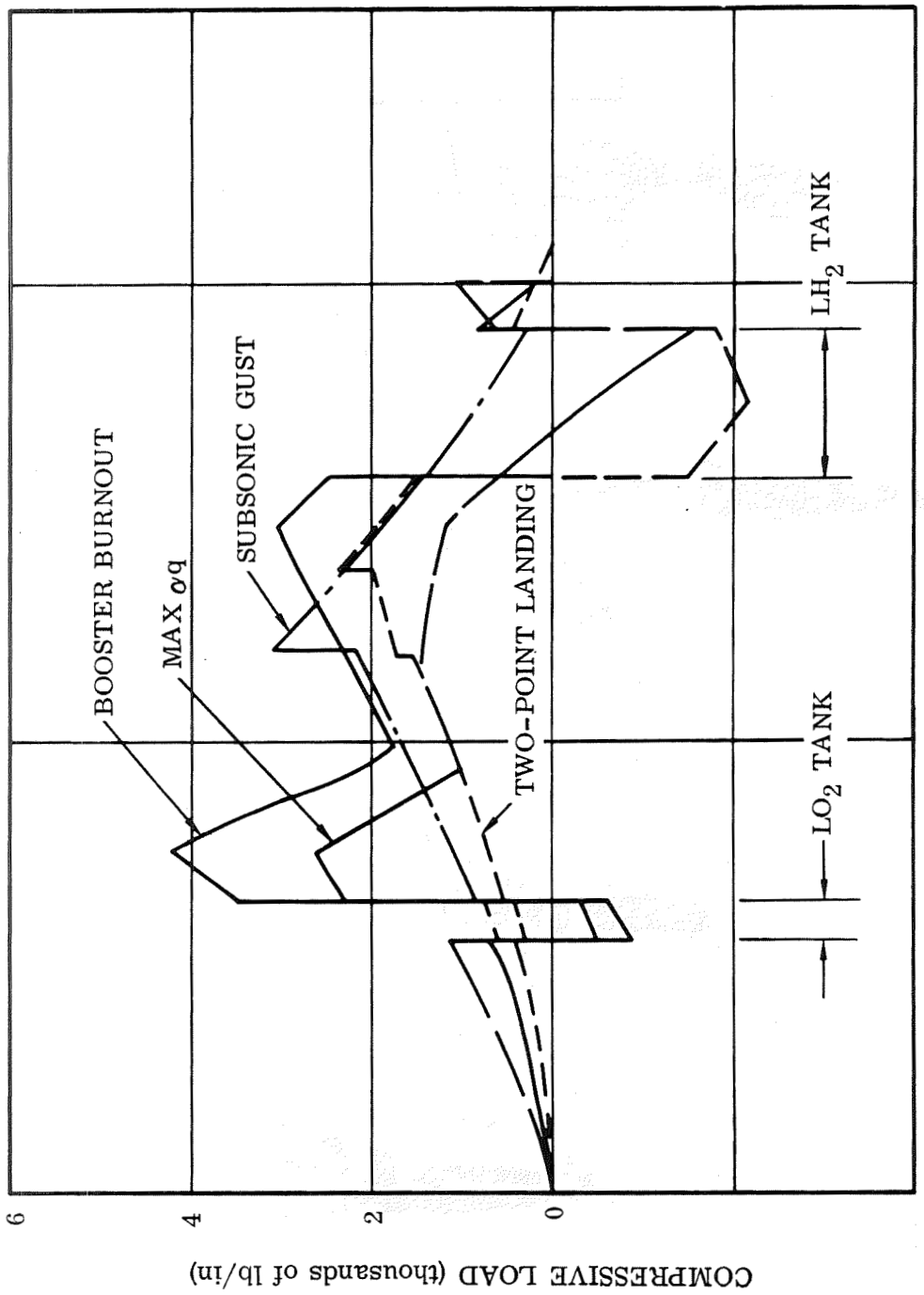

Figure 5-39. FR-3 Orbiter Peak Compression Loads (Nose-to-Nose)

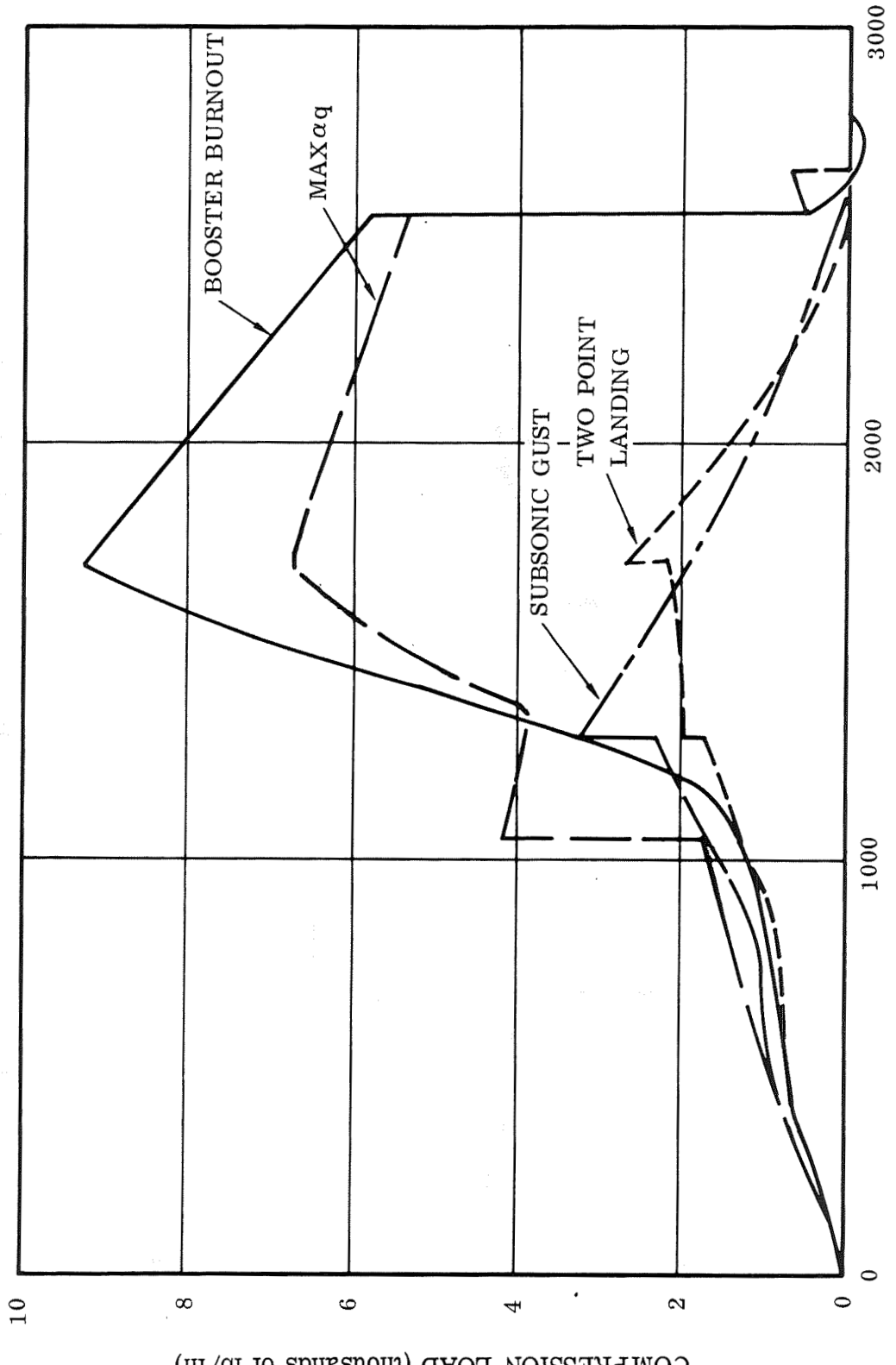

Figure 5-40. FR-3 Booster Peak Compression Loads (Nose-to-Nose)

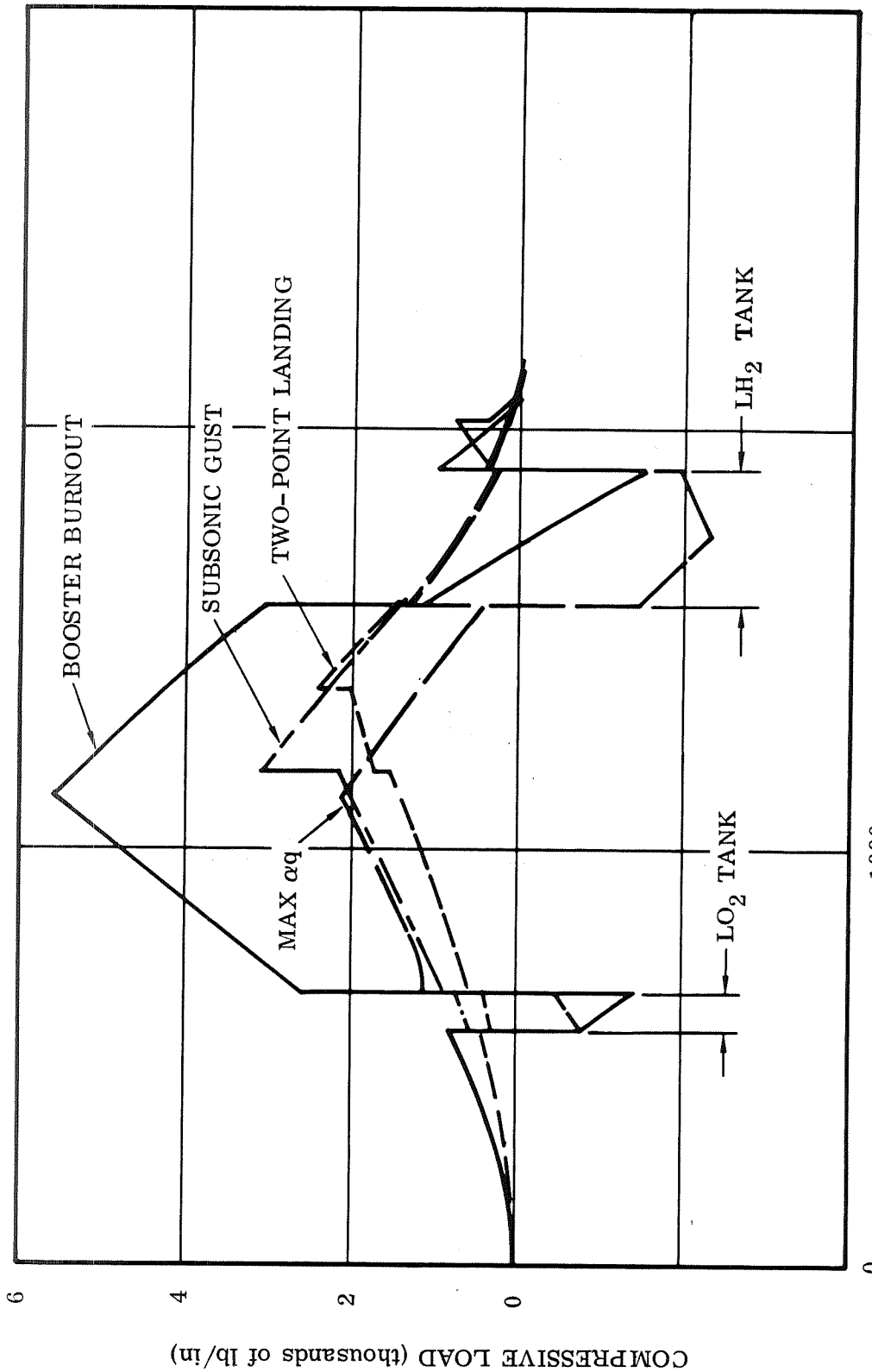

Figure 5-41. FR-3 Orbiter Peak Compression Loads (Tail-to-Tail)

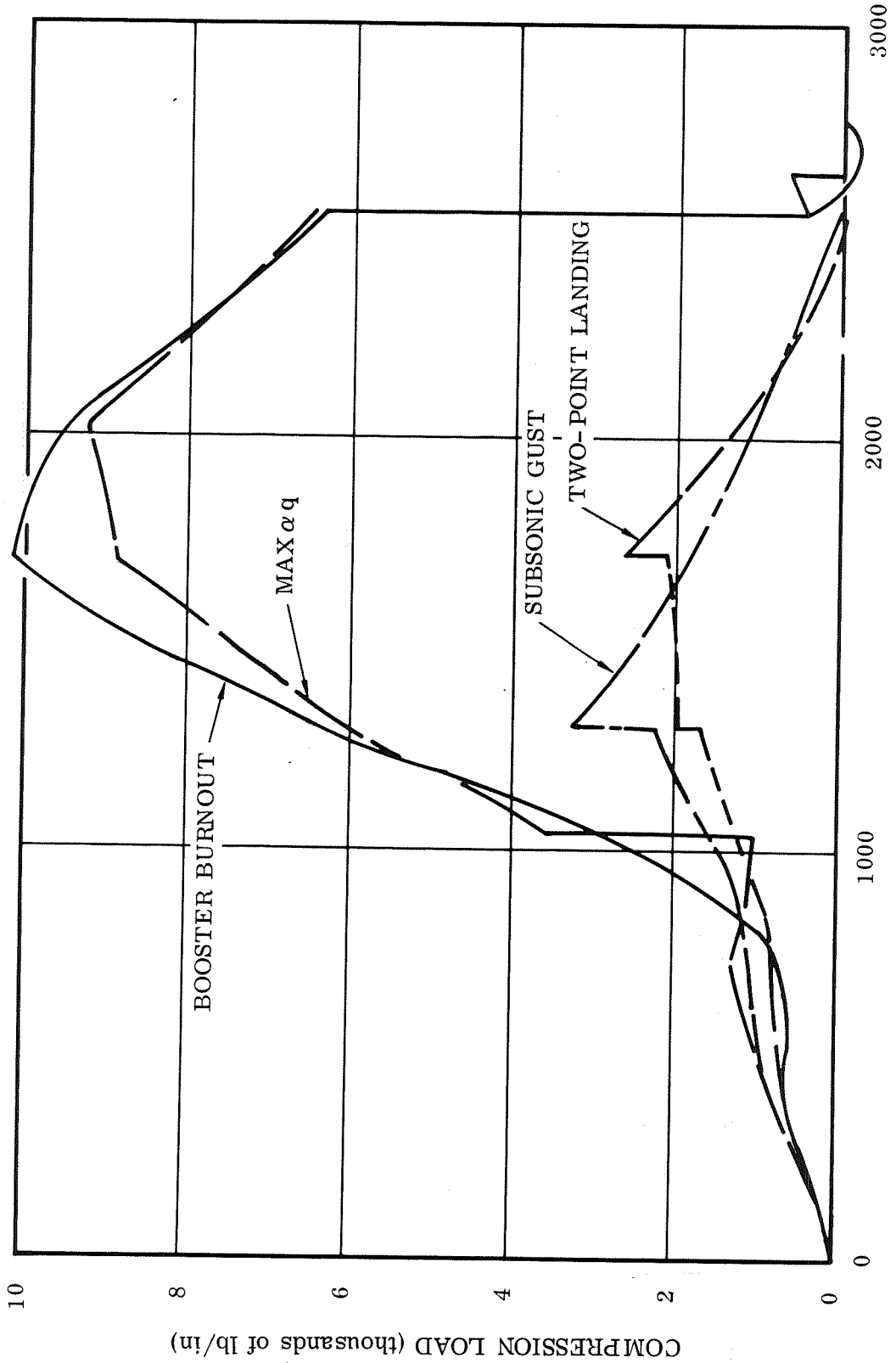

Figure 5-42. FR-3 Booster Peak Compression Loads (Tail-

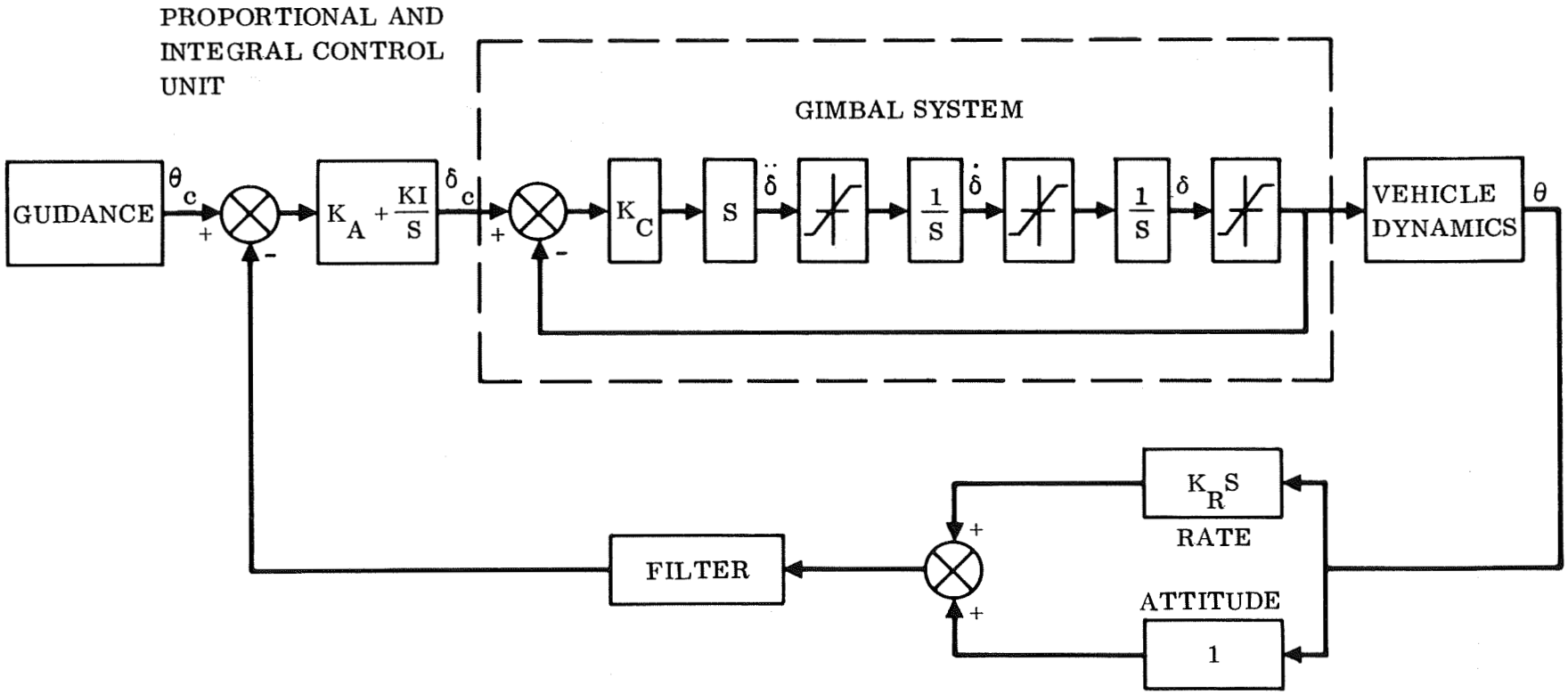

Figure 5-43. Boost Phase Control Block Diagram

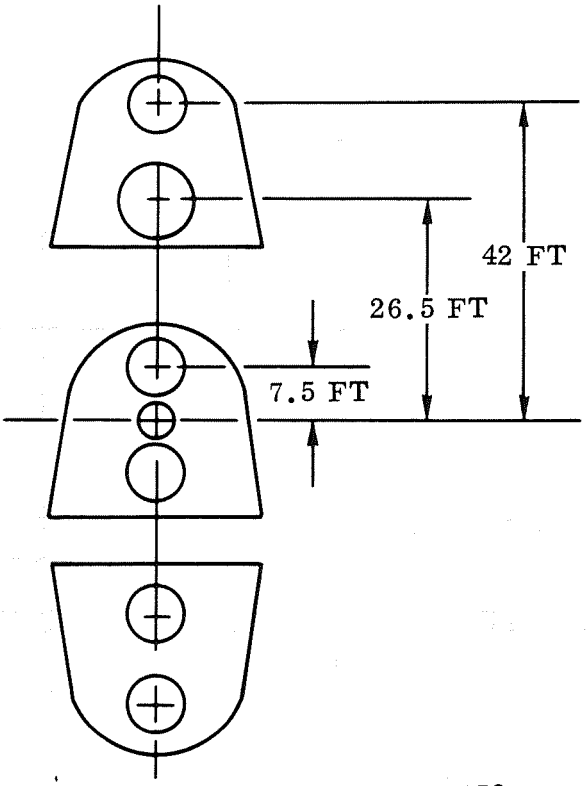

$MOMENT_{\text{Thrust modulation}} = 152$
$(\Delta THRUST)$
$MOMENT_{\text{Thrust gimbal}} = 14.05 \cdot \delta$

Figure 5-44. Thrust Modulation Geometry

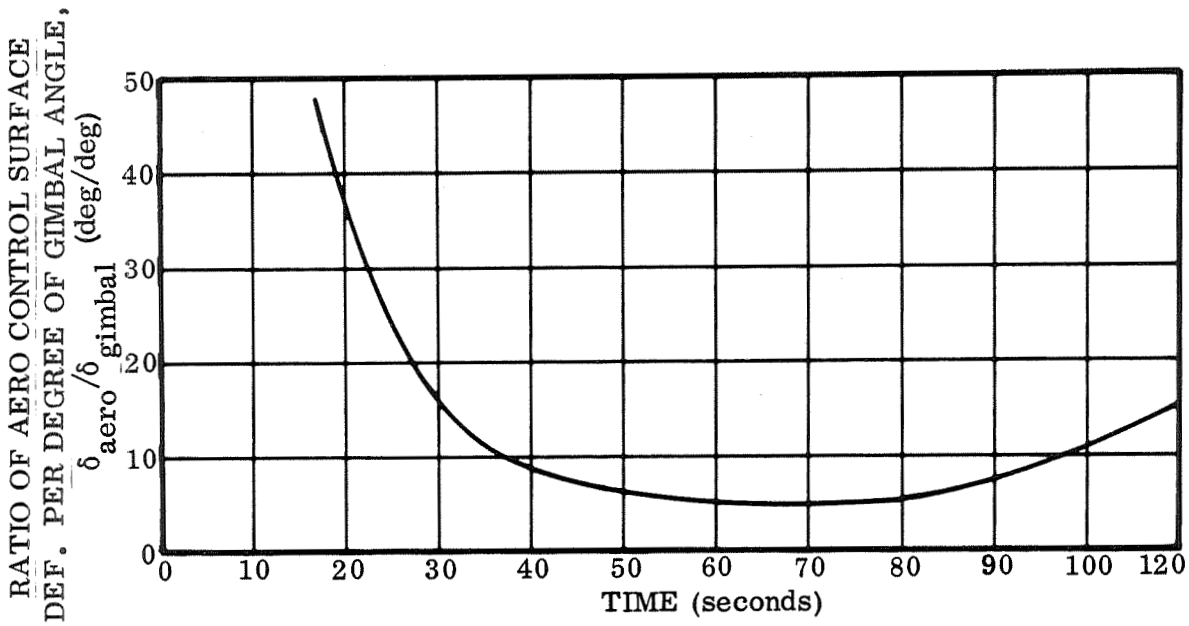

Figure 5-45. Aerodynamic Control Surface Effectiveness

SECTION 6

STRESS ANALYSIS AND SIZING

The structural design requirements, criteria, material properties, and structural concepts depicted in Section 4.7 of Volume II were used to size the structures of the main load-carrying components of the FR-1 orbiter and booster vehicles. These included propellant tanks, payload bay, thrust structure, wing, and stabilizer. Computerized sizing procedures were used in most of these analyses to obtain the gages of structural elements at various stations along each component. A combination of both optimum design and practical manufacturing considerations was used to select materials, structural concepts, and element sizes.

Details of the stress analysis performed and the structural gages obtained for main components are given in the following sections.

6.1 LIQUID OXYGEN TANK

The main LO_2 tanks for both orbiter and booster vehicles are integral tanks of skin/stringer/frame construction with ellipsoidal monocoque domes. The material used is 2219-T87 aluminum alloy. These tanks are designed to withstand a burst pressure equal to 1.5 (23.0 + LO_2 head) without failure and a pressure equal to 1.15 (23.0 + LO_2 head) without yield. In addition, they can sustain ultimate flight loads combined with maximum or minimum operating pressures including the LO_2 heads shown in Figure 6-1. The proof-test condition was assumed to be 1.10 times the maximum ullage pressure plus a hydrostatic head of 1 g in the vertical position. A return flight-tank pressure of 2.0 psig was selected.

The philosophy used in the design of the LO_2 tanks included the criterion of nonbuckling under ultimate load as well as designing the tank for each vehicle to withstand its own net loads. The LO_2 tank net loads on the orbiter vehicle are different than those on the booster vehicle because of substantially different LO_2 heads during boost. Commonality of overall dimensions, structural arrangement, concepts, material, and interfaces with adjacent strucutres was retained between orbiter and booster tanks, but the gages are different.

6.1.1 CRITICAL DESIGN CONDITIONS. A summary of limit applied axial loads, shear flows, and pressures at three tank sections for various conditions is shown in Table 6-1. Burst pressures design the skins, while net compressive loads during the subsonic gust condition dictate the amount of skin stiffening required. The different LO_2 heads in orbiter and booster tanks result in different skin/stringer and lower-dome gages, while the upper dome is identical for both vehicles. The frames

must satisfy shell stability as well as strength requirements for loads introduced by the transverse beams of the vehicle lower surface. The frames are sized for bending from the latter condition. The domes are sized for burst pressures, including LO_2 head for the lower domes.

6.1.2 STRUCTURAL SIZING. The gages and sizes of various elements of the tank structure were determined by computerized sizing programs. Skin, stringer, domes, and frames were included. Table 6-2 gives data on skin and stringer gages for the orbiter and booster tanks. The domes were sized by Program EDOMES, developed by Convair. Both domes have a major-to-minor axis ratio equal to $\sqrt{2}$. Lower values of this ratio for the lower dome should be investigated in future studies. Dome gages are given in Tables 6-3 and 6-4. The frame moments of inertia required for stability were determined by the Shanley criterion increased by 50 percent; those required for strength considerations were calculated from bending moments due to pressure loads on the lower-surface transversal beams. Columns 3 and 4 of Table 6-5 show that the bending case is the most critical. Also shown are typical frame sizes and gages for a frame pitch equal to 30 inches.

6.2 LIQUID HYDROGEN TANKS

The main LH_2 integral tanks for both orbiter and booster vehicles are of skin/stringer/frame construction with external stringers and frames and ellipsoidal monocoque domes. The material used is 2219-T87 aluminum alloy. These tanks are designed for a burst pressure equal to 1.5 (28.5 + LH_2) without failure and a pressure of 1.15 (28.5 + LH_2 head) without yield. They can also sustain ultimate flight loads combined with minimum or maximum operating pressures including the LH_2 heads given in Figure 6-2. During the return flight, the tanks are pressurized with 2 psig. The proof-test condition of the LH_2 tanks was assumed to be 1.10 times the maximum ullage pressure with no hydrostatic head. The design philosophy of the LH_2 tanks included the criterion of non-buckling under ultimate load as well as non-commonality in the gages of orbiter and booster tanks. Commonality of overall dimensions, structural arrangement, concepts, materials, and interfaces with adjacent structures was retained. This allows designing each tank to its own net loads and results in overall weight savings.

6.2.1 CRITICAL DESIGN CONDITIONS. A summary of limit applied loads for various flight and ground conditions at three tank stations is shown in Table 6-6, for both orbiter and booster. The skins are critical for burst pressure, which is larger in the orbiter tank than in the booster tank. The stringers are critical for net compressive loads occurring either during the unpressurized ground wind, maximum αq, or booster burnout condition. The frames must satisfy shell stability as well as strength requirements to distribute concentrated load introduced by the transversal beams on the vehicle lower surface. The latter case is the most critical, and requires larger frame moments of inertia. The domes are critical for burst pressures, which include the effects of fuel head.

6.2.2 STRUCTURAL SIZING. Geometry, load, and material property data was used with computerized sizing programs to obtain gages and sizes of various elements of the tank structure. These included skin, stringers, frames, and domes.

Typical gages of skin and stringers at three tank stations are shown in Table 6-7 for the orbiter and in Table 6-8 for the booster. The domes were sized by Program EDOMES developed by Convair. Dome gages and their distributions are shown in Tables 6-9 and 6-10. The frame moments of inertia were determined by the Shanley criterion, increased by 50 percent to provide shell stability, and by strength considerations due to loads introduced by the lower-surface transversal beams. The latter case is the most critical, as indicated by comparing values in Columns 3 and 4 of Table 6-11. (Frame sizes and gages are also shown.)

6.3 AUXILIARY TANKS

The booster vehicles carry additional propellants in a 25-foot-diameter, 62-foot-long nonintegral tank located in the payload bay. The LH_2 and LO_2 compartments are separated by a common ellipsoidal bulkhead. The tank construction is of the grid-stiffened skin type with external stringers and ribs. The material used is 2219-T87 aluminum alloy. Both tank compartments are designed to withstand burst pressures equal to 1.5 (ullage pressure + hydrostatic head) without failure and pressures equal to 1.15 (ullage pressure + hydrostatic head) without yield. The ullage pressures are 28.5 and 23.0 psi for the LH_2 and the LO_2 compartments, respectively. The hydrostatic heads as a function of time are shown in Figure 6-3. The tanks can sustain flight, transportation, and handling loads while empty without the use of internal pressure. During return flight, however, a nominal gage pressure equal to 2.0 psig is maintained to guarantee positive internal tank pressure at all times. The tank is supported at Stations 81 and 115.8. The aft support reacts transversal and axial loads, while the front support only reacts transverse loads.

6.3.1 CRITICAL DESIGN CONDITIONS. The skins are critical for burst pressures equal to 46 psi ultimate in the LH_2 compartment and 57 psi ultimate in the LO_2 compartment. The stringers were sized to provide a nominal compression capability equal to 100 lb/in. (limit). The domes are critical for burst pressures, which include the effects of hydrostatic head.

6.3.2 STRUCTURAL SIZING. Member sizes are shown in Table 6-12; dome gages and their distribution are given in Table 6-13.

6.4 CENTER BODY STRUCTURE

The center body structure is located between the aft end of the LO_2 tank and the forward end of the LH_2. The main difference between the orbiter and booster structures in this area is that the orbiter has payload bay doors. The use of doors in the orbiter also

requires heavy longerons at the edges of the opening. The rest of the shell perimeter is skin/stringer/frame construction in the orbiter. The open frames provide discrete elastic restraints to help stabilize the main longerons for compressive loads. The booster structure is an uninterrupted shell with continuous skin and stringers and ring-type frames. The material used in both vehicles is 2219-T87 aluminum alloy.

6.4.1 CRITICAL DESIGN CONDITIONS. Net loads at six stations for three load conditions are given in Table 6-14. The longerons used in the orbiter are critical for ground wind loads. The forward part of the orbiter body center structure is critical for the booster burnout condition, while the aft part is critical for maximum αq loads. The reverse is true of the booster; the booster burnout condition is critical in the aft portion and the maximum αq loads are critical in the front. Refer to Figures 5-15 and 5-16.

6.4.2 STRUCTURAL SIZING - ORBITER. The payload bay longerons were sized for a compressive load of 300,000 pounds each, corresponding to a 2,000 lb/in. ultimate load during the ground-wind condition. The longeron was analyzed as a beam-column on elastic supports. Figure 6-4 shows the model idealization and a feasible combination of frame and longeron section properties that will provide the required load capability. The maximum design compressive allowable stress used was 45,000 psi for 2219-T87 aluminum alloy.

The upper longerons, at the forward end of the payload bay and adjacent to the payload bay doors, make a transition to the integral skin/stringer LO_2 tank as shown in Figure 6-5. Primary loads and stresses in the longeron and transition structure are axial, but secondary bending stresses are induced because of thermal effects as the tank is filled with LO_2 and radial contraction, due to the 400° F temperature drop, takes place. Conservatively neglecting any relief due to pressurization, the thermal contraction of the LO_2 tank was calculated to be 0.80 inch. As shown in Figures 6-5 and 6-6, the longeron load is assumed distributed into the LO_2 tank at a 45-degree angle by the transition structure. The transition structure was idealized as a cantilever beam of non-uniform shape and constant cross-sectional area equal to the longeron area. The idealized beam was assumed cantilevered from the payload bay closing bulkhead and acted upon by a radial load sufficient to cause a 0.80-inch deflection at the forward end. Secondary bending stresses in the transition structure, based on no skin buckling, are shown in Table 6-15. To reduce the load and the resulting bending stresses caused by the 0.80-inch contraction of the LO_2 tank, the forward end of the transition structure must be made more flexible. This may be accomplished by reducing the height of the stringers or by eliminating the stringers at the forward end. For preliminary sizing of the payload bay upper longerons and stringers at the closing bulkhead, the allowable axial compressive stress was reduced by 10,000 psi to account for secondary bending effects.

Each of the six body stations analyzed was considered as an open section of a multiple longeron shell. A computerized sizing procedure was used to determine the sizes of

skins and stringers required to take the critical loads. Because of the open nature of the body cross-section, a sensitivity study was initially performed to investigate the influence of neutral axis position on total cross-sectional area required. This study showed that neutral axes located in correspondence with tank longitudinal axis resulted in lower areas in the front, while neutral axes below the tank axis yielded smaller cross-sectional areas toward the aft end. The results of this study are shown in Figure 6-7. All the curves are higher toward the ends because lower allowable stresses were used to account for thermal stresses due to the proximity of cryogenic tanks. Typical values of stringer sizes and skin gages are given in Table 6-16.

A redundant frame analysis was performed on the payload compartment closing bulkheads for the redistribution of shear and axial load around the door cutout. It was determined that a ring-type frame was lighter than a fully webbed bulkhead. Typical frame cross-sectional dimensions and gages are shown in Figure 6-8.

6.4.3 STRUCTURAL SIZING - BOOSTER. The booster centerbody structure differs from that for the orbiter since there are no doors or payload bay longerons. The body structure in this area consists of an uninterrupted shell with continuous stringers, skin, and ring-type frames. A parametric study was conducted to investigate the effects of neutral axis position on total shell cross-sectional area. The results are shown in Figure 6-9; typical values of stringer areas and skin gages are given in Table 6-17.

6.5 AFT BODY STRUCTURE

The main subcomponents of the aft body structure are the thrust and holddown beams, the cylindrical skirt, the longerons, the aft end closure bulkhead, and the forward thrust ring. These structures are schematically shown in Figure 6-10.

6.5.1 THRUST BEAMS. The criteria, material, and type of construction used in the thrust beams are given in Table 6-18. The applied loads and corresponding reactions for the maximum thrust condition are given in Figure 6-11, and the resulting internal loads are given in Figures 6-12 and 6-13. The gages of webs and cross-sections of caps shown in Figure 6-14 correspond to the loads and criteria given previously.

6.5.2 HOLDDOWN BEAMS. The holddown beams consist of a corrugated titanium web welded to a light titanium cap, which is bonded to unidirectional aluminum-boron flange members. The applied loads for the ground-wind condition are shown in Figure 6-15; the resulting internal loads and gages of webs and caps are shown in Figure 6-16.

6.5.3 THRUST SKIRT. The thrust skirt is a stiffened titanium shell with integral-T stringers. The critical design condition is maximum engine thrust, which imposes

are average compressive load equal to 3,400 lb/in. ultimate. A typical skin/stringer cross-section is shown in Figure 6-17.

6.5.4 FORWARD THRUST RING. The forward thrust ring consists of a shear-carrying, corrugated titanium web welded to titanium caps which in turn are bonded to aluminum/boron flange members. The three ctitical loading conditions and the idealized ultimate applied loads are:

a. Maximum αq (high fin loads applied to the thrust ring).

b. Ground wind (high hold-down fitting kick loads).

c. Maximum thrust (high thrust-beam kick loads).

Internal loads for the three critical loading conditions and component sizes are shown in Table 6-19.

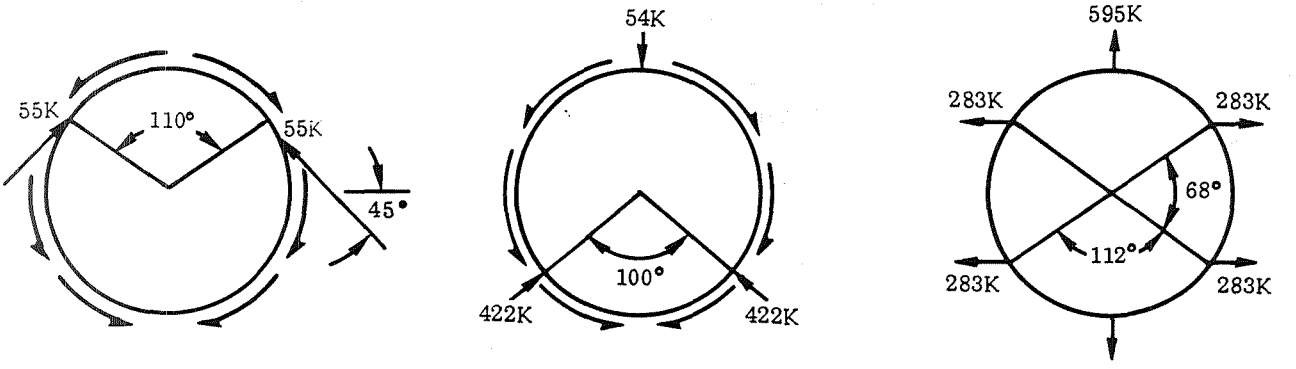

MAXIMUM αq GROUND WIND MAX. ENGINE THRUST

6.6 WING

The wing is of the variable-geometry type consisting of a titanium alloy wing box and aluminum alloy leading and trailing edges. The spars are located at 10 and 70 percent of the chord, and define the width of the wing box. The wing profile is NACA 4421 at the root and NACA 4418 at the tip. The upper and lower covers extend from spar to spar and consist of skin-stiffened concepts, the upper cover having integral-T stringers and the lower cover using integral blades. Integral-T stringers were used to provide a concept with higher structural efficiency in compression which is critical for the upper cover. The lower cover is primarily designed in tension, with the blade stringers providing capability for a compressive load equal to 40 percent (minimum) of the tensile load. The webs are stiffened skin panels and are attached to the covers by a T cap.

The wing ribs are trusses consisting of diagonals attached to rib caps. The rib caps are attached to the wing skin/stringers with shear clips at every other stringer. Intercostals attach the caps to the skin near the front and rear spars. The cross-section of the diagonals is cruciform, and a Z section is used for the caps. All rib members are made of titanium.

Parametric studies were conducted to investigate various wing spans, exposed areas, thickness ratios, planform taper, and wing-box materials. The results of this parametric study indicated that the wing box was lighter in titanium than in aluminum and also yielded more manageable gages toward the wing root. It was also found that the wing box weight decreased with wing thickness and was a minimum at around 24 percent, with 21 percent being slightly heavier. A 21-percent thickness was selected because it led to a better wing stowage due to the smaller volume and also provided larger clearances with surrounding structure. Subsequently, several wing thickness ratios at the tip were investigated, while holding a 21 percent thickness at the root. An 18-percent thickness at the wing tip provided the lightest wing box. The study also showed that smaller exposed areas, spans, and planform tapers lead to smaller wing unit weights. Typical results of this study are shown in Table 6-20. The wing selected for the FR-1 vehicle had the following characteristics (one panel only).

Exposed plan area	880 ft^2
Plan taper ratio	0.8
Structural span	822 in. (pivot to tip)
Thickness ratio	0.21 (root) to 0.18 (tip)
Incidence	6 deg (reference body lower surface)

6.6.1 CRITICAL DESIGN CONDITION. The critical design condition for the wing is the subsonic gust condition, which generates a limit load factor equal to 2.32 g at the vehicle center of gravity. The lift acting on each wing panel is equal to 36 percent of the total. The resulting shear, bending and torsion moments are given in Table 6-21. Wing geometric data at each rib station is also shown.

The primary rib loads result from airloads and crushing due to wing bending. The airload is distributed according to the pressure distribution for the NACA 4421 airfoil with a lift coefficient of 1.25. The crushing load is assumed to act uniformly over the wing box chord. For most ribs, the crushing load is the major part of the total load. As the bending load decreases toward the outboard end, the airload becomes an increasingly higher percentage of the total load. Aeroelastic considerations for the wing are discussed in Section 7.

6.6.2 STRUCTURAL SIZING. A computerized multiple station analysis for sizing of wing boxes was used in the parametric study previously mentioned as well as in determining the gages of cover skins, stringers, and webs at various stations of the selected wing. The results are shown in Tables 6-22, 6-23, and 6-24.

The rib diagonals were sized for column action and crippling. The caps were sized for combined axial load and bending (tension and crippling). Table 6-25 presents the required cross-sectional areas of the rib members. The leading edge consisted of a corrugation-stiffened skin of aluminum alloy with ribs every 20 inches.

6.7 FIN

The fin consists of a leading edge, a main load-carrying box extending from 27.3 to 58.5 percent of the chord, and a rudder with a hinge line at 65 percent of the chord. Orbiter and booster fins are the same size and have the same overall structural arrangement. They differ mainly in the fact that the orbiter fin is an insulated 8-1-1 titanium structure with a coated tantalum leading edge, while the booster fin is a "hot" 718 Ni alloy structure. The fin-box covers were made of stiffened skins with Z stringers, and the webs of spars and ribs are corrugated panels to alleviate potential thermal stresses. The leading edges were segmented to accommodate thermal expansion. The rudder consists of a two-spar structure with corrugated webs on spars and ribs and with corrugation-stiffened covers.

6.7.1 CRITICAL DESIGN CONDITIONS. The critical load on the fins occurs during maximum αq, while the structure is at room temperature. Table 6-26 shows load and geometric data. The maximum temperature condition is not critical for sizing the structure because it has small loads associated with it, but it dictates the heat shield material and insulation requirements in the orbiter fin and the structural material for the booster fin.

6.7.2 STRUCTURAL SIZING. The structural boxes for both orbiter and booster fins were sized by a computerized multiple station analysis. This included gages of skin, stringers, and spar and rib webs. The results are shown in Tables 6-27, 6-28, and 6-29.

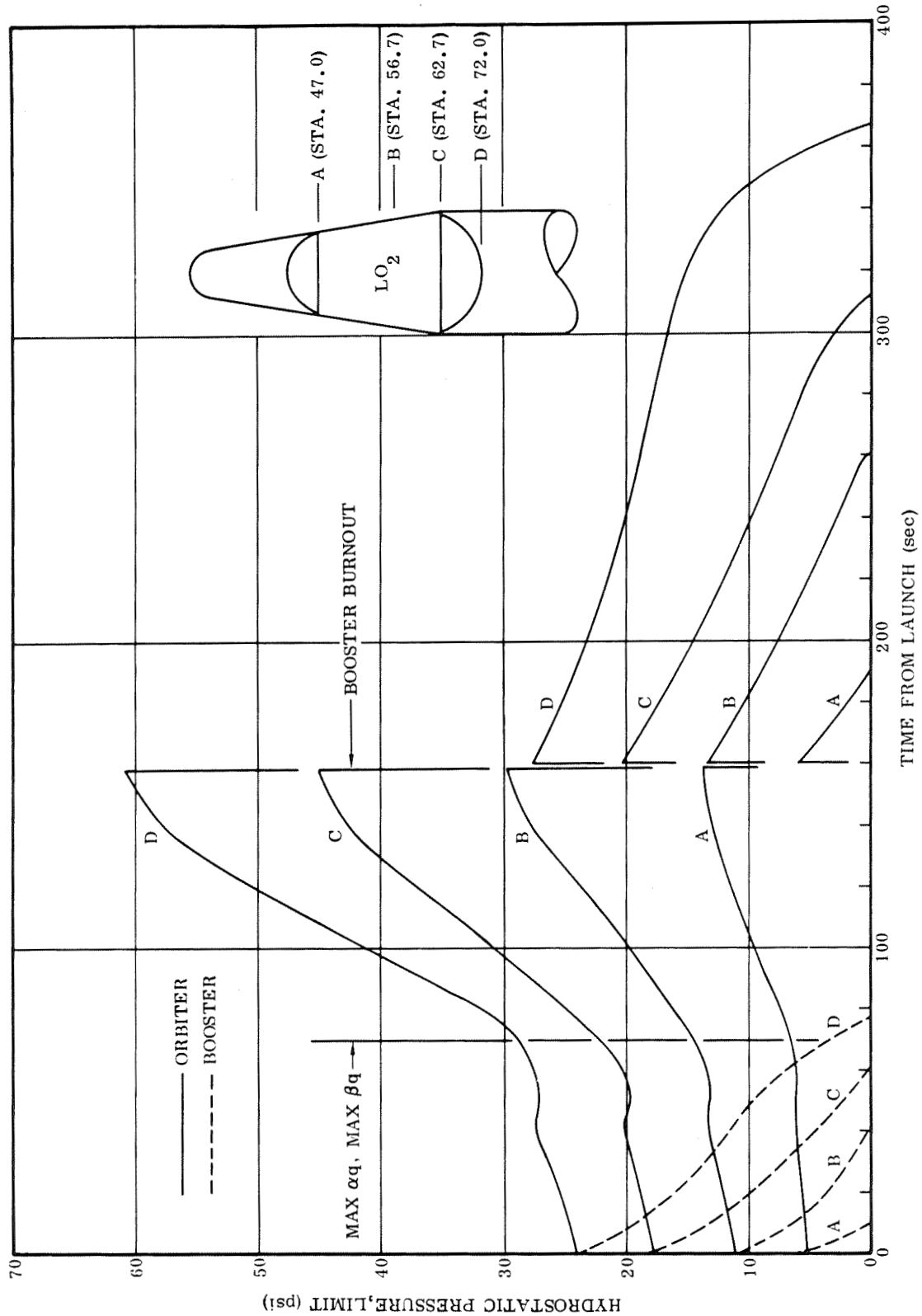

Figure 6-1. FR-1 LO_2 Tank Hydrostatic Pressures During Boost

Table 6-1. Summary of Integral LO_2 Tank Loads (Limit)

Condition	Point	P (psi)	Station 47.0				Station 54.6				Station 62.7			
			Orbiter		Booster		Orbiter		Booster		Orbiter		Booster	
			N_x (lb/in.)	N_{xy} (lb/in.)	N_x (lb/in.)	N_{xy} (lb/in.)	N_x (lb/in.)	N_{xy} (lb/in.)	N_x (lb/in.)	N_{xy} (lb/in.)	N_x (lb/in.)	N_{xy} (lb/in.)	N_x (lb/in.)	N_{xy} (lb/in.)
Ground Wind	1	0.0	-111	14	-128	14	-124	16	-138	16	-139	19	-150	19
Subsonic Gust	1	2.0	-633	359	-549	359	-792	362	-692	362	-962	370	-833	370
Subsonic Gust	4	2.0	834	359	724	359	983	362	853	362	1134	370	984	370
2-Pt Landing	1	2.0	-500	293	-433	293	-637	343	-552	308	-786	362	-678	326
2-Pt Landing	4	2.0	588	293	511	293	730	343	635	308	880	362	762	326
Max αq	1	23.0	-150	15	-66	140	-200	46	-43	97	340	122	-59	28
Max αq	4	23.0	-335	15	-432	140	-357	46	-502	97	-381	122	-535	28
Max βq	2	23.0	-482	139	-491	160	-566	111	-572	130	-524	57	-616	62
Max βq	3	23.0	-1	139	50	160	17	111	-16	130	14	57	-24	62
Booster Burnout	1-4	23.0	-374	0	-443	0	-405	0	-460	0	-424	0	-473	0
			Burst Pressure = 36.6×1.5=55 psi (Booster Burnout)		30.8 × 1.5 = 46 psi (Liftoff)		Burst Pressure = 56.0×1.5=84 psi (Booster Burnout)		37 × 1.5 = 55.5 psi (Liftoff)		Burst Pressure = 68.2×1.5=103 psi (Booster Burnout)		40.8×1.5=61.5 psi (Liftoff)	

NOTES: 1. P is ullage pressure (used to relieve applied compressive loads N_x, but additive to tensile N_x).

2. Loads are derived from Section 5.1.3. and include dynamic amplification factors.

3. N_{xy} is applied limit shear flow.

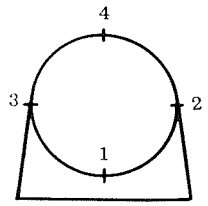

POINTS ON TANK SECTION

Table 6-2. FR-1 Integral LO_2 Tanks — Skin Stringer Element Sizes

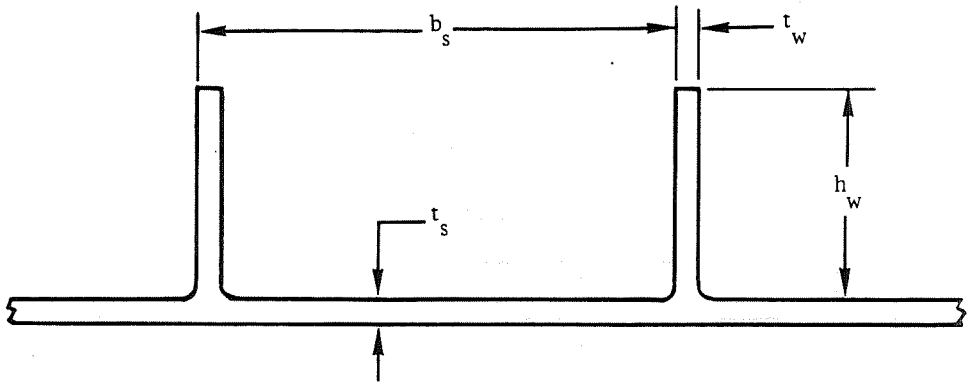

MATERIAL: 2219-T87 aluminum alloy

Condition	Station (ft)	Orbiter				Booster			
		t_s* (in.)	b_s (in.)	t_w (in.)	h_w (in.)	t_s* (in.)	b_s (in.)	t_w (in.)	h_w (in.)
Subsonic Gust	47.0	0.115	5.0	0.105	1.50	0.098	9.0	0.100	1.70
	54.6	0.195	5.0	0.155	1.35	0.129	9.0	0.110	1.60
	62.7	0.253	5.0	0.205	1.25	0.152	9.0	0.120	1.50

*Skin thickness t_s is sized for the burst pressures shown in Table 6-1.

Table 6-3. FR-1 Integral LO_2 Tank - Upper Dome

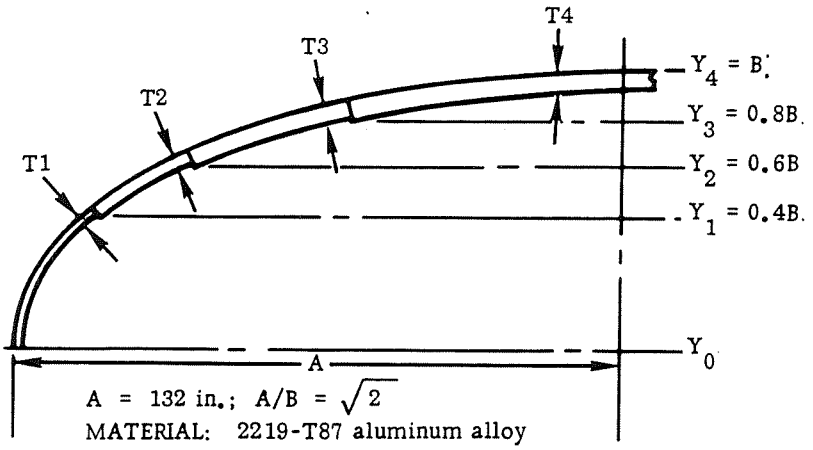

Thickness (in.)	Orbiter	Booster
T1	0.036	0.036
T2	0.036	0.036
T3	0.042	0.042
T4	0.051	0.051

Table 6-4. FR-1 Integral LO_2 Tank - Lower Dome

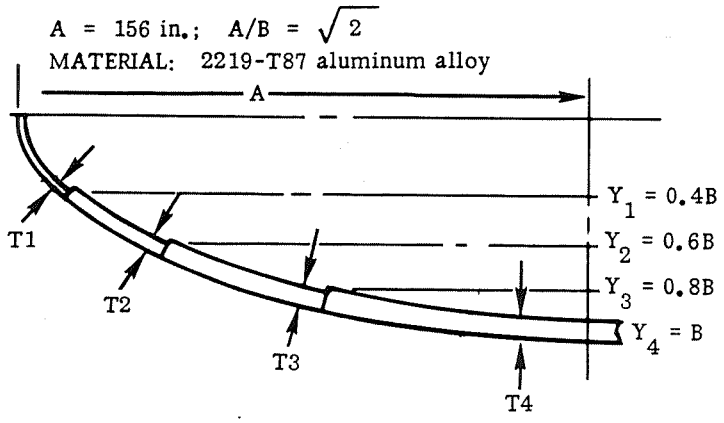

Thickness (in.)	Orbiter	Booster
T1	0.179	0.092
T2	0.199	0.100
T3	0.230	0.116
T4	0.278	0.140

Table 6-5. LO_2 Tank Internal Frames - Orbiter and Booster

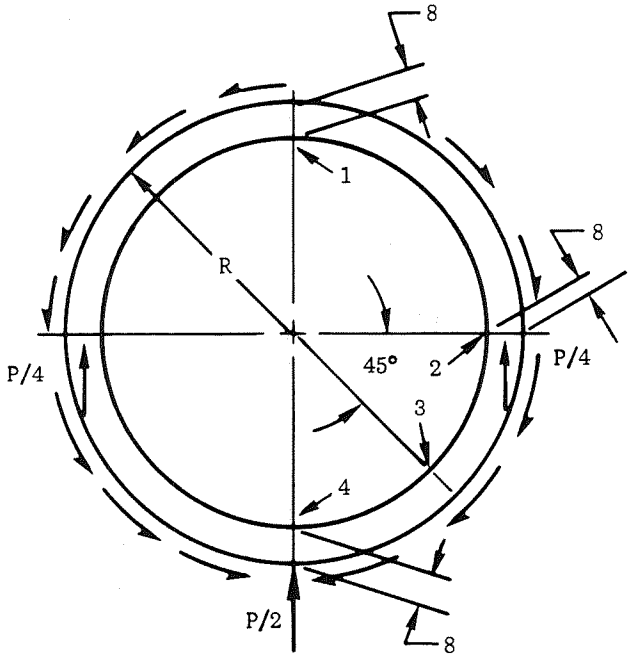

P = 1.5 (30) (396) = 17,650 lb
FRAME PITCH = 30 in.

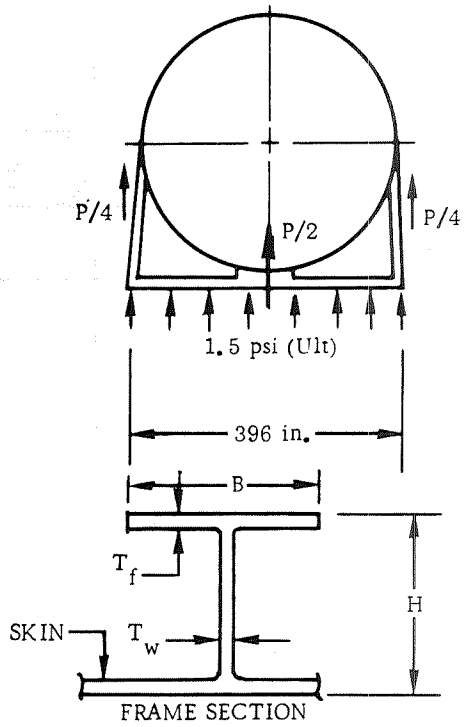

Station (ft)	Point	I Required		Frame Dimensions				
		Stability ($in.^4$)	Bending ($in.^4$)	H (in.)	B (in.)	T_f (in.)	T_w (in.)	Area ($in.^2$)
47.0 R = 132 in.	1	1.7	10.4	8.0	2.95	0.080	0.065	1.00
	2		8.3	8.0	2.80	0.067	0.053	0.81
	3		0.9	8.0	2.80	0.060	0.050	0.74
	4		14.6	8.0	3.05	0.113	0.085	1.37
54.6 R = 146 in.	1	2.3	11.5	8.0	3.00	0.090	0.067	1.08
	2		9.2	8.0	2.86	0.073	0.058	0.89
	3		1.0	8.0	2.80	0.060	0.050	0.74
	4		16.1	8.0	3.08	0.123	0.092	1.50
62.7 R = 156 in.	1	2.8	12.3	8.0	3.03	0.095	0.072	1.15
	2		9.9	8.0	2.90	0.078	0.062	0.95
	3		1.1	8.0	2.80	0.060	0.050	0.74
	4		17.2	8.0	3.20	0.128	0.096	1.59

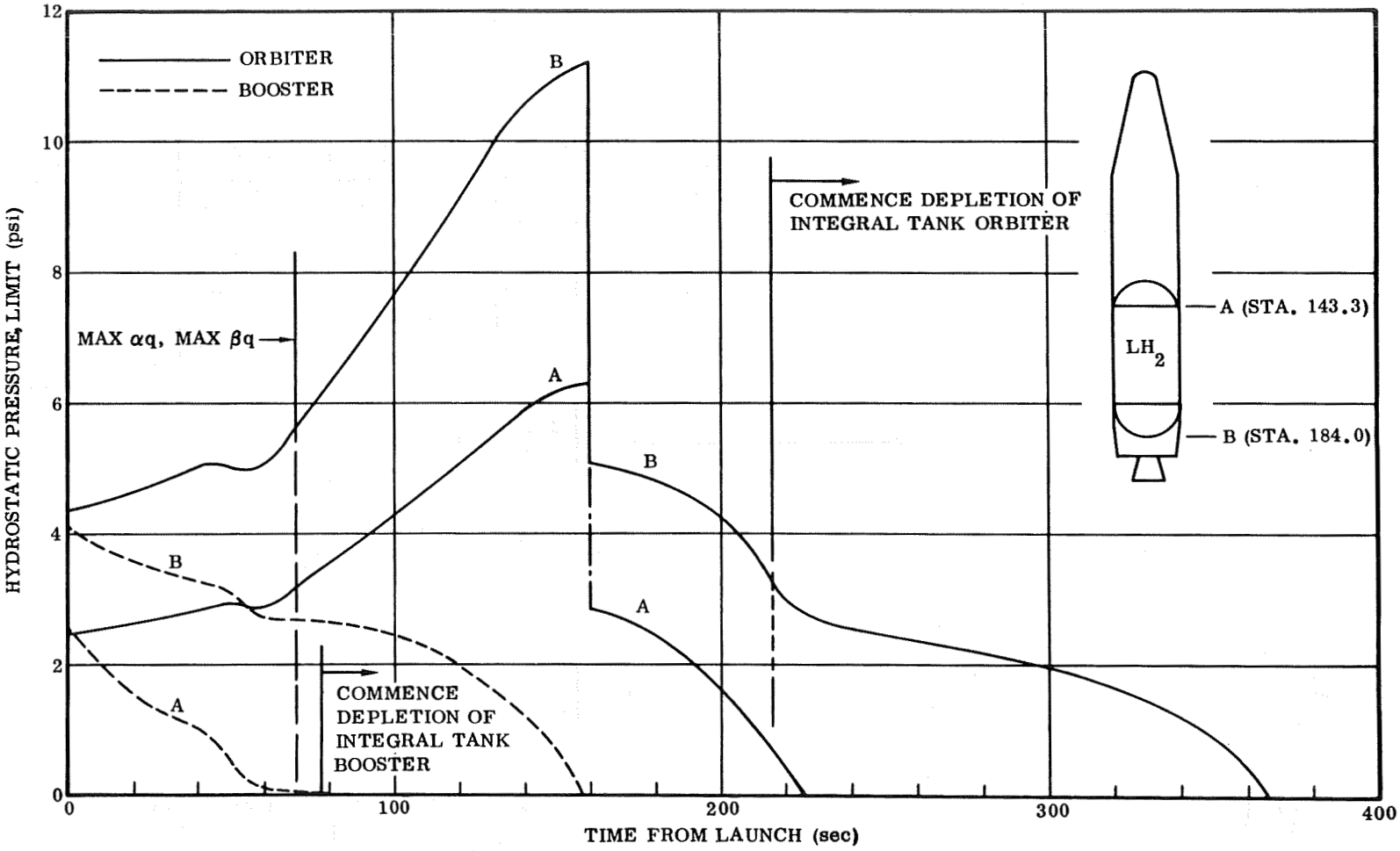

Figure 6-2. FR-1 LH_2 Tank Hydrostatic Pressures During Boost

Table 6-6. Summary of Integral LH_2 Tank Loads (Limit)

Condition	Point	P (psi)	Station 143.3				Station 159.0				Station 174.8			
			Orbiter		Booster		Orbiter		Booster		Orbiter		Booster	
			N_x (lb/in.)	N_{x_y} (lb/in.)	N_x (lb/in.)	N_{x_y} (lb/in.)	N_x (lb/in.)	N_{x_y} (lb/in.)	N_x (lb/in.)	N_{x_y} (lb/in.)	N_x (lb/in.)	N_{x_y} (lb/in.)	N_x (lb/in.)	N_{x_y} (lb/in.)
2 Pt Landing	4	2.0	2650	636	1920	552	1620	533	1404	464	768	433	666	375
2 Pt Landing	1	2.0	-2556	636	-1850	552	-1554	538	-1344	464	-725	433	629	375
Ground Wind	2,3	0.0	-1760	60	-2150	54	-1880	70	-2370	63	-2130	78	-2650	71
Maximum αq	1	28.5	-238	27	-637	95	-332	64	-562	60	-562	180	-620	55
Maximum αq	4	28.5	-2980	27	-4200	95	-2900	64	-4360	60	-2780	180	-4430	55
Maximum βq	2,3	28.5	-2500	0	-3660	0	-2700	0	-3840	0	-2650	10	-3880	0
Booster Burnout	1	28.5	-1195	0	-5000	310	-1320	0	-4540	310	-1420	0	-4150	310

NOTES:
1. P is the ullage pressure (used to relieve applied compressive loads N_x, but additive to tensile N_x).
2. Burst pressures are (39.7)(1.5) = 59.5 psi on the orbiter (at booster burnout), and (32.6)(1.5) = 49 psi on the booster (at liftoff). The maximum burst pressure at Station 174.8 was also used at Stations 143.3 and 159.0.
3. N_{x_y} is applied limit shear flow.
4. Loads are derived from Section 4.7.1.3, and include dynamic amplification factors.

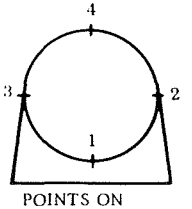

POINTS ON TANK SECTION

Table 6-7. Orbiter Integral LH_2 Tank - Skin/Stringer Element Sizes

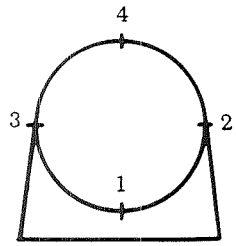

POINTS ON TANK SECTION

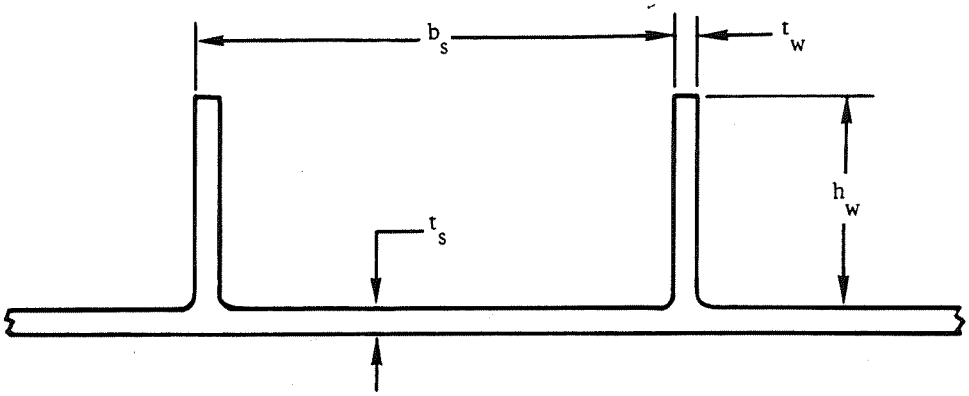

MATERIAL: 2219-T87 aluminum alloy

Station (ft)	Condition	Point	t_s* (in.)	b_s (in.)	t_w (in.)	h_w (in.)
143.3	2 Pt Landing	1	0.150	6.0	0.140	1.70
	Ground Wind	2	0.150	6.0	0.120	1.50
	Ground Wind	3	0.150	6.0	0.120	1.50
	Maximum αq	4	0.150	6.0	0.120	1.40
159.0	Maximum αq	1	0.150	6.0	0.120	1.43
	Ground Wind	2	0.150	6.0	0.120	1.55
	Ground Wind	3	0.150	6.0	0.120	1.55
	Maximum αq	4	0.150	6.0	0.120	1.43
174.7	Ground Wind	1	0.150	6.0	0.120	1.43
	Ground Wind	2	0.150	6.0	0.120	1.60
	Ground Wind	3	0.150	6.0	0.120	1.60
	Ground Wind	4	0.150	6.0	0.120	1.43

*Skin thickness t_s is sized for a burst pressure equal to 59.5 psi.

Table 6-8. Booster Integral LH_2 Tank - Skin/Stringer Element Sizes

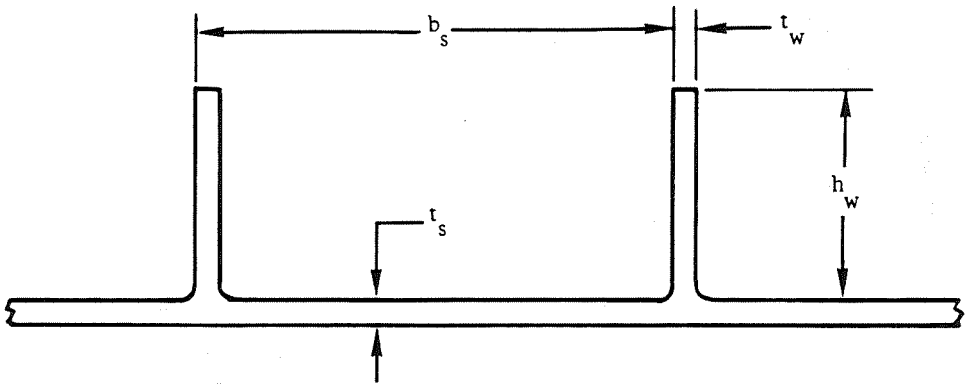

MATERIAL: 2219-T87 aluminum alloy

Station (ft)	Condition	Point	t_s* (in.)	b_s (in.)	t_w (in.)	h_w (in.)
143.3	Booster Burnout	1	0.123	5.0	0.130	1.76
	Ground Wind	2	0.123	5.0	0.100	1.66
	Ground Wind	3	0.123	5.0	0.100	1.66
	Maximum αq	4	0.123	5.0	0.105	1.73
159.0	Booster Burnout	1	0.123	5.0	0.110	1.75
	Ground Wind	2	0.123	5.0	0.110	1.70
	Ground Wind	3	0.123	5.0	0.110	1.70
	Maximum αq	4	0.123	5.0	0.110	1.73
174.7	Booster Burnout	1	0.123	5.0	0.100	1.73
	Ground Wind	2	0.123	5.0	0.120	1.78
	Ground Wind	3	0.123	5.0	0.120	1.78
	Maximum αq	4	0.123	5.0	0.110	1.78

*Skin thickness t_s is sized for a burst pressure equal to 49 psi.

Table 6-9. FR-1 Integral LH_2 Tank - Upper Dome

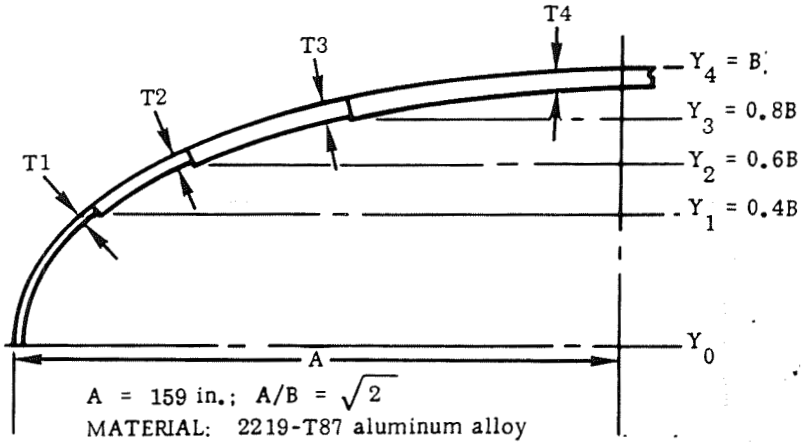

Thickness (in.)	Orbiter	Booster
T1	0.051	0.051
T2	0.054	0.054
T3	0.063	0.063
T4	0.076	0.076

Table 6-10. FR-1 Integral LH_2 Tank - Lower Dome

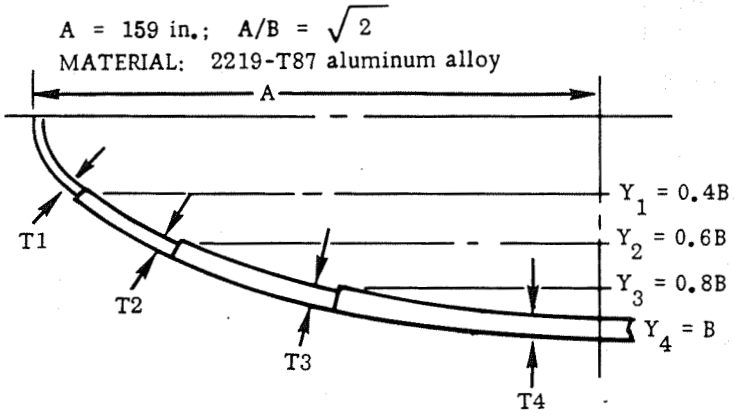

Thickness (in.)	Orbiter	Booster
T1	0.076	0.060
T2	0.080	0.063
T3	0.093	0.073
T4	0.112	0.088

Table 6-11. LH_2 Tank External Frames - Orbiter and Booster

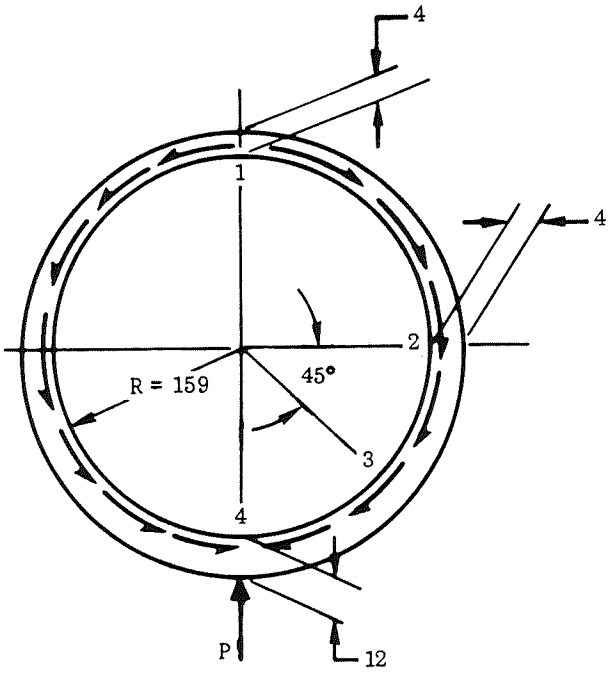

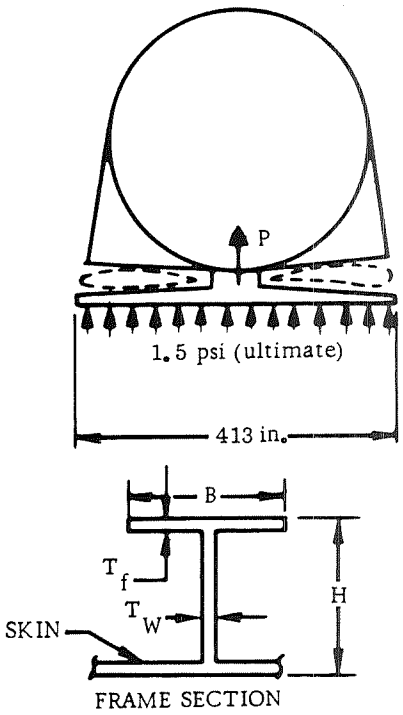

P = (1.5) (30) (413) = 18600 lb (ultimate)
FRAME PITCH = 30 in.

Station (ft)	Point	I Required		Frame Dimensions				
		Stability ($in.^4$)	Bending ($in.^4$)	H (in.)	B (in.)	T_f (in.)	T_w (in.)	Area ($in.^2$)
143.3	1	4.8	8.5	4.00	2.85	0.350	0.104	2.41
	2		9.6	4.00	3.20	0.350	0.104	2.66
	3		21.1	8.00	3.20	0.200	0.104	2.11
	4		75.6	12.00	4.00	0.220	0.104	3.01
159.0	1	5.2	8.5	Identical to frame at Station 143.3				
	2		9.6					
	3		21.1					
	4		75.6					
174.7	1	5.7	8.5	Identical to frame at Station 143.3				
	2		9.6					
	3		21.1					
	4		75.6					

PRECEDING PAGE BLANK NOT FILMED.

Table 6-12. FR-1 Booster Auxiliary Tank Member Sizes

Auxiliary Tank Loads*

Tank	Condition	N_x (lb/in.)	N_{xy} (lb/in.)	P (psi)	P_{burst} (psi)
LH_2	Static Ground	-100	0	0	46
LO_2	Liftoff	-152	0	23	57
	Static Ground	-100	0	0	57

*All loads shown are limit except P_{burst}, which is ultimate.

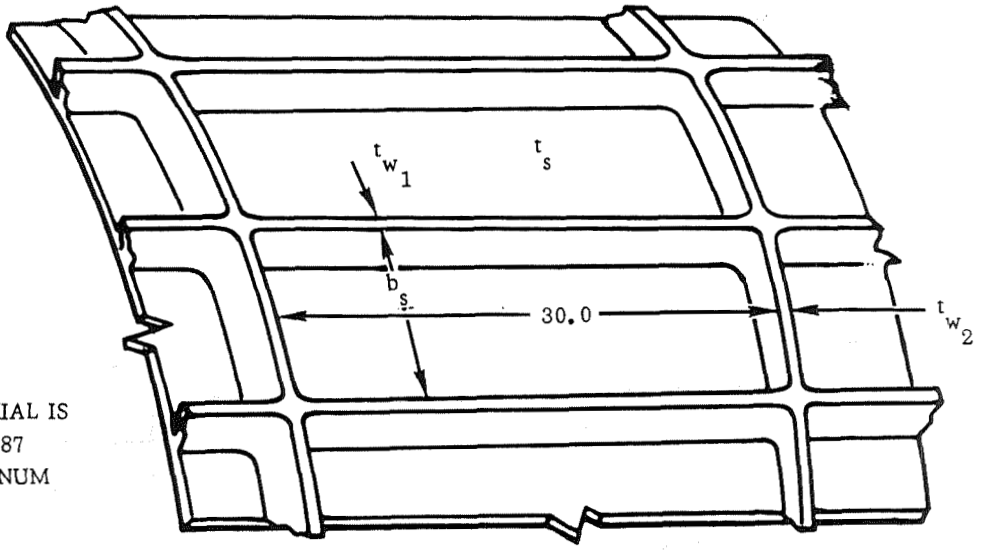

MATERIAL IS
2219-T87
ALUMINUM
ALLOY

Auxiliary Tank Member Sizes

Tank	Condition	t_s (in.)	b_s (in.)	h_w (in.)	t_{w1} (in.)	t_{w2} (in.)
LH_2	Static Ground	0.107	12.0	1.0	0.24	0.20
LO_2	Static Ground	0.132	12.0	1.0	0.24	0.20

Table 6-13. FR-1 Booster Auxiliary Tank Domes

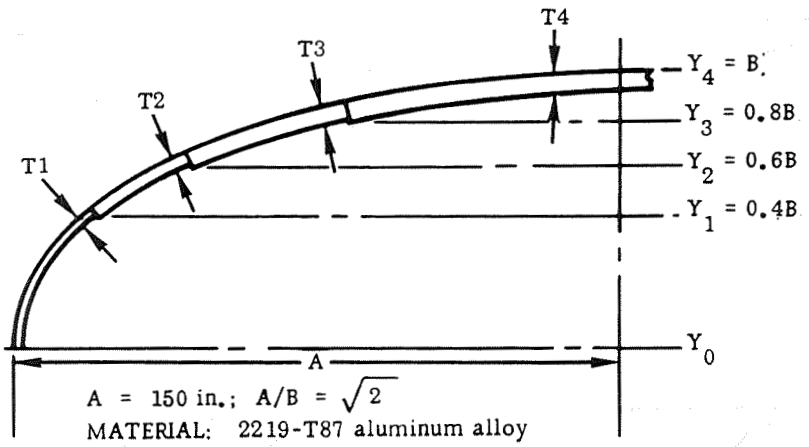

Thickness (in.)	Upper Dome	Common Bulkhead	Lower Dome
T1	0.048	0.052	0.073
T2	0.050	0.055	0.081
T3	0.058	0.063	0.094
T4	0.070	0.076	0.114

Table 6-14. Orbiter and Booster Center Body Structure Loads (Ultimate)

Station (ft)	Maximum αq		Booster Burnout		Subsonic Gust			Neutral Axis Location (in.)
	M_y (in.-lb $\times 10^6$)	P_x (lb $\times 10^6$)	M_y (in.-lb $\times 10^6$)	P_x (lb $\times 10^6$)	M_y (in.-lb $\times 10^6$)	P_x (lb $\times 10^6$)	S_z (lb $\times 10^3$)	
Orbiter								
72.0	-4.95	-2.48	-0.053	-4.76	-134.5	0.105	-283	0
80.9	-21.8	-2.43	-0.095	-4.32	-166.3	0.105	-305	0
99.5	-59.6	-2.32	-0.182	-3.36	-239.0	0.095	-339	0
103.6	-68.3	-2.28	-0.202	-3.16	-255.5	0.051	-423	0
124.3	-51.9	-2.04	+60.0	-2.01	-251.0	0.058	-337	-30
134.0	-76.2	-1.93	+43.9	-1.93	-251.0	0.060	-302	-30
Booster								
72.0	20.3	-2.00	-1.0	-0.61	-106.3	0.083	-225	0
80.9	2.0	-2.10	-43.6	-0.92	-132.1	0.081	-242	0
99.5	-77.5	-2.14	-133.9	-1.56	-189.6	0.076	-269	0
103.6	-88.3	-2.21	-153.8	-1.70	-274.7	0.041	-336	0
124.3	-134.8	-2.53	-217.1	-2.43	-198.0	0.046	-267	0
134.0	-159.1	-2.68	-246.6	-2.79	-168.1	0.048	-240	0

NOTES:
1. M_y, P_x, and S_z are bending moment, axial load, and vertical shear, respectively.
2. Shear values for maximum $_{\alpha}q$ and booster burnout conditions are very small, so subsonic gust shears were conservatively used.
3. Bending moments are a function of neutral axis location due to axial load eccentricity.

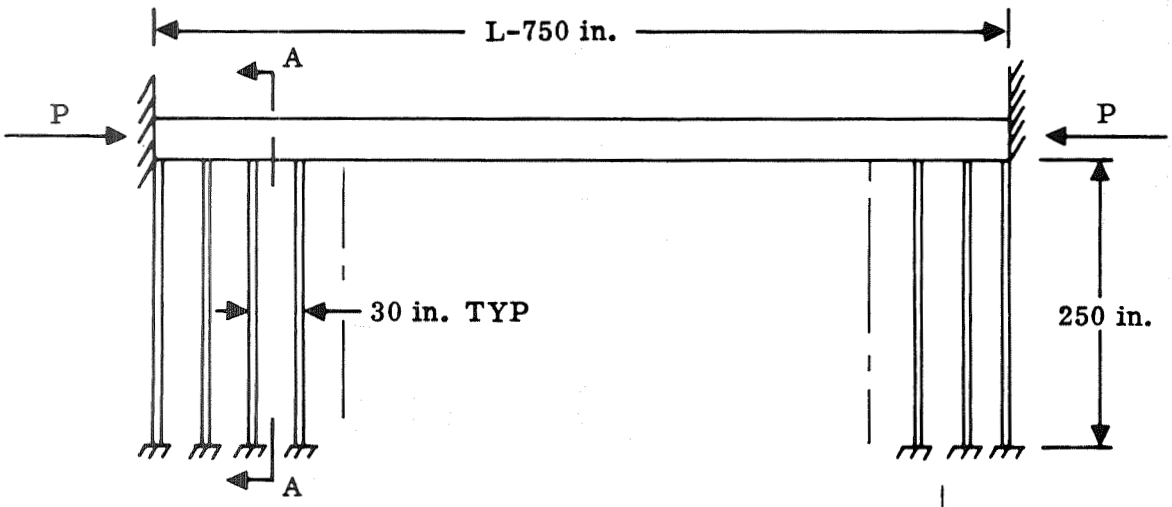

$P = 300,000$ lb (ult)

$L = 750$ in.

$L_f = 250$ in.

$$K = \frac{3(EI)_f}{30\,L_f^3} = 2.88 \text{ lb/in.}^2$$

$$Pcr = \frac{4\pi^2(EI)\ell}{L^2} + 2\sqrt{K(EI)\ell}$$

$$= 147,500 + 155,500 = 303,000 \text{ lb}$$

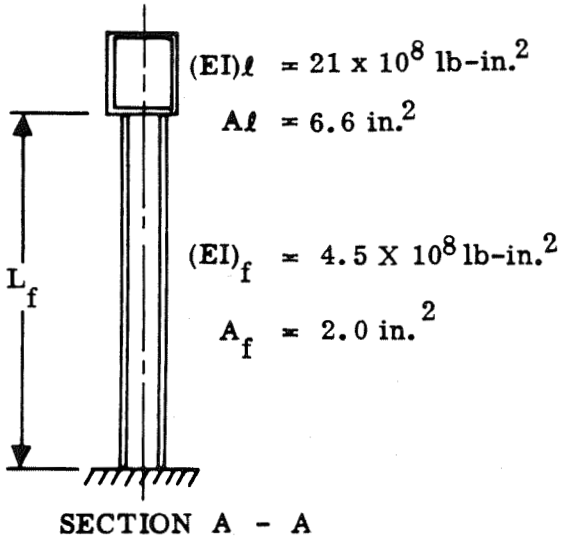

SECTION A - A

Figure 6-4. Orbiter Payload Bay Longeron

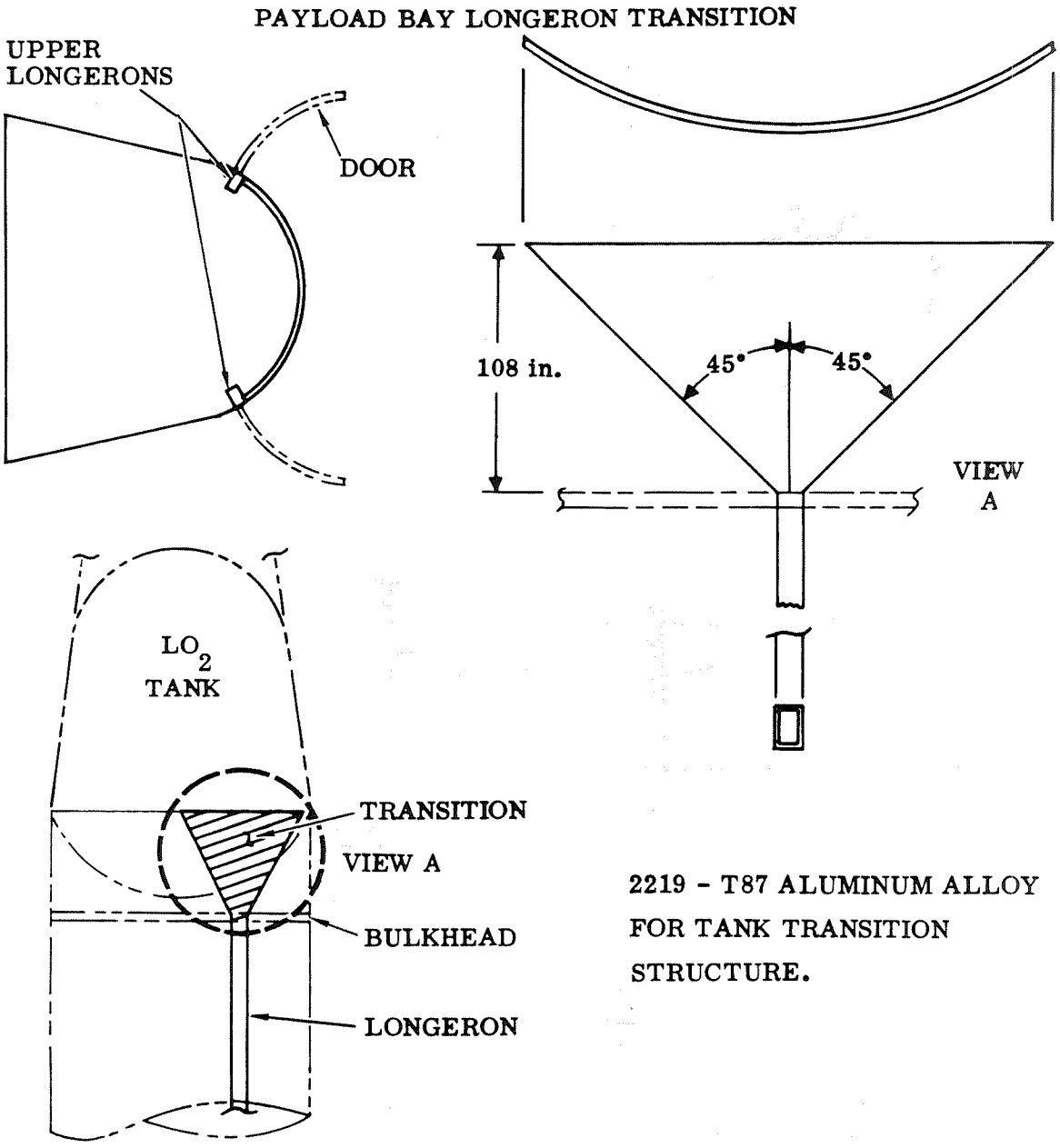

Figure 6-5. Payload Bay Longeron Transition

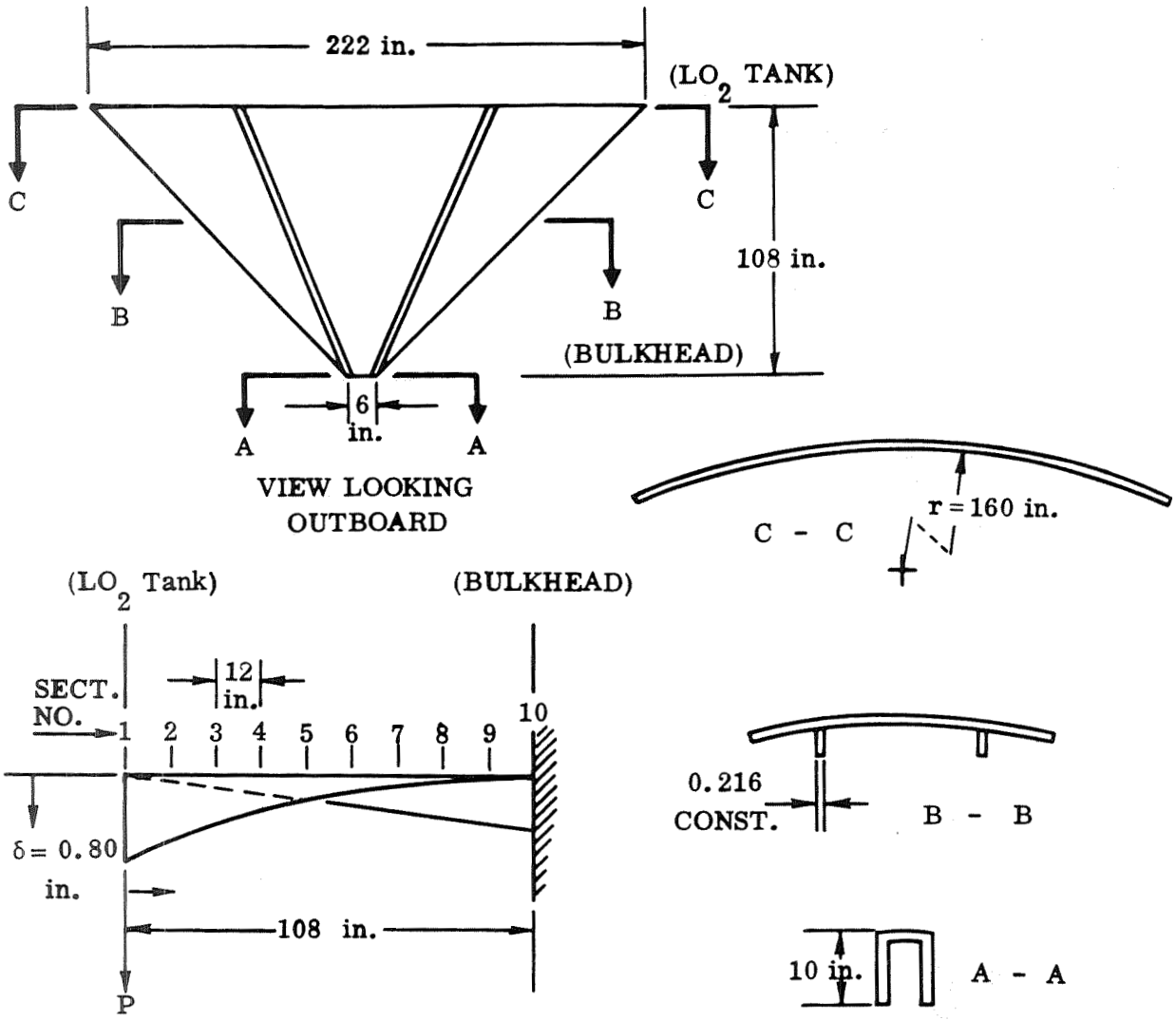

Figure 6-6. Payload Bay Longeron Transition Structure

Table 6-15. Payload Bay Longeron - Summary of Secondary Bending Stresses

Section	σ_T (psi)	σ_C (psi)
1	0	-0
2	266	-546
3	776	-1590
4	1705	-3320
5	3720	-6200
6	6300	-7470
7	6540	-9100
8	5820	-10,300
9	5480	-9380
10	5900	-9340

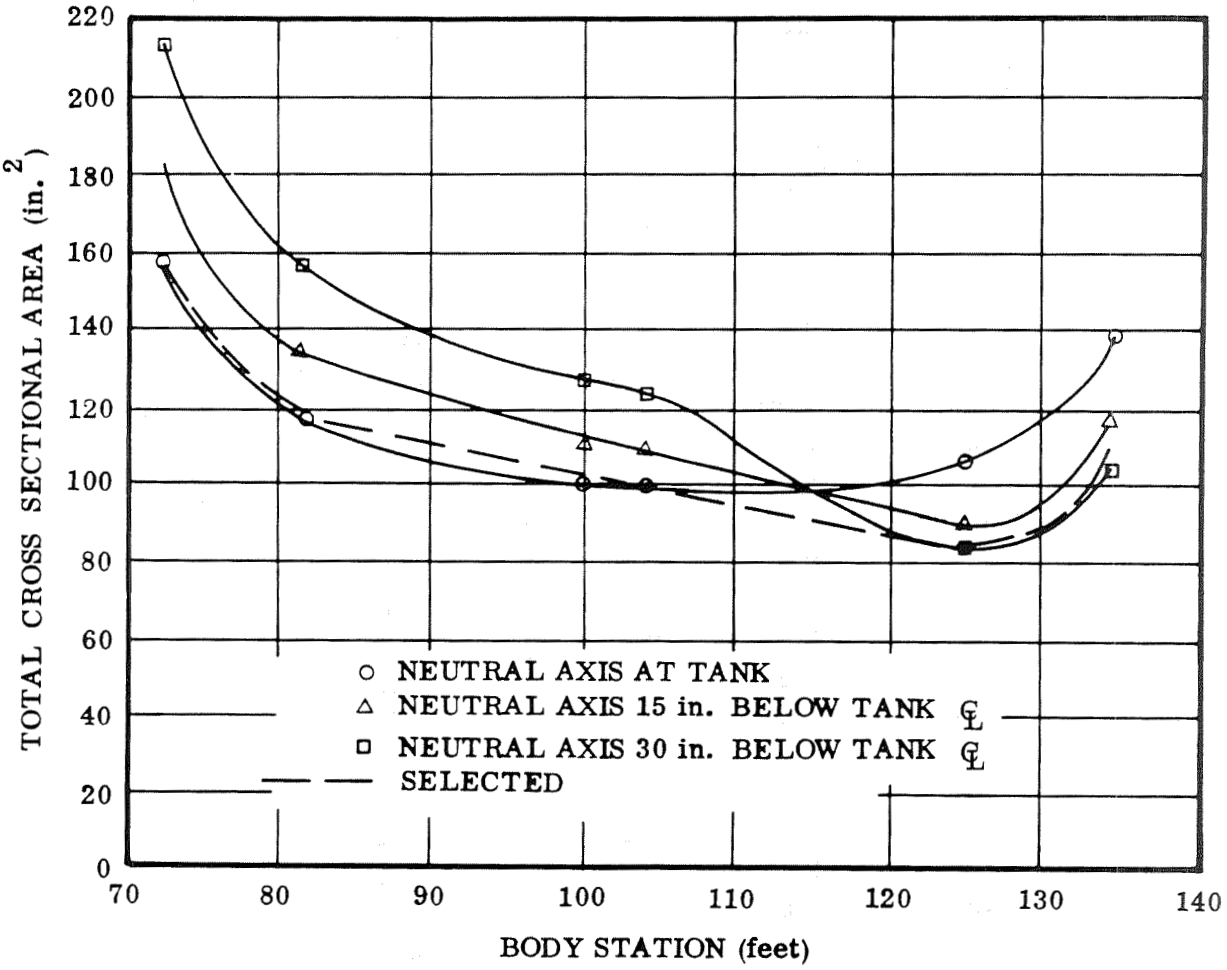

Figure 6-7. Orbiter Centerbody Structure - Cross-sectional Area of Skins and Stringers

Table 6-16. **Orbiter Centerbody Structure - Typical Gages at Station 103.6 Required for Maximum αq Loads**

Longeron	Gross Area ($in.^2$)	Stress (psi)	Skin Area ($in.^2$)	Skin Thickness (in.)	Skin Stress (psi)
1	6.600	-21,449	0.272	0.0200	19,946
2	2.882	-22,334	0.345	0.0253	22,000
3	2.605	-23,290	0.424	0.0311	22,000
4	2.311	-24,308	0.486	0.0356	22,000
5	2.001	-25,379	0.527	0.0389	22,000
6	1.681	-26,486	0.561	0.0411	22,000
7	1.348	-27,637	0.579	0.0425	22,000
8	1.007	-28,814	0.588	0.0432	22,000
9	0.661	-30,009	0.591	0.0434	22,000
10	0.314	-31,213	0.591	0.0434	22,000
11	0.387	-32,417	0.589	0.0433	22,000
12	0.460	-33,612	0.585	0.0430	22,000
13	0.532	-34,789	0.578	0.0424	22,000
14	0.602	-35,940	0.564	0.0416	22,000
15	0.669	-37,046	0.553	0.0405	22,000
16	0.734	-38,118	0.533	0.0391	22,000
17	0.796	-39,136	0.508	0.0373	22,000
18	0.854	-40,092	0.478	0.0352	22,000
19	0.908	-40,977	0.444	0.0327	22,000
20	0.958	-41,791	0.406	0.0298	22,000
21	1.002	-42,526	0.363	0.0266	22,000
22	1.042	-43,172	0.316	0.0231	22,000
23	1.076	-43,730	0.271	0.0200	21,270
24	1.104	-44,190	0.273	0.0200	16,834
25	1.126	-44,553	0.272	0.0200	12,181
26	1.141	-44,810	0.272	0.0200	7,374
27	1.151	-44,969	0.272	0.0200	2,469
28	0.577	-45,022	0.272	0.0200	2,469

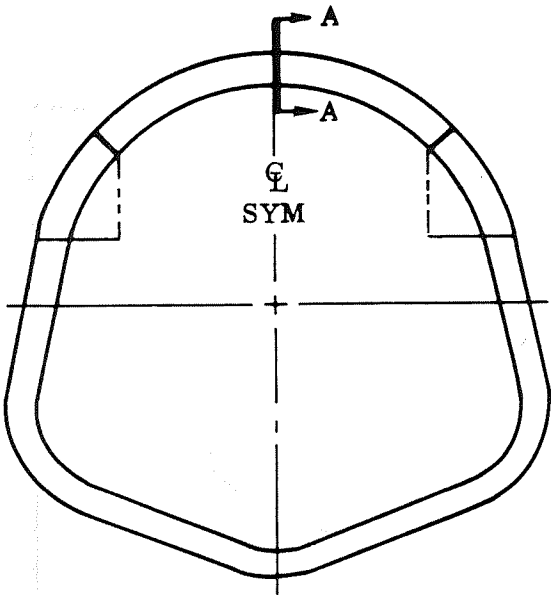

VIEW LOOKING FORWARD
AT FORWARD CLOSING FRAME
(BODY STATION 72)

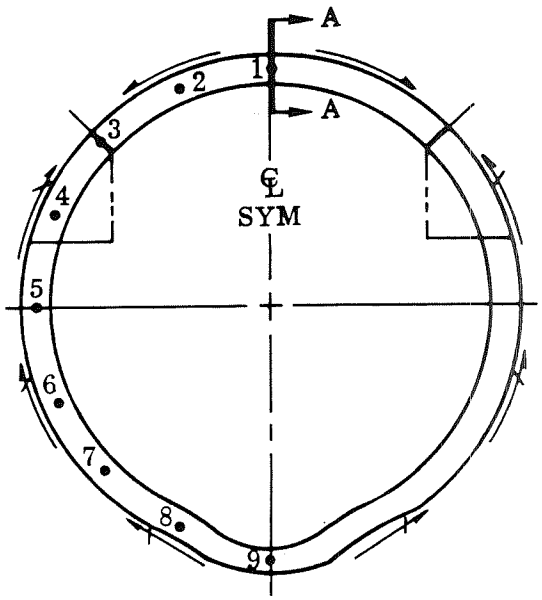

VIEW LOOKING FORWARD
AT AFT CLOSING FRAME
(BODY STATION 134)

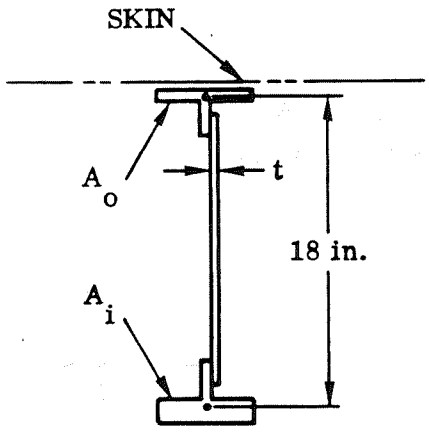

SECTION A - A

Pt	A_o	A_i	t	A_{total}
	($in.^2$)	($in.^2$)	(in.)	($in.^2$)
1	2.04	4.70	0.050*	7.64
2	1.38	2.21	0.079	5.01
3	1.70	0.90*	0.072	3.89
4	1.53	2.54	0.050	4.97
5	1.71	2.44	0.050	5.05
6	0.97	1.31	0.050	3.18
7	0.50*	0.90*	0.050	2.40
8	1.22	1.74	0.050	3.86
9	1.56	2.44	0.050	4.90

* ASSUMED MINIMUMS

MATERIAL = 2219 - T87 ALUMINUM ALLOY

Figure 6-8. Orbiter Centerbody Structure - Payload Bay End Bulkheads

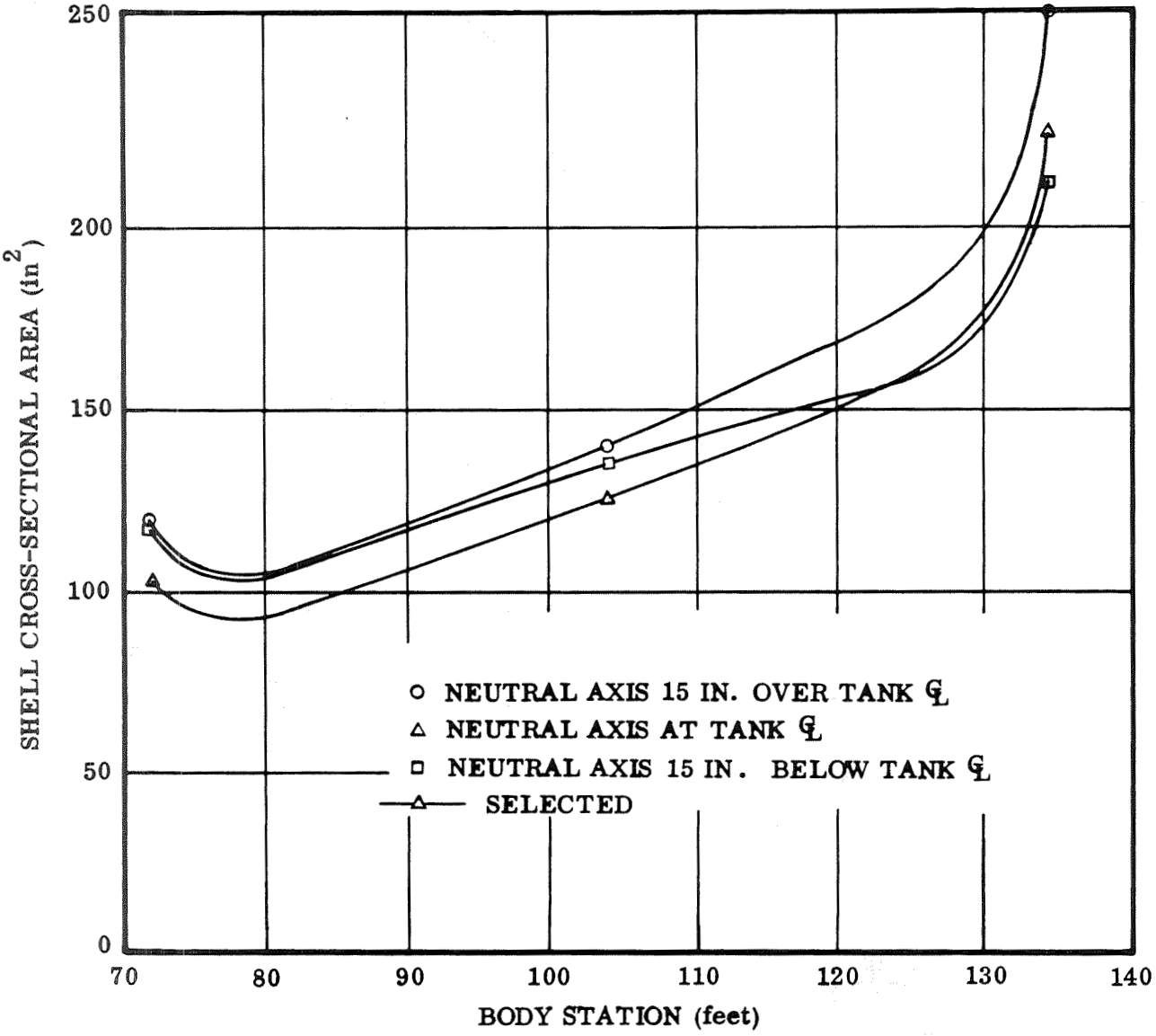

Figure 6-9. Booster Centerbody Structure - Cross-sectional Area of Skin/Stringers

Table 6-17. Booster Centerbody Structure - Typical Gages at Station 103.6 Required for Maximum αq Loads

Longeron	Gross Area ($in.^2$)	Stress (psi)	Skin Area ($in.^2$)	Skin Thickness (in.)	Skin Stress (psi)
1	0.757	-45,000	0.272	0.0200	2,175
2	1.511	-44,961	0.272	0.0200	6,496
3	1.501	-44,842	0.272	0.0200	10,735
4	1.486	-44,652	0.273	0.0200	14,841
5	1.463	-44,383	0.271	0.0200	18,763
6	1.435	-44,042	0.279	0.0204	22,000
7	1.401	-43,628	0.321	0.0235	22,000
8	1.362	-43,149	0.359	0.0264	22,000
9	1.317	-42,604	0.393	0.0289	22,000
10	1.268	-42,000	0.423	0.0312	22,000
11	1.214	-41,344	0.472	0.0347	22,000
12	1.156	-40,635	0.472	0.0347	22,000
13	1.094	-39,880	0.490	0.0359	22,000
14	1.028	-39,086	0.499	0.0369	22,000
15	0.961	-38,265	0.512	0.0376	22,000
16	0.891	-37,412	0.517	0.0380	22,000
17	0.819	-36,539	0.520	0.0381	22,000
18	0.760	-35,652	0.519	0.0381	22,000
19	0.784	-34,760	0.516	0.0379	22,000
20	0.807	-33,867	0.510	0.0375	22,000
21	0.830	-32,981	0.501	0.0368	22,000
22	0.853	-32,108	0.489	0.0359	22,000
23	0.875	-32,254	0.471	0.0348	22,000
24	0.897	-30,434	0.456	0.0334	22,000
25	0.917	-29,639	0.433	0.0318	22,000
26	0.937	-28,884	0.409	0.0300	22,000
27	0.956	-28,176	0.380	0.0279	22,000
28	0.973	-27,519	0.349	0.0257	22,000
29	0.988	-26,915	0.316	0.0232	22,000
30	1.003	-26,370	0.279	0.0205	22,000
31	1.015	-25,891	0.273	0.0200	19,416
32	1.026	-25,478	0.271	0.0200	16,121
33	1.035	-25,136	0.273	0.0200	12,687
34	1.042	-24,867	0.272	0.0200	9,142
35	1.047	-24,677	0.272	0.0200	5,518
36	1,050	-24,559	0.272	0.0200	1,845
37	0.525	-24,519	0.272	0.0200	1,845

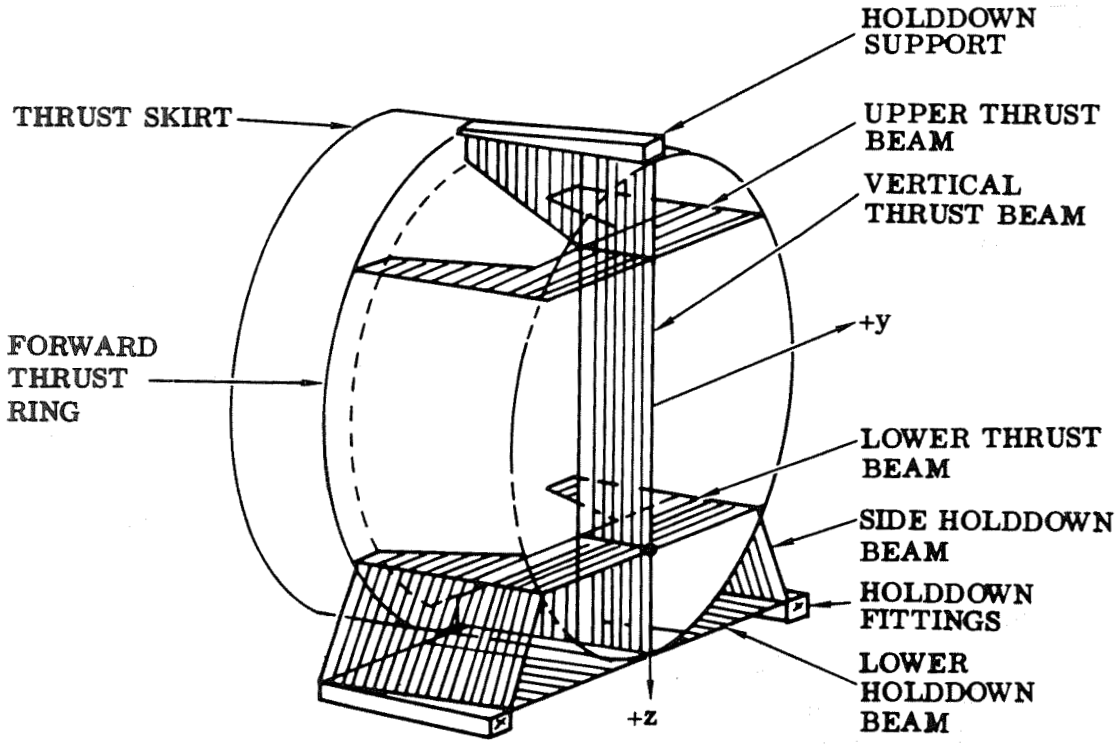

Figure 6-10. Thrust and Holddown Structure

Table 6-18. Thrust Beam Criteria

Component	Material and Construction	Ultimate Safety Factor	Avg. Temp. (°F)	Allowables at Avg. Temp.
Webs	Corrugated Ti-8Al-1Mo-1V Web Welded to a Light Titanium Cap Member	1.25	600	F_s = 60 ksi
Flanges	Unidirectional Al/Boron Flange Bonded to the Above Ti Cap Member	1.50	600	$F_c = F_t$ = 132 ksi

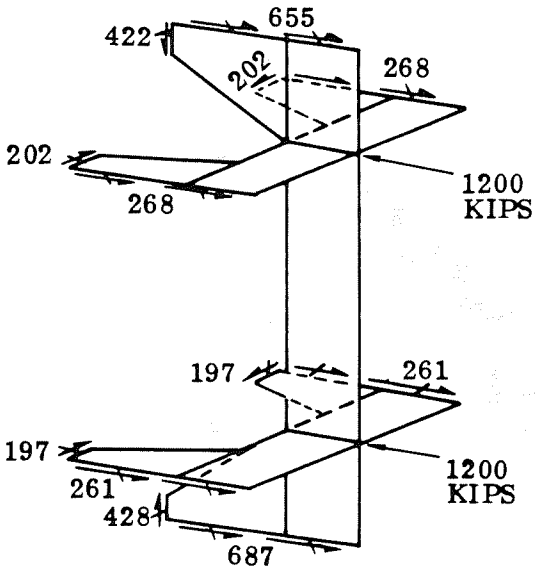

Figure 6-11. Thrust Beam Loads and Reactions (Limit)

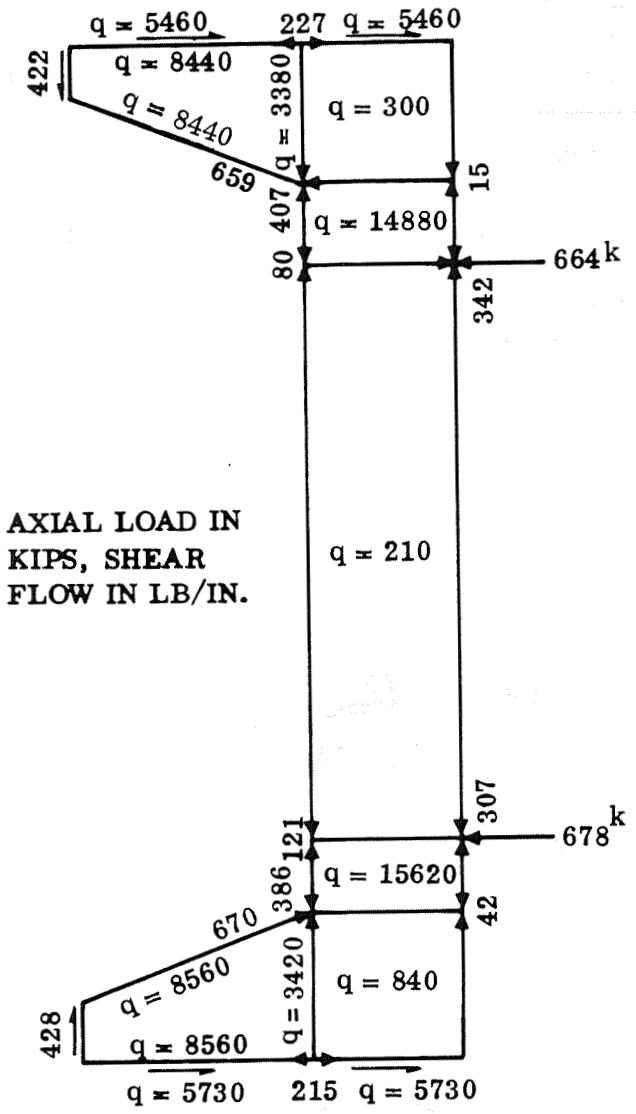

Figure 6-12. Vertical Thrust Beam Internal Loads (Limit)

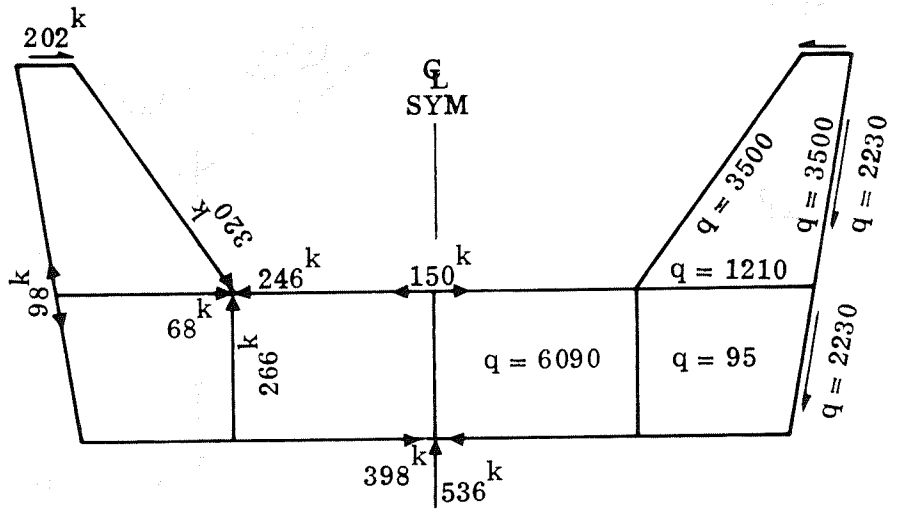

Figure 6-13. Horizontal Thrust Beam Internal Loads (Limit)

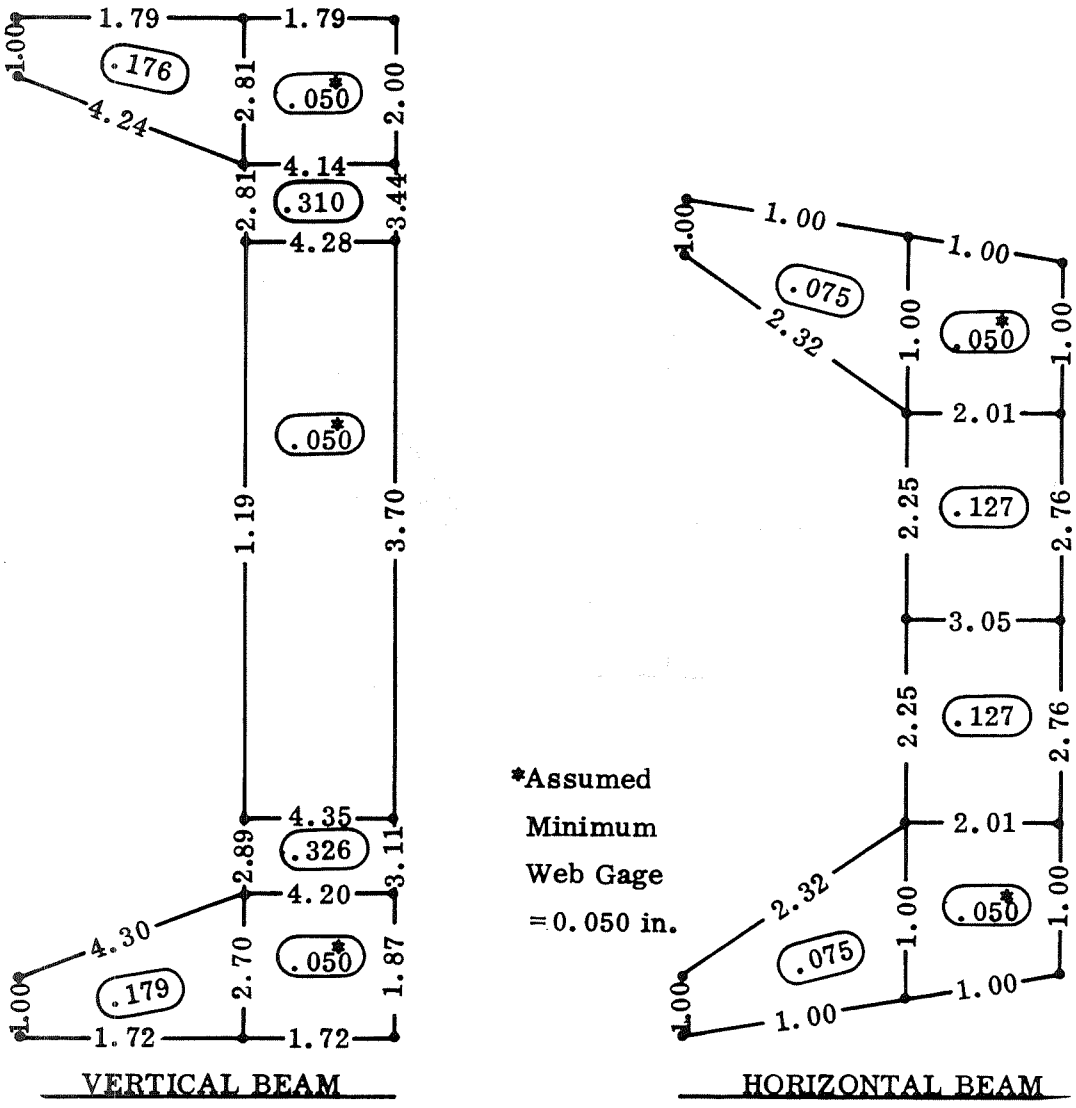

Figure 6-14.. Thrust Beam Areas and Thickness

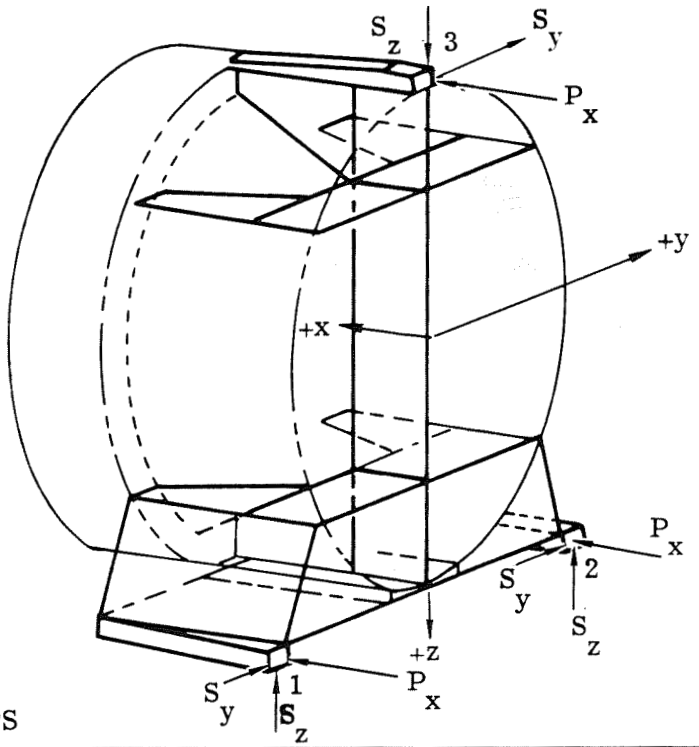

LOADS IN KIPS

FITTING NO.	LOADS	ORBITER		BOOSTER	
		± My	±M z	±My	±Mz
1	P_x	310 498	245 563	443 631	378 696
	S_y		±13.1		±13.1
	S_z	±17.5		±17.5	
2	P_x	310 498	563 245	443 631	696 378
	S_y		±13.1		±13.1
	S_z	±17.5		±17.5	
3	P_x	993 613	805 805	1255 879	1073 1073
	S_y		±26.2		±26.2
	S_z	±17.5		±17.5	

Figure 6-15. Ultimate Holddown Fitting Loads - Ground-Wind Condition

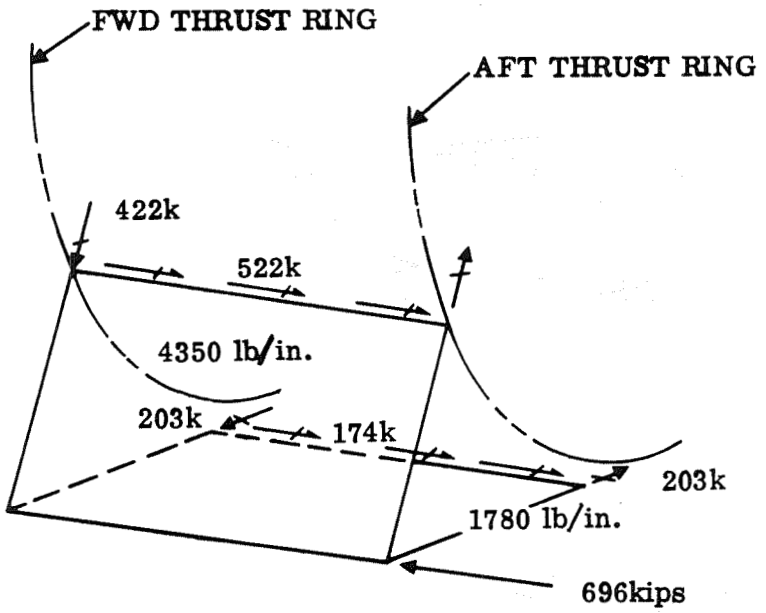

LOADS AND REACTIONS

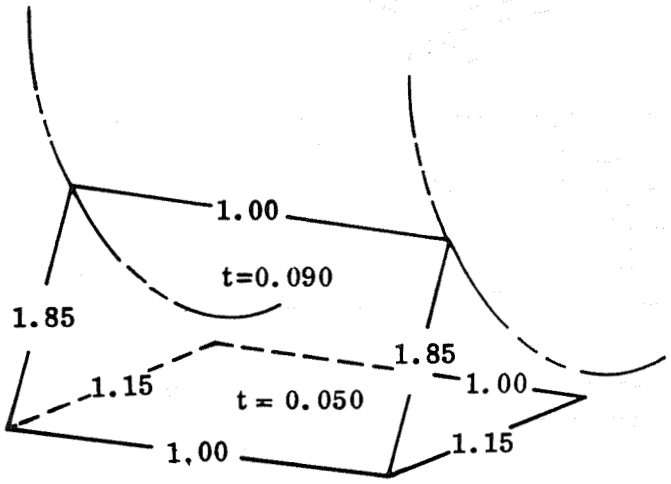

CAP AREAS AND WEB GAGES

Figure 6-16. Holddown Beams

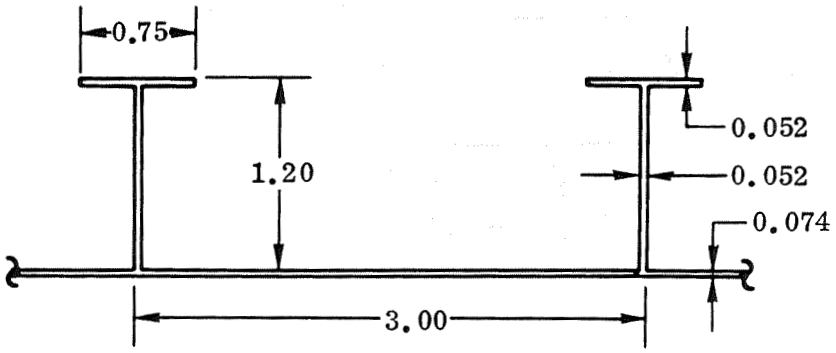

MATERIAL: Ti-8al-1Mo-1V

Figure 6-17. Thrust Skirt Skin/Stringer Section

Table 6-19. Forward Thrust Ring - Ultimate Internal Loads and Component Sizes

θ (deg)	Max. αq Fin Loads			Ground Wind Loads			Max. Thrust Loads			Sizes*		
	M (in.-k)	A.L. (kips)	S (kips)	M (in.-k)	A.L. (kips)	S (kips)	M (in.-k)	A.L. (kips)	S (kips)	A_0 (in.2)	A_1 (in.^{2})	t (in.)
0	-1,030	-27.8	0	-14,729	-13	-27	-17,201	283	298	7.76	5.62	0.248
20	-783	-26.7	9.6	-9,110	-25	-22	-4,571	368	183	3.36	3.56	0.153
40	-48	-24.0	18.5	-4,841	-42	-18	1,435	408	46	1.70	2.35	0.092
60	688	16.8	2.2	621	-61	-20	2,596	258	149	1.27	2.24	0.124
80	314	12.6	-3.0	4,108	-76	-30	7,871	293	52	2.25	4.47	0.080
100	55	6.6	-6.4	6,552	-84	-49	7,871	293	-52	2.73	4.35	0.080
120	28	0	-7.6	8,102	-79	-74	2,596	258	-149	3.40	2.80	0.124
140	298	-5.9	-6.6	3,081	-222	210	1,435	408	-46	1.97	2.18	0.175
160	897	-9.8	-3.7	-4,845	-287	114	-4,571	368	-183	3.20	2.86	0.153
180	1,790	-11.3	0	-7,607	-309	0	-17,201	283	-298	7.76	5.62	0.248

+θ is clockwise from top ℄
+M is compression in outer flange
+A.L. is tension
+S is outward
* Assuming $F_c = F_t = 132$,ksi, $F_s = 60$ ksi, and $t_{min} = 0.080$ in.

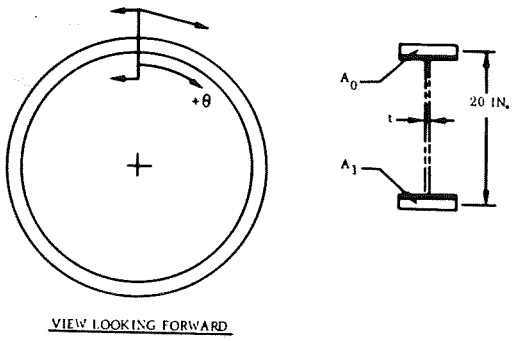

Table 6-20. Parametric Wing Studies - Subsonic Condition

Exposed Wing Area (ft^2)	Wing Incidence (deg)	Structural Span (in.)	Planform Taper Ratio	Thickness Ratio	Wing Lift Per Panel (lb)	Wing Weight (lb)	Wing Unit Weight (lb/ft^2)
				Root Tip			
2,000	6	912.4	0.8	0.21 - 0.18	308,610	22,518	11.26
2,000	6	912.4	0.8	0.18 - 0.154	308,610	23,919	11.96
2,000	6	912.4	0.8	0.15 - 0.129	308,610	26,050	13.03
2,000	6	1,019.6	0.6	0.21 - 0.18	308,610	24,598	12.30
2,000	6	826.7	1.0	0.21 - 0.18	308,610	21,046	10.52
1,800	6	826.7	0.8	0.21 - 0.18	292,370	18,810	10.45
2,200	6	998.2	0.8	0.21 - 0.18	320,000	26,311	11.96
2,400	6	1,084.0	0.8	0.21 - 0.18	332,970	30,719	12.80
2,000	3	912.4	0.8	0.21 - 0.18	268,000	20,687	10.34
2,000	8	912.4	0.8	0.21 - 0.18	321,600	22,979	11.49

Table 6-21. FR-1 Wing Geometry and Load Data

Station (in.)	Chord (in.)	Thickness Ratio	Rib Spacing (in.)	Shear (lb)	Pos. B. Mom. (in.-lb $\times 10^6$)	NY (+M) (lb/in.)	Torsion (in.-lb $\times 10^6$)
0.00	184.00	0.2100	23.18	418,153	165.2	48,411	7.7
23.18	182.92	0.2092	23.18	405,029	155.6	46,342	7.4
46.37	181.84	0.2083	23.18	391,982	146.4	44,289	7.1
69.55	180.76	0.2075	23.18	379,012	137.4	42,256	6.9
92.74	179.68	0.2066	23.18	366,120	128.8	40,243	6.6
115.92	178.60	0.2058	23.18	353,304	120.5	38,251	6.3
139.11	177.52	0.2049	23.18	340,566	112.4	36,283	6.0
162.29	176.44	0.2041	23.18	327,906	104.7	34,340	5.8
185.47	175.36	0.2032	23.18	315,322	97.2	32,423	5.5
208.66	174.28	0.2024	23.18	302,815	90.1	30,535	5.3
231.84	173.21	0.2015	23.18	290,386	83.2	28,677	5.0
255.03	172.13	0.2007	23.18	278,034	76.6	26,852	4.8
278.21	171.05	0.1998	23.18	265,760	70.3	25,061	4.5
301.39	169.97	0.1990	23.18	253,562	64.3	23,307	4.3
324.58	168.89	0.1982	23.78	241,442	58.5	21,591	4.1
348.36	167.78	0.1973	24.45	229,089	52.9	19,874	3.8
372.81	166.64	0.1964	25.20	216,475	47.5	18,158	3.6
398.01	165.47	0.1955	26.04	203,565	42.2	16,443	3.4
424.05	164.26	0.1945	27.01	190,317	37.1	14,733	3.1
451.06	163.00	0.1935	28.14	176,678	32.1	13,029	2.9
479.21	161.69	0.1925	29.48	162,580	27.3	11,335	2.6
508.69	160.32	0.1914	31.10	147,934	22.8	9,657	2.4
539.79	158.87	0.1903	33.11	132,620	18.4	8,000	2.1
572.90	157.33	0.1891	35.72	116,468	14.3	6,375	1.8
608.61	155.66	0.1878	39.28	99,221	10.4	4,794	1.5
647.89	153.83	0.1864	44.57	80,467	6.9	3,279	1.2
692.47	151.76	0.1847	53.73	59,451	3.8	1,873	0.9
746.19	149.26	0.1828	75.82	34,500	1.3	666	0.5
822.01	145.73	0.1800	0.00	-4	0.0	0	0.0

NOTE: All loads are ultimate.

Table 6-22. FR-1 Wing Box - Compression Cover Gages

Station (in.)	SIGC (psi)	RHORQD (in.)	TSKIN (in.)	BSKIN (in.)	TSTR (in.)	BSTR (in.)	TBC (in.)
0.00	126,000	0.617	0.2298	2.59	0.1609	1.55	0.3842
23.18	126,000	0.617	0.2200	2.59	0.1540	1.55	0.3678
46.37	126,000	0.617	0.2102	2.59	0.1472	1.55	0.3515
69.55	126,000	0.617	0.2006	2.59	0.1404	1.55	0.3354
92.74	126,000	0.617	0.1910	2.59	0.1337	1.55	0.3194
115.92	126,000	0.617	0.1816	2.59	0.1271	1.55	0.3036
139.11	126,000	0.617	0.1722	2.59	0.1206	1.55	0.2880
162.29	126,000	0.617	0.1630	2.59	0.1141	1.55	0.2725
185.47	126,000	0.617	0.1539	2.59	0.1077	1.55	0.2573
208.66	126,000	0.617	0.1449	2.59	0.1015	1.55	0.2423
231.84	126,000	0.617	0.1361	2.59	0.0953	1.55	0.2276
255.03	126,000	0.617	0.1275	2.59	0.0892	1.55	0.2131
278.21	126,000	0.617	0.1190	2.59	0.0833	1.55	0.1989
301.39	126,000	0.617	0.1106	2.59	0.0774	1.55	0.1850
324.58	119,918	0.618	0.1077	2.59	0.0754	1.55	0.1800
348.36	113,475	0.618	0.1048	2.59	0.0733	1.55	0.1751
372.81	106,843	0.618	0.1016	2.59	0.0712	1.55	0.1699
398.01	100,006	0.618	0.0983	2.59	0.0688	1.55	0.1644
424.05	92,944	0.618	0.0948	2.59	0.0664	1.55	0.1585
451.06	85,632	0.618	0.0910	2.59	0.0637	1.55	0.1521
479.21	78,041	0.618	0.0869	2.59	0.0608	1.55	0.1452
508.69	70,135	0.618	0.0824	2.59	0.0576	1.55	0.1377
539.79	61,865	0.618	0.0773	2.59	0.0541	1.55	0.1293
572.90	53,171	0.618	0.0717	2.59	0.0502	1.55	0.1199
608.61	43,969	0.618	0.0652	2.59	0.0456	1.55	0.1090
647.89	34,137	0.618	0.0575	2.59	0.0402	1.55	0.0961
692.47	23,498	0.618	0.0574	2.59	0.0400	1.55	0.0960
746.19	11,800	0.618	0.0574	2.59	0.0400	1.55	0.0960
822.01	0	0.000	0.0574	2.59	0.0400	1.55	0.0960

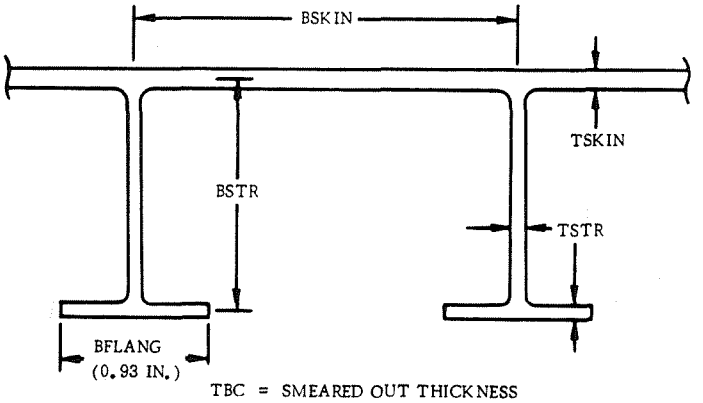

TBC = SMEARED OUT THICKNESS
MATERIAL: Ti-8Al-1Mo-1V

Table 6-23. FR-1 Wing Box - Tension Cover Gages

Station (in.)	SIGT (psi)	RHORQD (in.)	TSKIN (in.)	BSKIN (in.)	TSTR (in.)	BSTR (in.)	TBT (in.)
0.00	140,000	0.412	0.1976	2.65	0.2964	1.32	0.3458
23.18	140,000	0.412	0.1891	2.65	0.2837	1.32	0.3310
46.37	140,000	0.412	0.1808	2.65	0.2712	1.32	0.3164
69.55	140,000	0.412	0.1725	2.65	0.2587	1.32	0.3018
92.74	140,000	0.412	0.1643	2.65	0.2464	1.32	0.2874
115.92	140,000	0.412	0.1561	2.65	0.2342	1.32	0.2732
139.11	140,000	0.412	0.1481	2.65	0.2221	1.32	0.2592
162.29	140,000	0.412	0.1402	2.65	0.2102	1.32	0.2453
185.47	140,000	0.412	0.1323	2.65	0.1985	1.32	0.2316
208.66	140,000	0.412	0.1246	2.65	0.1869	1.32	0.2181
231.84	140,000	0.412	0.1170	2.65	0.1756	1.32	0.2048
255.03	140,000	0.412	0.1096	2.65	0.1644	1.32	0.1918
278.21	140,000	0.412	0.1023	2.65	0.1534	1.32	0.1790
301.39	140,000	0.412	0.0951	2.65	0.1427	1.32	0.1665
324.58	140,000	0.423	0.0881	2.71	0.1322	1.36	0.1542
348.36	140,000	0.434	0.0811	2.79	0.1217	1.40	0.1420
372.81	135,855	0.441	0.0764	2.83	0.1146	1.42	0.1337
398.01	127,161	0.441	0.0739	2.83	0.1108	1.42	0.1293
424.05	118,181	0.441	0.0712	2.83	0.1069	1.42	0.1247
451.06	108,884	0.441	0.0684	2.83	0.1026	1.42	0.1197
479.21	99,232	0.441	0.0653	2.83	0.0979	1.42	0.1142
508.69	89,179	0.441	0.0619	2.83	0.0928	1.42	0.1083
539.79	78,664	0.441	0.0581	2.83	0.0872	1.42	0.1017
572.90	67,609	0.441	0.0539	2.83	0.0808	1.42	0.0943
608.61	55,908	0.441	0.0539	2.83	0.0808	1.42	0.0943
647.89	43,407	0.441	0.0539	2.83	0.0808	1.42	0.0943
692.47	29,878	0.441	0.0539	2.83	0.0808	1.42	0.0943
746.19	13,329	0.416	0.0539	2.67	0.0808	1.34	0.0943
822.01	0	0.000	0.0539	2.67	0.0808	1.34	0.0943

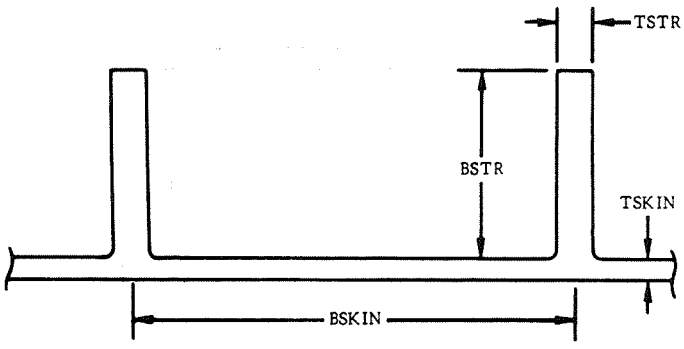

TBT = SMEARED OUT THICKNESS
MATERIAL: Ti-8Al-1Mo-1V

Table 6-24. FR-1 Wing Box - Web Gages and Torsional and Flexural Rigidities

Station (in.)	Webs		Rigidities	
	TBW (in.)	TAU (psi)	GJ (N) (lb-in.^{2} $\times 10^6$)	EI (N) (lb-in.^{2} $\times 10^6$)
0.00	0.1208	64,000	264,342	345,587
23.18	0.1182	64,000	248,518	322,412
46.37	0.1155	64,000	233,259	300,268
69.55	0.1128	64,000	218,556	279,129
92.74	0.1101	64,000	204,399	258,971
115.92	0.1073	64,000	190,783	239,769
139.11	0.1045	64,000	177,700	221,500
162.29	0.1016	64,000	165,141	204,139
185.47	0.0987	64,000	153,100	187,663
208.66	0.0958	64,000	141,569	172,050
231.84	0.0928	64,000	130,540	157,275
255.03	0.0898	64,000	120,007	143,316
278.21	0.0868	64,000	109,963	130,152
301.39	0.0839	63,804	100,469	117,761
324.58	0.0819	62,926	93,285	108,603
348.36	0.0798	61,971	86,186	99,628
372.81	0.0775	60,928	80,209	92,302
398.01	0.0752	59,782	75,371	86,611
424.05	0.0727	58,515	70,498	80,882
451.06	0.0701	57,104	65,575	75,098
479.21	0.0672	55,517	60,579	69,237
508.69	0.0641	53,711	55,484	63,265
539.79	0.0607	51,624	50,250	57,139
572.90	0.0569	49,165	44,819	50,794
608.61	0.0525	46,182	39,097	44,125
647.89	0.0473	42,407	32,925	36,955
692.47	0.0406	37,275	25,977	28,924
746.19	0.0400	22,584	19,126	20,361
822.01	0.0400	3	16,462	17,326

Table 6-25. FR-1 Wing Box - Truss Rib Member Cross-sectional Areas

Station (in.)	Diagonals ($in.^2$)						Caps ($in.^2$)						
	FB	BG	GC	CH	HD	DJ	AB	BC	CD	DE	FG	GH	HJ
23.18	0.36	0.45	0.38	0.32	0.31	0.22	0.29	0.52	0.52	0.29	0.90	0.90	0.90
115.92	0.32	0.37	0.35	0.28	0.26	0.19	0.25	0.42	0.42	0.25	0.69	0.69	0.69
208.66	0.26	0.30	0.28	0.23	0.21	0.15	0.25	0.34	0.34	0.25	0.55	0.55	0.55
301.39	0.22	0.24	0.24	0.19	0.17	0.15	0.25	0.26	0.26	0.25	0.42	0.42	0.42
398.01	0.17	0.18	0.18	0.15	0.15	0.15	0.25	0.25	0.25	0.25	0.31	0.31	0.31
508.69	0.15	0.15	0.15	0.15	0.15	0.15	0.25	0.25	0.25	0.25	0.25	0.25	0.25
608.61	0.15	0.15	0.15	0.15	0.15	0.15	0.25	0.25	0.25	0.25	0.25	0.25	0.25
692.47	0.15	0.15	0.15	0.15	0.15	0.15	0.25	0.25	0.25	0.25	0.25	0.25	0.25
746.19	0.15	0.15	0.15	0.15	0.15	0.15	0.25	0.25	0.25	0.25	0.25	0.25	0.25

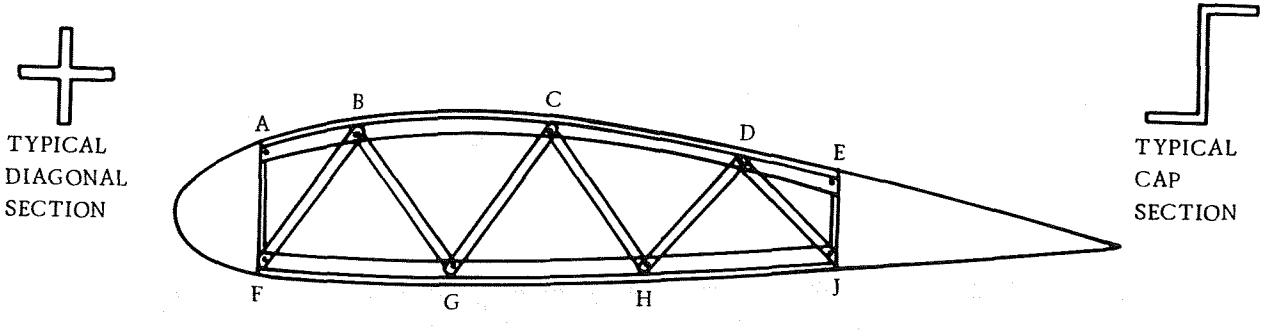

Table 6-26. FR-1 Orbiter and Booster Fin - Geometric Data and Maximum αq Loads

Station (in.)	Chord (in.)	Rib Spg (in.)	Ultimate			
			Shear (lb)	B. Mom. (in.-lb $\times 10^6$)	NY (+M) (lb/in.)	Torsion (in.-lb $\times 10^6$)
0.00	304.00	26.74	408,000	102.2	28,444	7.44
26.74	298.06	26.74	383,317	91.7	26,745	6.86
53.47	292.11	26.74	359,120	81.7	25,035	6.29
80.21	286.17	26.74	335,412	72.5	23,315	5.76
106.94	280.23	26.74	312,190	63.8	21,590	5.25
133.68	274.28	26.74	289,456	55.8	19,862	4.76
160.41	268.34	27.56	267,209	48.3	18,137	4.30
187.97	262.21	28.52	244,789	41.3	16,367	3.85
216.49	255.87	29.66	222,132	34.6	14,551	3.41
246.15	249.28	31.04	199,158	28.4	12,689	3.00
277.19	242.38	32.77	175,753	22.5	10,782	2.56
309.96	235.09	35.02	151,756	17.2	8,835	2.14
344.99	227.31	38.12	126,921	12.3	6,854	1.73
383.10	218.83	42.74	100,844	8.0	4,860	1.32
425.85	209.33	50.79	72,779	4.3	2,897	0.91
476.64	198.04	70.36	41,051	1.4	1,090	0.49
547.00	182.40	0.00	0	0.0	0	0.00

Table 6-27. FR-1 Orbiter and Booster Fin Boxes - Cover Gages

Station (in.)	SIGC (psi)	RHORQD (in.)	TSKIN (in.)	BSKIN (in.)	TSTR (in.)	BSTR (in.)	BFLANG (in.)	TBC (in.)
Orbiter: Material Ti-8Al-1Mo-1V								
0.00	121,005	0.730	0.1378	3.33	0.0965	2.10	0.63	0.2351
27.97	115,908	0.730	0.1349	3.33	0.0944	2.10	0.63	0.2301
56.56	110,544	0.730	0.1317	3.33	0.0922	2.10	0.63	0.2247
85.82	104,881	0.730	0.1283	3.33	0.0898	2.10	0.63	0.2188
115.87	98,884	0.730	0.1246	3.33	0.0872	2.10	0.63	0.2125
146.82	92,509	0.730	0.1205	3.33	0.0843	2.10	0.63	0.2055
178.81	85,701	0.730	0.1160	3.33	0.0812	2.10	0.63	0.1978
212.05	78,393	0.730	0.1109	3.33	0.0776	2.10	0.63	0.1892
246.80	70,494	0.730	0.1052	3.33	0.0736	2.10	0.63	0.1794
283.46	61,888	0.730	0.0985	3.33	0.0690	2.10	0.63	0.1681
322.57	52,410	0.730	0.0907	3.33	0.0635	2.10	0.63	0.1547
365.08	41,820	0.730	0.0810	3.33	0.0567	2.10	0.63	0.1382
412.66	29,744	0.730	0.0683	3.33	0.0478	2.10	0.63	0.1165
469.08	14,600	0.707	0.0528	3.23	0.0369	2.03	0.61	0.0900
547.05	0	0.000	0.0528	3.23	0.0369	2.03	0.61	0.0900
Booster: Material 718 Ni Alloy								
0.00	135,000	0.581	0.1235	2.65	0.0865	1.67	0.50	0.2107
26.74	135,000	0.581	0.1161	2.65	0.0813	1.67	0.50	0.1981
53.47	135,000	0.581	0.1087	2.65	0.0761	1.67	0.50	0.1854
80.21	135,000	0.581	0.1012	2.65	0.0709	1.67	0.50	0.1727
106.94	135,000	0.581	0.0937	2.65	0.0656	1.67	0.50	0.1599
133.68	131,284	0.573	0.0887	2.61	0.0621	1.65	0.49	0.1513
160.41	123,568	0.573	0.0860	2.61	0.0602	1.65	0.49	0.1468
187.97	115,391	0.573	0.0831	2.61	0.0582	1.65	0.49	0.1418
216.49	106,690	0.573	0.0799	2.61	0.0560	1.65	0.49	0.1364
246.15	97,382	0.573	0.0764	2.61	0.0535	1.65	0.49	0.1303
277.19	87,365	0.573	0.0723	2.61	0.0506	1.65	0.49	0.1234
309.96	76,499	0.573	0.0677	2.61	0.0474	1.65	0.49	0.1155
344.99	64,591	0.573	0.0622	2.61	0.0435	1.65	0.49	0.1061
383.10	51,362	0.573	0.0555	2.61	0.0388	1.65	0.49	0.0946
425.85	36,379	0.573	0.0555	2.61	0.0388	1.65	0.49	0.0946
476.64	18,953	0.573	0.0555	2.61	0.0388	1.65	0.49	0.0946
547.00	0	0.000	0.0555	2.61	0.0388	1.65	0.49	0.0946

Note: TBC is smeared out thickness.

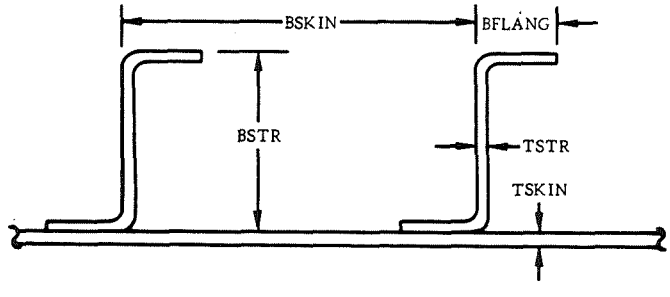

Table 6-28. FR-1 Orbiter and Booster Fin Boxes - Spar and Rib Corrugated Web Gages

Orbiter: Material Ti-8Al-1Mo-1V				Booster: Material 718 Ni Alloy			
	Spar Webs		Ribs		Spar Webs		Ribs
Station (in.)	TBW (in.)	TAU (psi)	TBR (in.)	Station (in.)	TBW (in.)	TAU (psi)	TBR (in.)
0.00	0.1065	59,466	0.0488	0.00	0.0839	75,480	0.0313
27.97	0.1030	59,271	0.0467	26.74	0.0813	75,245	0.0303
56.56	0.0995	59,010	0.0445	53.47	0.0787	74,941	0.0300
85.82	0.0958	58,668	0.0423	80.21	0.0760	74,558	0.0300
115.87	0.0920	58,228	0.0400	106.94	0.0734	74,087	0.0300
146.82	0.0879	57,665	0.0400	133.68	0.0706	73,515	0.0300
178.81	0.0837	56,946	0.0400	160.41	0.0679	72,829	0.0300
212.05	0.0792	56,025	0.0400	187.97	0.0650	71,983	0.0300
246.80	0.0743	54,834	0.0400	216.49	0.0619	70,937	0.0300
283.46	0.0689	53,267	0.0400	246.15	0.0586	69,632	0.0300
322.57	0.0630	51,150	0.0400	277.19	0.0550	67,985	0.0300
365.08	0.0560	48,161	0.0400	309.96	0.0512	65,864	0.0300
412.66	0.0500	41,444	0.0400	344.99	0.0468	63,056	0.0300
469.08	0.0500	25,242	0.0400	383.10	0.0417	59,167	0.0300
547.05	0.0500	16	0.0400	425.85	0.0354	53,349	0.0300
				476.64	0.0300	38,252	0.0300
				547.00	0.0300	0	0.0300

Table 6-29. FR-1 Orbiter and Booster Fin Boxes - Torsional and Flexural Rigidities

Orbiter: Material Ti-8Al-1Mo-1V			Booster: Material 718 Ni Alloy		
Station (in.)	GJ (lb-in.^{2} $\times 10^6$)	EI (lb-in.^{2} $\times 10^6$)	Station (in.)	GJ (lb-in.^{2} $\times 10^6$)	EI (lb-in.^{2} $\times 10^6$)
0.00	246,485	281,238	0.00	348,557	406,134
27.97	222,773	254,369	26.74	307,774	354,149
56.56	200,267	228,830	53.47	270,362	307,022
85.82	178,932	204,581	80.21	236,139	264,458
115.87	158,732	181,584	106.94	204,931	226,171
146.82	139,628	159,800	133.68	180,144	197,316
178.81	121,582	139,183	160.41	160,877	176,263
212.05	104,550	119,689	187.97	142,520	156,174
246.80	88,484	101,264	216.49	125,039	137,014
283.46	73,324	83,841	246.15	108,395	118,743
322.57	58,991	67,335	277.19	92,542	101,312
365.08	45,365	51,610	309.96	77,422	84,658
412.66	32,698	36,417	344.99	62,950	68,691
469.08	21,722	22,527	383.10	48,993	53,267
547.05	15,755	16,233	425.85	35,290	38,108
			476.64	21,797	22,482
			547.00	12,218	11,626

SECTION 7

AEROELASTIC EFFECTS

The aeroelastic analyses consisted of a preliminary flutter analysis, a wing-deployment deflections analysis, and an analysis of the static aeroelastic effects on the body. The flutter analysis was conducted on the FR-3 configuration; however, since the wings of the FR-1, FR-3, and FR-4 vehicles are quite similar, the results are generally applicable to all of the vehicles.

7.1 FLUTTER ANALYSIS

The flutter analysis for FR-3 was performed using a digital program utilizing Theodorsen incompressible aerodynamics. The wing model used is shown in Figure 7-1. The first three uncoupled wing bending modes and the first uncoupled wing torsion mode were used in the analysis.

The results of runs made at sea level and 25,000 feet are shown in Figures 7-2 and 7-3 respectively. Figure 7-2 shows a flutter speed of 920 feet per second at sea level. This speed should be reduced to about 810 feet per second to allow for compressibility effects. Specification MIL-A-8870 (ASG) requires a 15-percent flutter margin beyond the limit dive speed. Depending on the limit dive speed envelope, some additional torsional stiffness may be required to meet this requirement at the lower altitudes. The effects of torsional stiffness are presented in Figure 7-4. It is concluded from these results that flutter presents no significant design problems for these deployable-wing vehicles.

7.2 WING DEPLOYMENT DEFLECTION

An investigation of the FR-1 vehicle was performed to determine the magnitude of wing bending deflections during wing deployment, with consideration given to interference between wing and body structure.

To define the basic geometry, a layout was made showing the wing at various sweep angles and the location of the relevant body structure (Figure 7-5). Based on this geometry, the wing loadings at several sweep angles were derived (Figure 7-6).

The wing-loading curves were used to obtain the bending moments shown in Figure 7-7. These moment curves were then used to obtain the deflection curves for several sweep angles given in Figure 7-8.

From the basic geometry layout, the interference points of the wing with the upper body structure were located for each sweep angle, assuming the wing would make contact at the highest point on the airfoil. (For the NACA 4421 airfoil, the maximum height is at 30 percent chord.) A plot showing the wing interference station as a function of sweep angle is given in Figure 7-9.

Expanding the deflection scale of Figure 7-8, the plot of wing interference station versus sweep angle (Figure 7-9) was used to establish the wing deflections at the interference points (Figure 7-10). The resulting dashed curve may be used in sizing the opening and/or locating tracks or guides to eliminate scraping and binding during wing extension.

The dashed curve also indicates that nominal clearances of approximately 1.5 inches at the front and 2.5 inches at the aft end of the opening are required without the use of tracks or guides.

7.3 STATIC AEROELASTIC ANALYSIS

Static aeroelastic factors for the FR-1 vehicle during boost were computed. The vehicle was assumed to be trimmed in pitch against a 99 percentile WTR headwind. This was found to be the worst case in the rigid vehicle analysis. The elastic representation was identical to that used to compute vibration modes. Fundamental bending mode frequencies for the booster and orbiter are:

Vehicle	Mass Condition	Frequency (cps)
Booster	Full	2.5
Booster	t = 75 secsond	3.3
Booster	Empty	3.7
Orbiter	Full	2.6
Orbiter	Burnout + Payload	3.1
Orbiter	Flyback	3.3

The ratio of elastic-to-rigid total normal force coefficient for the booster and orbiter at maximum αq is 1.02 for each vehicle.

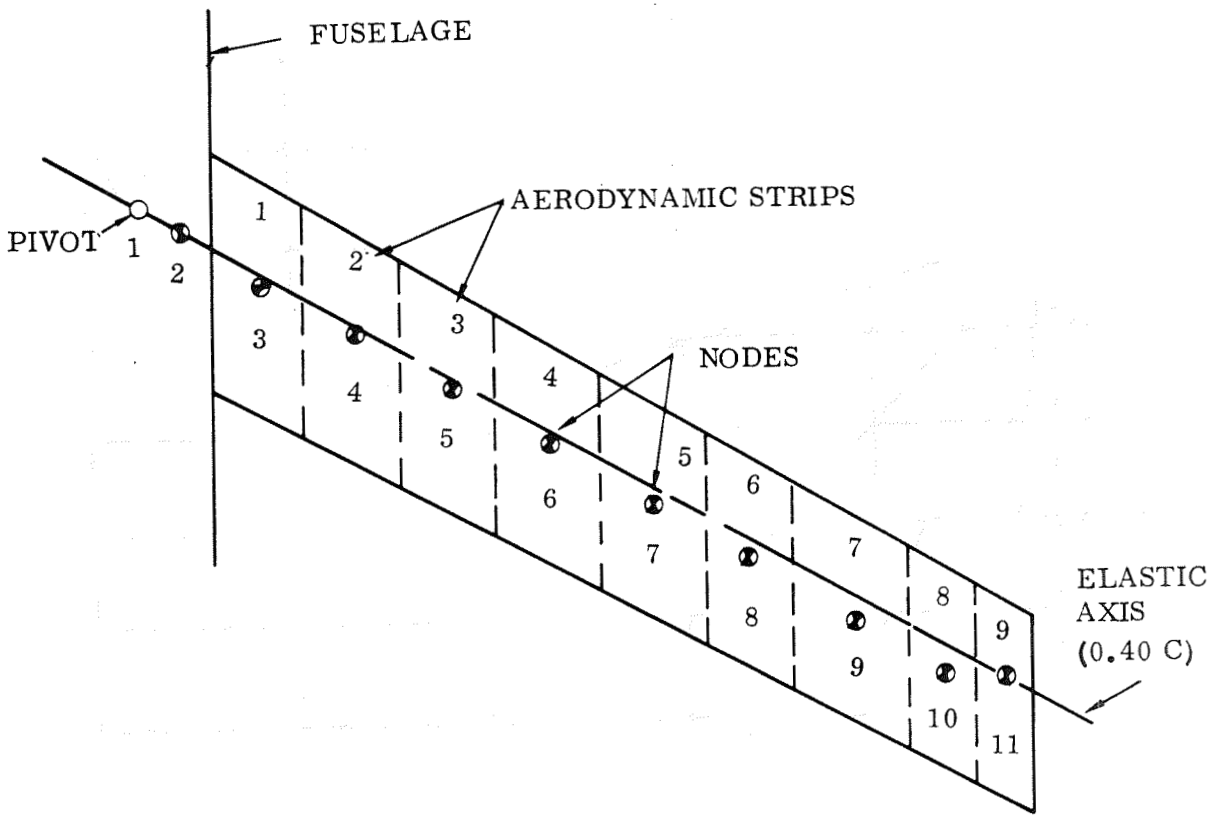

Figure 7-1. Wing Flutter Model

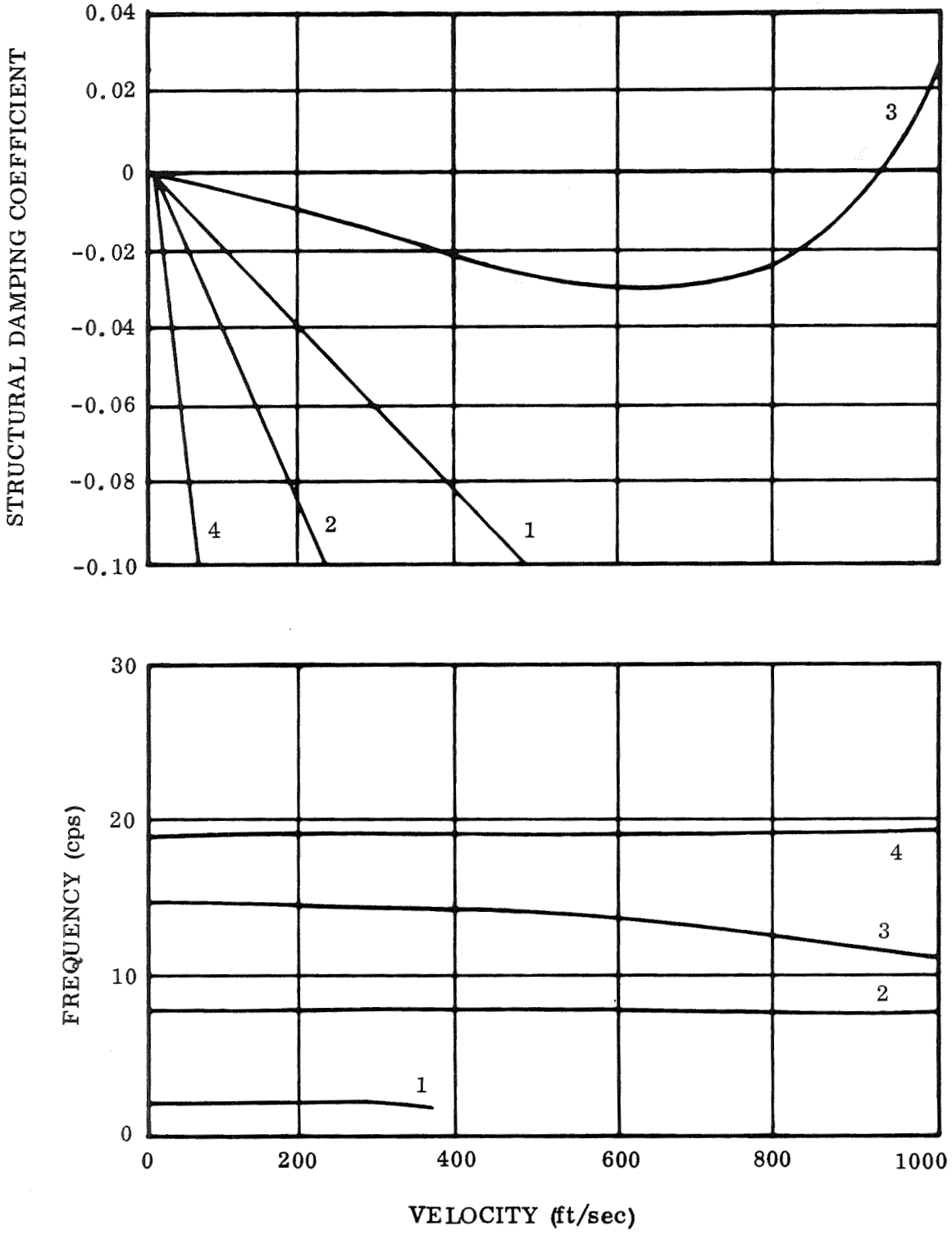

Figure 7-2. Sea Level Incompressible Flutter Results

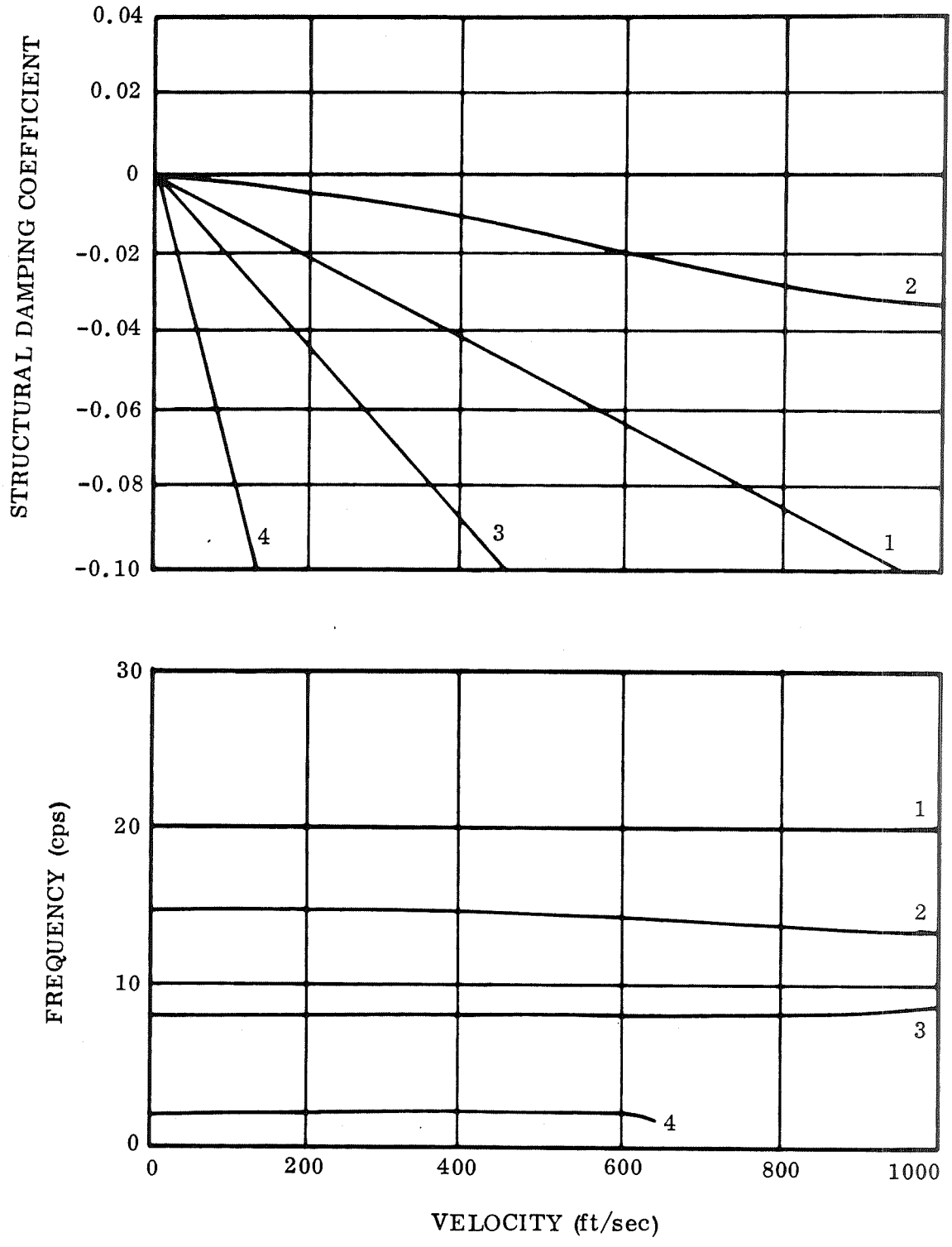

Figure 7-3. 25,000-Foot Altitude Incompressible Flutter Results

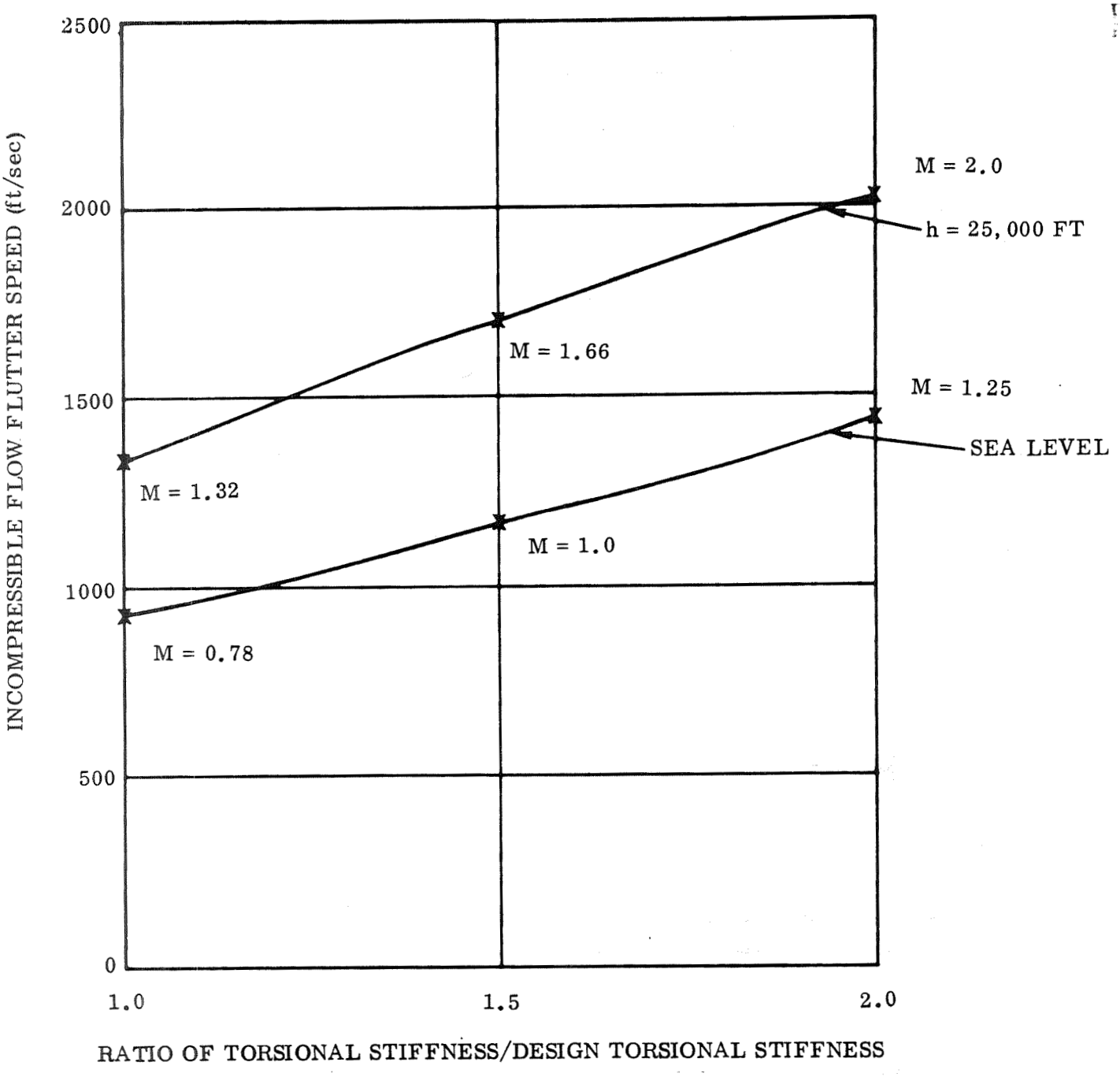

Figure 7-4. Effect of Wing Torsional Stiffness on Flutter Speed

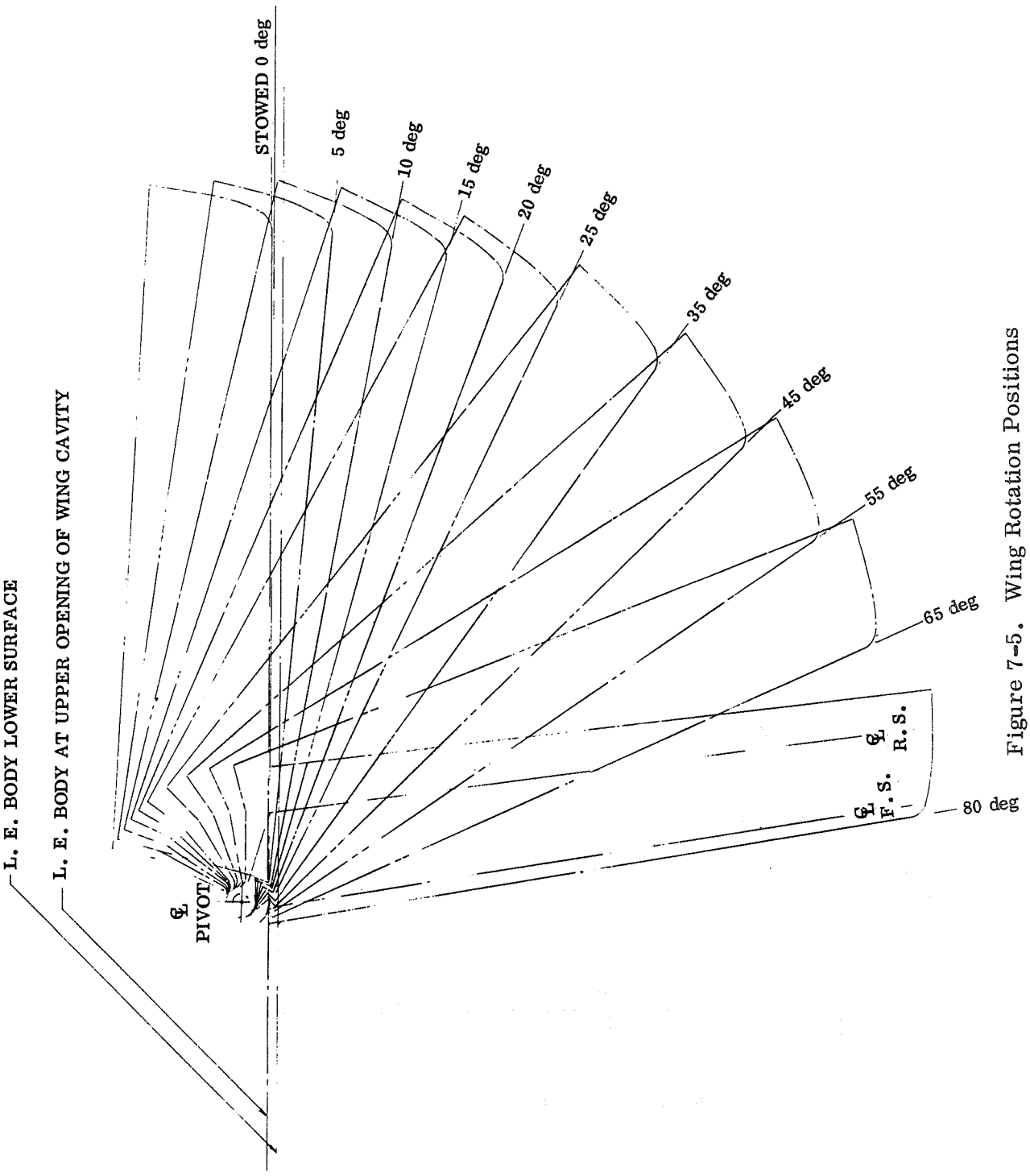

Figure 7-5. Wing Rotation Positions

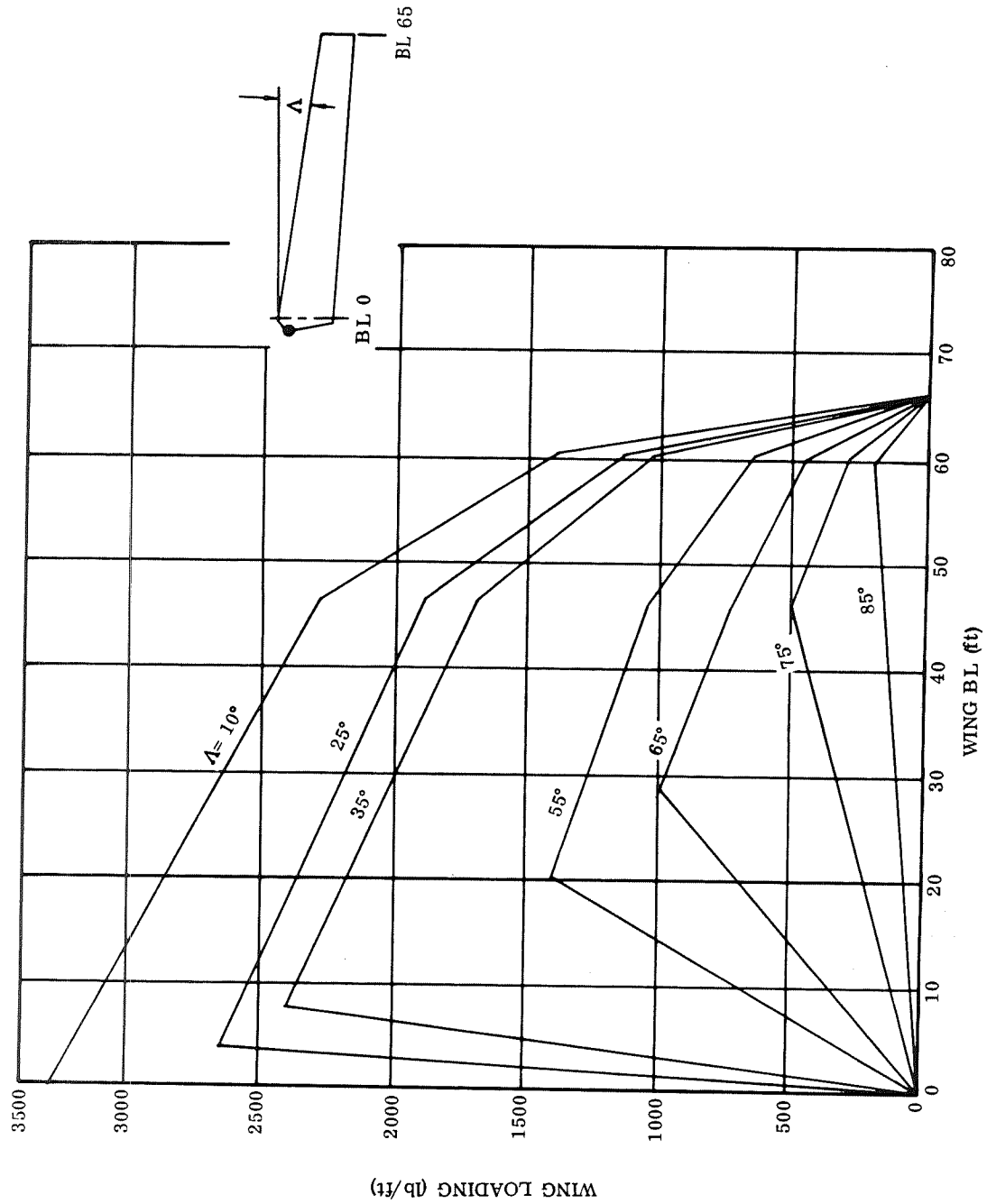

Figure 7-6. Wing Deployment Loads

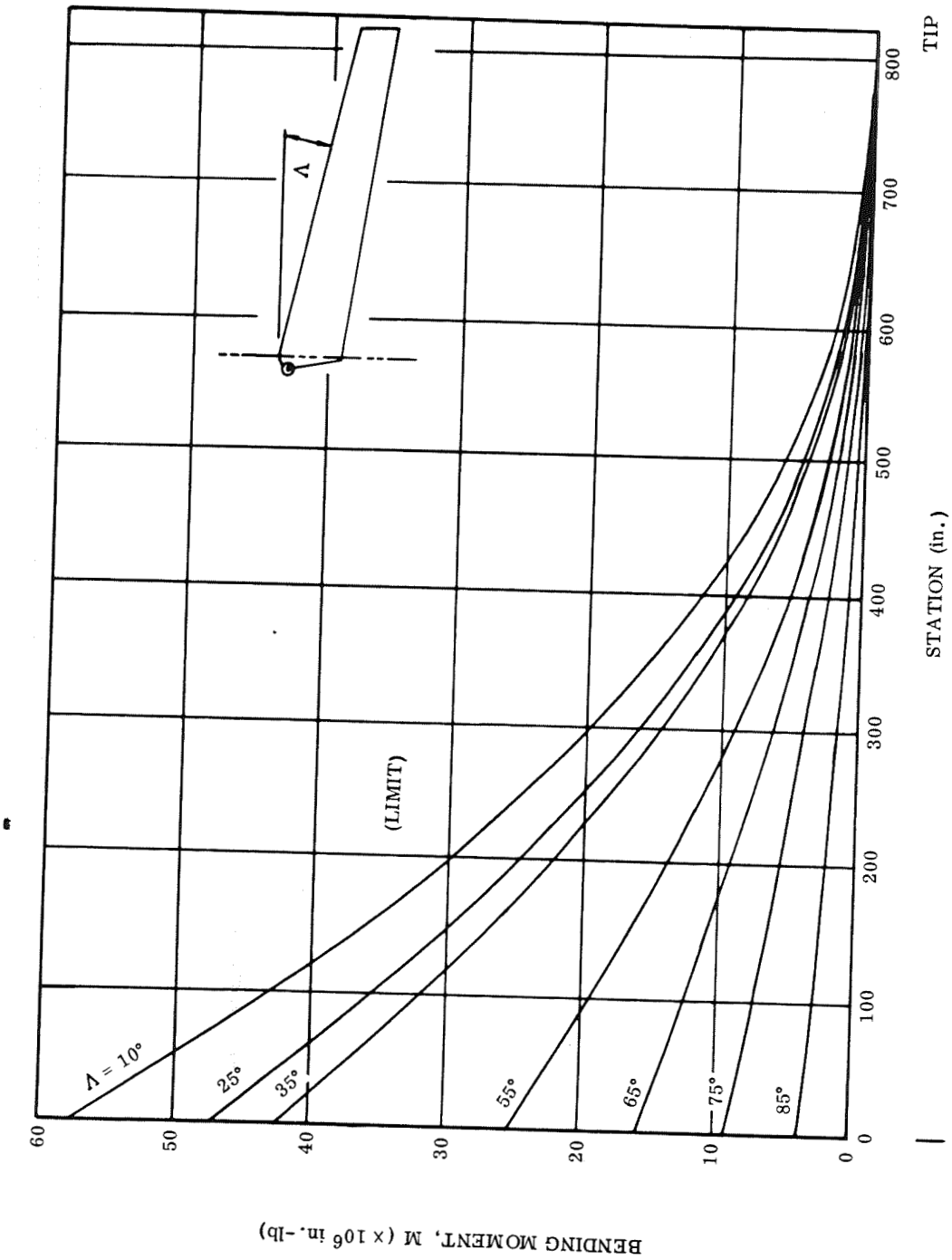

Figure 7-7. Wing Bending Moments at Various Sweep Angles

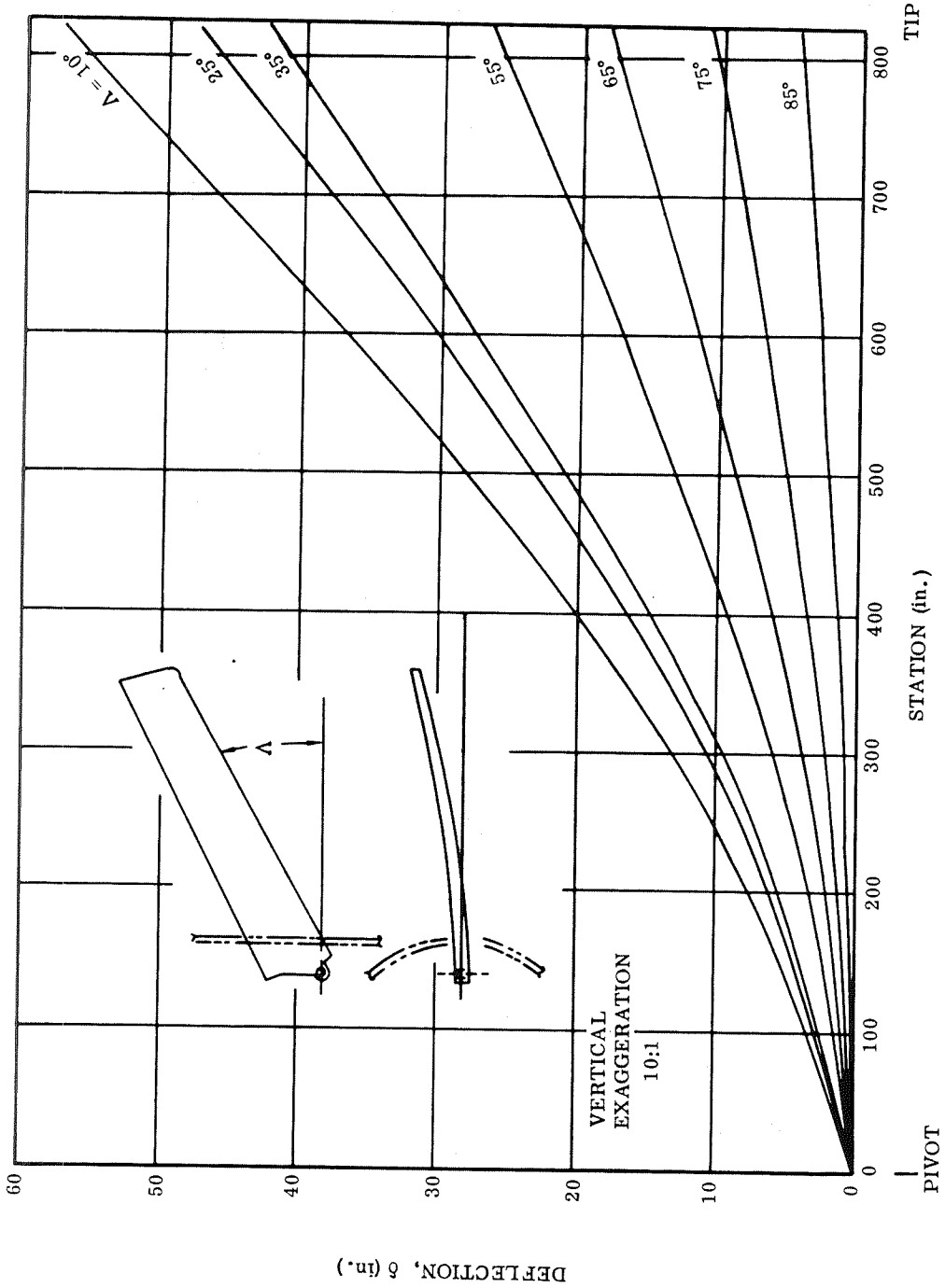

Figure 7-8. Wing Deflections at Various Sweep Angles (Limit Deployment Loads)

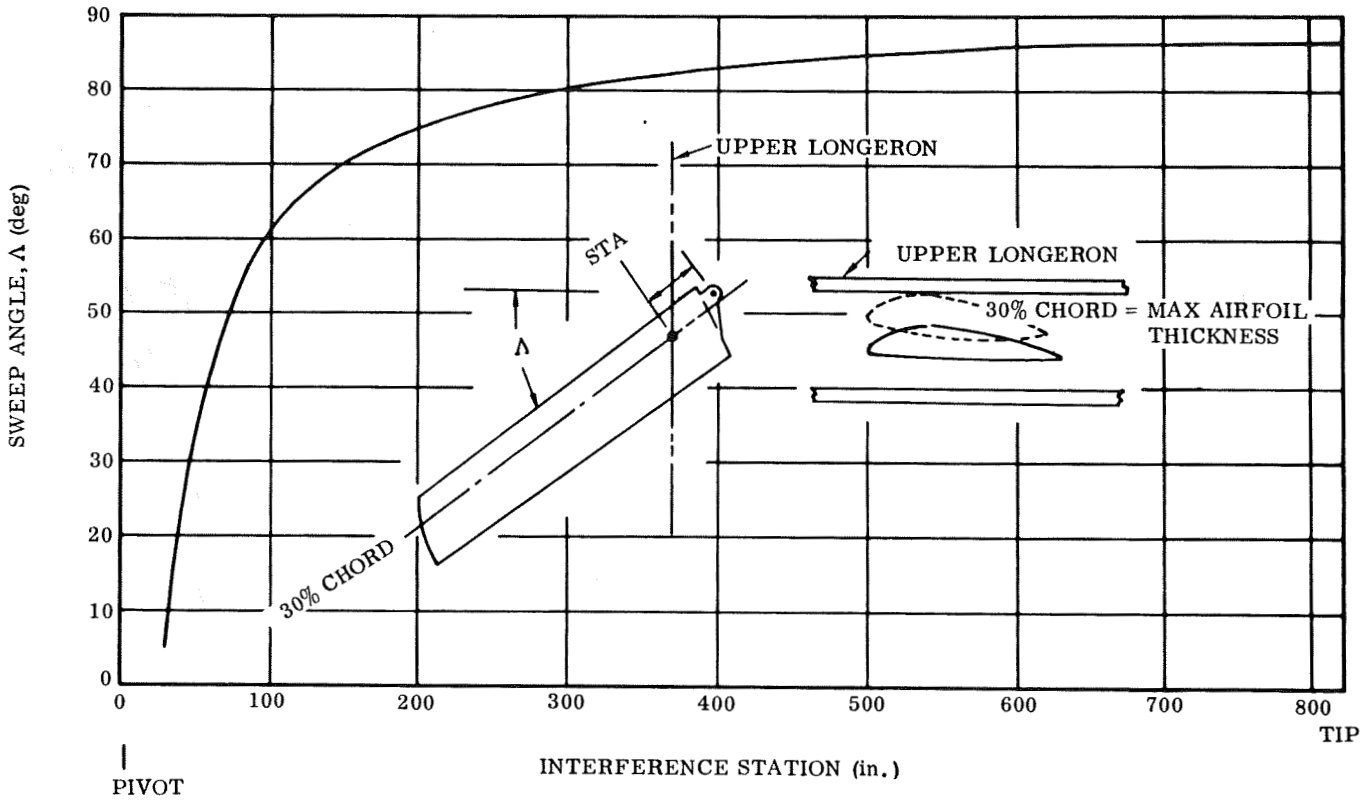

Figure 7-9. Wing Interference Station versus Sweep Angle

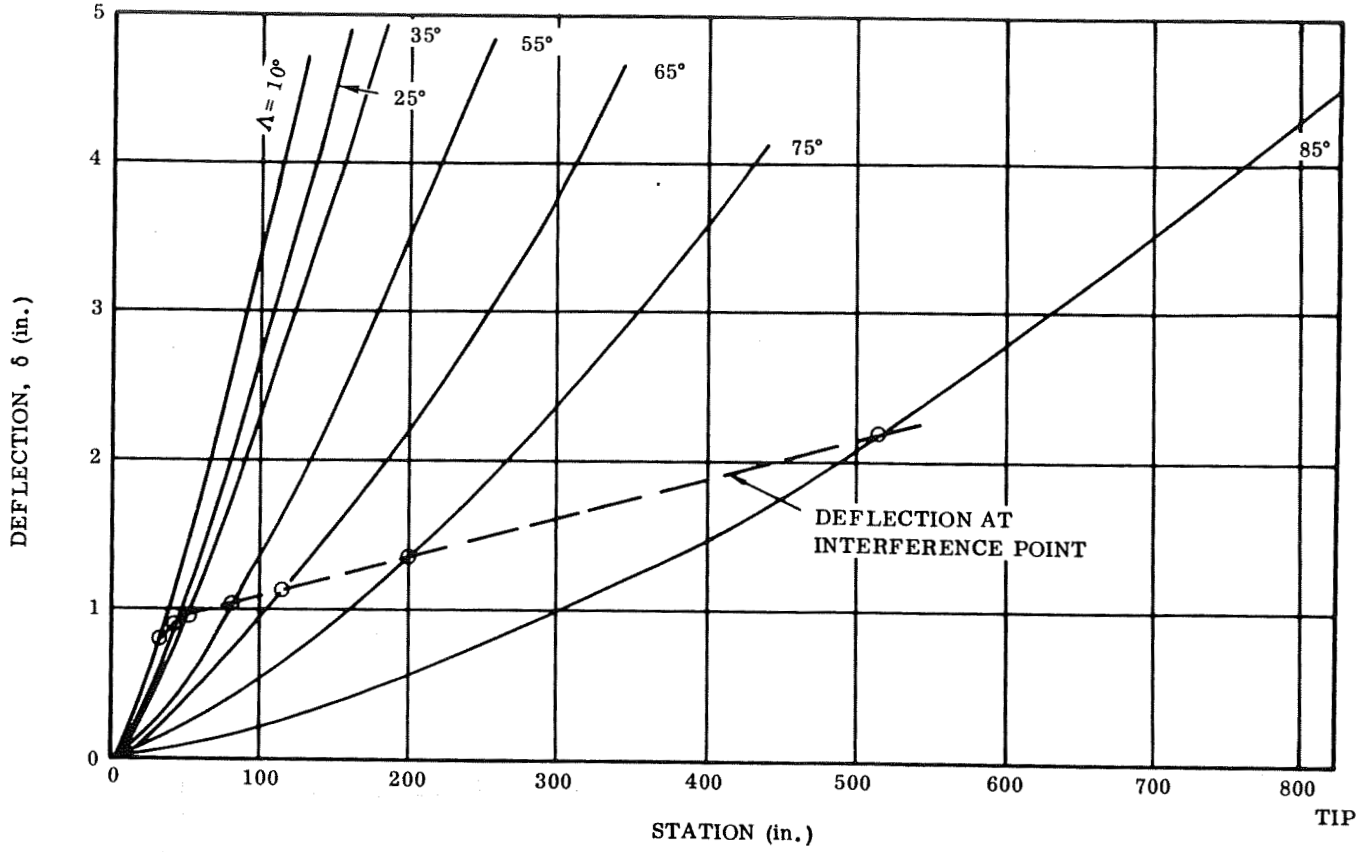

Figure 7-10. Deflection versus Station (Limit)